



SAPIENZA
UNIVERSITÀ DI ROMA

Design study of plasma targets for laser driven wakefield acceleration experiments

Ph.D. School on Accelerator Physics

Dottorato di Ricerca in Fisica degli Acceleratori – XXXIII Ciclo

Candidate

Gemma Costa

ID number 1256488

Thesis Advisors

Prof. Alessandro Cianchi

Prof. Massimo Ferrario

31 January 2021

Thesis defended on 28 April 2021
in front of a Board of Examiners composed by:
Prof. Pasquale Arpaia (chairman)
Prof. James Rosenzweig
Prof. Giovanni Mettivier

Design study of plasma targets for laser driven wakefield acceleration experiments


Ph.D. thesis. Sapienza – University of Rome

© 2021 Gemma Costa. All rights reserved

This thesis has been typeset by L^AT_EX and the Sapthesis class.

Version: April 29, 2021

Author's email: gemma.costa@lnf.infn.it



Design study of plasma targets for laser driven wakefield acceleration experiments

G. Costa

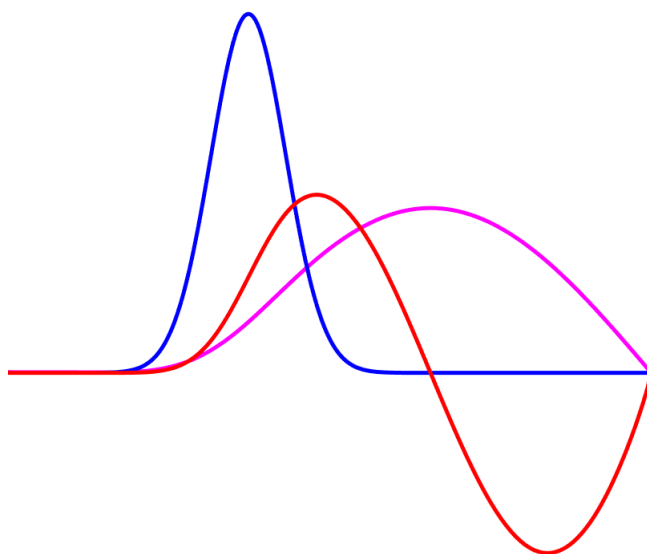
PLASMA PHYSICS FOR COMPACT ACCELERATORS

SPARC_LAB - INFN FRASCATI

A mamma, papà e Giada che hanno accolto e subito le mie ansie e i miei nervosismi in un posto insostituibile chiamato famiglia.

A Marco che mi rende una persona migliore ogni giorno in mille abbracci diversi.

A Settimia e Zia Mariella. A chi è vicino anche se lontano.



Abstract

The strength of plasma-based accelerators is their compactness, thanks to the plasma accelerator modules, which have dimensions of the order of cm. The limitation of this type of acceleration lies in the difficult control of the characteristics of the plasma itself, and therefore in the synchronisation between it and the particle beam to be accelerated. This issue has a major influence on the quality of the accelerated bunches.

In this work, a characterisation conducted in the SPARC_LAB (LNF-INFN) laboratories on some plasma targets, i.e. different nozzle geometries and different types of capillaries, is presented. The main goal of the work is the study and the realisation of the plasma guiding process of a laser pulse, inside a plasma-filled capillary discharge. This technique is necessary to increase the acceleration length and thus the energy gain of the accelerated beam, in the external-injection scheme of the Laser Wake Field Acceleration (LWFA). Plasma density is a characteristic of fundamental importance as it determines both the guiding and the acceleration process. Two different methods of plasma density measurement, interferometric and spectroscopic, are therefore reported. Preliminary studies of new techniques for the diagnostics of plasma inside channels and new schemes for the delivery/extraction of laser pulses inside capillaries are proposed. All topics covered include theoretical study, one-dimensional and/or fluid-dynamic simulations, and experimental data.

Contents

Contents	1
List of Figures	3
List of Tables	13
1 Introduction	15
1.1 Motivation to plasma based accelerators	15
1.2 What is the project of this PhD?	16
2 Plasma based Acceleration	19
2.1 Plasma definition and high acceleration gradient	19
2.2 Laser driven plasma acceleration	23
2.2.1 Electron motion in a laser field	24
2.2.2 Ponderomotive force and self-injection in the blow-out regime	25
2.3 Limitations to laser wakefield acceleration	28
3 Plasma based experiments at LNF-INFN	31
3.1 The SPARC_LAB test facility	31
3.2 The FLAME laser	34
3.2.1 The EXIN project	36
4 Targets for self-injection experiments	39
4.1 Supersonic gas jet study	39
4.2 Nozzle fluid-dynamics simulations	43
4.2.1 One-dimensional stationary model	44
4.2.2 OpenFOAM fluid-dynamic simulations	46
4.3 Plasma density from nozzles gas jet	48
4.3.1 Interferometric method for plasma measurements	50
4.3.2 Analysis of plasma density measurements	51
5 Plasma channels for laser confinement	55
5.1 Theoretical introduction and state of the art	55
5.1.1 Guiding of Gaussian pulses	56
5.1.2 Capillary discharge channels	57
5.1.3 Matched spot size r_m	59
5.1.4 Laser heating mechanism	61

5.2	Theoretical introduction to the Stark broadening plasma measurements	62
5.2.1	Balmer lines characterisation	64
5.3	Low-power laser guiding tests	65
5.3.1	Set-up and discharge circuit	65
5.3.2	Test with 270 A discharge maximum current	69
5.3.3	Guiding test through a density hollow profile	81
5.3.4	Guiding tests for different capillary geometry	92
6	Plasma density measurements for alternative geometries	95
6.1	Plasma density in a 500 μm -diameter capillary	95
6.2	Plasma density saturation	97
6.3	Different capillary diameters	102
6.4	Different capillary gas injection methods	105
6.5	Plasma density ramps for different capillary geometries	107
7	Future perspectives	113
7.1	Ongoing projects and their perspectives	113
7.1.1	Interferometric methods for capillary density measurements	113
7.1.2	Capillary aging and new geometry designs	120
7.1.3	Curved capillary channel	124
7.2	Future developments	128
	Conclusions	133
	A The Mach-Zender interferometer	135
	B OpenFOAM simulations for gas-filled capillaries	137
	Bibliography	141
	Acknowledgments	155

List of Figures

2.1	Slab or capacitor model of oscillating electron layer [1], where n_0 is the total plasma density.	20
2.2	Schematic of the plasma laser acceleration process proposed by T. Tajima and J.M. Dawson in 1979 [2]. The driver pulse, which can be a short laser pulse or an electron beam, generates a separation of charge in a gas, or plasma, forming a bubble: the electric field E_z thus created is capable of accelerating the charged particles, located at the back of the bubble, which move in the direction of the field itself.	21
2.3	Trajectory of an electron in the laser transverse field, in the laboratory frame for two values of the laser strength. The longitudinal momentum scales with the square of the laser strength as a_0^2 , while the transverse one linearly depends on a_0 [3].	25
2.4	Illustration of the two regimes of the laser wakefield: Left) Excitation of a plasma wave in the linear regime. 3D view and projection in the horizontal plane of the normalized laser intensity, a_0 , and wake potential, φ . Right) Excitation of a plasma wave in the non-linear regime. Map of density in the horizontal plane (grey scale, white is zero) and superposition of laser amplitude (color scale, red is a maximum) [3].	27
2.5	Single particle orbits in phase space for an electron in a small amplitude sinusoidal plasma wave: the dashed curve is the cold fluid orbit, the solid curve is the separatrix orbit [4].	28
3.1	Layout of the SPARC bunker. The RF gun is followed by an hybrid acceleration system consisting of two S-band and a C-band Traveling Wave (TW) structures, a THz source station and a vacuum chamber devoted to plasma-based experiments. A 14° dipole delivers the electron beam towards four beam lines devoted to FEL physics, beam diagnostics, Thomson back-scattering and plasma acceleration external injection experiments using the FLAME laser pulse.	32
3.2	Example of gas-filled capillary discharge used for PWFA in SPARC_LAB (COMB interaction chamber). The capillary has a length of 3 cm and a diameter of 1 mm.	33
3.3	CPA schematic for the compression of a laser pulse, showing the two processes of stretching and compression through grating pairs [5].	34

3.4	Layout of the Flame high-power laser, including the clean room, with the laser chain from the oscillator to the third amplifier, the target area, with the compressor and interaction chamber, and the control room.	35
4.1	Sketch of the setup for a gas jet, on which a laser pulse is focused, coming out of a nozzle, generating a plasma channel inside the jet. The nozzle shown is a real CAD drawing of prototypes made at SPARC_LAB.	40
4.2	Sketch of the inner wall section of a nozzle: the tube has a narrowing, i.e. a point of minimum area in the transverse section, followed by a conical widening. The nozzle shown is a real CAD drawing of prototypes made at SPARC_LAB.	41
4.3	Representation of functions for the main nozzle restriction geometries, considered within the developed analytical model: a) smooth narrowing, b) linear narrowing, c) sharp narrowing. The red lines set the limits of the narrowings.	45
4.4	Flow density reproduced by the stationary analytical model for nozzle narrowing geometries: a) smooth, b) sharp. The flux density in the laser focal plane are about $2.8 \times 10^{18} \text{ cm}^{-3}$ and $1 \times 10^{18} \text{ cm}^{-3}$, respectively.	46
4.5	CAD drawings showing the inside walls of the two nozzles with different geometries: a) smooth throat, b) sharp throat. The first one is based on the second one, smoothing the corners by 0.2°	47
4.6	Results of OpenFOAM simulations of flow density and longitudinal velocity for the two nozzle geometries considered: a) smooth throat, b) sharp throat. The case of sharp throat appears to be too turbulent to be computed in this way.	47
4.7	Results of an OpenFOAM simulation for the flow density in the of smooth throat nozzle, as a function of the simulation evolution time.	48
4.8	Spot of the main laser pulse in the focal plane: FW $1/e^2 = 20 \mu\text{m}$	49
4.9	Photo of one of the nozzles installed, in the centre of the interaction chamber. The objective that is next to the nozzle belongs to the CCD used to measure the pulse focus.	49
4.10	Interferogram in the absence of plasma, i.e. without fringe shift. At the bottom the nozzle shadow can be seen, the width of which has a known size and can be used to calibrate the measurements.	50
4.11	Interferograms in the presence of plasma, produced by gas jets from the two different types of nozzle considered: a) smooth throat, b) sharp throat.	51
4.12	Plasma density longitudinal profile. Interferogram analysis produced by gas jets from the two different types of nozzle considered: a) smooth throat, b) sharp throat.	52
5.1	Sketch of a typical beam geometry around the focal point.	56
5.2	Schematic diagram of the gas-filled slow capillary discharge, and the associated discharge circuit [6].	58

5.3	Inside and outside images of the vacuum chamber in the guiding station: The red path represents the laser pulse line, while the blue one represents the plasma recombination light, described in the next Sections.	66
5.4	3D printed capillary with length 3 cm, diameter 500 μm and double-inlet injection.	67
5.5	Laser pulse signal (blue) and current curve signal coming from the discharge circuit output channel (blue), for a capillary of 3 cm long and 500 μm	67
5.6	Laser line setup, including interaction zone and output beam diagnostics.	68
5.7	Discharge detected by <i>CCD 3</i> , triggered with respect to the trigger of the high voltage circuit.	68
5.8	Photos of the inside of the discharge circuit, including the fast high voltage switch.	69
5.9	Output signals from the discharge circuit (red) and from the photodiode on the laser line (blue), in presence and absence of the pulse (up). Photodiode signal in the presence of the laser, subtracted from the noise coming from the discharge (down). Capillary diameter 1 mm.	70
5.10	Time zoom: photodiode signal in the presence of the laser, subtracted noise from the discharge, superimposed on the respective discharge curve. Capillary diameter 1 mm.	71
5.11	Photodiode signal on the laser line, superimposed on the relative discharge curve: the two green horizontal lines represent the threshold of the initial laser intensity and the maximum increase obtained, while the two black vertical lines delimit the chosen guiding time window, like the one in which there is a laser signal increase of 30%. Capillary diameter 0.5 mm	72
5.12	Schematic of the trigger system used to time the experiment with a single pulse. It involves the use of two DG535 Delay Generator and includes a monitor to display the time overlap of the signals created.	73
5.13	Oscilloscope screenshots with laser pulse and discharge signals: a) Laser synchronised before the start of the discharge; b) Laser synchronised in the guiding window; c) Laser synchronised in the tail of the discharge curve.	73
5.14	Scan of laser pulses superimposed on a discharge curve: the delays are set at 100 ns each and a statistical acquisition has been made for each one.	74
5.15	Scan of laser pulses superimposed on a discharge curve: the delays are set at 100 ns each and a statistical acquisition has been made for each one. Only the maximum signal pulses for each delay are shown.	74
5.16	Average variation of the laser pulse intensity with respect to the time position between the arrival of the laser and the discharge curve area. Here the laser intensity values were corrected for the filters used to attenuate the signal.	75
5.17	Scan the variation in intensity of the laser pulse with respect to the position in the discharge curve, detail of the guiding window. Only the maximum signal pulses for each delay are shown.	75

5.18	Oscilloscope screenshots with persistence setting: laser pulse (blue) over time: a) approx. 30 minutes and b) approx. 3 hours respectively. The other waveforms represent the signals on which the laser pulse is triggered.	76
5.19	Analysis of drift and jitter data of the laser pulse: variation of the arrival time of the pulse and variation of its energy after a) about 30 minutes and b) about 3 hours.	77
5.20	Images of the laser pulse used: a) spot in focus, b) image on the capillary output plane but without the capillary on the laser line. . .	78
5.21	Images of the capillary output plane, synchronising the impulse respectively a) before the discharge, b) in the guiding window, c) in the discharge tail.	78
5.22	Scan of the laser exiting the capillary around the delays already considered previously. Pulse intensity signal (blue), current signal in the considered delay (red), intensity of the laser output spot on the <i>CCD imaging</i> (green).	79
5.23	CAD file profile containing the objects positioned on the Hexapod plane, including the capillary: a support to hold the capillary anchoring the plane, a bridge support to bind the solenoid valve, a fire plane sight, an iris system and a diaphragm. The iris system, which is only used for laser diagnostics without the capillary, is on a line parallel to the one of the capillary, as it is moved by a motorised sled below. . .	80
5.24	Image taken from the <i>imaging CCD</i> , positioned so as to look at the laser focus plane. Since this parallelepiped is on the same transverse plane, by focusing on it, it is possible to calibrate the camera and identify the capillary input plane, as well as the output plane. . . .	81
5.25	Setup upgraded for the second experimental guiding campaign. Two lines capable of diagnosing the emitted plasma radiation (longitudinal and transverse) have been added.	82
5.26	Laser spot on the focus plane and analysis of its horizontal profile: it is not a perfectly Gaussian beam due to non-uniformity in the transverse profile of the initial laser beam, before the focusing. . . .	84
5.27	Screenshot of a time measurement of the beam, made with the <i>LX Spider</i> in the Clean Room.	85
5.28	Upgrade of the discharge circuit to provide a peak current of approximately 500 A, while maintaining the same input voltage. The schematic of the connections of the delay generator and gas distribution, as well as that of the capillary and longitudinal plasma diagnostics, are also shown in the figure. <i>This sketch is courtesy of A. Biagioni.</i>	85
5.29	Example of data from the spectrometer. Radiation from the entire longitudinal profile of the capillary. Image rotated by 90% to be visually superimposed on the geometry of a capillary sketch.	86
5.30	Analysis of longitudinal plasma profiles: time scan inside the guiding window from 200 ns to 400 ns in steps of 20 ns.	87
5.31	Statistical analysis of the longitudinal plasma profile in the chosen delay (300 ns), average and statistical error of 50 acquisitions. . . .	87

5.32	Example of transverse profile data of plasma radiation, on the capillary output plane. A sketch of the capillary profile has been superimposed. The hollow profile effect used for guiding is evident, along the vertical direction, i.e. the one representing the imaging of the source.	88
5.33	Analysis of transverse plasma profiles: time scan inside the guiding window from 200 ns to 300 ns in steps of 20 ns (a). Statistical analysis of the chosen delay (300 ns), average and statistical error on 50 acquisitions, with the simulated curve (b).	88
5.34	Statistical analysis of the laser signal output from the capillary for three different delays from the beginning of the discharge. Discharge curve with statistical average of the whole laser run, superimposed on the laser pulses. The average intensity obtained in the guiding window is approximately 88% of its initial value, since the beam transmission before the discharge (blue) is the 50% of the focus intensity.	89
5.35	Images of the capillary output plane, subtracted from the background: a) pulse propagation without the capillary on the line, b) pulse propagation inside the capillary without plasma, c) pulse output from the guiding window.	89
5.36	Example of statistical acquisition of guided beam out of the capillary, delay of 300 ns with respect to the beginning of the discharge. . . .	90
5.37	Examples of data analysis of horizontal profiles of guided spots. Although the laser spot is slightly larger than the focus spot, the transverse profile is really similar.	90
5.38	Statistical analysis of laser signals coming out of the capillary with a diameter of 700 μm , superimposed on the signal of a discharge curve also averaged. The delay shown in the central part of the discharge is the one that maximises the intensity of the laser pulse. The average intensity obtained in the guiding window is approximately 60% of its initial value, since the beam transmission before the discharge (blue) is the 50% of the focus intensity.	92
5.39	Longitudinal density profile analysis for the capillary with diameter 700 μm . Since the other initial conditions have remained unchanged, the plasma density obtained is lower than that obtained for the capillary with a diameter of 500 μm	93
5.40	Transverse density profile analysis for the capillary with diameter 700 μm . The trend obtained is not attributable to a hollow profile, and therefore it is not suitable for guiding the laser pulse.	93
5.41	CAD image of the capillary with a length of 3 cm, a diameter of 500 μm and a single central inlet, also of diameter of 500 μm	94
5.42	Statistical analysis of laser signals coming out of the capillary with a diameter of 500 μm and 1 inlet, superimposed on the signal of a discharge curve also averaged. The delay shown in the central part of the discharge is the one that maximises the intensity of the laser pulse. The average intensity obtained in the guiding window is approximately 70% of its initial value, since the beam transmission before the discharge (blue) is the 50% of the focus intensity.	94

6.1	Comparison of the longitudinal plasma density profile measured using the Balmer alpha line (red) and beta line (blue). Between the two curves' intensities there is a factor 2, compatible within the error with the expected theoretical data [7,8].	96
6.2	Scan of the mean values of longitudinal density with relative statistical error (blue), superimposed on the discharge curve also averaged for each acquired time (red). Statistical analysis of 50 samples.	96
6.3	Different output current curves of the discharge circuit, for the same capillary, for three different input voltages: 20 <i>kV</i> (red), 15 <i>kV</i> (blue) and 10 <i>kV</i> (black).	97
6.4	Comparison of plasma densities obtained with different voltages applied to the capillary extremities: 20 <i>kV</i> (red), 15 <i>kV</i> (blue) and 10 <i>kV</i> (black). The errors on the measured plasma density vary from 8% (20 <i>kV</i>), up to about 10% (10 <i>kV</i>) due to the different signal to noise ratio. Statistical analysis of 50 samples.	98
6.5	Results at the final time-step (1 <i>ms</i>) of four simulations of the longitudinal hydrogen profile, at the centre of the capillary channel, with initial pressures on the main inlet respectively of 360 <i>mbar</i> (red), 100 <i>mbar</i> (magenta), 38 <i>mbar</i> (blue), 10 <i>mbar</i> (light blue). The two maxima in the curves are at the two inlets where the gas pressure is highest.	99
6.6	Scan of output current curves of the discharge circuit, for the same capillary, for different input voltages since 18 <i>kV</i> to 22 <i>kV</i> , with a step of 1 <i>kV</i>	100
6.7	Scan of the longitudinal plasma density profiles with varying input voltage to the discharge circuit: from 18 <i>kV</i> to 22 <i>kV</i> , with step of 1 <i>kV</i> . Statistical analysis of 50 samples.	100
6.8	Saturation curve of the mean value of the plasma density with respect to the discharge voltage (left) and the maximum value of the current pulse (right) respectively.	101
6.9	Degree of ionisation along the radial position of the channel, obtained through a 1D simulation using the model [9], input voltage 20 <i>kV</i> - input max current 450 <i>A</i> . The simulation presents cylindrical symmetry, therefore the quantities are calculated only for half of the channel diameter. The curves are then mirrored for visual convenience.	101
6.10	Comparison of the longitudinal gas density profile for capillaries with diameters of 500 μm (blue) and 1 <i>mm</i> (red). Curves obtained through OpenFOAM simulations, resulting at the end of the solenoid valve closure gate. The gas injection pressure applied is the same and equal to 100 <i>mbar</i>	102
6.11	Comparison of the longitudinal plasma density profile for capillaries with diameters of 500 μm (red) and 1 <i>mm</i> (blue) respectively. The gas injection geometry and the discharge conditions are the same. Statistical analysis of 50 samples.	103

- 6.12 Comparison of the longitudinal plasma density profile for capillaries with diameters of $500\ \mu\text{m}$ (red) and $700\ \mu\text{m}$ (blue) respectively. The gas injection geometry and the discharge conditions are the same. Statistical analysis of 50 samples. 103
- 6.13 Degree of ionisation along the radial position of the channel, obtained through a 1D simulation using the model [9], input voltage $20\ \text{kV}$ - input max current $450\ \text{A}$, three different diameters: $0.5\ \text{mm}$, $0.7\ \text{mm}$ and $1\ \text{mm}$. The simulation presents cylindrical symmetry, therefore the quantities are calculated only for half of the channel diameter. 104
- 6.14 Temperature along the radial position of the channel, obtained through a 1D simulation using the model [9], input voltage $20\ \text{kV}$ - input max current $450\ \text{A}$, three different diameters: $0.5\ \text{mm}$, $0.7\ \text{mm}$ and $1\ \text{mm}$. The simulation presents cylindrical symmetry, therefore the quantities are calculated only for half of the channel diameter. 104
- 6.15 Comparison of the measured longitudinal plasma density profile for capillaries both with diameter of $500\ \mu\text{m}$ and with two secondary inlet (red), 1 central inlet (blue). The gas injection and the discharge conditions are the same. Statistical analysis of 50 samples. 105
- 6.16 Comparison of the measured longitudinal plasma density profile for capillaries both with diameter of $1\ \text{mm}$ and with two secondary inlets (blue), 1 central inlet (red). The gas injection and the discharge conditions are the same. Statistical analysis of 50 samples. 106
- 6.17 Comparison of the longitudinal and transverse gas velocity profile for capillaries both with 2 inlets, and different diameter of $500\ \mu\text{m}$ (blue) and $1\ \text{mm}$ (red). Curves from the same OpenFOAM simulations whose gas density profile was previously shown. The transverse component considered is that parallel to the central axis of the inlets. 107
- 6.18 Schematic of a capillary with a straight spacer at the entrance, before the electrode. The channel of the spacer is the same size as the channel of the capillary. The blue arrow represents the gas injection direction. 108
- 6.19 Image of the CAD file of the capillary with one of the two electrodes and a spacer with two symmetrical deflectors. The capillary has length $3\ \text{cm}$ and channel diameter $1\ \text{mm}$, while the spacer has length $1\ \text{cm}$ and size of all channels $1\ \text{mm}$. The thickness of the electrode is $1\ \text{mm}$ 109
- 6.20 Spectroscopic measurements of plasma densities for different configurations of capillary plus spacers: capillary without spacers (black), capillary with straight spacers (blue), capillary with spacers with two symmetrical deflectors (red). Plasma density was detected only in the area of interest (end of capillary and plasma plumes), and along the main channel. The peak current used is $550\ \text{A}$. *Measurements made in Plasma_Lab*. 109

6.21	Images taken with the intensified CCD representing a temporal plasma intensity scan of the end of the capillary and a spacer with two symmetrical deflectors. The delays are from 100 ns to 500 ns from the start of the discharge, in steps of 50 ns. The dark area where there is no recombination light emission along the channel line is the electrode area, which is useful for dividing the capillary channel from the spacer channel. <i>Measurements made in Plasma Lab.</i>	110
6.22	Neutral gas density and velocity along the main channel for the case of spacers with the deflectors. OpenFOAM simulations performed with the same capillary and the same initial conditions (100 mbar). . .	111
6.23	Neutral gas density and relative velocity along the axis of a deflector. The presence of gas is evident in the first half of the deflector length, beyond which the gas velocity drops significantly. OpenFOAM simulation performed with the geometry presented in Fig. 6.19. . . .	112
7.1	Setup made in Zemax, with the use of custom optics, to compensate for the phase shift that the internal walls of the capillary introduce, due to their curvature. It consists of three lenses in addition to the curved inner and outer surfaces of the channel.	115
7.2	CAD file of the central part of the interferometric setup: the capillary between the first two lenses; the two halves of the capillary joined together form a channel with a diameter of 0.5 mm and a length of 3 cm.	115
7.3	Photos of some example <i>VeroClear</i> printed components of the setup before and after polishing: a) first half of capillary, b) third lens. . .	116
7.4	Photo of the comparison detected with the profile projector for the third lens before and after polishing. The difference in thickness is about 2 tenths of a millimetre.	116
7.5	Interference fringes generated in air a) and in the <i>VeroClear</i> sample b), focused by varying the delay line between the two interferometer arms.	117
7.6	Installed experimental setup to compensate for the phase shift that the internal walls of the capillary introduce, due to their curvature. The yellow path represents the laser line; the two halves of the capillary are assembled together and the CCD is positioned in the final configuration, i.e. on the image plane.	117
7.7	Beam initial conditions: a) simulated, b) experimental. The beam size is larger than the CCD chip size. The beam has a diameter of 7.5 mm.	118
7.8	Images of the output beam at a distance of 4.5 cm from the second lens (up), and relative vertical profiles (down).	118
7.9	Simulated beam obtained at a distance of 4.5 cm from the second lens with the original setup a); beam in the same plane after the second lens, but varying the curvature of the first lens by about 5% b). . . .	119
7.10	Final image plane: a) experimental beam with horizontal dimensions larger than the chip and vertical of about 1.5 mm (up), vertical profile (down), b) simulated beam in Zemax of dimensions 7.5 mm × 1.56 mm.	120

7.11	Comparison of used (up) versus new (down) capillary channel sizes for a) 10 hours use, b) 30 hours use, c) more than 100 hours use respectively. d) Comparison of the face exposed to the electrode from which the discharge starts for the same four pieces: new, used 10, 30 and more than 100 hours, from right to left and from top to bottom. Images obtained using a <i>Nikon V-12</i> profile projector.	121
7.12	Trend in channel diameter as a function of longitudinal position, for different levels of capillary wear.	123
7.13	Example of a prototype of a new capillary model composed of two parts, able to facilitate the cleaning of the internal channels after printing, and in which it will be possible to install a sapphire tube along the line of the main channel of the capillary, to slow down the consumption of the internal walls due to ablation caused by the discharge.	123
7.14	Schematic representation of the compact staging idea of the CAMEL project: several laser pulses (two shown) are conveyed and guided within curved plasma channels into a main straight channel, which can be used for electron beam acceleration.	124
7.15	Image of the CAD file of the 6 <i>cm</i> long capillary, with a straight channel section that splits into two channels at the center of the capillary: one continues straight, the other has a radius of curvature of about 55 <i>mm</i> . The gas injection has two secondary inlets with smoothed curvatures to facilitate gas production and flow. The diameter of all channels is 500 μm	125
7.16	Longitudinal profiles of neutral gas density within the capillary in Fig. 7.15. In blue is the profile of the entire straight channel (on the left is the common side), in red is the profile inside the curved channel. Results coming from a OpenFOAM simulation with a pressure applied on the main inlet of 100 <i>mbar</i>	126
7.17	Average profile with statistical error of the discharge curve from the equivalent circuit of discharge plus capillary. Data are averaged over 100 acquisitions.	126
7.18	Photo of the discharge generated inside the curved channel with 500 μm diameter in the 6 <i>cm</i> long capillary. No plasma is present in the uncommon straight channel. At the bottom there is the reflection of the channel containing the plasma on the support plane of the capillary holder. Plasma plumes are present in entrance and exit from the curved-straight channel. The typical colour of the light emitted by pure hydrogen plasma (purple) is caused by the stronger lines emitted in the visible range, which are in the red (Balmer alpha line) and in the blue (Balmer beta) spectrum.	127
7.19	Statistical analysis of the longitudinal plasma profile of the 6 <i>cm</i> long curved capillary channel. Data averaged over 50 acquisitions, selected delay with respect to discharge start equal to 300 <i>ns</i>	128
7.20	CAD drawing of the new interaction chamber for guiding high-power laser pulses, already installed in the Flame bunker. It has dimensions of approximately 2.3 <i>m</i> \times 1 <i>m</i>	129

7.21	Zemax simulation of the transport and focusing of the main laser pulse, before and after the point of interaction with the plasma. After focusing there are two beam imaging systems: capillary exit plane (right), $L3$ plane to reproduce the pierced beam (left).	129
7.22	CAD design of a portion of the EXIN line: in addition to the laser transport chambers, the beam injection chamber, the plasma interaction chamber and the laser beam extraction chamber are highlighted.	131
A.1	Mach-Zender interferometer setup scheme for plasma density measurement.	136
B.1	OpenFoam simulation: gas density n_0 after 3 ms , for a capillary of length 3 cm and diameter 0.5 mm . The pressure on the main inlet is 100 $mbar$	138
B.2	OpenFoam simulation: gas pressure p after 3 ms , for a capillary of length 6 cm and diameter 0.5 mm , with a central bifurcation into two channels, one of which is curved. The pressure on the main inlet is 100 $mbar$	139
B.3	OpenFoam simulation: gas pressure p after 3 ms , for a capillary of length 3 cm and diameter 1 mm , with two 1 cm long spacers at each end. The pressure on the main inlet is 100 $mbar$	139

List of Tables

3.1	Main parameters of the SPARC electron beam from the photo-injector.	32
3.2	High-power laser parameters.	36
4.1	Laser parameters for plasma gas jet tests.	49
5.1	Probe laser parameters.	65
5.2	Discharge circuit output parameters.	69
5.3	Probe laser parameters for the second guiding experimental campaign.	84
5.4	Capillary, gas and discharge parameters.	85
5.5	Summary of the conditions and results obtained for the guiding experiments, with the necessary plasma density characteristics included. The experimental values are compared with the theoretical values obtained.	91
6.1	Comparison between experimental and theoretical channel ionisation degree.	97
6.2	Comparison of the electronic plasma densities, and the relative gas molar densities, both experimental and theoretical, together with the temperature value resulting from simulations, obtained for different diameters. The experimental errors on the density measurements, and thus on the molar densities, are about 8% in all three cases. . .	103
7.1	FLAME laser parameters for the EXIN project.	130

Chapter 1

Introduction

PARTICLE ACCELERATORS are now used in a wide range of fields: they are the fundamental tools for research into elementary particles and high-energy physics in general, but at the same time they are an important resource used in many other areas, from medicine and biology to industry. More than 42000 accelerators exist today for studies in a multitude of applications in physics, chemistry, medicine and structure analysis [10]. There is therefore a great demand for these machines from both industry and research institutes, even though a high energy particle accelerator is extremely expensive, especially for its size. The basic of the modern accelerators' operation is the transfer of energy from an electromagnetic field, excited in resonant radio-frequency (RF) cavities, to the particles. A possible way to reduce the size of the machine is to increase the acceleration gradient, i.e. the amplitude of the electromagnetic field. The peak value of the latter is, however, limited by the breakdown of the components themselves, since, above a certain threshold of electric field, charge begins to be extracted from the walls and a discharge occurs. This limitation keeps their acceleration gradient to $20 - 100 \text{ MV/m}$. Consequently, linac of tens or hundreds of metres are required to reach the multi- GeV beam energies needed [11], for example, to drive short wavelength radiation sources; while to reach particle energies of interest to high-energy physics, even kilometres are needed.

1.1 Motivation to plasma based accelerators

The new frontier of particle accelerators today is therefore the compactness to allow their use in places beyond research facilities, such as hospitals and industries. The goal is then the generation of beams of charged particles, stable and repeatable, to be accessible to public and private institutions for different applications. The plasma acceleration finds its goal in this framework because, through it, it is possible to generate high accelerating gradients in an extremely small space, since this method is able to overcome the limit of the breakdown of the components of which the accelerating sections of the accelerators are composed of [2].

One of the main characteristics of the plasma is that its components can give rise to collective behaviour: this means that, by generating a charge separation in a neutral plasma, it is possible to obtain very high electric fields [12]. In fact, the maximum plasma acceleration field scales proportionally to the electron plasma

density, therefore accelerating gradients up to TV/m in a centimetre scale are in principle achievable. The charge separation within a plasma can be induced using a driver beam, which can be a laser pulse or a charged particle beam. One of the easiest way to perform plasma acceleration is by using an ultra-short high-power laser (Laser WakeField Acceleration, LWFA), combined with a gas-based plasma module. To generate an electric field in the plasma from a gas, it is necessary first to ionise the gas. This can be done via the laser driver pulse itself or via an external source. Once the state of neutral plasma has been obtained, it is thus necessary to create the charge imbalance. This is possible using a laser pulse with intensity of the order of $10^{18}W/cm^2$, value achievable through the Chirped Pulse Amplification method [5]. The ponderomotive force of the driver pulse sweeps away the electrons in the plasma, generating a positively charged bubble. If the laser is sufficiently intense, the electrons that accumulate at the back of the bubble as the laser advances, are injected into the bubble and thus accelerated by the wakefield [4]. This method of injection is called *self-injection* (see Chapter 2).

However, this scheme currently has a big limit due to the poor quality of the accelerated beams: the electrons are injected into the bubble at different times and they consequently feel different accelerating fields. The beams produced have high energy spread and divergence, and this makes them difficult to be used for a large number of applications [13].

A possible solution to this problem is represented by the external-injection scheme, consisting in the acceleration of a pre-existing electron bunch coming from a RF Linac, by exploiting the plasma wakefield stimulated by an intense laser in a gas. In this way, it is in principle possible to obtain a high energy boost at the exit of the plasma channel, keeping the initial electron beam quality. The main advantage of this scheme, since the bunch generation is decoupled by the acceleration process, is that it might be possible to have more control on the injection of the electron bunches into the accelerating field. In this case, however, it is also necessary to solve several constraints of LWFA: the slippage between the accelerated electrons and the laser wake, i.e. the dephasing; the laser energy depletion, absorption of laser energy by the plasma itself; and the limitation of the accelerating distance due to the laser diffraction.

1.2 What is the project of this PhD?

The purpose of this project is to study and test different types of plasma targets for laser-plasma acceleration, with a focus on some possible methods to overcome the limitations of the external-injection scheme. In detail, guiding the laser pulse through a gas-filled capillary discharge has several advantages, as for example the phenomenon of pulse diffraction that can be solved by means of an optical guide in plasma channels [14, 15].

In general, since the electron energy gain from the wakefield is proportional to the product of the accelerating field by the effective propagation distance of the laser, guiding the high-power laser pulse in a preformed plasma channel leads to a higher energy of the accelerated electrons, with the same initial parameters of the two beams.

In this work, following a theoretical overview of the LWFA (Chapter 2), studies and results of laser-plasma interaction experiments carried out in the *SPARC_LAB* laboratories (Chapter 3) are reported: a characterisation of gas jets for self-injection experiments is analysed in Chapter 4, while Chapter 5 provides tests of low-power laser pulse guiding in plasma channels. Since the plasma module is one of the main elements of plasma-based accelerators, and monitoring its operation is thus crucial during operation, diagnostics related to this component must be given particular attention. For this reason, spectroscopic and interferometric diagnostic methods for measuring plasma density are given in Chapters 6 and 7, as well as studies on the variation of the plasma density as a function of the initial parameters of the plasma module. Experimental measurements are supported by theoretical models and fluid-dynamic simulations of the gas used.

Chapter 2

Plasma based Acceleration

Plasma-based accelerators represent an interesting innovation in the field of accelerator physics, due to their ability to sustain high acceleration gradients and to their compact size. Electron plasma waves can be obtained through ionised plasmas, and they can achieve electric fields of the order of the non-relativistic wave-breaking field [16, 17]:

$$E_{max} = c m_e \frac{\omega_p}{e} \simeq 96 \sqrt{n_e [cm^{-3}]} , \quad (2.1)$$

where $\omega_p = (4\pi n_e e^2 / m_e)^{1/2}$ is the plasma frequency, n_e is the electron density, e is the electron's charge and m_e its mass at rest. For example, a plasma density $n_e = 10^{18} cm^{-3}$ gives an electric field $E_{max} \approx 100 GV/m$, which is three orders of magnitude greater than that which can be achieved in conventional RF linacs. This general method of using plasmas to accelerate particles was first presented in 1979 [2], and just a few years later it was experimentally demonstrated that electrons gain energy in the wake of a plasma wave [18–20]. The different plasma acceleration schemes can be classified into two main categories, the laser-driven and particle beam-driven: in the first case a laser pulse is required to create an electron plasma wave, while in the second the electron plasma wave is formed by means of an electron beam.

In this chapter an overview on the theory of plasma wakefield acceleration is given, focusing on laser-based plasma acceleration.

2.1 Plasma definition and high acceleration gradient

Plasma is usually described as the fourth state of matter, since it can assume behaviour characteristic of all three other states, depending on its density and temperature. It has been defined as a quasi-neutral gas of charged particles that exhibit collective behaviour [12]. The condition of *quasi-neutrality* implies that even if the particles composing the plasma consist of free electrons and ions, they are in equilibrium, and their overall charge density is zero. For n_e and n_i , respectively the electron and ion densities, it results that within a plasma these are locally balanced:

$$n_e = Z n_i , \quad (2.2)$$

where Z is the atomic number. The characteristic of *collectivity* is instead due to the long-range nature of the $1/r$ Coulomb potential: regions of the plasma can be

strongly influenced by local disturbances in the equilibrium. A net charge imbalance $\rho = e(Zn_i - n_e)$ gives then rise to an electrostatic field, according to Gauss's law $\nabla \cdot E = \rho/\epsilon_0$ [1].

Plasma ionisation can take place in several ways, e.g. through collisions of fast particles with atoms, or through *field* ionisation (photo-ionisation by electromagnetic radiation or electrical breakdown in strong electric fields). The latter mechanism is the most important in the context of plasma-based accelerators. An example of field ionisation can be given by calculating the typical field strength required to strip electrons from an atom: the atomic electric field strength, at the Bohr radius a_B , is

$$E_a = \frac{e}{4\pi\epsilon_0 a_B^2} \simeq 5.1 \times 10^9 \text{ V/cm} ; \quad (2.3)$$

this value provides the threshold intensity for field ionisation, the *atomic intensity*, that is

$$I_a = \frac{\epsilon_0 c E_a^2}{2} \simeq 3.51 \times 10^{16} \text{ W/cm}^2. \quad (2.4)$$

Therefore, ionisation for any material is ensured if laser intensity is $I_L > I_a$. It can occur, however, below this threshold (around 10^{14} W/cm^2) because of multi-photon effects.

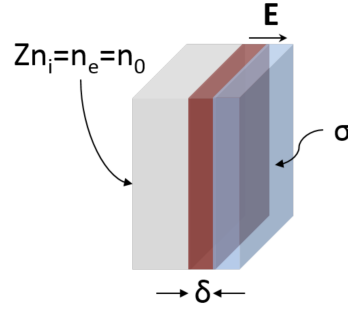


Figure 2.1. Slab or capacitor model of oscillating electron layer [1], where n_0 is the total plasma density.

Particle beams or a laser pulse (i.e. an electromagnetic wave), can be external disturbances to the plasma, and it is possible to analyse its response to them: consider a quasi-neutral plasma slab in which an electron layer is displaced from its initial position by a distance δ , Fig. 2.1. Two capacitor plates are then created with surface charge $\sigma = \pm en_e \delta$, ensuing an electric field

$$E = \frac{\sigma}{\epsilon_0} = \frac{(en_e \delta)}{\epsilon_0} ; \quad (2.5)$$

the restoring force that accelerates the electron layer back towards the slab will be

$$m_e \frac{dv}{dt} = -m_e \frac{d^2 \delta}{dt^2} = -eE = \frac{e^2 n_e \delta}{\epsilon_0} . \quad (2.6)$$

It follows that

$$\frac{d^2 \delta}{dt^2} + \omega_p^2 \delta = 0 , \quad (2.7)$$

where

$$\omega_p \equiv \sqrt{\frac{e^2 n_e}{\epsilon_0 m_e}} \quad (2.8)$$

is the electron plasma frequency [21].

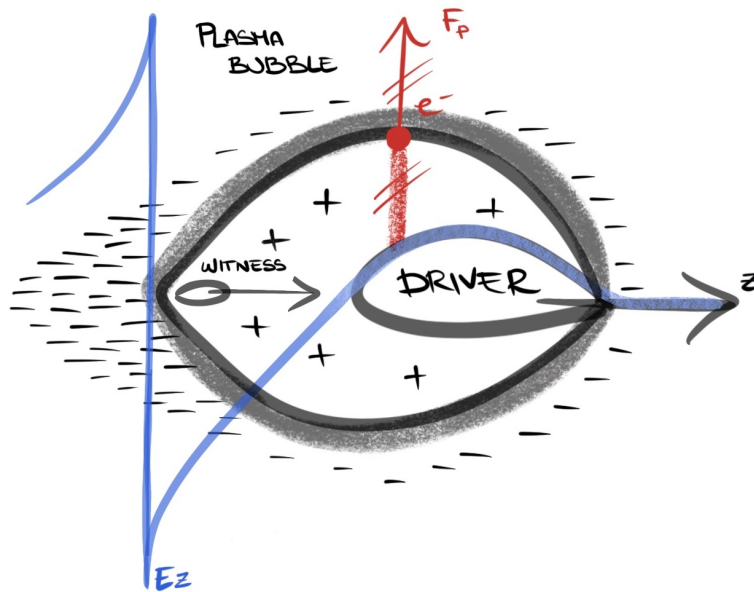


Figure 2.2. Schematic of the plasma laser acceleration process proposed by T. Tajima and J.M. Dawson in 1979 [2]. The driver pulse, which can be a short laser pulse or an electron beam, generates a separation of charge in a gas, or plasma, forming a bubble: the electric field E_z thus created is capable of accelerating the charged particles, located at the back of the bubble, which move in the direction of the field itself.

The potential usefulness of this plasma feature lies in the possibility of introducing a wave travelling through it, generating a very high charge separation. For example, by applying a high-power laser to a suitably prepared plasma, such a wave can be created: the electric field of the driving laser beam, travelling through the plasma, separates electrons and ions. The electrons, which are lighter and therefore faster than the ions, cover a greater displacement, generating a charge separation. It can therefore be said that the laser wavefront exerts a ponderomotive force on the plasma charges, which pushes the electrons away from their equilibrium position. This creates an emptying zone in which only the positive charges remain: this zone is called a plasma bubble because of its shape (see Fig. 2.2). At this point the removed charges oscillate around their equilibrium position with plasma frequency (Eq. 2.8). The point of maximum expansion of the bubble is the one at which the two forces of repulsive ponderomotive and ionic attraction are balanced. The fact that the electrons are attracted and oscillate gives the bubble an oscillating structure. Similarly, the wakefield in the plasma is generated if a driver beam of charged particles, e.g. electrons, is applied to the plasma, instead of a high-power laser pulse, this scheme is known as *particle driven* [4].

In the *laser-driven scheme*, as the pulse advances, the negative charges are pushed

back towards the back of the bubble, where they accumulate (see Fig. 2.2). What is therefore generated is a relativistic harmonic oscillator effect, which lengthens the tail of the bubble. The more powerful the driver, the bigger the bubble. The electric field generated by charge separation, i.e. the plasma wave, has a longitudinal component that can accelerate charged particles moving in the same direction as the field.

The normalised intensity of a laser beam, i.e. its strength parameter, is defined as

$$a_0 \equiv eE_0 / (m_e \omega_0 c) . \quad (2.9)$$

If the laser pulse is intense enough, i.e. if its normalised intensity $a_0 > 1$, the field of the wave is so high that it produces a break in the plasma wave, ripping off the electrons and bringing them into the bubble. This field is called the *wave-breaking field*. The electrons then acquire enough kinetic energy to break away from the crest of the wave, and are injected into the bubble. These charges then find themselves in the area of the accelerating electric field and are accelerated to high energies. This plasma-based acceleration mechanism is called *self-injection* [22, 23]. In the particle-driven scheme instead, or in the laser-driven scheme in the linear regime, i.e. a_0 up to 1, a pre-existing electron beam, called *witness beam*, can be injected into the plasma bubble and exploit the accelerating wakefield. The latter mechanism is called *external-injection* (see Section 3.2.1 for more detail).

Starting from Gauss's law, it is possible to estimate the accelerating electric field E , which can be excited in a *cold* plasma, i.e. with negligible thermal velocity [24]:

$$\nabla \cdot \mathbf{E} = \frac{\rho}{\epsilon_0} = \frac{e(n_i - n_e)}{\epsilon_0} , \quad (2.10)$$

where ρ is the charge density, e is the electron charge, n_i and n_e are the ions and electrons densities, respectively. Assuming the largest wakes occurring for $n_e = 0$ and $n_i = n_0$, where n_0 is the plasma density, all the electrons are blown out. For a one-dimensional plane, wave perturbation of the charge density occurs:

$$\nabla = \hat{z} \frac{\partial}{\partial z} , \quad n_0(z) = n_0 \exp(ik_p z) , \quad (2.11)$$

where $k_p = \omega_p / c$ is the plasma frequency, e is the electron charge, while m_e and ϵ_0 are its rest mass and the dielectric constant, respectively. For the non-relativistic approximation

$$E = E_0 \exp(ik_p z) ; \quad (2.12)$$

it follows that

$$|\nabla \cdot \mathbf{E}| = |-ik_p E_0| \simeq \frac{\omega_p}{c} E_0 = \frac{e}{\epsilon_0 n_0} , \quad (2.13)$$

and so the amplitude of the electric field is given by

$$E_0 \left[\frac{V}{m} \right] = \frac{m_e c}{e} \omega_p = c \sqrt{\frac{m_e}{\epsilon_0 n_0}} \simeq 96 \sqrt{n_0 [cm^{-3}]} = E_{max} , \quad (2.14)$$

where, due to the fact that the ions' frequency is much lower than the electrons' one, the ions have been assumed fixed. Eq. 2.1 was thus derived. In this way quite a large field can be obtained, many orders of magnitude greater than the

maximum accelerating gradient currently attainable by the conventional RF LINAC ($\approx 100 \text{ MV/m}$). For example assuming a plasma density equal to 10^{18} cm^{-3} , it is possible to obtain a wave with a peak electric field of 100 GV/m .

2.2 Laser driven plasma acceleration

Two different laser-based schemes for particle acceleration in a plasma were first proposed by T. Tajima and J.M. Dawson in 1979 [2]: in the first one, already mentioned in Section 2.1, a plasma wave was formed using a high intense laser pulse (10^{18} W/cm^2), while the second one relied on combining two different laser beams with a precise frequency difference ($\delta\omega_L = \omega_p$). The first one is nowadays known as *Laser WakeField Acceleration* (LWFA) and the second one as *Beat Wave Acceleration* (BWA). Laser wakefield acceleration has become more widespread and it is now being studied in several facilities around the world. Its operation is detailed below.

The dielectric constant of the plasma is

$$\epsilon = 1 - \frac{\omega_p^2}{\omega_L^2}, \quad (2.15)$$

where ω_L is the pulse frequency of the laser propagating in a plasma.

To be transparent to a laser beam, an under-dense plasma (where $\epsilon > 0$) is needed, because $\omega_p \propto \sqrt{n_0}$. So, if $\omega_L > \omega_p$, it can be used as a particle accelerator. In detail, the laser phase velocity is $v_p = c/n = c/\sqrt{\epsilon}$, and, assuming that the perturbed amplitudes are small compared to the equilibrium values [1], it can be derived that [11]:

$$\omega_L^2 = k^2 c^2 + \omega_p^2. \quad (2.16)$$

The latter expression is called *dispersion relation*, and determines the laser frequency for the medium. Assuming that the group and phase velocities are larger than the thermal velocity, the laser phase velocity can then be determined using

$$v_p^{laser} = \frac{c}{\sqrt{1 - \frac{\omega_p^2}{\omega_L^2}}} \approx \frac{c}{2} \left(1 + \frac{\omega_p^2}{\omega_L^2} \right), \quad (2.17)$$

which is greater than c . The laser group velocity with which the pulse propagates through a plasma is therefore

$$v_g^{laser} = v_p - \lambda_L \frac{\partial v_p}{\partial \lambda_L} \approx \frac{c}{2} \left(1 - \frac{\omega_p^2}{\omega_L^2} \right). \quad (2.18)$$

This is, on the contrary, smaller than c . Since the plasma oscillation is driven by the laser pulse, the phase velocity of the plasma wave is equal to the group velocity of the laser pulse. Therefore, from Eq. 2.18 and considering relativistic accelerated electrons, so that the speed difference between the plasma wave and the particles is $\delta v = c - v_g^{laser}$, the latter outrun the wave, i.e. they reach the bottom of the potential well at $\lambda_p/2$, in

$$l_d = c\delta t = \frac{\lambda_p}{2} \frac{c}{\delta v} = \frac{\lambda_p}{2} \frac{c}{c - v_g} \approx \frac{\omega_L^2}{\omega_p^2} \lambda_p : \quad (2.19)$$

that is a distance called *dephasing length*. The energy gain that is obtained as a result is $W_{max} \approx eE_0 l_d$, where E_0 is given by Eq. 2.14.

At this point, it can be stated that in LWFA, thanks to the ponderomotive force, a wake of plasma oscillations can be excited by a short laser pulse with $\omega_L > \omega_p$. Indeed, if the laser pulse propagates through an underdense plasma, as it was said before (Section 2.1) the electrons are expelled by the ponderomotive force F_p from the region of the laser pulse. Thus, electron plasma waves are generated as a result of the driving laser pulse. If the plasma wavelength and the pulse length are comparable, i.e. $c\tau_L \approx \lambda_p$, plasma waves are excited by the ponderomotive force with a phase velocity equal to the laser group velocity [25].

2.2.1 Electron motion in a laser field

The Lorentz equation describes the motion of a single electron with charge $-e$ and mass m_e in the laser field \mathbf{E} and \mathbf{B} [26], that is

$$\frac{d\mathbf{p}}{dt} = -e(\mathbf{E} + \mathbf{v} \times \mathbf{B}) , \quad (2.20)$$

where $p = \gamma m_e \mathbf{v}$ is the electron momentum, $\gamma = (1 - \beta^2)^{-1/2}$ is the relativistic factor, and $\beta = v/c$. The electric field, in the laser plane wave approximation, is described by

$$\mathbf{E}(z) = E_L \cos(k_0 z - \omega_0 t) e_x , \quad (2.21)$$

which moves along the z axis and is polarised along x . In the non-relativistic regime ($\beta \ll 1$), the Eq. 2.20 becomes

$$\frac{d\mathbf{p}}{dt} = -e\mathbf{E} = e \frac{\partial \mathbf{A}}{\partial t} , \quad (2.22)$$

where the vector potential

$$\mathbf{A}(z) = A_0 \sin(k_0 z - \omega_0 t) e_x , \quad (2.23)$$

with $A_0 = E_L/\omega_0$, is used [3].

If an electron is initially at rest at $z = 0$, it starts oscillating in the direction of the electric field with a velocity

$$\beta = -\frac{aA_0}{mc} \sin(\omega_0 t) \equiv -a_0 \sin(\omega_0 t) . \quad (2.24)$$

Therefore, in this situation, the result is that the electron simply oscillates in the laser field without gaining energy.

When the laser normalised intensity is $a_0 > 1$, the electron velocity nears c and the $\mathbf{v} \times \mathbf{B}$ term in the Eq. 2.20 cannot be neglected anymore. In particular, in the frame that it is co-moving with the laser pulse it results

$$a(z) = a_0 \sin(k_0 \xi) e_x , \quad (2.25)$$

where $\xi = z - ct$ is this reference system coordinate, so the electron normalised momentum can be described as [27]

$$\begin{aligned} u_x &= \gamma\beta_x = \frac{dx}{d\xi} = a_0 \sin(k_0\xi) , \\ u_z &= \gamma\beta_z = \frac{dz}{d\xi} = a_0^2 \sin^2(k_0\xi) . \end{aligned} \quad (2.26)$$

The velocity of the electron is always positive in the z direction, so the force $\mathbf{v} \times \mathbf{B}$ pushes the electron forward. By integrating Eq. 2.26, the coordinates of the electron can be calculated:

$$\begin{aligned} x &= \frac{a_0}{k_0} \cos(k_0\xi) , \\ z &= \frac{a_0^2}{8k_0} [2k_0\xi - \sin(2k_0\xi)] . \end{aligned} \quad (2.27)$$

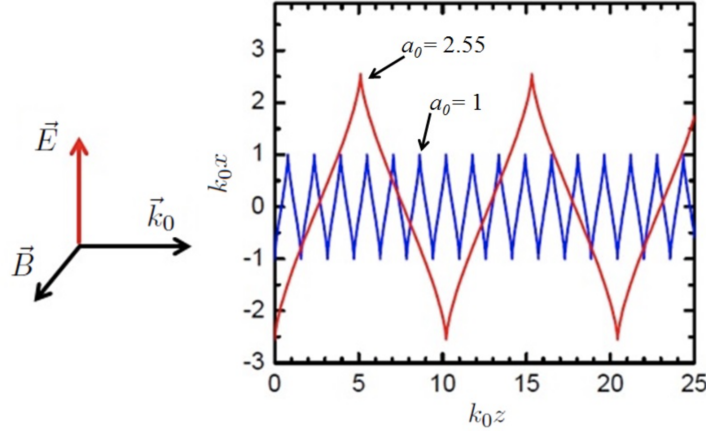


Figure 2.3. Trajectory of an electron in the laser transverse field, in the laboratory frame for two values of the laser strength. The longitudinal momentum scales with the square of the laser strength as a_0^2 , while the transverse one linearly depends on a_0 [3].

It is thus shown that, while moving forward, the electron oscillates at twice the frequency of the laser, in the longitudinal direction z . As shown in Fig. 2.3, the transverse momentum depends linearly on the laser intensity for a_0 , while the longitudinal momentum scales with the square of the laser intensity as a_0^2 . Consequently, for $a_0 \gg 1$, the longitudinal motion of the electron dominates over its transverse oscillation. This example is valid in plane wave approximation, for the generation of the oscillation but not of a gradient, for which instead a ponderomotive force is required.

2.2.2 Ponderomotive force and self-injection in the blow-out regime

As already mentioned, a ponderomotive force is needed to create an accelerating field: in the relativistic regime it becomes effective. More in detail, this force is associated with the second-order electron motion (see Eq. 2.20), averaged over a

time-scale longer than the laser period. The three-dimensional ponderomotive force for an electron can be written as [28]

$$\begin{aligned} \mathbf{F}_p &= -e\mathbf{v} \times \mathbf{B} = \\ &= -\frac{e^2}{m_e c^2} \mathbf{A} \times (\nabla \times \mathbf{A}) = -m_e c^2 \mathbf{a} \times (\nabla \times \mathbf{a}) = -m_e c^2 \nabla \frac{a_0^2}{2}. \end{aligned} \quad (2.28)$$

It can be observed from Eq. 2.28 that F_p is proportional to the negative gradient of a_0^2 , thus of E_0^2 (see Eq. 2.9), the laser envelope then conditions the ponderomotive force. For this reason, in laser-plasma accelerators, a plasma wave is excited by the action of the ponderomotive force.

One definition of the ponderomotive force can be the radiation pressure of laser intensity. Charged particles are driven out of the region of high laser intensity by this force, which is independent of the sign of the charged particle, and inversely proportional to particle mass $F_p \propto 1/m$. Therefore, ion motion can be ignored because the acceleration applied to a proton is only 10^{-6} times than the one applied on an electron.

Since in LWFA the short laser pulse gives the plasma a single kick, the total amount of energy required for a full stage of the accelerator must be comprised in a single pulse shorter than a plasma period. To give an example, for a 10^{16} cm^{-3} plasma density, a laser pulse shorter than 1 ps is needed. Furthermore, the ponderomotive force of the laser can never be exceeded by the electric force of the plasma. Specifically, for LWFA in non linear regime, the maximum wakefield amplitude is

$$\frac{E_{max}}{E_0} = \frac{a_0^2}{\sqrt{1 + a_0^2}}. \quad (2.29)$$

The ponderomotive force varies along with the laser energy gradient, creating a density distribution in the transverse and longitudinal directions, to which transverse and longitudinal fields can be associated. Adjusting the transverse size of the laser focal spot and its pulse duration allows to control them individually. The accelerating structure has the shape of a sine wave with wavelength λ_p , commonly in the range (10 – 100) μm , and it can be tuned with the plasma electron density. The accelerating field is limited to the wavebreaking field for a non-relativistic cold plasma, as expressed in Eq. 2.1. As previously mentioned, in wavebreaking conditions, electrons can escape the collective motion because electron oscillations become large enough. In the non-linear regime ($a_0 > 1$), this may be the source of electron injection. Nonetheless, in the linear regime ($a_0 < 1$) wavebreaking does not take place: an external source is needed to deliver relativistic electrons, and to inject them into the linear plasma wave where they are accelerated.

The plot on the right side of Fig. 2.4 illustrates the main features of the non-linear regime. As the laser propagates into the plasma, its front edge diffracts while the rest of the pulse self-focuses. Electrons are expelled by the ponderomotive force and a plasma cavity void of electrons, the white area in Fig. 2.4, is left behind the laser pulse. The expelled electrons travel along the field lines and accumulate at the back of the cavity, where they can be injected and accelerated. The cavity size is typically of the order of 10 μm , and produces accelerated electron bunches with a transverse

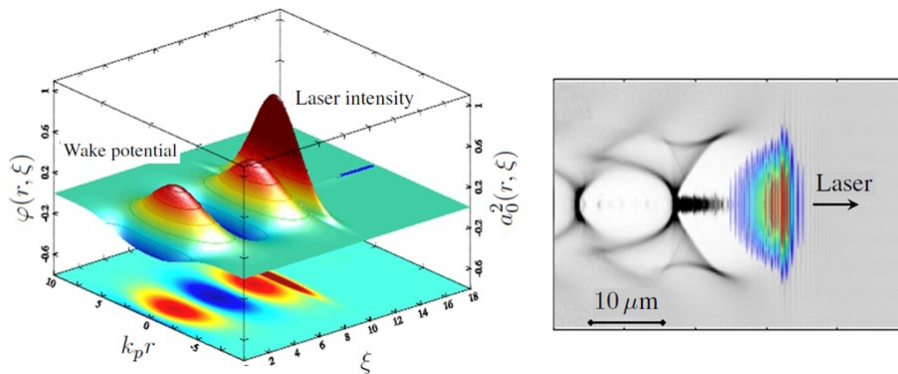


Figure 2.4. Illustration of the two regimes of the laser wakefield: Left) Excitation of a plasma wave in the linear regime. 3D view and projection in the horizontal plane of the normalized laser intensity, a_0 , and wake potential, φ . Right) Excitation of a plasma wave in the non-linear regime. Map of density in the horizontal plane (grey scale, white is zero) and superposition of laser amplitude (color scale, red is a maximum) [3].

size of the order of a few μm , owing to the focusing field inside the cavity. This regime is also called the blow-out or bubble regime [3, 23, 29].

In the self-injection scheme, i.e. if the intensity of the laser is sufficiently high, nearly all plasma electrons are expelled from the region of propagation, and a high-density electron layer is formed by accumulating electrons. Electron accelerating fields are present at the back of the positive charged bubble, and they can be strong enough that a part of the background plasma electrons are captured into the bubble. The plasma bubble structure can focus and accelerate to high energies these electrons. In a laser wakefield accelerator, a normalised laser vector potential $a_0 \gg 1$ is required for spot-sizes of a few skin-depths [30], to reach these strongly non-linear regimes.

In this regime, the Hamiltonian in the co-moving frame regulates the dynamics of an electron in the presence of a plasma wave and a laser pulse. It can be written as:

$$H = \sqrt{\gamma^2 + p^2} - \beta_p p - \phi, \quad (2.30)$$

where γ is the relativistic factor and $\phi \propto \cos[k_p(z - v_p t)]$. For an electron with initial momentum p_t , it can be obtained

$$H = \sqrt{\gamma^2 + p_t^2} - \beta_p p_t - \phi = H_t. \quad (2.31)$$

When the orbit given by H_t coincides with a trapped orbit defined within the separatrix orbit H_s (see Fig. 2.5), i.e. when $H_t \leq H_s$, self-injection occurs. When $H_t = H_s$, the minimum initial electron momentum for trapping in the plasma wave is given by:

$$p_t = \gamma_p \beta_p (\gamma_\perp - \gamma_p \phi_{min}) - \gamma_p \sqrt{(\gamma_\perp - \gamma_p \phi_{min})^2 - 1}, \quad (2.32)$$

where ϕ_{min} is the minimum of the plasma wave potential. The threshold momentum required for self-injection decreases for larger plasma wave amplitude and for lower plasma wave velocity.

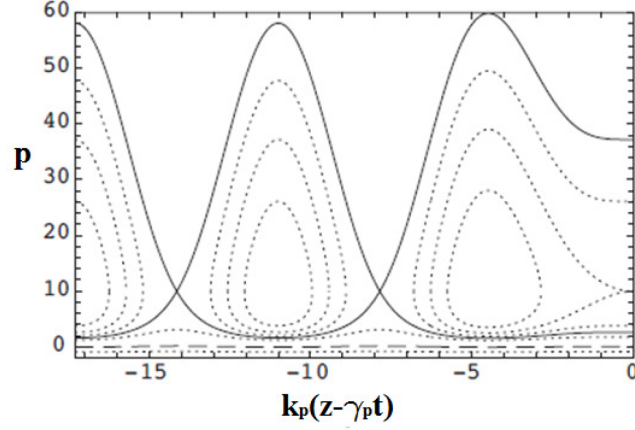


Figure 2.5. Single particle orbits in phase space for an electron in a small amplitude sinusoidal plasma wave: the dashed curve is the cold fluid orbit, the solid curve is the separatrix orbit [4].

2.3 Limitations to laser wakefield acceleration

As anticipated in Section 1.2, the acceleration process in laser-based schemes is limited by some effects:

- The first to interfere is the *laser diffraction*. The transverse spot size of a laser Gaussian beam propagating along the z axis is

$$\omega(z) = \omega_0 \sqrt{1 + \left(\frac{z}{z_R}\right)^2}, \quad (2.33)$$

where

$$z_R = \pi \omega_0^2 / \lambda \quad (2.34)$$

is called *Rayleigh length* and w_0 is the beam waist, i.e. the radius at $1/e^2$ of the laser intensity in the focal plane. This length z_R is equal to the distance at which the intensity is reduced by a factor of two, and it gives a measure of the longitudinal extension of the focus. In order to extend such a distance, a bigger spot would be needed, which would lead to a lower pulse intensity in the focus spot. This would then mean a lengthening of the accelerator size and a weak acceleration gradient.

- A second issue is represented by the *phase slippage*, due to the laser group velocity, which is smaller than the electron velocity $v_e \simeq c$. The dephasing happens when the electrons reach the decelerating region in the wave. This restricts the acceleration distance to the dephasing length [11, 31, 32], which is given by

$$L_d \simeq \frac{\lambda_p^3}{2\lambda_L^2} \quad \text{if} \quad a_0 \ll 1$$

$$L_d \simeq \frac{\lambda_p^3}{2\lambda_L^2} \times \frac{\sqrt{2}}{\pi} \frac{a}{N_p} \quad \text{if} \quad a_0 \gg 1, \quad (2.35)$$

where N_p is the number of plasma periods that were created behind the laser driver pulse. From the Eqs. 2.35 it can therefore be concluded that for $a_0 \gg 1$, the factor $1/N_p$ relates to the plasma wave period increasing as the laser pulse steepens: this effect is dominant in determining the plasma wave phase velocity. In the linear regime $a_0 \ll 1$, the electron energy gain is however limited by dephasing, assuming an axially uniform plasma.

- *Pump depletion length* is the effect that arises when the laser loses its power due to propagation in the plasma. An expression of this length can be given [23, 33, 34] as:

$$\begin{aligned} L_{pd} &\simeq \frac{\lambda_p^3}{\lambda_L^2} \times \frac{2}{a_0^2} & \text{if } a_0 \ll 1 \\ L_{pd} &\simeq \frac{\lambda_p^3}{\lambda_L^2} \times \frac{\sqrt{2}}{\pi} a_0 & \text{if } a_0 \gg 1. \end{aligned} \quad (2.36)$$

These equations are valid with the idealised assumptions made above and neglecting various non-ideal effects, such as self-focusing and laser-plasma instabilities.

The previous three characteristic lengths fix the maximum achievable acceleration distance for laser plasma based accelerators. For example, in a linear regime with the parameters $a_0 = 0.3$, $\lambda_L = 0.8 \mu\text{m}$ and $\lambda_p = 33 \mu\text{m}$, which lead to $P = 3.3 \text{ TW}$ and $n_e = 10^{18} \text{ cm}^{-3}$, the propagation lengths are $z_R = 0.43 \text{ cm}$, $L_d \approx 2.8 \text{ cm}$ and $L_{pd} \approx 1.2 \text{ m}$, i.e. $z_R \ll L_d \ll L_{pd}$ [35].

However, in laser plasma acceleration, there are some methods of overcoming these limitations. The *relativistic self-focusing* is a possible solution to the limit set by the Rayleigh length. At relativistic speeds, the plasma wave is non-linear, so as the relativistic mass γm_e increases, its amplitude affects its frequency:

$$\omega_p^2 \rightarrow \frac{\omega_p^2}{\gamma}, \quad (2.37)$$

where γ is the relativistic factor. Since the plasma refractive index is

$$\eta = \sqrt{1 - \left(\frac{\omega_p}{\omega_L}\right)^2} \quad (2.38)$$

it is greater in a region of lower ω_p , and vice versa. The plasma channel acts therefore as a lens, in which the laser beam is focused and the natural divergence is balanced. The relativistic self-focusing occurs when the power of the laser pulse is greater than the *critical power* [36–38]: $P \simeq P_c[\text{GW}] = 17(\omega_L/\omega_p)^2$. For example, for $\lambda_L = 0.8 \mu\text{m}$ and $n_e = 7 \times 10^{18} \text{ cm}^{-3}$, $P_c = 4.25 \text{ TW}$.

In order to lower the laser energy or to make a longer accelerator, preformed plasma channels can be used: the laser pulse can be guided via a specific plasma profile, thus also overcoming the limitation imposed by the diffraction length. Several advantages lie in the use of preformed plasma channels in order to overcome the diffraction limit, instead of exploiting relativistic self-focusing. For example, by using a plasma channel, it is possible to operate lasers at lower intensities, as it is not

necessary to respect the condition $P \gg P_c$. This results in using a lower a_0 and thus being able to use a more stable regime. In addition, by appropriately tapering the axial plasma density profile, also dephasing limitations could be overcome: spatially tapering the radius of the plasma channel increases the energy gain. Furthermore, in this way the phase velocity of the wakefield behind the laser pulse increases with distance from the back of the pulse. Then, depending on the tapering gradient, the wakefield phase velocity can equal the speed of light, several plasma wavelengths behind the laser pulse [39, 40]. An in-depth discussion on laser guiding in preformed-plasma channel will be given in the Section 5.1.

Chapter 3

Plasma based experiments at LNF-INFN

The *National Laboratories of Frascati (LNF)*, built in the 1950s, were the first Italian research facility for the study of nuclear and subnuclear physics with accelerator machines. They are part of the public institution *INFN (National Institute of Nuclear Physics)* whose mission is the theoretical, experimental and technological research in the field of subnuclear, nuclear and astro-particle physics. The main feature of the LNF has always been the ability to build particle accelerators: nowadays this also translates into the design and implementation of new acceleration techniques based on plasma. This latter activity is carried out in the laboratories of *SPARC_LAB (Sources for Plasma Accelerators and Radiation Compton with Lasers And Beams)* [41]. In this context, the *EuPRAXIA@SPARC_LAB* project was launched in the last few years: it intends to put forward the LNF as host of the new *EuPRAXIA European Facility (European Plasma Research Accelerator with eXcellence In Applications)* [42, 43]. The EuPRAXIA project aims at the construction of an innovative electron accelerator using laser and electron beam driven plasma wakefield acceleration. EuPRAXIA envisions a beam energy of up to 5 GeV and a beam quality equivalent to present RF-based linacs [44].

3.1 The SPARC_LAB test facility

SPARC_LAB is based on the unique combination of high brightness electron beams, from the SPARC photo-injector [45], with high intensity ultra-short laser pulses, from FLAME (*Frascati Laser for Acceleration and Multidisciplinary Experiments*) [46–49]. Both the laser and the photo-injector can operate independently as well as together for a wide variety of experiments. The joint presence of these two systems allows for the investigation of plasma acceleration with different configurations, i.e. self and external injection, laser and particle beam driven. In addition, it allows for the development of a wide spectrum of inter-disciplinary leading-edge research activity based on advanced radiation sources, i.e. Free Electron Laser (FEL) experiments, the production of X-rays by means of Thomson back-scattering and high peak power THz radiation [41, 50]. The SPARC project has been mainly devoted to the research activity on ultra-brilliant electron beam photo-injector and on FEL

physics: the test facility hosts a 180 MeV high brightness photo-injector which feeds a 12 m long undulator. A scheme of the facility is represented in Fig. 3.1 and the main characteristics are exposed in Tab. 3.1. The machine layout lets the investigation of several beam manipulation techniques and Linac matching schemes, such as the emittance compensation process in the gun region [51], the velocity bunching scheme to apply an RF beam compression through the photo injector with emittance preservation [52] or the experimental observation of the double-emittance minimum [53].

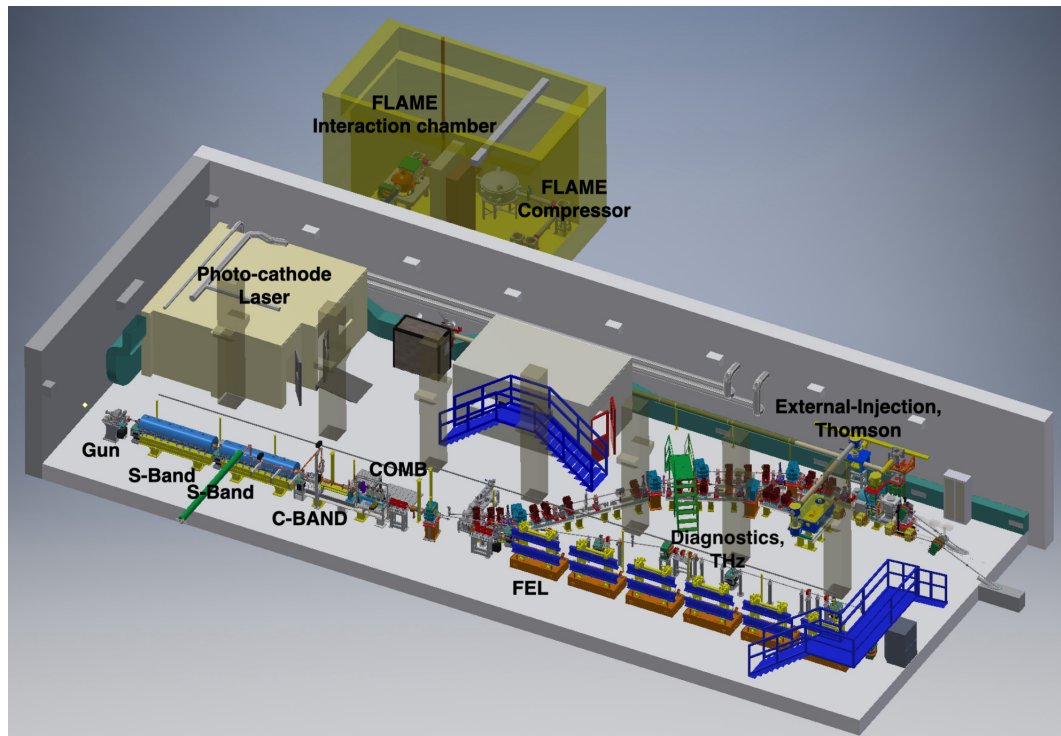


Figure 3.1. Layout of the SPARC bunker. The RF gun is followed by an hybrid acceleration system consisting of two S-band and a C-band Travelling Wave (TW) structures, a THz source station and a vacuum chamber devoted to plasma-based experiments. A 14° dipole delivers the electron beam towards four beam lines devoted to FEL physics, beam diagnostics, Thomson back-scattering and plasma acceleration external injection experiments using the FLAME laser pulse.

Table 3.1. Main parameters of the SPARC electron beam from the photo-injector.

Energy	$(30 - 180) \text{ MeV}$
Energy Spread	$\simeq 0.01\% - 1\%$
Charge	$10 \text{ pC} - 1 \text{ nC}$
Bunch length range (FWHM)	$50 \text{ fs} - 10 \text{ ps}$
Normalised Emittance	$(1 - 3) \text{ mm mrad}$
Max Rep. Rate	10 Hz

The SPARC_LAB photo-injector is composed of a 1.6 cell BNL/ UCLA/ SLAC type gun, operating at S-band (2.856 GHz) with high peak field (120 MV/m) on the incorporated metallic photo-cathode (Cu), generating a 5.6 MeV electron beam [54,55]. The gun is then followed by three sections: two S-band travelling wave (TW) sections and one C-band (TW) section, whose accelerating gradient can boost the beam energy up to 180 MeV . The first one is also used as an RF compressor (velocity bunching regime) by varying the beam injection phase. Solenoid coils embedding the first two sections can be powered to provide additional magnetic focusing to better control the beam envelope and the emittance oscillations under RF compression. A diagnostics transfer line allows to fully characterise the accelerated beam by measuring transverse emittance [32], longitudinal profile, and slice emittance through a Radio-Frequency Deflector (RFD) [56]. The electron beam is generated by a photo-cathode laser operating in single pulse mode at 10 Hz repetition rate. It is a TW-class Ti:Sapphire system and can provide UV pulses with an energy up to 3 mJ on the cathode, with the oscillator pulse train locked to the RF. The high brightness electron beam can be then properly focused and matched into the three accelerating sections, which accelerate it up to the maximum energy: in this way the beam has a high peak current ($> 1\text{ kA}$) and low emittance ($< 2\text{ mm mrad}$). Then, by injecting the LINAC electrons into an undulator, a *Free Electron Laser* (FEL) can be obtained.

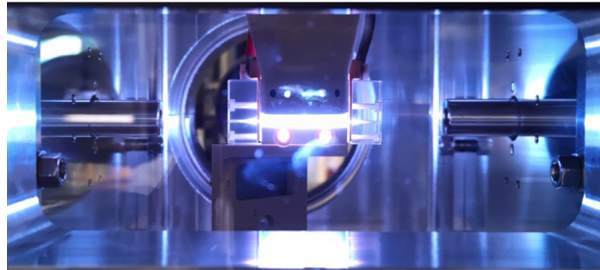


Figure 3.2. Example of gas-filled capillary discharge used for PWFA in SPARC_LAB (COMB interaction chamber). The capillary has a length of 3 cm and a diameter of 1 mm .

The current activity of the SPARC_LAB test-facility is focused on the realisation of plasma-based acceleration experiments with the aim of providing accelerating field of the order of several GV/m , while maintaining the overall beam quality, in terms of energy spread and emittance, of the accelerated electron bunch [57]. As described in Section 2.1, there are two possible methods for performing plasma acceleration: the particle-driven scheme in which the accelerating field is generated by a beam of charged particles, i.e. electrons, and the laser-driven scheme in which the wakefield is obtained through the use of a high-power laser pulse. In particular, in the SPARC_LAB test-facility, particle-driven plasma acceleration experiments are in progress, like the *COMB* experiment [58]: by using a gas-filled capillary discharge, it exploits different particle beam-driven configurations (one or more driver bunches with different charge profiles), with the goal to achieve large accelerating fields [59–61].

Another activity that is being carried out in SPARC is the plasma-based focusing of the electron beam, by means of the *active plasma lens*. It consists on the generation of high magnetic fields inside the plasma while the discharge is occurring; if the particles are introduced in this narrow time window, these fields can highly focus the beam. The active plasma lens is tested for different discharge currents, and the degradation of the beam emittance, due to the generation of a non-linear focusing field, is studied. The aim of this experiment is to obtain the best compromise in terms of emittance preservation and effective focusing [62–64].

3.2 The FLAME laser

Inside SPARC_LAB finds its place the FLAME Laboratory [46], a high-power ultra-short pulse laser, used for various kinds of experiments, including plasma laser acceleration activities, e.g. using solid [65–69] or gaseous targets [13, 47–49, 70–75] to generate and accelerate electron beams. The 250 TW Pulsar laser system is a compact femtosecond laser source providing up to 7 J pulse energy at 10 Hz repetition rate, with $\lambda = 800 \text{ nm}$. The pulse can be as low as 25 fs and leads to a peak power higher than 250 TW. The system is a Titanium-Sapphire laser based on the CPA (Chirped Pulse Amplification) scheme [5]. This technique is based on the reversible manipulation of the temporal characteristics of the laser beam. It allows to amplify a laser beam without damaging the optics, obtaining high powers and ultra-short pulses (order of magnitude of a few tens of fs). To achieve this result, an ultra-short pulse from an oscillator is time-stretched so that it can be safely amplified. After the amplification, the pulse is compressed to a value as close as possible to the initial one. Stretching and compression are achieved by dispersive systems such as prisms or gratings, because the principle is to create different optical paths for each wavelength of the spectrum. A schematic layout of CPA chain is shown in Fig. 3.3.

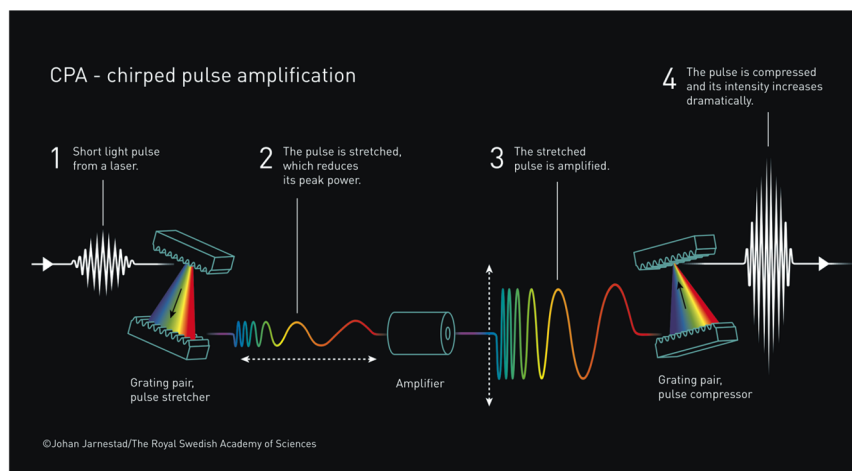


Figure 3.3. CPA schematic for the compression of a laser pulse, showing the two processes of stretching and compression through grating pairs [5].

The FLAME laser system is a custom-made Amplitude Technologies laser, and

it comprises a full integrated Ti:Sa oscillator with its *DPSS* (Diode Pumped Solid State) pump laser, a stretcher, a regenerative amplifier, three multi-pass amplifiers pumped by eleven *Nd:YAG* lasers and a compressor. A general layout of the FLAME laser is shown in Fig. 3.4. A mode-locked oscillator generates the seed of the whole system, with a 80 nm bandwidth centred at 800 nm and a repetition rate equal to about 80 MHz . The system presents a front-end part with pulse contrast enhancement (*booster*) and *regenerative amplifier*, producing pulses with 7 mJ in 80 nm bandwidth at 10 Hz . This bandwidth is achieved thanks to two acoustic-optic devices: the *Fastlite Dazzler*, performing simultaneous and independent spectral phase and amplitude programming of ultra-fast laser pulses, and *Mazzler*, a programmable intra-cavity gain filter which allows control of regenerative amplifiers' spectral gain. At the exit of this first stage, which also includes the stretcher (which is used to elongate the laser pulses up to hundreds of picoseconds), the laser pulse is further amplified by the first amplifier up to the 25 mJ level while the second amplifier brings the energy up to 600 mJ . The third cryogenic amplifier is based on a $5\text{ cm} \times 5\text{ cm} \times 5\text{ cm}$ Ti:Sa crystal pumped by ten *Propulse+*, frequency doubled Nd:YAG lasers, for a total of up to 20 J of pumping energy per pulse. The extraction energy can reach up to 7 J , with a r.m.s. stability less than 1% . Pulses are then transported in air to the compressor placed in the underground target area. Once compressed, the laser beam is transported under vacuum (10^6 mbar) to the interaction chamber through remotely controlled beam steering mirrors.

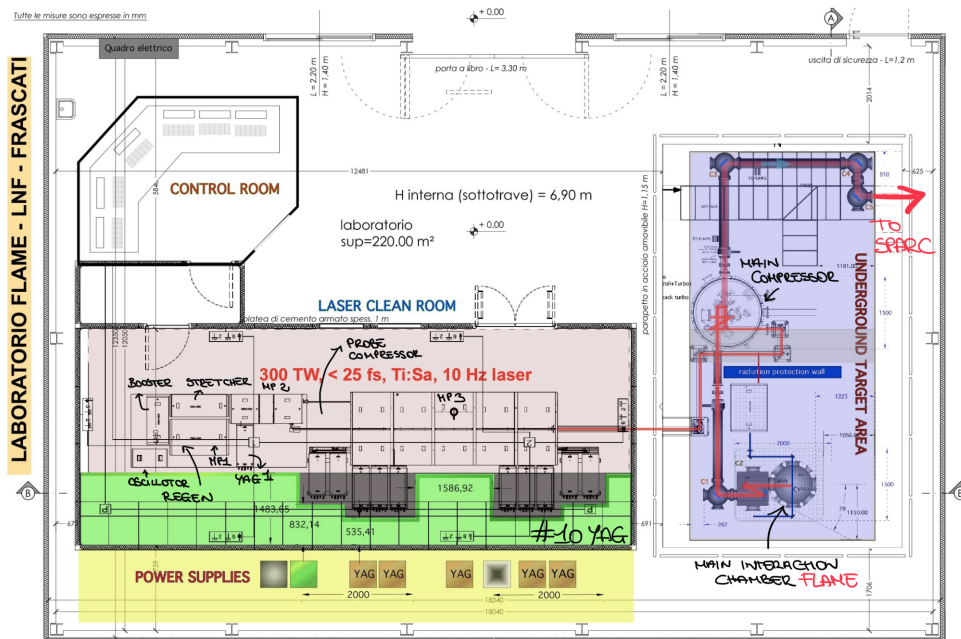


Figure 3.4. Layout of the Flame high-power laser, including the clean room, with the laser chain from the oscillator to the third amplifier, the target area, with the compressor and interaction chamber, and the control room.

As shown in Fig. 3.4, the FLAME Facility takes place in a two levels building: the ground floor is devoted to host the laser clean room, the control room and all the power supplies; at the underground level there is the FLAME bunker. Here, the

optical compressor is installed in a vacuum chamber, in order to reach fs-scale laser pulse duration, exploiting the wide spectrum coming from the Ti:Sa-based CPA amplification chain. After that, the beam goes to the FLAME target area through a dedicated laser transport line up to the off axis parabolic (OAP) mirror, which has a focal length $f = 1\text{ m}$, able to provide a focal spot with a diameter of $20\ \mu\text{m}$ at $1/e^2$ in the middle of the interaction chamber, in the FLAME target area. The main parameters of the high-power laser pulse are shown in Tab. 3.2, where, from this point onward, FW indicates the full width of the beam.

Table 3.2. High-power laser parameters.

Energy	7 J
Temporal length	25 fs
FW $1/e^2$ @ focus	$20\ \mu\text{m}$
Intensity	10^{19} W/cm^2
Contrast-ratio	10^{10}

In the second multipass amplifier, before compression, a fraction of the main laser pulse (usually 10%) is split to create a probe beam, which in turn has a dedicated compressor, not in vacuum, in the clean room. This is a beam of about 10 mJ and time length like that of the main laser ($\sim 30\text{ fs}$). It is generally used as a probe laser for plasma diagnostics in acceleration experiments, in combination with the main laser. The probe can also be used separately from the main pulse, to study particular processes and test diagnostics in experiments, before they are placed on the high-power line.

3.2.1 The EXIN project

As shown in Fig. 3.1 and Fig. 3.4, the laser beam of FLAME, after compression, instead of entering the adjacent interaction chamber, can be transported to the SPARC bunker for laser-plasma interaction experiments, such as for example a *Thomson back-scattering* experiment, coupling the electron bunch to the high-power laser to generate a quasi coherent, monochromatic X-ray radiation. Another ongoing project involving the use of the high-powered FLAME laser in the Sparc bunker is the *EXIN* (External-Injection) project [76, 77]. It is dedicated to exploit the wakefield acceleration with particular care to the quality of the accelerated bunches. In this scheme, the wakefield will be created by the FLAME laser pulse propagating in a hydrogen gas-filled capillary discharge, and it will be used to accelerate the electron bunches produced by the high brightness SPARC photo-injector. The main advantages of this scheme are twofold:

- All the electron bunch characteristics, such as the emittance, the energy spread and the charge, are already well defined before the wakefield acceleration stage;
- Since the bunch generation is decoupled by the acceleration process, it will be possible to have more control on the injection mechanism, i.e. the injection of the electron bunches into the accelerating field.

Being able to control this process is crucial to preserving the initial quality of the electron bunches during acceleration. However, in this configuration the main problem lies in the precision with which the two beams, laser driver and electron witness beam, must be synchronised. In particular, since the duration of the laser pulse is in the order of a few tens of fs , the time matching of the process will have to be in the order of fs . Furthermore, of particular importance will be the realisation of the process of high-power laser pulse guiding inside the plasma-filled capillary discharge, process which is indispensable to overcome the pulse diffraction and to increase the acceleration length (see the theoretical Section 2.3 and the experimental Chapter 5).

Chapter 4

Targets for self-injection experiments

In laser wakefield acceleration, all that is needed to obtain an accelerated electron beam is a high-power laser and a gas source. As discussed in Chapter 2, in this case the laser pulse is able to ionise the gas to a plasma state, generating the accelerating electric field. Then, for a_0 of the pulse $\gg 1$, the same can create a wave break and inject the plasma background electrons into the wakefield, thus accelerating them [22, 23]. Nonetheless, the limitation of this technique lies in the poor quality of the accelerated bunches [78–80]. Applications, e.g. in particle physics or free-electron lasers, however, require bunches with a rather small energy spread, of the order of 1%. Conventional accelerators generally exceed these requirements.

In this chapter, a method for optimising this issue by shaping the plasma density will be presented. In detail, the behaviour of a supersonic gas jet has been studied, both theoretically and experimentally. Fluid-dynamics simulations of the jet will be provided, together with interferometric plasma density measurements.

4.1 Supersonic gas jet study

The large energy spread in LWFA results from the uncontrolled injection and trapping of electrons in the acceleration phases of the wakefield [80, 81]. This phenomenon originates because acceleration in the bubble regime relies on a nonlinear evolution of the laser pulse as it propagates through the plasma, before reaching a sufficient high intensity to induce breaking of the plasma wave [82]. Furthermore, the low shot-to-shot reproducibility generally experienced in this kind of acceleration contributes to the controllability problems of the electron beam generation process. In order to improve reproducibility from shot to shot and to obtain a greater degree of control over the wave breaking process, and hence the injection and trapping of electrons, several schemes have been proposed [23, 83, 84]. One possible approach is to model the flow gas profile on which the laser pulse is focused in order to control the plasma density profile [85].

A supersonic gas jet can be used to produce the required gas density profile. It is a flux of gas travelling at a speed greater than the speed of sound and emanating from an orifice, called a *nozzle*. The nozzle is shaped in such a way that it can

control the properties of the gas jet, such as the density [85]. Supersonic nozzles can therefore be designed to produce a collimated gas jet, i.e. a gas jet that does not diverge sharply after exiting the nozzle. In particular, the edge of such a nozzle provides a density descent with a narrow width. Since supersonic gas jets offer a large degree of control over the gas density and density profile, they are very suitable to be used as targets in laser wakefield acceleration experiments [85–87].

The typical setup discussed is schematised in Fig. 4.1: an ultra-short, high-intensity laser pulse is focused into a jet of gas, typically helium, coming from a nozzle. The driver pulse then completely ionises the gas, creating a plasma channel within the jet. Helium is used as a low atomic number gas that is easy to ionise, but mixtures of it with other gases are often used to increase the charge of the bunches generated.

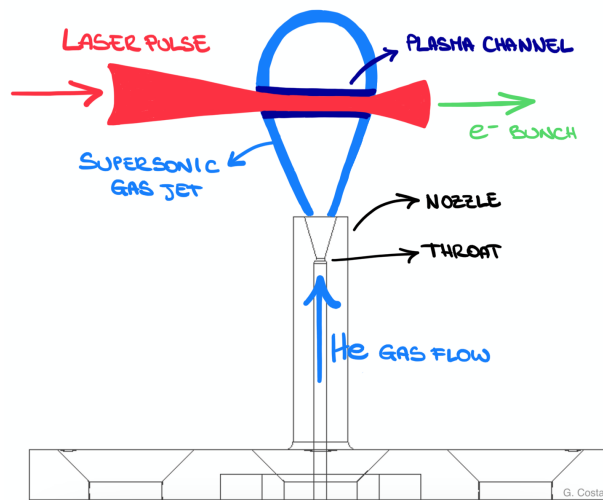


Figure 4.1. Sketch of the setup for a gas jet, on which a laser pulse is focused, coming out of a nozzle, generating a plasma channel inside the jet. The nozzle shown is a real CAD drawing of prototypes made at SPARC_LAB.

To understand how the density distribution in a supersonic gas jet can be controlled, it is necessary to study the flow within a supersonic nozzle. To do so, the thermodynamic properties and flow relationships of an ideal gas must be determined. Then, a continuous approach must be followed to construct a framework that determines the kinetic behaviour of the gas flow, neglecting viscous effects and conductive heat transfer. Since the gas flows at speeds greater than the speed of sound, it is essential to take into account the effects of gas compressibility [88–90].

In more detail, gas molecules forced into a tube are deflected by its walls: if the gas velocity is much lower than the speed of sound of the gas, its density remains constant. Otherwise, when the flow velocity approaches the speed of sound, the effects of compressibility on the gas must be considered. With regard to a flow through a tube (nozzle) of a shape as in Fig. 4.2, i.e. with a narrowing and then a new increase in its diameter, the flow is gradually compressed and then gradually expanded, then its conditions return to their original values. In this case the flow is called *isentropic flow*, as the process is reversible. A flow that becomes supersonic while there is an increase in area experiences an isentropic expansion. If, on the

other hand, it is made supersonic abruptly and its area decreases, the process is irreversible.

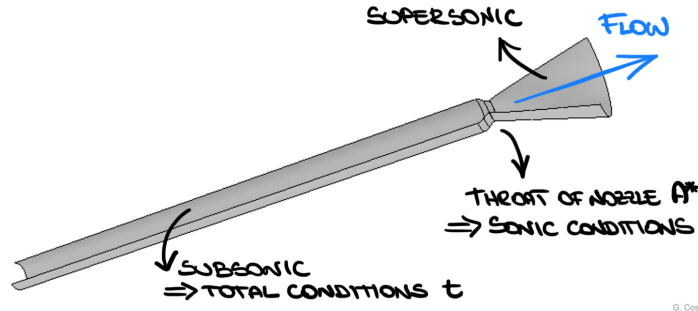


Figure 4.2. Sketch of the inner wall section of a nozzle: the tube has a narrowing, i.e. a point of minimum area in the transverse section, followed by a conical widening. The nozzle shown is a real CAD drawing of prototypes made at SPARC_LAB.

In the case of isentropic flow, the following equations can be derived, describing precisely the concept of entropy from the coefficients of specific heat:

$$\begin{aligned} \gamma &= c_p/c_V \\ c_p - c_V &= R, \end{aligned} \quad (4.1)$$

where c_p is the specific heat coefficient at constant pressure, c_V is the specific heat coefficient at constant volume, γ is the ratio of specific heats, and R is the gas constant from the equation of state. From Eqs. 4.1 it follows that

$$\frac{c_p}{R} = \frac{\gamma}{\gamma - 1}. \quad (4.2)$$

Given the equations of state and entropy of a gas as:

$$\begin{aligned} p &= r R T \\ ds &= c_p \frac{dT}{T} - R \frac{dp}{p} = 0, \end{aligned} \quad (4.3)$$

where p is the pressure, r is the density, and T is the temperature, while ds is the differential change in entropy (which is zero for an isentropic process), dT is the differential change in temperature, and dp is the differential change in pressure. By substituting and differentiating, the Eqs. 4.3 result in

$$\left(\frac{c_p}{R} - 1 \right) \frac{dp}{p} = \frac{c_p}{R} \frac{dr}{r}. \quad (4.4)$$

Using Eq. 4.2 and integrating it results in

$$\frac{p}{r^\gamma} = C. \quad (4.5)$$

Considering the constant C as the total of pressure and density that occurs when the flow is brought to rest isentropically [91], and using the equation of state it is possible to obtain

$$\frac{p}{p_t} = \left(\frac{T}{T_t} \right)^{\frac{\gamma}{\gamma - 1}}, \quad (4.6)$$

where p_t and T_t are the total pressure and temperature respectively.

Given the following relations of Mach number M definition, enthalpy h , and derived expression for the conservation of energy

$$\begin{aligned} M &= \frac{v}{a} = \frac{v}{\sqrt{\gamma RT}} \\ H &= c_p T \\ h_t &= h + \frac{v^2}{2}, \end{aligned} \quad (4.7)$$

where v is the flow velocity and a is the speed of sound, and since it can be expressed that $a^2 = \gamma R T$, it follows

$$c_p T_t = c_p T + M^2 \left(\frac{\gamma RT}{2} \right). \quad (4.8)$$

Dividing by c_p and using Eq. 4.2 it results

$$\frac{T}{T_t} = \left[1 + \frac{M^2(\gamma - 1)}{2} \right]^{-1}, \quad (4.9)$$

Therefore, by means of Eq. 4.6 and the equation of state, since

$$\frac{p}{p_t} = \left(\frac{r}{r_t} \right)^\gamma = \left(\frac{T}{T_t} \right)^{\frac{\gamma}{\gamma - 1}}, \quad (4.10)$$

the following relations are also obtained:

$$\begin{aligned} \frac{p}{p_t} &= \left[1 + \frac{M^2(\gamma - 1)}{2} \right]^{-\frac{\gamma}{\gamma - 1}} \\ \frac{r}{r_t} &= \left[1 + \frac{M^2(\gamma - 1)}{2} \right]^{-\frac{1}{\gamma - 1}}. \end{aligned} \quad (4.11)$$

where r_t is the total density. The Eqs. 4.9 and 4.11 can be used to obtain the relations between the static and total temperature, pressure and density respectively, in terms of the Mach number.

In real fluids, as the velocity increases, the density does not remain the same due to compressibility effects, as already mentioned. For high velocities it is therefore necessary to take into account how the *mass flow rate* \dot{m} varies in relation to the density. Since

$$\dot{m} = r v A, \quad (4.12)$$

where A is flow area, using the Mach number equation in 4.7 and the equation of state, it can be found that

$$\dot{m} = A M p \sqrt{\frac{\gamma}{RT}}. \quad (4.13)$$

Exploiting now Eq. 4.9 and the first one in 4.11, it is possible to derive

$$\dot{m} = \frac{A pt}{\sqrt{T_t}} \sqrt{\frac{\gamma}{R}} M \left[1 + M^2 \frac{(\gamma - 1)}{2} \right]^{-\frac{\gamma + 1}{2(\gamma - 1)}}, \quad (4.14)$$

which is a compressible form of the mass flow rate equation. If the flow velocity v reaches the speed of sound a , i.e. for $M = 1$, the flow is in *sonic condition*. For a tube with changing area, such as a nozzle for example, the maximum mass flow rate through the system occurs when the flow is *choked* at the smallest area A^* . This location is called the *throat of the nozzle*. For the mass conservation, the mass flow rate through a nozzle is a constant and, if no heat is added and there are no pressure losses in the nozzle, the total pressure and temperature are also constant. By substituting the sonic conditions into the mass flow equation 4.14, it follows that

$$\dot{m} = \frac{A^* pt}{\sqrt{T_t}} \sqrt{\frac{\gamma}{R}} \left[\frac{\gamma + 1}{2} \right]^{-\frac{\gamma + 1}{2(\gamma - 1)}}. \quad (4.15)$$

It is possible to define the Mach number M at any nozzle point as a function of the ratio between the area A at that point and the area of the throat A^* :

$$\frac{A}{A^*} = \left(\frac{\gamma + 1}{2} \right)^{-\frac{\gamma + 1}{2(\gamma - 1)}} \frac{\left[1 + M^2 \frac{(\gamma - 1)}{2} \right]^{-\frac{\gamma + 1}{2(\gamma - 1)}}}{M}. \quad (4.16)$$

Since the Mach number is related to the flow velocity, the exit velocity of the nozzle can be determined, knowing the area ratio [91]. Therefore it can be concluded that, known M , all of the other flow relations can be calculated.

4.2 Nozzle fluid-dynamics simulations

In order to study possible nozzle geometries aimed at having a certain controlled gas flow for LWFA experiments in the self-injection scheme, it is necessary to reconstruct the variables pressure p , volume V and temperature T , then density r , at each point of the geometry, at the arrival time of the laser pulse. Since the geometry of the object is known, so is its volume, as are the initial conditions generally used for an experiment of this type. For example, with regard to the experiments already carried out with the high-power FLAME laser [13, 46, 70–73] in the SPARC_LAB laboratories (see Chapter 3), the nozzles have a length of about few tens of mm , and a tube diameter and aperture in the order of few mm . The gas used is usually helium, sometimes with a low percentage of nitrogen (1–10%) for the reasons already mentioned in Section 4.1, with a pressure inside the mixing chamber typically around 20 bar . The exit of the gas from the nozzle is controlled by a solenoid valve, with an opening time of a few ms , synchronised with the arrival of the laser pulse.

As described, the flow generated in this type of geometry reaches supersonic speeds, taking the speed of sound in helium to be around 965 m/s , for example. For this reason, codes generally used for fluid-dynamic simulations encounter problems

in calculating velocities, which slows down the computation of processes. In order to obtain a quick prediction of the flow properties at the outlet of a particular type of nozzle geometry, a stationary one-dimensional model was developed, starting from the equations derived in Section 4.1. The results obtained by this method were then compared with fluid-dynamic simulations in OpenFOAM (see Appendix B), at a final time of a few hundreds of μs .

4.2.1 One-dimensional stationary model

Considering the ideal fluid model approximation¹, with laminar flow, the following relations were used:

- The mass flow equation 4.14 as a constant, i.e.

$$r v A = C_1 . \quad (4.17)$$

- The equation for an isentropic flow 4.5, i.e.

$$p n_0^{-\gamma} = C_2 . \quad (4.18)$$

- The equation for momentum conservation, i.e.

$$-\frac{dp}{dx} = n_0 v \frac{dv}{dx} , \quad (4.19)$$

where x is the longitudinal coordinate. It is already a one dimensional steady form of Euler's Equation, and it is possible to note that the pressure drop of the fluid (the term on the left) is proportional to both the value of the velocity and the gradient of the velocity.

- The equation of state of perfect gases, i.e.

$$p = n_0 k_B T , \quad (4.20)$$

where n_0 is the number density expressed in [*molecules/m³*] and k_B the Boltzmann constant.

Since the constants C_1 and C_2 are known, as they can be estimated from the initial conditions, the following relations can be expressed:

$$\begin{aligned} v &= \frac{C_1}{n_0 A} \\ p &= C_2 n_0^\gamma . \end{aligned} \quad (4.21)$$

By substituting Eqs. 4.21 into Eq. 4.19 and deriving, it is possible to obtain:

$$\begin{aligned} -C_2 \frac{dn_0^\gamma}{dx} &= \frac{C_1^2}{A} \frac{d}{dx} \left(\frac{1}{n_0 A} \right) \Rightarrow \\ -C_2 \gamma n_0^{\gamma-1} \frac{dn_0}{dx} &= \frac{C_1^2}{A} \left[- \left(\frac{1}{A n_0^2} \right) \frac{dn_0}{dx} - \left(\frac{1}{A^2 n_0} \right) \frac{dA}{dx} \right] \Rightarrow \\ -\frac{C_1^2}{A^3} \frac{dA}{dx} &= \left[\frac{C_1^2}{A^2 n_0} - C_2 n_0^\gamma \gamma \right] \frac{dn_0}{dx} . \end{aligned} \quad (4.22)$$

¹because the free mean path of the molecules is \ll of the spaces of the simulation geometry.

Using the expression obtained and assuming a steady-state condition, it is then possible to determine the variation in the flow density n_0 as a function of the variation in area A . Knowing the change in density then, it is possible to calculate the change in velocity and pressure of the gas using Eqs. 4.21.

The Eq. 4.22 can be integrated, given a known variation in internal diameter of the nozzle. For this purpose, different duct geometries were considered, varying the shape of the nozzle throat. In order to fit the actual objects used for FLAME's laser self-injection experiments, the nozzle length was set at 17 mm, the straight line diameter at 0.8 mm, the throat diameter at 0.5 mm and the aperture diameter at 2 mm.

With these dimensions, a nozzle radius function was reconstructed with respect to its longitudinal position. The aim here is to study the behaviour of the outflow as the type of nozzle narrowing varies. For this reason, a *logistic function* (i.e. a *sigmoid function*) has been chosen to reproduce the internal radius of the nozzle:

$$f(x) = \frac{a e^{c m} + b e^{m x}}{e^{c m} + e^{m x}}, \quad (4.23)$$

where a and b correspond to the radius of the tube and aperture of the nozzle, while $m \geq 0$ and c represent the slope and position of the narrowing, respectively. In this way, by modifying m , it is possible to vary the radii of curvature of the throat in a simple way, inside the analytical model. Fig. 4.3 a) shows this possibility within the code. Three main nozzle restriction geometries have been considered and are the ones shown in Fig. 4.3: a soft smooth narrowing, a linearly decreasing/increasing one, and a sharp one, represented by a step function.

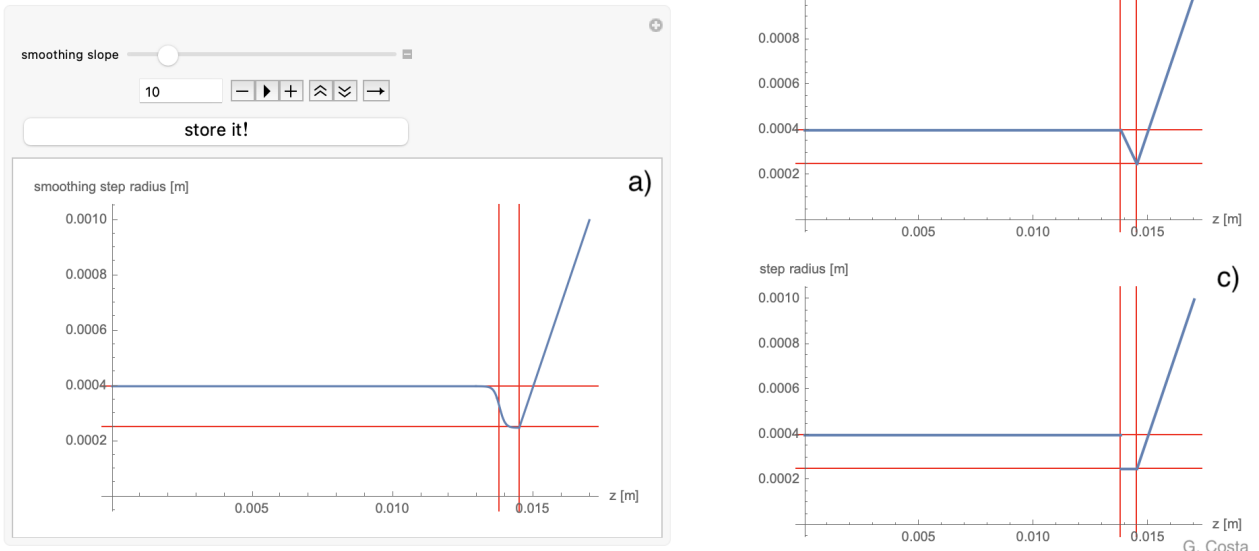


Figure 4.3. Representation of functions for the main nozzle restriction geometries, considered within the developed analytical model: a) smooth narrowing, b) linear narrowing, c) sharp narrowing. The red lines set the limits of the narrowings.

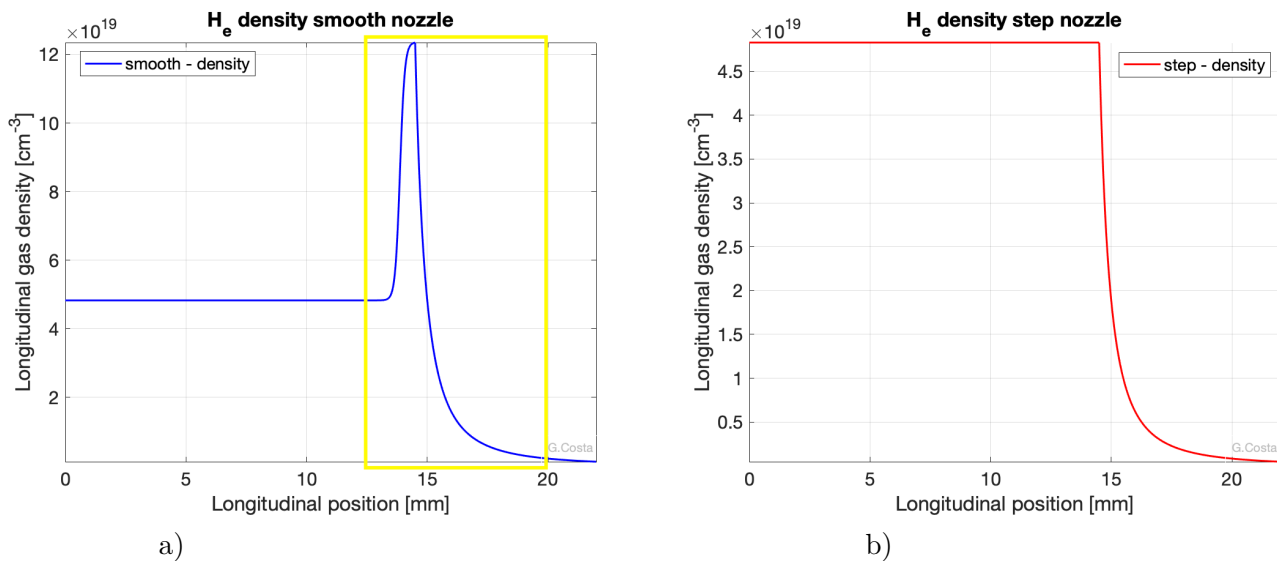


Figure 4.4. Flow density reproduced by the stationary analytical model for nozzle narrowing geometries: a) smooth, b) sharp. The flux density in the laser focal plane are about $2.8 \times 10^{18} \text{ cm}^{-3}$ and $1 \times 10^{18} \text{ cm}^{-3}$, respectively.

Fig. 4.4 shows the results obtained from this analytical estimation, in terms of flow density, for the case of smoothed narrowing and that of the step function.

The initial conditions are well reproduced by the model, while the plane to be considered in order to have a useful estimation of the output flux density is that of the laser pulse focus, i.e. typically at a distance of 1 mm from the nozzle aperture. In this case, the laser focal plane is therefore at the longitudinal position of 18 mm. It is possible to observe that the smoothed narrowing geometry (Fig. 4.4 a)) gives a flux density in the laser focal plane of about $2.8 \times 10^{18} \text{ cm}^{-3}$, while the stepped narrowing geometry (Fig. 4.4 b)) gives about $1 \times 10^{18} \text{ cm}^{-3}$. Since this is an estimate obtained from a one-dimensional stationary model, these values can be considered averaged over the aperture's transverse position and at the time of fluid-dynamic equilibrium of the outflow process. In addition, the density peak present at the exit of the nozzle throat in Fig. 4.4 a) can be clearly seen, due to the strong increase in flow velocity and thus its transition to the supersonic regime. Furthermore, as expected, this analytical model is not able to reproduce the narrowing point represented by the step function (see Fig. 4.4 b)), since continuous functions with continuous derivatives are obviously required to solve the differential equations of the flow. With this model, the linear narrowing geometry of the nozzle (see Fig. 4.3 b)), reproduces exactly the same density as in the case of the nozzle with the smoothed narrowing as in Fig. 4.3 a), since both velocities have the same trend.

4.2.2 OpenFOAM fluid-dynamic simulations

Starting from the same initial conditions used for the analytical model previously shown (see Section 4.2.1), and from the same two nozzle geometries presented, fluid-dynamic simulations in OpenFOAM were set up. The two geometries used for the mesh are shown in Fig. 4.5: in order to reproduce the modelled smoothed

narrowing, a smoothing chamfer of approximately 0.2° was made at the corners of the stepped narrowing.

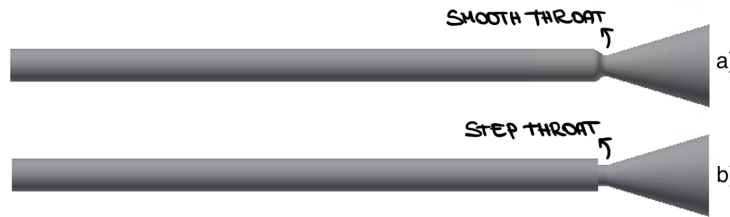


Figure 4.5. CAD drawings showing the inside walls of the two nozzles with different geometries: a) smooth throat, b) sharp throat. The first one is based on the second one, smoothing the corners by 0.2° .

The results obtained for the two cases are shown in Fig. 4.6. Regarding the geometry with smoothed narrowing, the simulation has a final time step of about $500 \mu\text{s}$ and it has not yet reached equilibrium. In order to compute supersonic velocities, it is necessary to use a very small time step ($10^{-15} - 10^{-10} \text{ s}$), to satisfy the *CFL condition*², which is the basis of the code resolution. The flux density obtained at this time, in the plane of the laser focus is about $1 \times 10^{17} \text{ cm}^{-3}$, so about than a factor 2 – 3 less than expected. The yellow box highlights the area to be compared with the theoretical model (Fig. 4.4 a)).

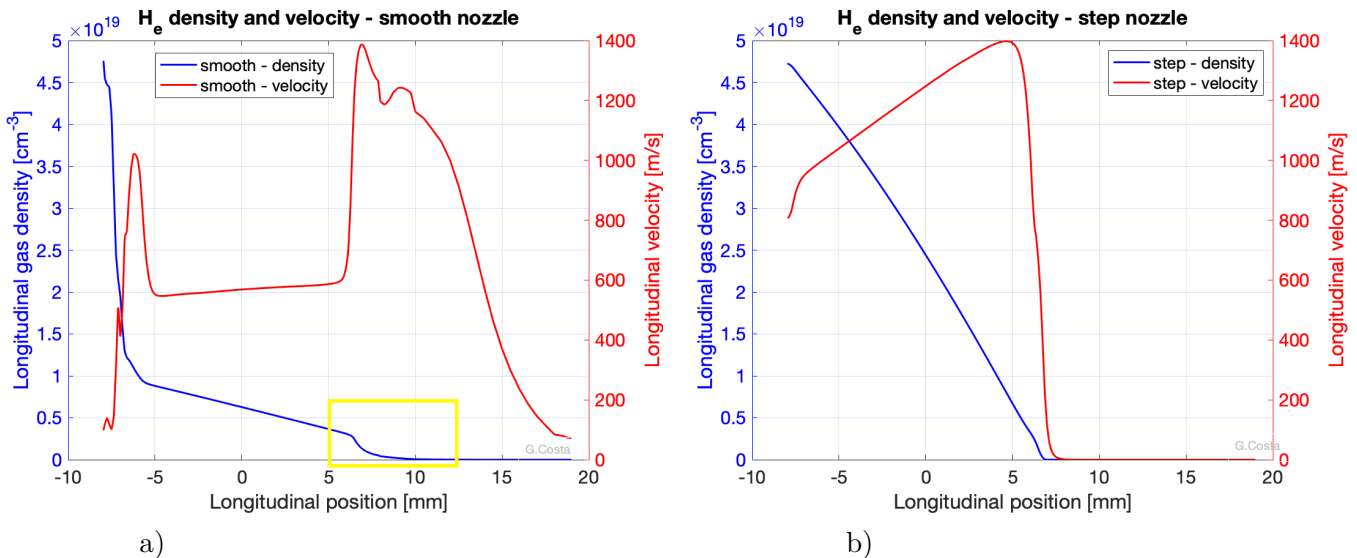


Figure 4.6. Results of OpenFOAM simulations of flow density and longitudinal velocity for the two nozzle geometries considered: a) smooth throat, b) sharp throat. The case of sharp throat appears to be too turbulent to be computed in this way.

The longitudinal velocity curve (in red) has a very precise trend: it has a rapid growth due to the initial pressure applied, then it has a constant propagation zone inside the straight section, and then it grows steeply at the exit of the nozzle

²The *Courant-Friedrichs-Lewy condition* is a convergence condition used, for example, in fluid-dynamics, for solving certain partial differential equations.

narrowing, reaching supersonic values in few hundreds of microns. In the straight tube section, despite there being a constant velocity, the density decreases (Fig. 4.4 a)), in contrast to what happens in the same area computed with the analytical model (Fig. 4.6 a)). This is due to the approximations made by moving from the 3D mesh of the simulation to the one-dimensional model.

In the case of sharp narrowing (Fig. 4.6 b)), on the other hand, the simulation fails to reproduce the turbulence due precisely to the geometry of the throat: this happens when the laminar flow approximation is broken, as already described in Section 4.1, and very close particles have very different velocities. The result is therefore that the flow quantities obtained cannot be considered reliable, for example in this case we have an average density in the plane of the fire $\ll 10^{17} \text{ cm}^{-3}$.

Since experimentally the opening time of the solenoid valve is always about a few *ms*, the evolution of the flow density over time, in the case of a smoothed narrowing, was verified, in order to obtain a possible flow estimate for longer simulation times. Fig. 4.7 shows a plot of the density trend at the nozzle outlet as a function of the simulation evolution time.

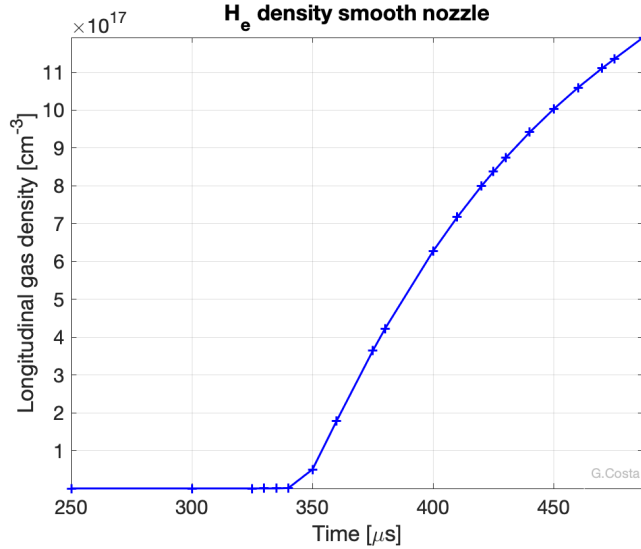


Figure 4.7. Results of an OpenFOAM simulation for the flow density in the of smooth throat nozzle, as a function of the simulation evolution time.

From this density time trend, it can be deduced that the flux has not yet reached a stationary condition after $500 \mu\text{s}$, and therefore it can be concluded that for a time of about 2 – 3 times the simulated time, flux densities similar to those expected would probably be obtained.

4.3 Plasma density from nozzles gas jet

In order to obtain experimental evidence of the difference between the two nozzle geometries treated in Section 4.2, plasma generation tests using these two targets were carried out. To do this, the main Flame laser was used, employing about 300 mJ of its energy: the pulse is focused by means of a parabolic mirror with focal

length $f = 1\text{ m}$ at the centre of the interaction chamber, at a height of about 1 mm above the nozzle opening. The arrival of the pulse is synchronised with the opening of the solenoid valve, upstream of which there is a pressure of few *bar* of helium, in this case. The laser parameters for this experiment are summarised in Tab. 4.1, in Fig. 4.8 there is a spot of the laser pulse in the focal plane, while Fig. 4.9 shows one of the nozzles installed.

Table 4.1. Laser parameters for plasma gas jet tests.

Energy	$\sim 300\text{ mJ}$
Temporal length	25 fs
FW $1/e^2$ @ focus	$20\text{ }\mu\text{m}$
Intensity	$\sim 2 \times 10^{18}\text{ W/cm}^2$
a_0	~ 1

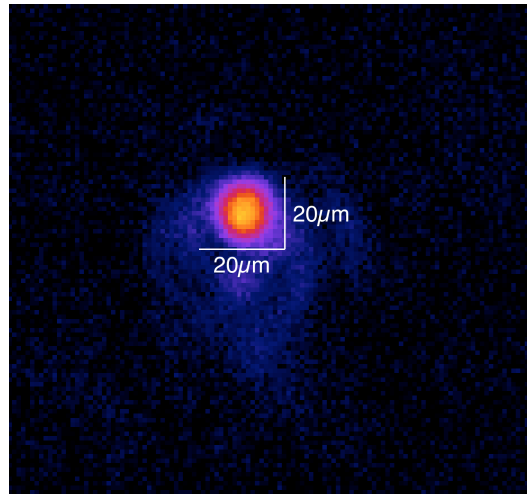


Figure 4.8. Spot of the main laser pulse in the focal plane: FW $1/e^2 = 20\text{ }\mu\text{m}$.

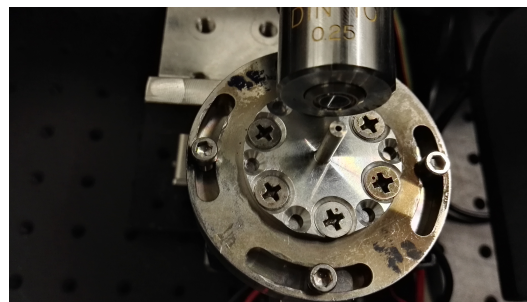


Figure 4.9. Photo of one of the nozzles installed, in the centre of the interaction chamber. The objective that is next to the nozzle belongs to the CCD used to measure the pulse focus.

Since the aim of these tests is to detect differences in the plasma density obtained for the two different nozzle configurations, a Mach-Zehnder interferometer (see

Appendix A) was used for the measurements, exploiting Flame's probe laser at the point of interaction. The expanding plasma, coming from the nozzle and ionised by the main pulse, is placed in one of the two arms of the interferometer, while the reference arm passes parallel to the first one.

4.3.1 Interferometric method for plasma measurements

Interferometric methods use the dependence of the refractive index on the density in a transparent medium. The refractive index variation can be detected by experimentally measuring the dephasing of a probe beam, caused by the different phase velocity of the light propagating through the plasma. The phase velocity v_p is indeed inversely related to the refractive index η , i.e.

$$v_p = \frac{c}{\eta}, \quad (4.24)$$

and by analysing its variation it is possible to find the density of the plasma crossed by the beam [92]. If there is no phase difference between the two beams, the interference fringes are straight (see Fig. 4.10). However, when a beam passes through the plasma, the introduced phase velocity difference results in a measurable fringe shift [93].

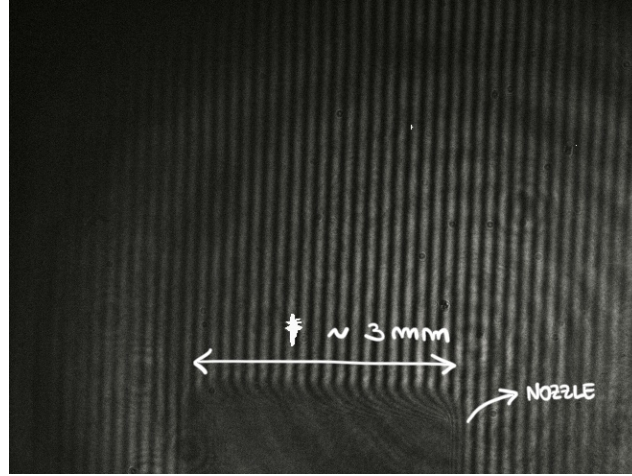


Figure 4.10. Interferogram in the absence of plasma, i.e. without fringe shift. At the bottom the nozzle shadow can be seen, the width of which has a known size and can be used to calibrate the measurements.

The refractive index of the plasma depends on the electron density and on the laser wavelength. It can be expressed as:

$$\eta = \sqrt{1 - \frac{n_e}{n_c}}, \quad (4.25)$$

where n_e is the electron density, and n_c is the critical electron density for the specific probe laser wavelength (800 nm), which can be expressed as $n_c = 10^{21} \lambda^{-2} \text{ cm}^{-3}$, with λ in μs .

Assuming that there is no difference between the two interferometer paths other than that due to the presence of the plasma, and since the variation of the plasma density is negligible in the range of the laser wavelength, the rules of geometric optics can be applied. The path difference Δs between the two beams can then be written as follows [93]:

$$\Delta s = \int_{z_1}^{z_2} \eta_{vacuum} dz - \int_{z_1}^{z_2} \eta(z) dz , \quad (4.26)$$

and from which the phase shift $\Delta\phi$ can be obtained:

$$\frac{\Delta\phi}{2\pi} = \frac{\Delta s}{\lambda} \quad \text{and} \quad \eta_{vacuum} \simeq 1 \Rightarrow \Delta\phi = \frac{2\pi}{\lambda} \int_{z_1}^{z_2} \frac{n_e}{n_c} dz . \quad (4.27)$$

4.3.2 Analysis of plasma density measurements

The interferograms produced for the two nozzle cases with the same initial flux and laser pulse conditions are shown in Fig. 4.11: it can be observed that in the case of the smoothed narrowing nozzle (a), the interferogram obtained has a cleaner and more defined shape and also extends over a longer length than in the case of the sharp narrowing nozzle (b). Typically, the maximum length of the plasma channel, and therefore of achievable acceleration, is defined by the aperture angle of the nozzle. However, statistical analysis of these measurements, carried out on 100 shots, shows that the shape of the nozzle throat plays a role in addition to its aperture.

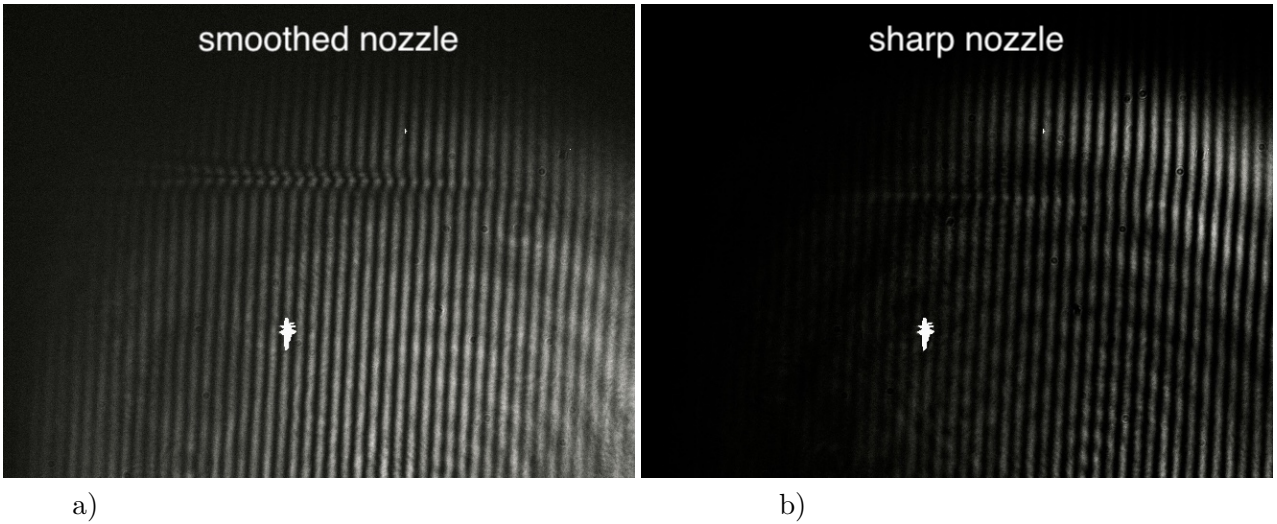


Figure 4.11. Interferograms in the presence of plasma, produced by gas jets from the two different types of nozzle considered: a) smooth throat, b) sharp throat.

The analysis of these data consists of a reconstruction of the dephasing. By means of the shift of the fringes recorded on the interferogram, a phase map is produced. By using the Fast Fourier Transform (FFT) methods [94], the dephasing

map can be extracted by the spatial variation of the fringe intensity and visibility, through the FFT of the interferogram. Once the phase-map is evaluated, since it is assumed to be an Abel transform of the crossed refractive index, it is inverted by using the Abel inversion [95]. *The software used [96,97] for interferogram analysis was kindly provided by ILIL - CNR laboratory.*

An example of data analysis for the two nozzles studied is shown in Fig. 4.12: as expected, the plasma density profile obtained with the smoothed nozzle (a) is more homogeneous and reaches a peak of about $2.6 \times 10^{18} \text{ cm}^{-3}$, while the profile obtained with the nozzle with sharp narrowing is irregular and the maximum density reached is about $1 \times 10^{18} \text{ cm}^{-3}$. The statistical error on this plasma density generated by the laser beam is around 10%, and is mainly due to the shot-to-shot instability of the main pulse [13]. These density values are then compatible with those found analytically or estimated via fluid-dynamics simulations, this confirms the fact that the plasma is completely ionised by the laser pulse. Additionally, this analysis confirms what was mentioned about the differences between the plasma channel length in the two cases: the relative difference is approximately 0.5 mm , since the average channel length found is 2.4 mm in the case of smoothed narrowing and 1.9 mm in the case of sharp narrowing. A statistical error of 10% must also be taken into account here, while the estimated dephasing length for these parameters is about 3 mm .

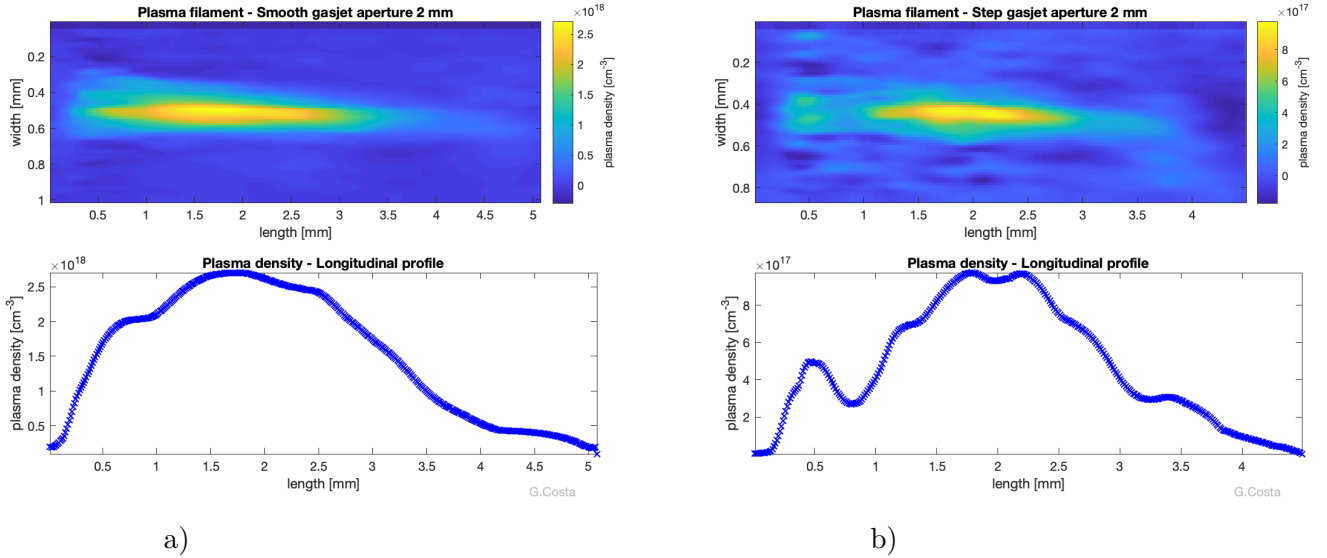


Figure 4.12. Plasma density longitudinal profile. Interferogram analysis produced by gas jets from the two different types of nozzle considered: a) smooth throat, b) sharp throat.

In conclusion, the results obtained through the analytical model and the OpenFOAM gas flow simulations, together with the experimental plasma density data, point to the evidence that a net narrowing of the nozzle throat, used for LWFA experiment, leads to limitations in the control of the flow relations and the quality of the produced plasma. This occurs because of the turbulence generated by the net step present in the narrowing, which slows or compromises the supersonic flow condition [88]. Having a supersonic gas flow out of the nozzle is key to being able to

influence the flow density, and therefore of plasma density [85], starting from the nozzle aperture and its geometry. Quick tests carried out on the stationary model show that varying the smoothing angle of the nozzle throat has an influence on the output flow density value, as it affects the flow velocity.

Chapter 5

Plasma channels for laser confinement

The confinement of a laser pulse in a plasma channel is very important because it allows to increase the acceleration length of an electron beam feeling the field generated by the laser pulse.

A theoretical introduction of the guiding process will be carried out, with a study of the possible plasma device and its matching conditions between the laser beam and the plasma. The results of two experimental campaigns for the guiding of a low power laser pulse will be presented, supported by plasma density measurements within the target and by 1D model simulations.

5.1 Theoretical introduction and state of the art

To excite a wakefield suitable for electron acceleration, laser intensities of the order of 10^{18} W/cm^2 are required. To achieve these intensities, the ultra-short laser pulses must be focused in spots of the size of tens of microns. A small focus spot, however, will quickly diverge beyond the minimum spot, reducing the intensity of the pulse and limiting the length of laser interaction with the particles to be accelerated. To increase this interaction length, the laser can be guided, for example, by a plasma channel. If this channel has the right density profile, the plasma can act as a lens, keeping the laser confined [4, 98].

This concept is essential to increase the energy of particles accelerated by laser-plasma acceleration. Plasma channels capable of guiding ultra-short, high-intensity laser pulses can be formed by pre-ionisation of a gas flux by a laser or by an electrical discharge into a capillary-discharge waveguide. This plasma waveguide can be formed by applying high voltage to a cylindrical capillary with a diameter of less than one millimetre filled with gas. The resulting ionisation of the gas creates a plasma channel with a typically parabolic radial density profile. This gradient causes a radially variable refractive index, which keeps the laser confined [9]. A characteristic measure for the shape of the channel is the matched spot size, which governs the propagation and confinement of the laser. Meanwhile, the on-axis density in the plasma determines the group velocity of the laser, and thus the velocity of the wake. This means that a low density (in the order of 10^{17} cm^{-3}), i.e. a fast wake, is

required to accelerate electrons to high energies (GeV level) [99].

5.1.1 Guiding of Gaussian pulses

Lasers are attractive tools in many fields because they can be used to transfer energy over long distances with minimal loss, and because of the ability to focus energy tightly and accurately in small spots. In many situations, the interaction of the laser with matter is limited by the propagation of the laser, which typically diffracts quickly after coming to a focus, limiting the high intensity field to a small region near focus.

In the case of plasma accelerators, useful laser intensities can only be obtained by focusing the laser beam on a small spot of a few tens of microns in diameter. The divergence of the laser beam after focusing is usually characterised by the Rayleigh length (Eq. 2.34), defined as the distance beyond which the beam intensity is reduced by a factor of 2 with respect to the focal plane. Equivalently, the beam diameter increases by a factor of $\sqrt{2}$ with respect to its minimal diameter, i.e. the focal spot (Fig. 5.1).

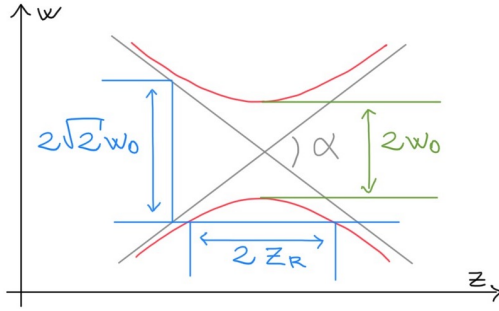


Figure 5.1. Sketch of a typical beam geometry around the focal point.

It is shown in [100] that for a beam focused by a parabolic mirror or a lens with the focal length f , if D is the diameter illuminated on the lens by the initial beam, the Rayleigh length and the waist radius are

$$z_R = \frac{\lambda}{\pi} \cot^2 \alpha = \frac{4f^2}{\pi D^2} \lambda, \quad (5.1)$$

$$w_0 = \frac{\lambda}{\pi} \cot \alpha = \frac{2f}{\pi D} \lambda, \quad (5.2)$$

where λ is the laser wavelength and α is the divergence angle (see Fig. (5.1)).

The electron energy gain from the wakefield is proportional to the product of the accelerating field by the effective propagation distance of the laser, that is about πz_R , in the absence of guiding.

For example, a 10 *cm* beam of a 800 *nm* laser focused by a 1 *m* parabolic mirror will have a Rayleigh length lower than 1 *mm*, whereas the dephasing length of an electron accelerating in plasma wakefield is typically (1 – 3) *cm*.

The diffraction length can be extended by focusing less tightly - employing a larger f-number - which for a given wavelength will require decreasing the source

beam diameter (or increasing focal distance), resulting in an increase in the focal spot size. In high power applications, the damage threshold of optics sets the minimum beam size at the focusing optic while the desired intensity puts an upper limit on the size of the focal spot. In practice, high power laser systems often have a fixed f-number, so that the Rayleigh length - and thus the interaction length - is fixed by design [101].

In laser plasma accelerators in particular, this means the laser can only drive a wakefield for a certain distance, typically on the order of millimeters to a few centimeters in a homogeneous plasma [4]. Increasing this interaction length requires a waveguide to confine the laser radially, such as a preformed plasma channel with radially increasing density, which acts as plasma waveguides, with a mechanism analogous to polymeric fibers: they both rely on the same phenomenon - total internal refraction resulting from axially-peaked refraction index.

5.1.2 Capillary discharge channels

In order to increase the distance over which the intensity of the laser pulse is maintained at a value close to that at its focus, it is necessary to channel the laser pulse. A wide variety of methods for channelling intense laser pulses has been investigated, including relativistic and ponderomotive channelling [102, 103], guiding by grazing incidence reflection from the walls of a hollow capillary [104, 105], and plasma waveguides.

In this last method, a plasma is formed with a transverse electron density profile with a minimum on the axis of propagation. An electron density profile of this form corresponds to a transverse refractive index profile that decreases with radius, providing a focusing effect that can counteract diffraction and refraction, such that the plasma acts as a lens with positive focal length. This refractive guiding can be achieved in several ways [4], depending on the radial profile of both laser intensity and plasma density.

A promising class of waveguide for high intensity laser pulses is the plasma waveguide, in which, ideally, the radial electron density profile of the plasma is parabolic:

$$n_e(r) = n_e(0) + \Delta n_e (r/r_m)^2, \quad (5.3)$$

where $n_e(0)$ is the axial electron density and Δn_e is the increase in the electron density at radius $r = r_m$. In the absence of further ionization of the plasma by the guided laser pulse, and where ponderomotive and relativistic effects can be neglected, a Gaussian laser pulse will propagate through the guide with a constant spot size $W_M = [r_m^2 / (\pi r_e \Delta n_e)]^{1/4}$, where r_e is the classical electron radius [6]. Here spot size is defined as the radius at which the pulse intensity is $1/e^2$ of the peak value.

A number of techniques for generating a plasma waveguide have been studied [106–109]. As for the capillary, a distinction can be made between ablative capillaries where ablation of wall material provides a significant fraction of the plasma particles [110–112], and gas-filled capillaries where breakdown is induced in an initially neutral gas [112–118]. The latter is the most widely used for recent laser pulse guiding applications because it allows for over 10^6 discharges without significant degradation of the structure, and provides a degree of controllability by adjusting neutral gas fill

pressure and gas composition [6, 119, 120]. Other reasons why capillary discharges are an attractive method for forming a plasma waveguide are that they require no auxiliary laser and they can be scaled to long lengths (up to tens of *cm*).

Spence et al. in [6] presented a hydrogen plasma waveguide formed by a slow discharge through a H-filled capillary. By means of the measurements of the electron density, using time-resolved interferometry, they demonstrated that this simple device is able to generate a guiding channel in a pure, almost fully ionized hydrogen plasma, with a stable and approximately parabolic transverse electron density profile. The device used is a tube with an inner-diameter of $300\ \mu\text{m}$; the gas, hydrogen, is injected through the side-wall of the capillary at two points (see Fig. (5.2)), the discharge circuit provides a discharge current that is an approximately half-sinusoidal pulse with a full width of $200\ \text{ns}$, and a peak of $300\ \text{A}$.

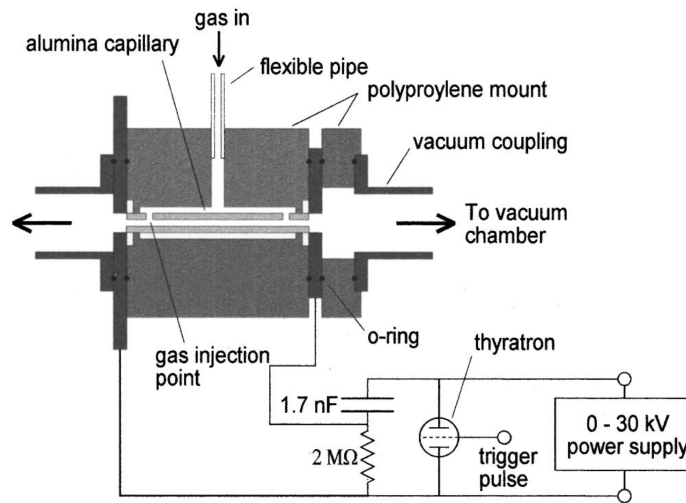


Figure 5.2. Schematic diagram of the gas-filled slow capillary discharge, and the associated discharge circuit [6].

In this case the gas flow reaches a steady state in which the pressure in the section of capillary between the injection points is axially uniform, while between each injection point and the capillary exit the pressure drops to the background pressure of the vacuum chamber. Furthermore, since the initial hydrogen density is uniform between the gas injection points, the plasma waveguide will also have a uniform guiding profile in its central section. The channel is formed due to cooling of the plasma at the walls of the capillary which creates a radially decreasing temperature. Longitudinal transport occurs on a time scale much slower than that of radial equilibration, and hence, is not expected to play a significant role in the channel formation in the middle of the capillary [6].

Gas-filled capillary discharge waveguides offer a number of advantages for guiding intense laser pulses, such as low transmission and coupling losses, the ability continuously to tune the plasma pressure, and a long device lifetime. In addition, for H-filled capillaries the plasma channel may be fully ionized, which minimizes spectral or temporal distortion of the guided laser pulse. In order to assist the development of this waveguide, it is important to understand the mechanisms by

which the guiding electron density profile is formed. Furthermore, a H-filled capillary discharge waveguide was used to guide laser pulses with peak intensities of greater than 10^{16} W/cm^2 , through tens of *mm* long capillaries with pulse energy transmissions up to 90% [121].

A description of the plasma dynamics inside a discharge capillary based on a numerical magnetohydrodynamic (MHD) code was given by Bobrova et al. [9, 122]. Three stages of the plasma evolution have been identified. During the first stage the magnetic field penetrates the plasma on a time scale of tens of *ns*, and the plasma is heated and ionized locally, while radial distributions of the plasma parameters remain homogeneous. As the electric current increases, the thermal conduction time decreases, and thermal conduction becomes significant at approximately the time of complete ionization of the plasma. A redistribution of the plasma temperature and density across the channel occurs during this second stage of the discharge evolution. In the third stage the discharge plasma is in dynamic and thermal quasi-equilibrium [9]. During this phase the plasma pressure is uniform, and the electron density profile is approximately parabolic with a minimum on the axis, where the plasma temperature is maximum. The plasma channel is shown to be fully ionised, which is important for applications of the waveguide in that pulse distortion and spectral blue-shifting due to laser-induced ionisation of the plasma will be avoided.

The results of the MHD simulation allowed to formulate a simple model to determine the plasma temperature and density during the third stage of the discharge, in which the distribution of plasma inside the capillary is determined by the balance between Ohmic heating and cooling due to electron heat conduction. Therefore there is a unique solution for the temperature profile within the capillary, and there are scaling laws for the dependence of the axial plasma temperature and electron density [9]. The key advantages of this simple model are that it provides analytical expressions, in terms of the parameters of the capillary discharge, for both the plasma distribution inside the capillary, and the matched spot size of the plasma channel that is formed. Conversely, using this local thermal equilibrium model means analysing the process with a quasi-static approach. It assumes the plasma pressure as constant and the channel as fully ionised; it does not allow to reproduce the process of the discharge and the plasma channel formation.

5.1.3 Matched spot size r_m

The matched spot size of a parabolic plasma channel governs guiding of the laser pulse and determines how the laser spot size varies inside the channel for low-power pulses. Even at higher power, where self-guiding starts to occur, r_m can be a major factor in controlling guiding distance and local intensity. Provided the laser is focused at the channel entrance (i.e., $r_s(z=0) = r_0$ and $r'_s(z=0) = 0$), where r_0 and $r_s(z)$ are the focal spot size and local spot size respectively, defined as the radial distance where the intensity reaches $1/e^2$ of the on-axis value, matched guiding occurs when $r_m = r_0$, and the laser pulse will be confined with a constant spot size $r_s(z) = r_0$ [123–125].

Bobrova et al., comparing the analytical model balancing Ohmic heating with electron heat conduction to the cold walls, and their one-dimensional dissipative MHD code described above, found good agreement in the stable regime after the

initial ionisation stages, and describe the matched spot size by [9]:

$$r_m[m] = 4.7 \times 10^3 \frac{(R_0[m])^{1/2}}{(Z_i n_{i0}[m^{-3}])^{1/4}}, \quad (5.4)$$

which depends most strongly on the capillary radius R_0 , and weakly on the ionisation degree Z_i and neutral gas number density before discharge n_{i0} . This model is in good agreement with Spence and Hooker's experimental result [6].

The equation (5.4) shows a dependence on the initial neutral hydrogen number density n_{i0} , but experimentally, it is more convenient to control and measure the capillary pressure p_{cap} . For the conversion, using the ideal gas law, it is possible to find

$$n_{i0}[m^{-3}] = \frac{p_{cap}[Pa]}{k_B T_0}, \quad (5.5)$$

with Boltzmann constant k_B , and assuming the neutral gas temperature T_0 to be equal to the ambient laboratory temperature of 295 K. It is possible to note that the relation (5.5) is independent of capillary end effects: due to the usual capillary design (see Fig. (5.2)) and vacuum conditions outside the structure, a linear drop in neutral hydrogen pressure is expected from each gas slot to the exit of the capillary, assuming gas-loading of the vacuum chamber is negligible. It is difficult to determine how this affects the temperature and density distributions near the capillary ends during the discharge, but an estimate is offered in [126, 127] and in the next chapter. Unless otherwise noted, we will assume expansion during the discharge results in a longitudinally constant plasma channel equal to the capillary length, effectively neglecting end effects.

Plasma channels with a parabolic shape have been therefore shown to form suitable waveguides for laser pulses with a Gaussian transverse profile [123, 124, 128]. Here we assume a laser pulse with a radial intensity profile defined by $I(r) = I_0(r_0/r_s)^2 \exp[-2r^2/r_s^2(z)]$, where I_0 is the peak on-axis intensity, and $I_0(r_0/r_s)^2$ is the on-axis intensity at any given location along the channel's longitudinal axis z . The parabolic plasma channel considered has the form

$$n_e(r) = n_0 + \frac{r^2}{\pi r_e r_m^4}, \quad (5.6)$$

where n_0 is the on-axis electron density of the plasma channel, $r_e = e^2/m_e c^2$ is the classical electron radius, e and m_e are the electron charge and mass, and c is the light speed.

While the matched spot size dominates guiding at low power, for high-power laser pulses self-guiding effects can result in optical guiding and have to be taken into account. In relativistic optical guiding, a refractive index change is induced by the relativistic mass change of electrons quivering in a laser field above a certain power threshold, and localised electron density changes due to the ponderomotive force [36, 129, 130]. Self-guiding is intensity-dependent, and changing laser power to control the wakefield changes the propagation of the laser, as well.

As a result, in this case a matched channel will no longer provide guiding with a constant spot size, as the laser self-focuses. Instead of considering only the density profile, other contributions to the index of refraction have to be taken into account.

In the linear regime, for the magnitude of the normalised vector potential a , $a^2 \ll 1$, the refractive index can be approximated by [11]

$$\eta(r) \simeq 1 - \frac{\omega_p^2}{2\omega^2} \left(1 - \frac{a^2}{2} + \frac{\Delta n_p}{n_0} + \frac{\delta_n}{n_0} \right), \quad (5.7)$$

where a generic radial density profile n with a minimum n_0 on axis is assumed. This can be described by $n = n_0 + \Delta n_p + \delta_n$, where $\Delta n_p = \Delta n r^2 / r_0^2$ defines the channel profile, and δ_n denotes a longitudinal plasma wave. In Eq. (5.7) it is shown that in this weakly relativistic case, in addition to the preformed density term Δn_p , relativistic optical guiding appears in the form of the $a^2/2$ term, and self-channeling, plasma wave guiding and self-modulation can occur as feedback from the wave excited in the plasma – the δ_n term [4, 101]. It should be noted that even when these effects occur, the density profile still plays a role, and may need to be tuned to compensate for increased self-guiding. Neglecting any self-focusing effect means to impose the condition that the power ratio $P/P_c \ll 1$, with the critical power for self-focusing approximated by

$$P_c[\text{GW}] \approx 17\lambda_p^2/\lambda^2, \quad (5.8)$$

where λ_p is the plasma wavelength and λ the laser wavelength. The plasma wavelength depends on the plasma frequency ω_p – the density-dependent oscillation frequency of plasma electrons – as $\lambda_p = 2\pi c/\omega_p$.

While matched guiding is a relatively simple concept, it can be hard to achieve under experimental conditions. It is therefore important to understand the implications of mismatched guiding, where either $r_m < r_0$ or $r_m > r_0$ [131].

5.1.4 Laser heating mechanism

As stated above, the energy gain of a single-stage of laser plasma acceleration [4] scales inversely with plasma density, n_0 , since the accelerating gradient scales as $E_0 z \propto n_0^{1/2}$, and the length is limited to the laser-depletion length, which scales as $L_d \propto n_0^{-3/2}$. However, due to the orders of magnitude of plasma densities used ($10^{17} - 10^{18} \text{ cm}^{-3}$) and for the capillary diameter required to avoid laser damage (several hundreds of μm), the capillary discharge waveguide produces a channel that is not deep enough to sufficiently confine the laser pulse. The confinement of the small focus (few tens of μm) requires a small matched spot size, which is obtained by using a relatively high gas pressure in the target. The resulting on-axis electron density is in the order of 10^{18} cm^{-3} , which caps the wake velocity such that the electrons overtake the wake after several centimetres. This dephasing causes deceleration of the electrons and is detrimental to accelerator performance. The channel depth of a capillary discharge waveguide can be increased using laser pulses of nanosecond length and of lower intensity (few hundreds of $m\text{J}$) than the wake-driving pulse, to locally heat the plasma along the capillary axis [132]. This method can extend the laser acceleration length to several diffraction lengths at the usual low density (in the order of 10^{17} cm^{-3}), because this heating causes a localised, on-axis depression of the plasma density profile, used to access a new regime of low-density, high-confinement waveguide for laser plasma acceleration pulses [15].

The laser heating mechanism [133, 134], using a *ns*-duration matched pulse inside a capillary discharge waveguide, works as follows: a *heater* laser pulse is guided by the discharge plasma and heats the plasma locally near the axis via inverse bremsstrahlung (IB) at rates on the order of 1 eV/ns . This creates a density depression through hydrodynamic motion, in addition to that created by the existing discharge-based channel. If a longer heater pulse is used (*ns*), it undergoes self-guiding, so it needs not be constrained by the low-power matching condition. Self-guiding occurs because the tail of the heater pulse encounters a plasma that is already modified by IB heating and hydrodynamic motion: i.e. the tail encounters a reduced on-axis density and lower matched spot size [15]. The matched spot size can also be improved by optimising the delay between the current pulse and the heater pulse. Since Ohmic heating is approximately proportional to the square of the current, the plasma temperature decreases at the bottom of the discharge current pulse slope. Consequently, adjusting the discharge current pulse timing, thus reducing the initial electronic temperature, is an efficient method to increase the heating rate and reduce the size of the matched spot size. The energy gain increase of an electron beam is therefore achieved by operating at low densities and with a reduced matched spot size. These conditions allow for effective guiding and acceleration over longer dephasing and pump depletion lengths.

5.2 Theoretical introduction to the Stark broadening plasma measurements

The key parameter in the laser pulse guiding process is the electron plasma density. Knowing of this property along the interaction length when the laser beams pass through the plasma is really useful to improve the matching conditions between beam and plasma and therefore to optimise the process itself. In the same way, in plasma accelerators, laser or electron beam based, knowing the properties of the plasma densities inside the device used is necessary for the optimisation of the beam quality after the acceleration. Online and non perturbing methods suitable for small ($\leq 1 \text{ mm}$ thick or less) and low dense plasma (lower than 10^{20} cm^{-3}) are mandatory. Spectroscopic techniques fit very well these requirements. Plasma density can be revealed by the analysis of the broadening of self emitted lines caused by the Stark effect [135–137].

Ionised plasma emits electro-magnetic radiation whose spectrum can be either continuous or discrete depending on the radiative mechanism. The radiation is emitted in processes involving transition of the electrons between different bound states (bound-bound transition), recombination or ionisation of an electron with an atom or molecule (free-bound transition) or interactions between charged particles, both ions and electrons, which remain unbounded at the end of the interaction (free-free transition). In general, the properties of the emitted radiation depend on the plasma characteristics, whose analysis allow to reconstruct the plasma conditions in the vicinity of the emitters [136].

As already noted in Section 5.1, for plasma based applications, hydrogen plasma filled capillaries are commonly used and, since hydrogen plasma produces strong lines in the visible range, the spectral analysis allows to reconstruct the electron

density of the surrounding plasma due to the Stark effect.

Hydrogen atoms emit light at different wavelengths usually referred as hydrogen spectral lines. The wavelengths of the emitted photons depend on both initial and final energy levels of an electron that decays from an excited state to another. Spectral lines are grouped in different series according to the lower level at which the electron falls. The Balmer series describes the emission of photons due to the transitions of electrons from the higher energy level to the second one. The first spectral lines of this series lie in the visible range: these lines are the so called alpha, beta and gamma lines, which have wavelengths of 656.3 nm, 486.1 nm and 434.1 nm, and are characterised by the electron transitioning from $n = 3$, $n = 4$ and $n = 5$, respectively, to $n = 2$. Each of these spectral lines undergo several line broadening mechanisms that are extremely useful for diagnostics [138].

One of the main source of broadening comes from the thermal motion of the emitters, which causes the *Doppler broadening*. It is also commonly called thermal broadening, since it is generated by thermal motion, which leads the emitters to move randomly with velocity v . If the velocity distribution of the emitter particles is Maxwellian, the line profile as a function of wavelength $I_D(\lambda)$ is a Gaussian and can be expressed by

$$I_D(\lambda) = I_D(\lambda_0) \frac{1}{\sigma\sqrt{2\pi}} e^{-\frac{(\lambda-\lambda_0)^2}{2\sigma^2}}, \quad (5.9)$$

where λ_0 is the central wavelength. The standard deviation of this distribution

$$\sigma = \sqrt{\frac{k_B T_i}{m_i c^2}} \quad (5.10)$$

is a function of the emitting ion temperature T_i and the ion mass m_i , while k_B is the Boltzmann constant and c the speed of light. To measure the spectral widening due to the Doppler effect, it is thus sufficient to correlate the width of the emission line with the standard deviation of the distribution in formula 5.9.

Another fundamental source of broadening is the pressure broadening, also named *Stark broadening*. The Stark broadening is caused by the presence of an electric field acting on the emitter. The electric field can be produced by nearby free electrons or can be generated externally. In the case of this project, no external field reaches the recombinant plasma atoms, but it is possible to relate the line widening with the interaction of the emitter with the nearby charges. This allows to reconstruct the electron density of the plasma near the emitters by measuring the FWHM of the emitted line. The Stark effect acts linearly for hydrogen, and the shape of the line profile $I_S(\lambda)$ when subjected only to this broadening effect is a Lorentzian distribution

$$I_S(\lambda) = I_S(\lambda_0) \frac{\Delta\lambda_{FWHM}^2}{4(\lambda - \lambda_0)^2 - \Delta\lambda_{FWHM}^2}, \quad (5.11)$$

where $\Delta\lambda_{FWHM}$ is the full width at half maximum of the profile.

An additional source of broadening is the so-called instrumental broadening. It is caused by the resolution of the acquisition device and it must be taken into account to retrieve the ultimate line profile. More in detail, the instrument line broadening is associated with the measurement setup, which comes, for example, from the spectrometer resolution, the spot size of the incident light on the grating,

and the detector calibration state [7]. Since it influences the measurement resolution, it must be measured experimentally and subtracted from the measurements.

Other effects that can influence the line shapes are usually negligible for plasma temperature of $1 - 4 \text{ eV}$ and densities between $10^{15} - 10^{19} \text{ cm}^{-3}$.

The Balmer alpha line is the most intense of the Balmer series, but it is also the one in which the contribution of the Doppler effect is more consistent. This effect is instead almost completely negligible for the Balmer beta, on which on the other hand the Stark effect causes a greater enlargement. However, the intensity of the Balmer beta line is lower than that of the Balmer alpha line, and this makes it more difficult to detect. The self-absorption of the emitted Balmer alpha must be taken into account especially for higher densities. Its effect is quite severe for pure composition plasma [139] like the one commonly used for plasma-based acceleration. Self-absorption of the central line makes the Balmer alpha broadened, then the fit of the line is affected by this variation and the measured density is often overestimated. In case of multiple broadening effects the resulting line profile is the convolution of the constituent profiles [138]. In general, the convolution between a Lorentzian and a Gaussian curve is the so-called *Voigt function* which well describes the contribution of both the Doppler and Stark effects on the Balmer lines. To take this contribution into account, it is usually considered that the measurements with the Balmer line alpha are overestimated by a factor of 2 compared to the real value [7, 8].

Results obtained with the Stark broadening analysis and with the interferometric technique have been compared [140]: in the interesting density range, it has been shown that the analysis of the alpha and beta Balmer lines gives higher density values compared with the values measured with the interferometry, but the Balmer beta results, reasonably due to the lower self-absorption, are closer to the interferometric values within few tens of percentage points, confirming the validity of this method [136]. Using the Balmer alpha line is advantageous for density measurements of mixtures of hydrogen with other gases (e.g. argon), where the Balmer beta line is almost absent [141].

5.2.1 Balmer lines characterisation

Via this spectroscopic method, the density inside the capillary can be acquired in a single shot, independently on the capillary shape, along the entire plasma beam interaction length, with a temporal resolution of few tens of nanoseconds and spatial resolution given by the imaging system used to collect the self emitted light during the plasma formation process.

In a typical setup, the light self-emitted by the hydrogen is collected and sent to the spectrometer by an imaging system which produces a demagnified image of the capillary onto the spectrometer slit. A correct demagnification allows to image the whole longitudinal capillary dimension onto the grating, where it is spectrally dispersed [142]. A gated ICCD is used to collect the emitted light. The gating of the camera allows to cut off the continuous emission of the early stages of the discharge and to collect light inside a window of few tens of nanoseconds (depending on the intensity of the collected light). By varying the delay between the camera and the discharge trigger it has been possible to scan the temporal evolution of the plasma. Each line of the spectrum, corresponding to a precise spatial position of the

capillary, is then analyzed by fitting it with a Lorentzian curve. The sensitivity of the collected data to temperature is very weak even for the Balmer alpha line, and the temperature measured with this method is unreliable.

It is possible to obtain the electron density from the width of the Stark-broadened spectral line, by means of the equation

$$n_e = 8.2 \times 10^{12} \left(\frac{\Delta\lambda_{1/2}}{\alpha_{1/2}} \right)^{3/2} \text{ cm}^{-3}, \quad (5.12)$$

used to analyse this type of measurements [8]. Here, $\Delta\lambda_{1/2}$ is the FWHM of the Stark-broadened spectral line in angstroms, and $\alpha_{1/2}$ values in angstrom units have been tabulated by Griem [7, 135].

5.3 Low-power laser guiding tests

To guide a high-power laser pulse through a plasma guide such as a capillary discharge, it is necessary to gain specific experience with the guiding process itself: managing the density profile within the channel, the method of beam injection and alignment, establishing and efficiently using diagnostics to verify the efficiency of the guide. For this reason, it was decided to begin the study of the guiding process and all related experimental features using a low-power laser beam. Therefore, in order to carry out guiding tests of a low-power laser pulse, a dedicated station has been built in the bunker of the Flame laser laboratory. The area chosen is the one adjacent to the Clean Room, in order to intercept the probe pulse of the main high-power laser (see Section 3.2). To do that, a 10/90 (R:T) beam-splitter has been positioned in place of the mirror on the line that carries the probe to the interaction chamber level. The beam that arrives at the new guiding test station is therefore a beam in the infrared range, temporally as short as the main one, about 1 *in* in size. In Fig. 5.3 the experimental setup is shown.

Table 5.1. Probe laser parameters.

Energy	10 <i>mJ</i>
Temporal length	50 <i>fs</i>
FW $1/e^2$ @ focus	120 μm

The laser pulse has its features summarised in Tab. 5.1: the energy is measured daily with an energy meter, the time length is measured with an *APE LX Spider*, following beam alignment operations in the Clean Room. The experimental station dedicated to guiding is composed of an optical table of dimensions (180 × 90) *cm*, on which a vacuum chamber of dimensions (60 × 80) *cm* is placed. The pumping system is composed of three Edwards XDS scroll pumps and three *Pfeiffer Vacuum* turbo pumps, able to guarantee an average vacuum level of 1×10^{-6} *mbar*.

5.3.1 Set-up and discharge circuit

The target chosen for the guiding is a capillary. This is designed and 3D printed, by means of *Object30 Stratasys*, thanks to the LNF technical support. This allows the

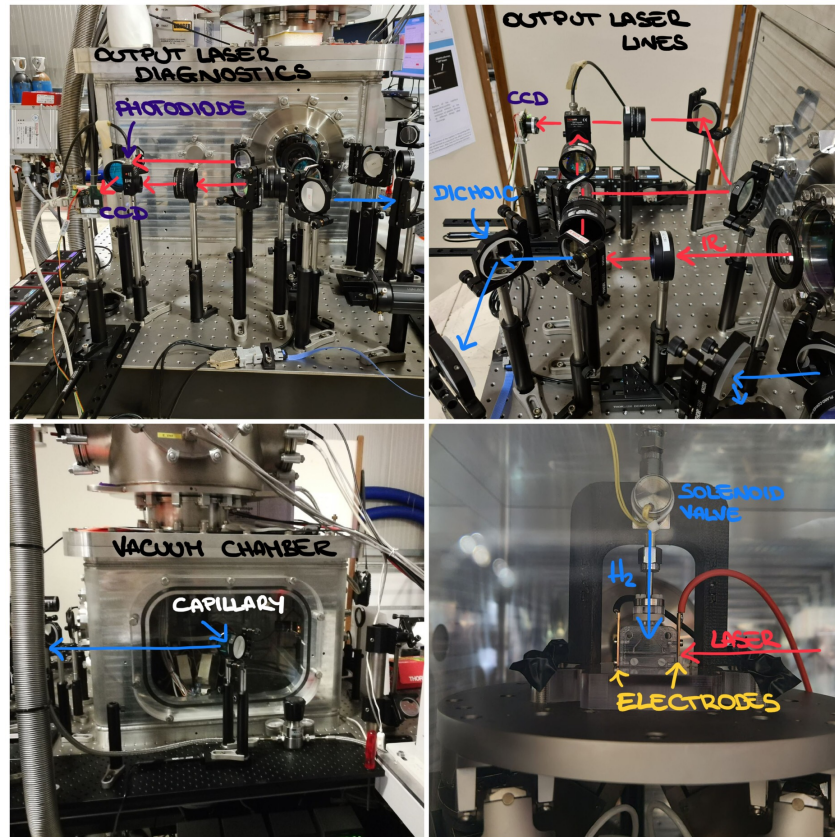


Figure 5.3. Inside and outside images of the vacuum chamber in the guiding station: The red path represents the laser pulse line, while the blue one represents the plasma recombination light, described in the next Sections.

testing of several designed and subsequently optimised prototypes. The material chosen for printing is VeroClear-RGD810 (Stratasys), a commercial acrylate polymer transparent to visible light. An example is in Fig. 5.4. Through an injection system consisting of a main inlet and one or more secondary inlets, the gas is brought into the capillary channel. The gas chosen is hydrogen, H_2 . It has a 1:1 ratio between electrons and protons, facilitating the formation of a uniform plasma. The hydrogen's ionisation energy is 13.6 eV and it is generated by a hydrogen generator (*CINEL Gas Generators Technology*) that works by electrolysis of water, and is able to provide an output hydrogen pressure of 3 bar .

Over the main capillary inlet there is a *Parker solenoid valve*, also shown in Fig. 5.3, to temporise the injection. Associated to this gas injection system there is a discharge circuit, able to ionise the gas and generate a hydrogen plasma. It is a high voltage generator able to provide a difference at the terminals of the capillary, a few centimetres long, higher than the discharge voltage of the gas used (of the order of tens of kV), according to Paschen's curve [143]. Since it is important that the discharge field within the capillary is homogeneous, metallic electrodes of planar geometry are used to apply high voltage to the ends of the channel.

The pressure of hydrogen entering the chamber is regulated and stabilised by a

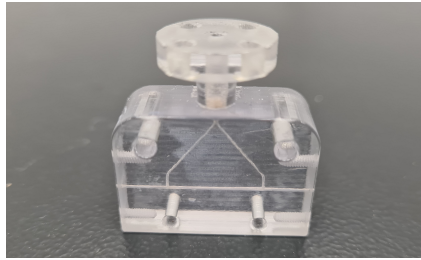


Figure 5.4. 3D printed capillary with length 3 cm, diameter 500 μm and double-inlet injection.

pressure regulator, while the opening times of the solenoid valve and the discharge start time are managed by a special *DG535 Delay Generator* (*Stanford*). They vary according to the size of the capillary used, and they are always triggered on the laser pulse. This allows to set the arrival time of the pulse, tens of *fs*, in a defined area of the discharge curve, which has a total duration of 1 – 2 *ms* [144]. An example of probe-discharge synchronisation is shown in Fig. 5.5: the discharge curve is the one at the exit of the system, i.e. the one generated by the equivalent capillary-circuit.

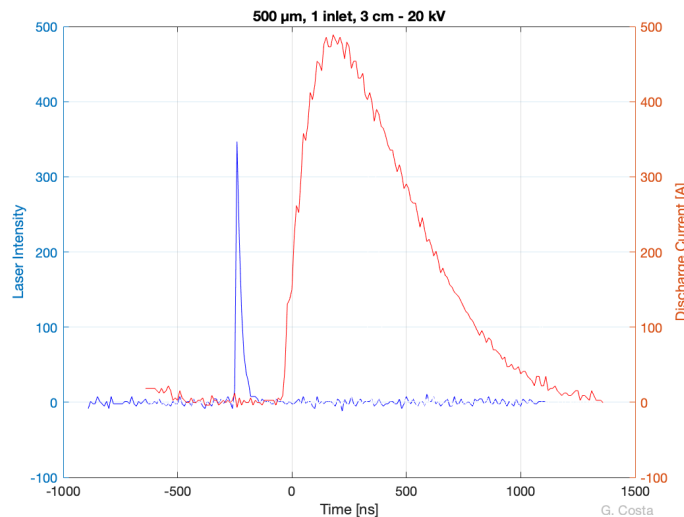


Figure 5.5. Laser pulse signal (blue) and current curve signal coming from the discharge circuit output channel (red), for a capillary of 3 cm long and 500 μm .

The experimental setup is shown in Fig. 5.6. The laser coming from the clean room is transported to the entrance of the guiding chamber: a diagnostic camera, *CCD REF*, is positioned on this line, to monitor the alignment and pulse pointing in the experimental station. A lens with focal length $f_{in} = 30$ cm focuses the pulse at the capillary entrance face. The capillary is positioned on a multi-axis hexapod, *Pi 6 axis Positioning System*: a 6-Axis positioner, thus with six degrees of freedom, which has travel ranges up to 45 mm (linear) and 25° (rotation), with 7 nm of resolution and 0.5 μm of repeatability. It allows the alignment of the channel on the laser line. Since this is a delicate phase, a precise procedure has been developed: it

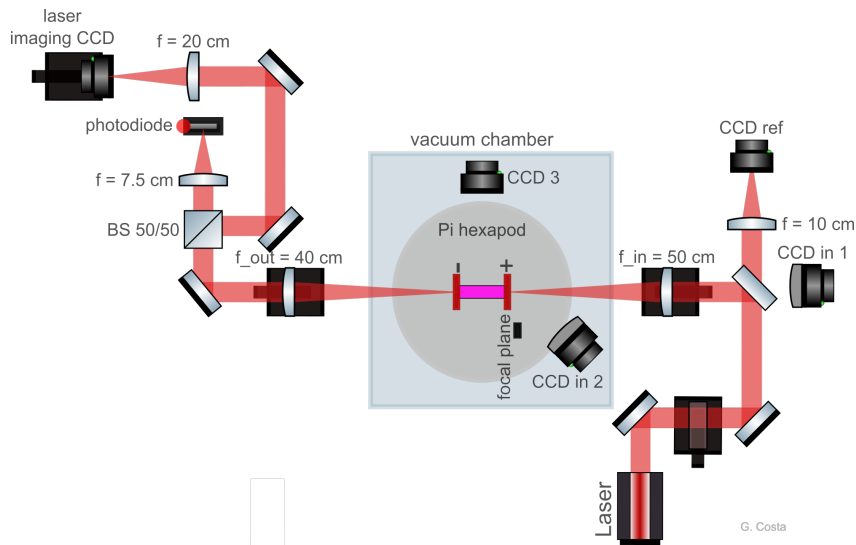


Figure 5.6. Laser line setup, including interaction zone and output beam diagnostics.

foresees the use of motorised filters on the laser line before focusing, and the use of two cameras *CCD in 1* and *CCD in 2*, both of which watch the channel input with two different angles. They are used to watch the position of the laser pulse on the capillary entrance electrode, moving the hexapod motors.

Another camera, *CCD 3*, inside the chamber watches the channel longitudinally, capturing the discharge. An example is in Fig. 5.7. In this image there is clearly a plume of plasma on only one side of the capillary, but this is an illusion created by the way the diagnostics is timed; in actuality from inside the sides there are plumes of comparable intensity. An in-depth examination of the subject will be given in Section 6.5.

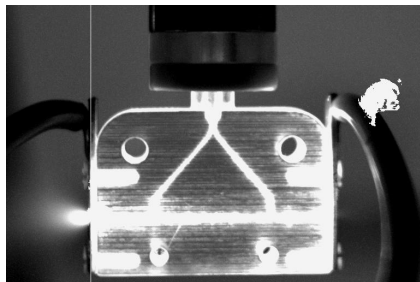


Figure 5.7. Discharge detected by *CCD 3*, triggered with respect to the trigger of the high voltage circuit.

The laser coming out of the capillary leaves the chamber and it is picked up by a telescope with focal length $f_{out} = 40\text{ cm}$. The pulse is then split into two arms with a 50/50 beam-splitter. The one in transmission is focused ($f = 7.5\text{ cm}$) on a photodiode, with which the arrival time of the laser is reprocessed. The reflective arm, on the other hand, is the one imaging the laser spot coming out of the capillary: the system is composed of the first lens f_{out} and a second one with focal length $f = 15\text{ cm}$, followed by a CCD with nominal resolution $2.2\text{ }\mu\text{m}/\text{px}$. The same

imaging system with the same CCD is also used to make the focus measurements of the pulse entering the capillary: this is possible by simply moving the f_{out} lens position of the capillary length towards the camera by means of a motorised slide.

5.3.2 Test with 270 A discharge maximum current

The laser pulse guiding tests in the experimental station described were carried out mainly in two experimental campaigns. The first one started with two capillaries printed in transparent 3D plastic, to allow the plasma diagnostics of the channel. The length of the capillaries was in both cases 3 cm, while the diameter of the channel was 1 mm and 0.5 mm. They were designed with a double inlet hydrogen injection system, positioned at 1/4 and 3/4 of the capillary length, in order to allow as much as possible a homogeneous filling of the canal. The discharge circuit used has its characteristics reported in Tab. 5.2. A photo taken during production is shown in Fig. 5.8.

Table 5.2. Discharge circuit output parameters.

Voltage range	6 – 18 kV
Max Current	270 A

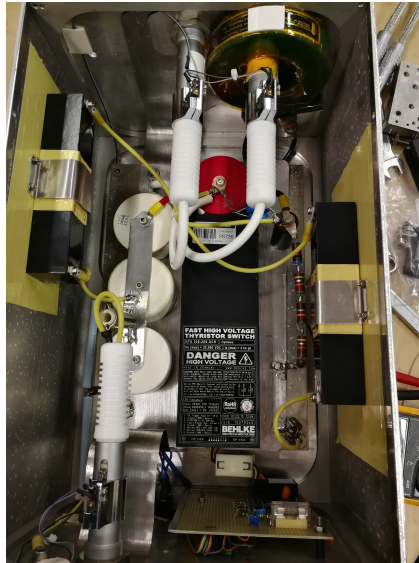


Figure 5.8. Photos of the inside of the discharge circuit, including the fast high voltage switch.

This section outlines the results obtained in this first phase, then used for the second experimental campaign optimisation.

As already discussed, the duration of the discharge covers a time compatible with at least 1 μs , in which the sudden rise of the current value happens, followed by a peak zone of maximum current, and a slow decrease (see Fig. 5.5), with tails that reach about 2 μs . The duration of a laser pulse that is usually used for this type of process is in the order of tens of fs. The density characteristics necessary to

drive a laser pulse matched to that density (see Section 5.1, Eq. 5.3 and Eq. 5.4) are therefore produced within a time window of the duration of the entire discharge. The position of this window depends on the shape of the current curve, determined by the construction of the discharge circuit and the geometry of the target.

In order to find this guiding time window experimentally, the first tests were carried out with a high repetition rate laser, i.e. the beam coming from the Flame oscillator (see Section 3.1). This is a low-power beam, about 200 mW , which has about 80 MHz . This means that the interesting part of the discharge, of about $1.5\text{ }\mu\text{s}$, overlaps with about 120 pulses, so that there is a laser pulse every 12.5 ns circa.

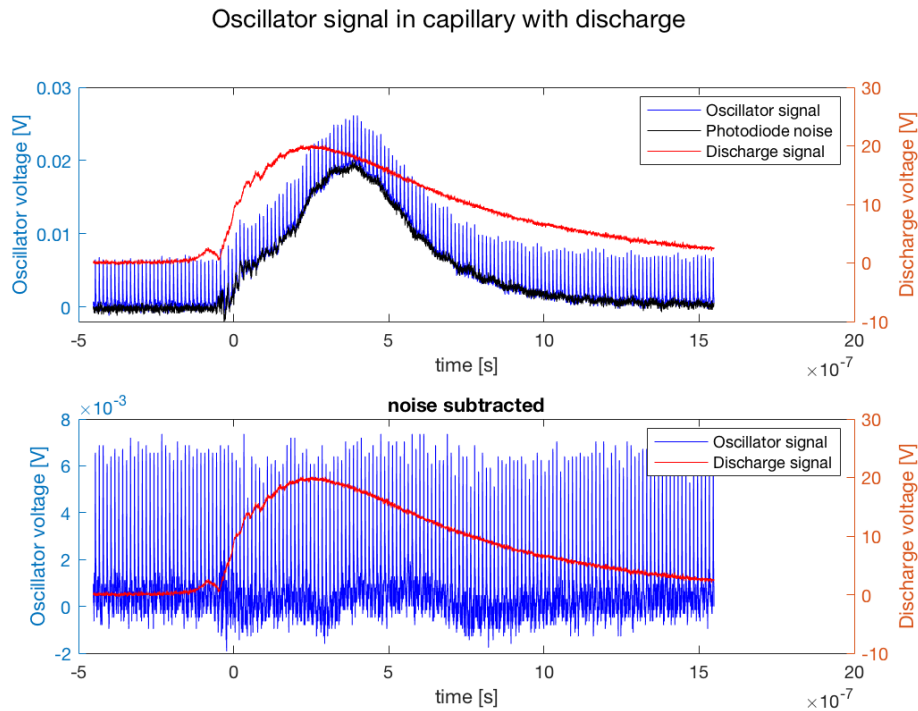


Figure 5.9. Output signals from the discharge circuit (red) and from the photodiode on the laser line (blue), in presence and absence of the pulse (up). Photodiode signal in the presence of the laser, subtracted from the noise coming from the discharge (down). Capillary diameter 1 mm .

An example of this type of test is shown in Fig. 5.9: the capillary that was tested first had a diameter of 1 mm . This diameter was chosen because it was already designed for other SPARC_LAB experiments, and was therefore easily and immediately available. The signals shown in Fig. 5.9 are: in red the signal coming from the output of the discharge circuit, while in blue the one coming from the photodiode positioned at the exit of the chamber, already shown in Fig. 5.6. In Fig. 5.9 (up) it is evident that the laser signal is dominated by electronic noise of the discharge: the signal-noise ratio is limited by the low power of the laser beam. For this reason, the contribution due only to the presence of the discharge, measured without the presence of the laser, has been subtracted (see Fig. 5.9 (down)). Fig.

5.10 instead highlights more closely the behaviour of the beam inside the discharge curve: the latter clearly has an impact on the pulses present in the central part of the curve, but they do not present a defined or repeatable trend. All the graphs of this type presented have an intensity that cannot be compared to each other in absolute value, as the presence of filters used to attenuate the input signal may vary.

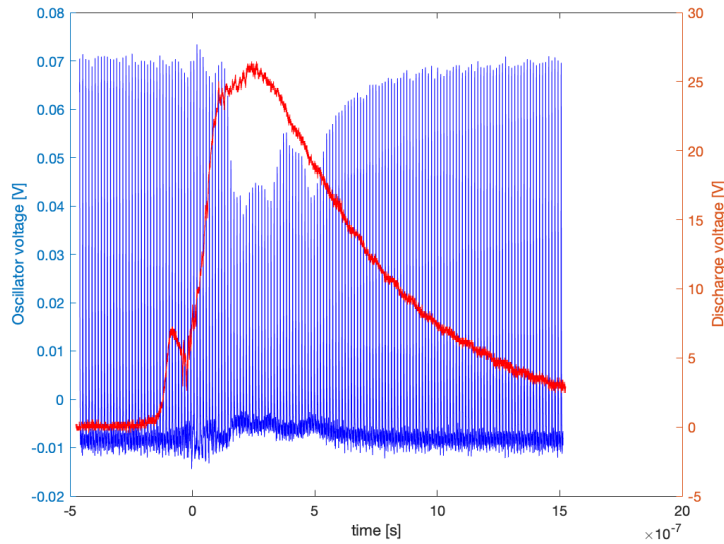


Figure 5.10. Time zoom: photodiode signal in the presence of the laser, subtracted noise from the discharge, superimposed on the respective discharge curve. Capillary diameter 1 *mm*.

Using the capillary with 0.5 *mm* diameter and the same identical pressure, discharge and laser conditions, the result changes completely. A clear and significant result of guiding effect is shown in Fig. 5.11. Here there is a time window of the discharge curve in which the intensity of the laser pulses increases substantially. Due to the presence of the capillary, without hydrogen or plasma, the measured intensity of the laser that propagates through the channel was about 50% of the initial one, i.e. the one that was measured at the input, as well as at the output by removing the capillary through the transverse Hexapod motor. This is related to the fact that in this way the beam after the focus is left free to propagate inside the capillary, and therefore the pulse diverges after a Rayleigh length (in this case in the order of about 10 *mm*). In this configuration then part of the beam energy is dispersed on the walls and this effect results in a lower intensity of the laser output signal.

The intensity that the laser pulses have in Fig. 5.11 in the initial part of the discharge is that which they have even without the presence of plasma. It is therefore possible to conclude that in a time window immediately following the peak of the discharge there is an increase in the intensity of the pulses transported by the channel, which are then guided by the plasma generated. The guiding window defined in the figure is the one for which the impulse increases by about 30% compared to the initial one, and is about 300 *ns*. The same figure also shows the behaviour that the pulses have after the guiding window and along the tail of descent of the discharge: the

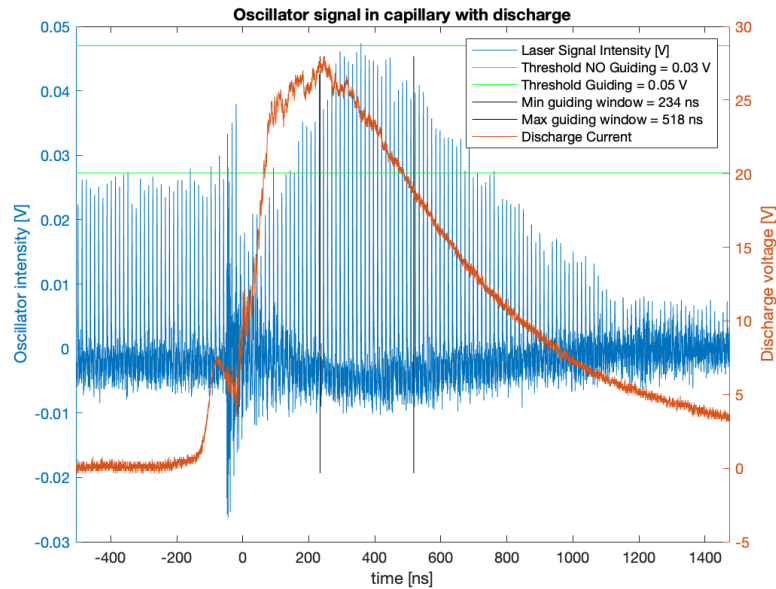


Figure 5.11. Photodiode signal on the laser line, superimposed on the relative discharge curve: the two green horizontal lines represent the threshold of the initial laser intensity and the maximum increase obtained, while the two black vertical lines delimit the chosen guiding time window, like the one in which there is a laser signal increase of 30%. Capillary diameter 0.5 mm

intensity decreases drastically, and then returns to the initial value after about $2 \mu\text{s}$. The peak in intensity that the pulses have instead at the beginning of the rise of the discharge is coinciding with a relative maximum that the discharge curve has in this area. It is formed for low voltage values, because the first electrons start to move and a preionisation of the gas is generated. This contribution can be seen as a sort of discharge ignition, and when the voltage increases and the breakdown mechanism is released, the two contributions merge. Since the avalanche is a high-frequency contribution, capacitors have been inserted in the circuit designed and built for the second experimental campaign in order to attenuate this contribution.

To avoid erroneous contributions depending on possible input laser variations, jitter or energy fluctuations, the laser output signal has been compared to the signal of another diagnostic photodiode. This was placed on a dielectric mirror leakage, before the laser entered the guiding chamber.

Having in this way tested the operation of setup and diagnostics, and once a window where the 80 MHz pulse guiding effect occurs was noticed, the latter has been replaced with the Flame laser probe pulse, with the characteristics described in Section 3.1. The two collimated beams have the same transverse dimensions before focusing, since the oscillator beam has been specially magnified with a telescope in the Clean Room before use. This allowed to use the same transport optics and the same focusing, imaging and diagnostic elements.

For this type of circuit and capillary, the schematic of the timings is shown in Fig. 5.12: two DG535 Delay Generators have been used, with the first triggering the

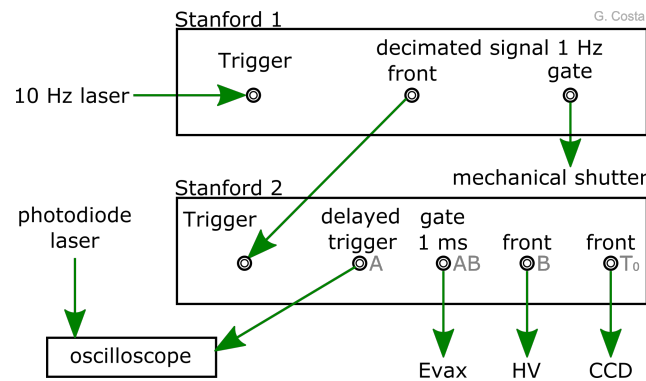


Figure 5.12. Schematic of the trigger system used to time the experiment with a single pulse. It involves the use of two DG535 Delay Generator and includes a monitor to display the time overlap of the signals created.

second. The initial input at 10 Hz , coming from a Clean Room pump laser (*CFR ULTRA*, see Section 3.1), is decimated to 1 Hz and a suitable gate is sent to the mechanical shutter on the laser beam line (beginning of MP2). The same trigger reaches the second Stanford as front and it is delayed to be sent to the solenoid valve (gate of 1 ms) and thus to the discharge circuit. Thanks to this possibility of delaying the triggers concerning the plasma generation, with respect to the trigger that controls the mechanical shutter of the laser, it is possible to set and display the arrival time of the laser pulse within the discharge curve. In the following text the expression *synchronise the laser beam with respect to the discharge curve* will sometimes be used for language convenience, even if the real meaning is that it is the laser in the discharge time windows that allows for the best guiding.

In Fig. 5.13 a collection of online screenshots from the oscilloscope is reported. The discharge is shown in yellow, and in light blue the probe pulse, timed respectively

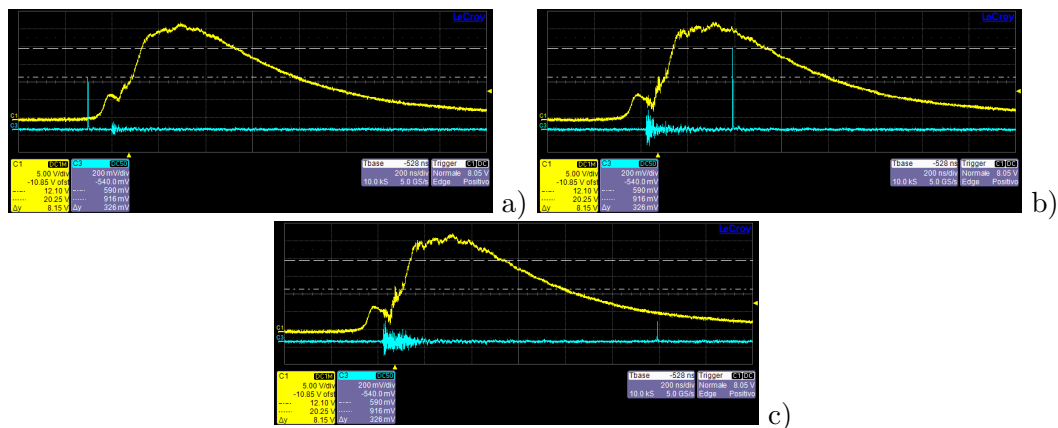


Figure 5.13. Oscilloscope screenshots with laser pulse and discharge signals: a) Laser synchronised before the start of the discharge; b) Laser synchronised in the guiding window; c) Laser synchronised in the tail of the discharge curve.

before (a), inside (b), and after (c) the found guiding window. The different effects shown are congruent with the results previously obtained with the high frequency

pulse. With this point of work some acquisitions for statistics have been made, of which an example is shown in Fig. 5.14: at intervals of 100 ns several pulse curves have been acquired. For visualisation convenience, these have been reported in the figure together with an example discharge curve.

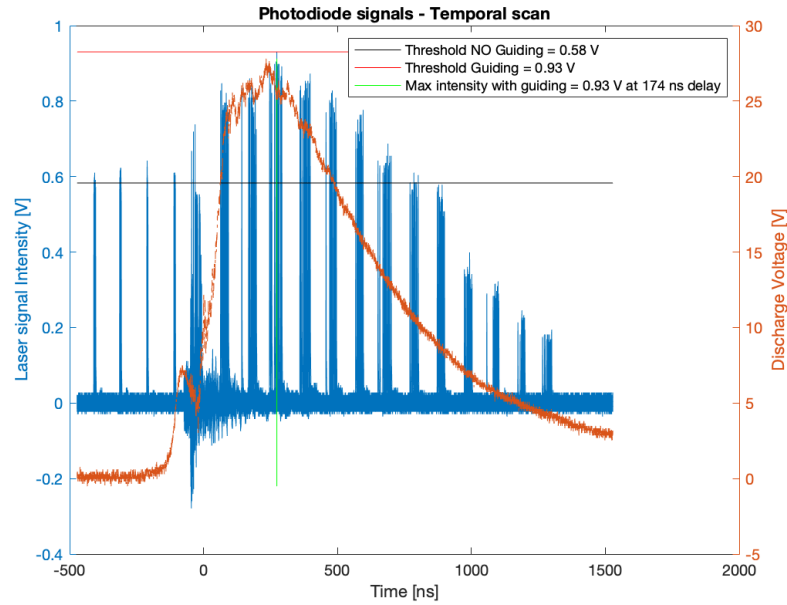


Figure 5.14. Scan of laser pulses superimposed on a discharge curve: the delays are set at 100 ns each and a statistical acquisition has been made for each one.

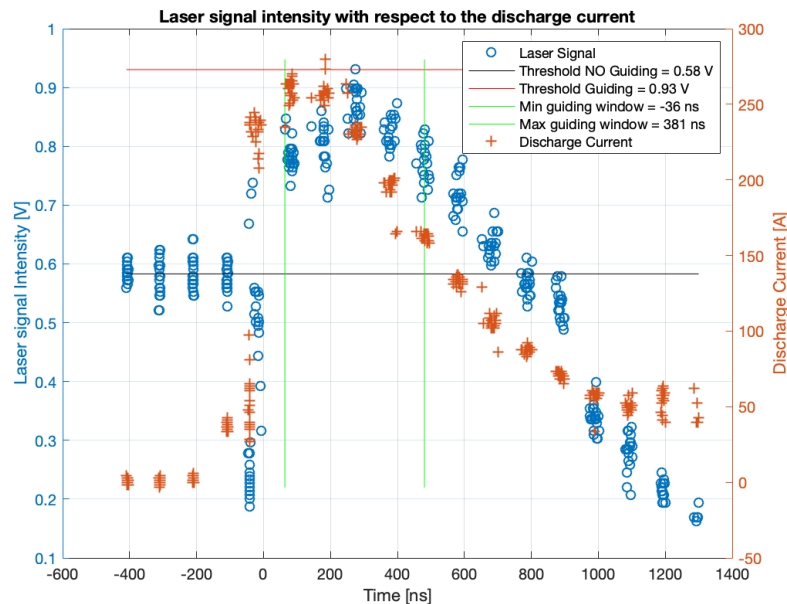


Figure 5.15. Scan of laser pulses superimposed on a discharge curve: the delays are set at 100 ns each and a statistical acquisition has been made for each one. Only the maximum signal pulses for each delay are shown.

In Fig. 5.14 the waveforms of the laser pulse were only superimposed on each other for all the selected delays, while in Fig. 5.15 only the maximum values of the beams, i.e. their peak intensity, are shown, and the same is true for the discharge data. Fig. 5.16 shows an average with statistical error of intensity and synchronisation for each delay considered, this time as well superimposed to a model discharge curve, while Fig. 5.17 shows a fine scan of the laser pulse in the guiding window.

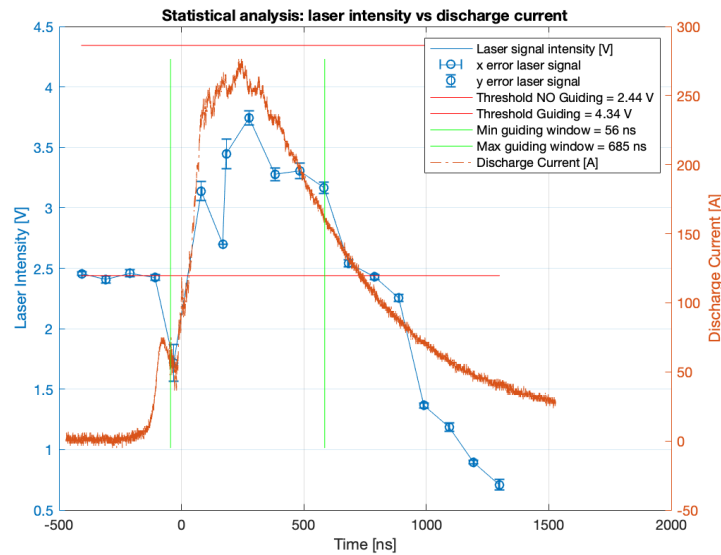


Figure 5.16. Average variation of the laser pulse intensity with respect to the time position between the arrival of the laser and the discharge curve area. Here the laser intensity values were corrected for the filters used to attenuate the signal.

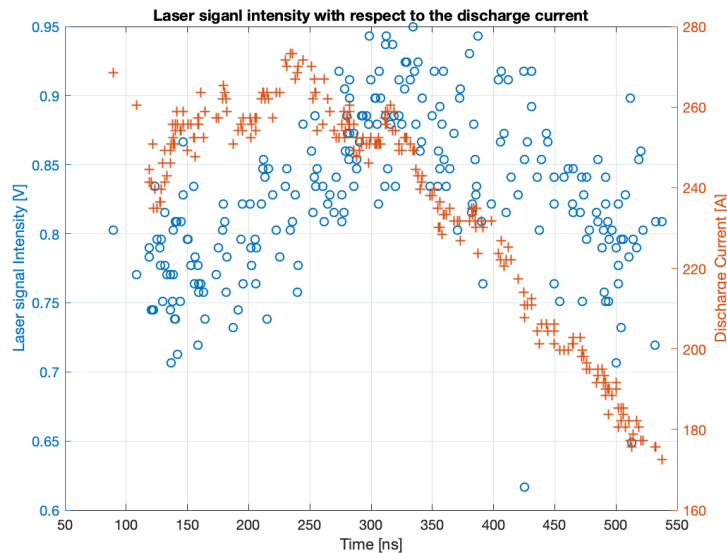


Figure 5.17. Scan the variation in intensity of the laser pulse with respect to the position in the discharge curve, detail of the guiding window. Only the maximum signal pulses for each delay are shown.

These latter plots with statistical analysis show not only variations in laser intensity for the same delay, but also a laser-discharge jitter of a few ns within the acquisitions of the single delay. The cause of this jitter has been identified in the need to set a very high delay on the second delay generator, between the trigger that goes to the mechanical shutter of the laser and the discharge. This setting is, given the current configuration in clean room, inevitable and due to the significant distance between the shutter inside the second multipass of the laser chain and the table for the guiding experiment outside the clean room. The necessary delay in question, being about $70\ ms$, does not allow the delay generator used to guarantee an accuracy higher than that obtained. Therefore the highlighted jitter is compatible with the specifications of the system. Even if not evident from the images shown so far, moreover, a long drift is added to this jitter. An example of drift combined with jitter is visible in Fig. 5.18: two screenshots of the oscilloscope used in *persistence mode* are reported, respectively after about half an hour (a) and three hours (b) of acquisition. Some data sets analysed to understand this problem are reported in Fig. 5.19, from which we can conclude that the overall variation is less than $40\ ns$ in the time range considered, while there are no significant differences in the pulse energy (shown in arbitrary units).

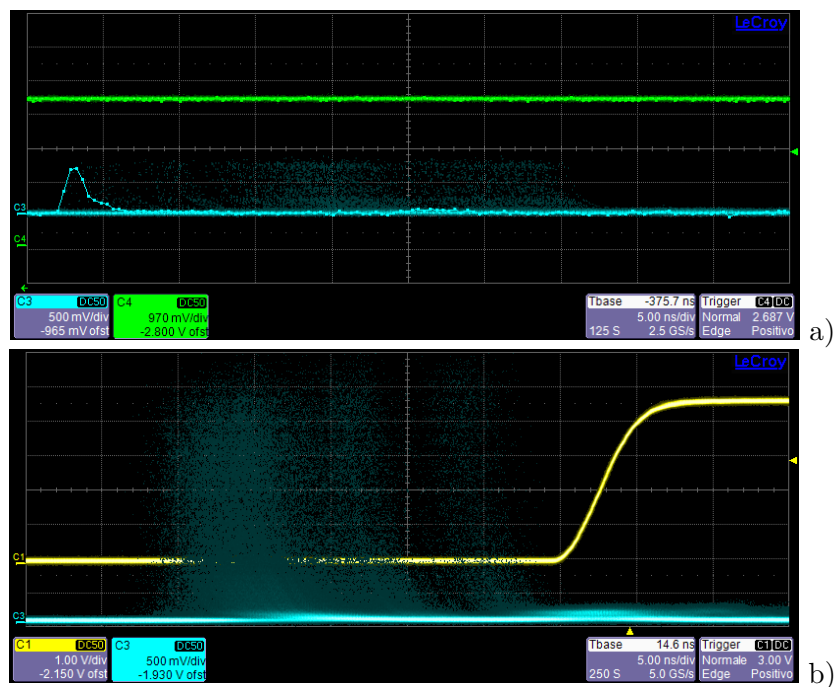


Figure 5.18. Oscilloscope screenshots with persistence setting: laser pulse (blue) over time: a) approx. 30 minutes and b) approx. 3 hours respectively. The other waveforms represent the signals on which the laser pulse is triggered.

If it is possible to consider the present jitter of some ns a systematic error that cannot be eliminated, in the same way it is possible to neglect the contribution of the long drift on the acquisitions of experiment for the guiding. This is because all the measurements are acquired in a time span much shorter than the long drift time.

In this first experimental phase with the use of the probe beam, with about ten

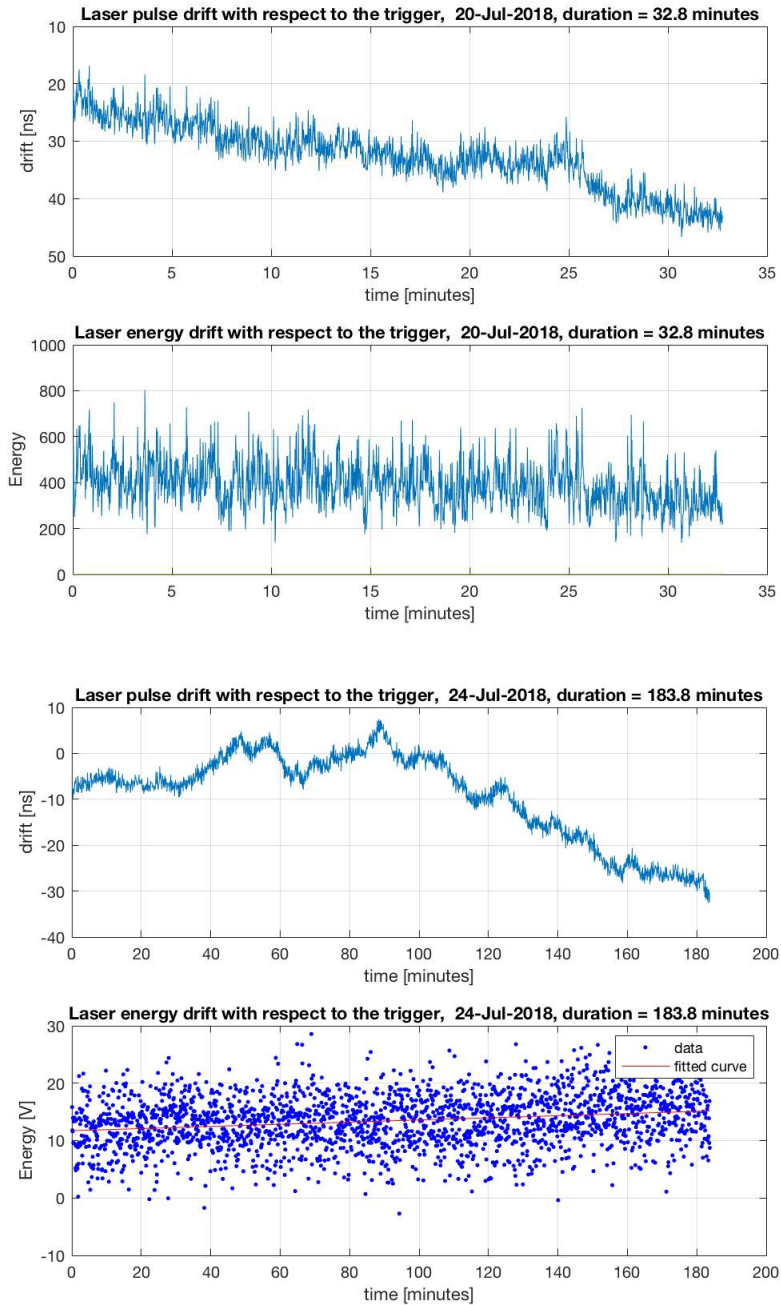


Figure 5.19. Analysis of drift and jitter data of the laser pulse: variation of the arrival time of the pulse and variation of its energy after a) about 30 minutes and b) about 3 hours.

mJ of energy, the setup related to the imaging diagnostics of the output laser pulse was installed, as shown in Fig. 5.6.

Fig. 5.20 shows two images of the laser pulse: (a) laser spot at focus, measured about $30 \mu m$ of radius at $1/e^2$ of the peak, (b) imaging of the capillary output plane in the condition of capillary removed from the laser line. In the latter case, as is natural, the beam has a larger size, due to the divergence accumulated in the $3 cm$ of capillary length (less than the Rayleigh length, which in this case is less than $4 mm$). Fig. 5.21 then shows the laser in the capillary output plane in the three representative delays of the three different phases already highlighted with the signal data.

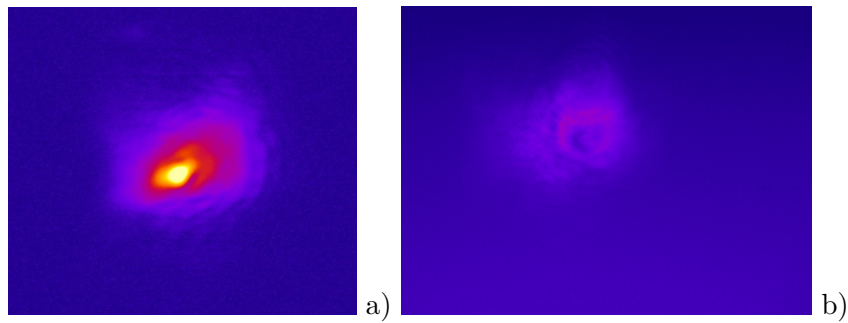


Figure 5.20. Images of the laser pulse used: a) spot in focus, b) image on the capillary output plane but without the capillary on the laser line.

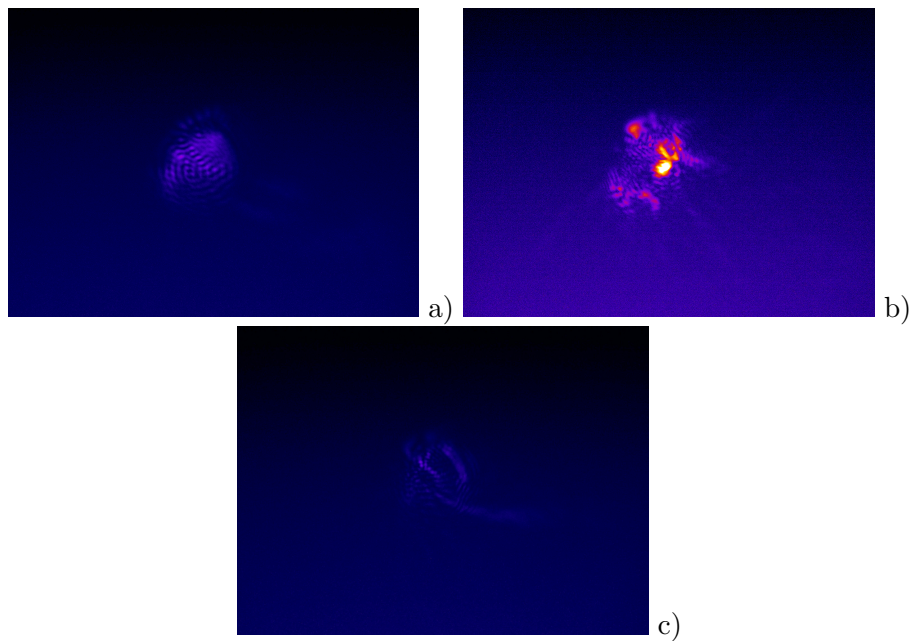


Figure 5.21. Images of the capillary output plane, synchronising the impulse respectively a) before the discharge, b) in the guiding window, c) in the discharge tail.

In Fig. 5.21 (a) there is the overlapping of the laser at the beginning of the discharge: the beam is dominated by diffraction due to the presence of a medium in

which the plasma is not yet formed. In this case the images are similar if referred only to the presence of the capillary, without plasma inside. The beam size here is consistent with the capillary channel size. In Fig. 5.21 (b) the laser arrives in the guiding window previously shown: the pulse is focused in a central point of greater intensity, but part of its energy is dispersed in the entire diameter of the channel where the diffraction effect is still present. In this timing zone, the output pulse is very unstable and the results are not widely repeatable, however, in this timing area of the discharge, the plasma has characteristics, even if in a partial way, to guide the pulse. Finally in Fig. 5.21 (c) the beam has been synchronised on the tail of the discharge and, coherently with what expected, the pulse is dispersed and attenuated. Fig. 5.22 summarises the results of the signals and laser imaging exiting the capillary, for different laser delays with respect to the current curve, in the zones already examined: just before discharge, in the guiding window, along the tail of the current curve.

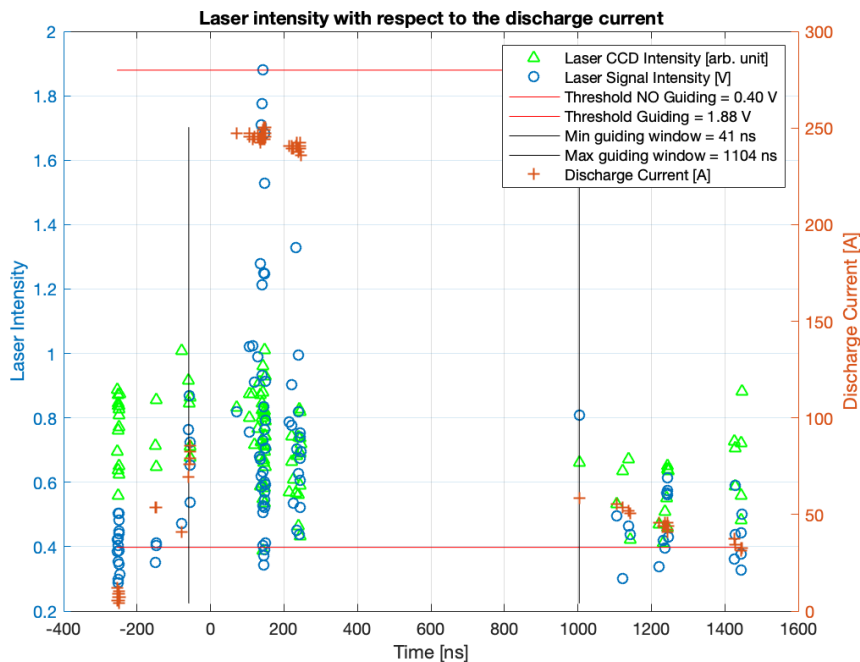


Figure 5.22. Scan of the laser exiting the capillary around the delays already considered previously. Pulse intensity signal (blue), current signal in the considered delay (red), intensity of the laser output spot on the *CCD imaging* (green).

From the results shown it is possible to conclude that the capillary channel, that must be chosen to match the spot used, must have a diameter less than 1 mm, as it is possible to calculate from Eq. 5.4. The second fact is that, although two different laser pulses have been shown to have clear effects of guiding within the same time window of the discharge, the guided pulse still does not have the desired spot on the channel output, so the guide and/or the process have some imperfections.

Two substantial problems related to the experimental setup, subsequently solved in a second experimental campaign have been identified as possible causes of these

discrepancies. The first is the absence of a support able to keep the capillary resting on the Hexapod plane. This leads to the inevitable positioning of the capillary with random angles, generated during assembly, for example for a different pressure applied to the different screws on the gas flange. These angles can be corrected by the Hexapod motors, placing the channel on the laser line. Although aligning the input laser to the channel is a relatively simple operation using the input cameras and moving the motors on the three axes, the situation is different with regard to the angles, which would require more diagnostics, for example by adding an iris and CCD immediately after the capillary output plane. Unfortunately, this type of diagnostics cannot be implemented for reasons of space inside the vacuum chamber. However, in order to compensate for this shortcoming, a support has been designed and realised to automatically position the capillary at the Hexapod plane (as shown in Fig. 5.23). This improvement in the setup allows to minimise the induced angles, and therefore to reduce the possibility of strong misalignment in the angle.

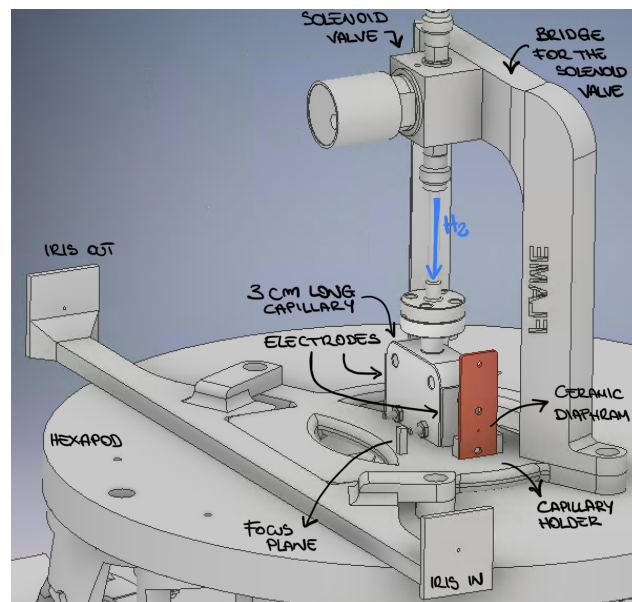


Figure 5.23. CAD file profile containing the objects positioned on the Hexapod plane, including the capillary: a support to hold the capillary anchoring the plane, a bridge support to bind the solenoid valve, a fire plane sight, an iris system and a diaphragm. The iris system, which is only used for laser diagnostics without the capillary, is on a line parallel to the one of the capillary, as it is moved by a motorised sled below.

The second problem that generates inaccuracy is the impossibility to verify the laser focus plane in the imaging system described in Section 5.3.1. Because of this fact the reliability of the pulse focus measurement can decrease substantially and this generates a difficulty in stable ideal beam-guide matching conditions. A big improvement from this point of view was made in the second campaign, positioning a small parallelepiped (shown in Fig. 5.23 as *focus plane*) that identifies the desired focal plane for the laser, i.e. the entrance plane of the capillary. By inserting this object on the laser line (i.e. the imaging line) using the Hexapod, the position of the laser output lens has been tuned by focusing the image of an edge of the

parallelepiped. The focal plane in question with the parallelepiped inserted and focused on the laser line is shown in Fig. 5.24. In this way the input plane of the capillary is uniquely defined by the position of the motorised slide underneath the lens exiting the chamber. At this point, the laser spot on the capillary input plane has been minimised by moving the slide below the focusing lens entering the chamber. Automatically, this operation defines the output plane of the laser, which will be exactly after 3.2 cm (the two additional millimetres are due to the presence of the electrodes).

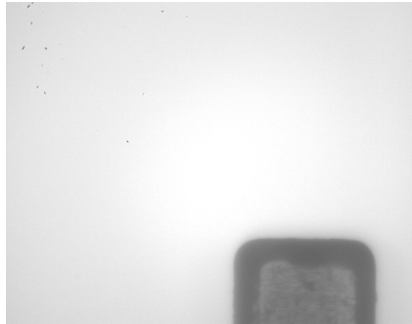


Figure 5.24. Image taken from the *imaging CCD*, positioned so as to look at the laser focus plane. Since this parallelepiped is on the same transverse plane, by focusing on it, it is possible to calibrate the camera and identify the capillary input plane, as well as the output plane.

This improvement and the repeatability of this series of operations make the focus measurements of the laser at the capillary input and the imaging of the output spot significantly more reliable. Furthermore, thanks to the presence of the aforementioned parallelepiped, which has a known width of 2 mm , a precise and easy calibration of the CCD used for laser focusing and imaging is possible. Fig. 5.23 also shows two other objects present on the Hexapod plane: a double iris system, useful to align the plane on the laser line, and a ceramic diaphragm (red in the picture) positioned at the entrance to the capillary (about 1 cm distance), useful to cut the tails of the beam, and thus avoid any damage to the walls of the channel.

5.3.3 Guiding test through a density hollow profile

In the second experimental campaign, two new Stark broadening diagnostic lines were mounted, both of plasma generated in the capillary. One was used to monitor the longitudinal density, the other was used the transverse density of the channel. The updated setup is presented in Fig. 5.25. Other plasma density measurements had been performed in another of SPARC_LAB's laboratory, the Plasma Laboratory, with similar instrumentation. However, the strength of this configuration is that a choice of these two lines of plasma diagnostics can be used and displayed during the guiding experiment. It is evident how this is translated into a big advantage that allows online optimisation of the initial parameters that determine the characteristics of the plasma itself (hydrogen pressure and voltage), and therefore the efficiency of the guiding process.

For these Stark broadening measurements, a spectrometer with a resolution of a

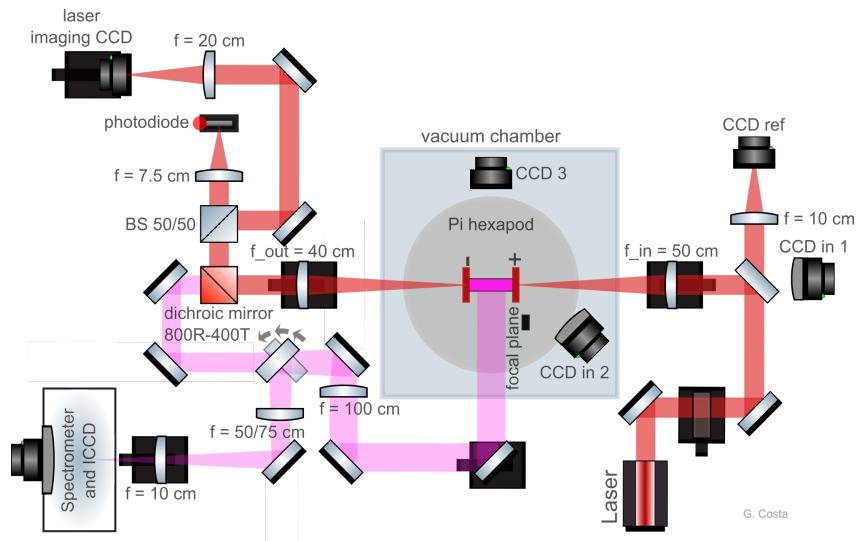


Figure 5.25. Setup upgraded for the second experimental guiding campaign. Two lines capable of diagnosing the emitted plasma radiation (longitudinal and transverse) have been added.

few Angstroms (*iHR Fully Automated Imaging Spectrometer iHR320*) is used, to be able to solve the chosen emission line ($H_{\alpha} = 656 \text{ nm}$ or $H_{\beta} = 486 \text{ nm}$), together with a setup assembled as follows: a first lens reproduces the longitudinal or transverse profile of the capillary, the light emitted is transported by an optical system on the slit of the spectrometer, then on its diffractive grating; a second lens conveys the scattered light on a CCD, which must be equipped with an intensifier to increase the signal/noise ratio, with active time of the order of tens of *ns* (*IStar 720 Andor Intensified CCD camera*). In this way it is possible to make a measurement resolved in time of the electronic density profile present inside the capillary. Although the discharge generally takes $1 - 2 \mu\text{s}$, due to the fact that electrons have a poor ability to transfer heat and therefore slowly exchange energy with the nuclei, the recombination process has a duration of tens of *ns*, therefore the recombination light of the emitted plasma is detectable.

In this setup (Fig. 5.25), the longitudinal plasma diagnostic line captures the light emitted by the entire channel through a mirror placed outside the chamber, in the direction transverse to the laser propagation direction. Along the line, a telescope is used to re-collimate the captured radiation, a periscope brings it to the level of the spectrometer, and a final short focal length lens focuses it on the aperture of the spectrometer (typically open in a range between $200 - 500 \mu\text{m}$). It is possible to pass between longitudinal and transverse plasma diagnostics by switching a mirror and changing the focal length of a lens. In this way, together with beam diagnostics, it is possible to display one or the other line of plasma diagnostics. The transverse plasma density diagnostic line uses the pre-existing line of laser pulse output diagnostics: a dichroic mirror is positioned after the f_{out} lens, transmitting only the radiation at 400 nm , after which this radiation as well is brought back on the line that reaches the aperture of the spectrometer. If the imaging lenses of the longitudinal diagnostic line are positioned so as to have the longitudinal plane of the capillary on the slit,

as far as the transverse density line is concerned, the focused plane is typically that of the capillary output, i.e. the one used to understand the trend of the laser pulse coming out of the guiding process. Theoretically, the plasma in the capillary is modelled with cylindrical geometry, i.e. with a constant transverse behavior along the longitudinal dimension. In reality, due to the flow asymmetry generated by the presence of injection inlets and the fact that the capillary is open, the transverse behavior of plasma is experimentally not exactly the same between the center of the capillary (area of interest) and the edges. This generates an error in the evaluation of the plasma transverse trend. By construction of the imaging system, it would theoretically be possible to move the plane of focus by moving the slide positioned under the first lens coming out of the chamber. However, in this way it is no longer possible to look at the output laser spot as the plasma transverse profile changes over time. Furthermore, by moving the observation to a point inside the capillary, the measurement would be distorted because, on the radiation transport line, an incoherent contribution deriving from the other emission planes crossed would be added. This contribution, on the other hand, becomes negligible when looking at the exit plane of the capillary, because only the contribution of the plasma plumes planes accumulates to it, whose emitted radiation is, however, about two orders of magnitude lower than that emitted in any other point of the channel. Measurements relative to this area will be presented in Section 6.5.

This spectroscopic method used to analyse the transverse trend of the plasma within a capillary is however an innovative method and solves the problem that arises when interferometric methods are used to observe the same transverse dimension: in order to exploit a system such as the one described in Chapter 4, the contribution of the phase shift of the branch that crosses the plasma, compared to the reference one, must come only from the presence of the plasma, and not also from the presence of the capillary itself on the same branch of the probe laser. However, since the front of the laser does not see the inner capillary's curved surface constant, this generates a contribution on the phase, that adds up and results in the interferogram coming from the two recombined branches. For this reason, interferometric measurements of transverse plasma density within capillary or gas-cells are performed on target models with square or rectangular cross-section, so as not to generate a further phase variation: the square cross-sectional geometry avoids refractive effects phase errors induced by capillary walls [118]. However, this modification of the target plasma geometry conflicts with the cylindrical geometry modelling that is used to describe the process, as already dealt with in the Section 5.1.2 and this consequently has an impact on the preparation of the conditions for the guiding process. An innovative idea to overcome this limitation and perform interferometric measurements of plasma density through capillary with round cross section will be presented in Section 7.1.1.

In consideration of these differences in the setup, the second experimental guiding campaign observed the following procedure:

- measurement of the laser parameters and consequent optimisation of the initial conditions,
- determination of the necessary plasma characteristics,
- simultaneous measurements of plasma density profiles and laser spot imaging

at channel output, compared to the delay between pulse and discharge curve.

In order to make improvements on the initial transverse profile of the pulse used for guiding tests, the dimensions of the incoming beam to the focusing lens have been changed: the focus entering the capillary, measured following the method previously described, is shown in Fig. 5.26, while Fig. 5.27 shows its longitudinal profile measured in the same way as the previous data acquisition.

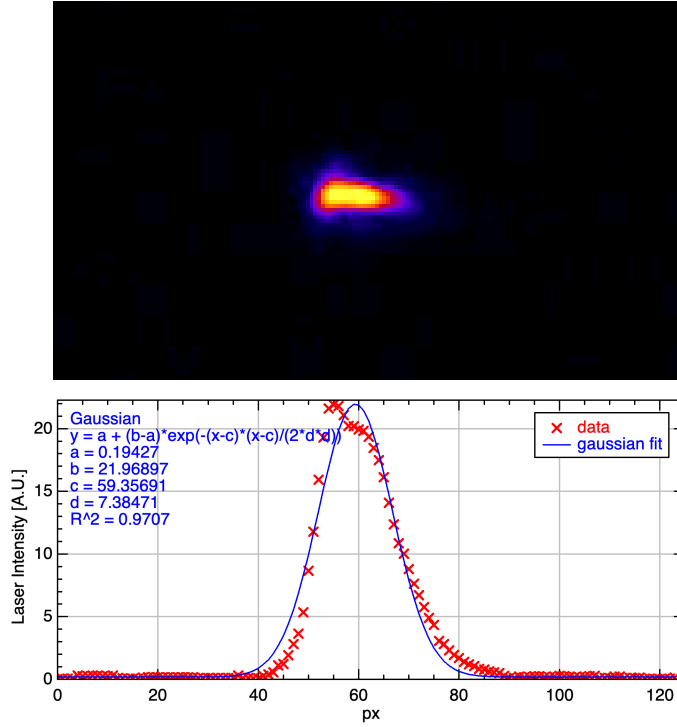


Figure 5.26. Laser spot on the focus plane and analysis of its horizontal profile: it is not a perfectly Gaussian beam due to non-uniformity in the transverse profile of the initial laser beam, before the focusing.

Using the laser and target parameters summarised in Tab. 5.3, it is possible to calculate the average plasma density using Eq. 5.4 and the depth of transverse plasma density using Eq. 5.3, information necessary for the success of the test.

Table 5.3. Probe laser parameters for the second guiding experimental campaign.

Energy	8 mJ
Temporal length	50 fs
FW $1/e^2$ @ focus	120 μm
Intensity	$3 \times 10^{15} \text{ W/cm}^2$
Normalised Intensity a_0	0.04

Thanks to the tests already carried out in the Plasma Laboratory, the experimental conditions in which it is possible to obtain a plasma density of the order of 10^{18} cm^{-3} , for a capillary of 3 cm of length and with a diameter of 0.5 mm, are

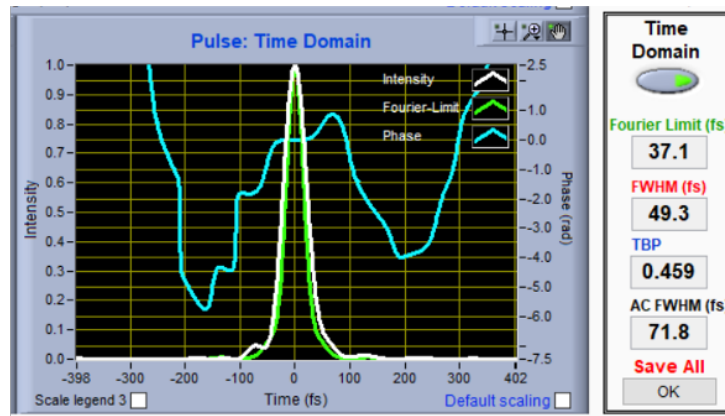


Figure 5.27. Screenshot of a time measurement of the beam, made with the *LX Spider* in the Clean Room.

already known and are summarised in Tab. 5.4. It also shows that the modifications made to the discharge circuit make it possible to progress by a factor of about 2 on the peak current, with the same voltage applied to the electrodes [145]. A schematic of the new discharge circuit used is shown in Fig. 5.28.

Table 5.4. Capillary, gas and discharge parameters.

Material	<i>VeroClear (Rigid Transparent Polyjet Material)</i>
Length	3 cm
Diameter	500 μm
Inlet number and diameter	2 - 500 μm
Gas used and pressure	H_2 - ~ 350 mbar
Valve opening time	1 ms
Discharge Max Current	450 A
Discharge Voltage	20 kV

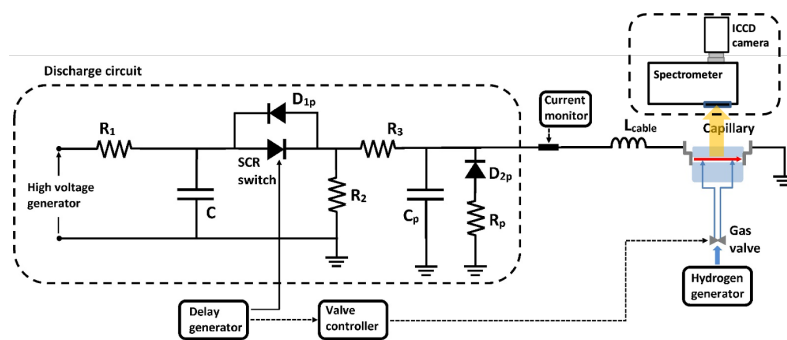


Figure 5.28. Upgrade of the discharge circuit to provide a peak current of approximately 500 A, while maintaining the same input voltage. The schematic of the connections of the delay generator and gas distribution, as well as that of the capillary and longitudinal plasma diagnostics, are also shown in the figure. *This sketch is courtesy of A. Biagioni.*

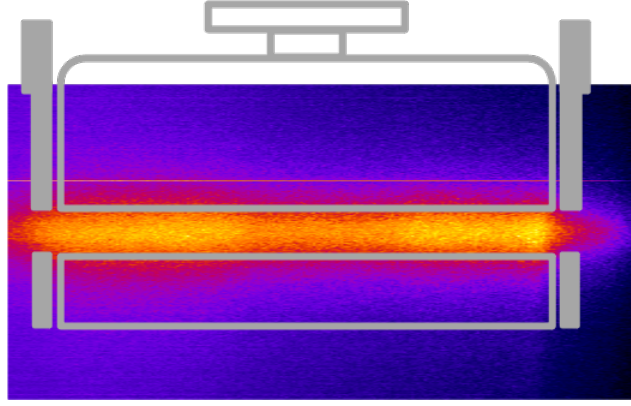


Figure 5.29. Example of data from the spectrometer. Radiation from the entire longitudinal profile of the capillary. Image rotated by 90° to be visually superimposed on the geometry of a capillary sketch.

An example of longitudinal profile measured as described above is shown in Fig. 5.29. It is rotated by 90° so that the change in enlargement, and therefore in density, can be more simply displayed in relation to the longitudinal position in the channel. Since the camera's acquisition gate may be delayed, this image refers to a delay within the guiding window of 300 ns from the start of the discharge curve. An accurate batch data analysis code has been developed to extrapolate the plasma density from the images coming from the spectrometer. This works as follows: for each image the horizontal axis represents the wavelengths while the vertical axis is simply related to the longitudinal dimension of the capillary: the horizontal axis has been calibrated with a dedicated calibration lamp, while the length axis can be calibrated by focusing on the edges of the electrodes. In this way each line of the original image represents a given longitudinal position of the capillary, and from its profile it is possible to obtain the plasma density: this is fitted by means of a Cauchy distribution, the Lorentzian curve $y(x) = \Gamma / \{2\pi[(x - x_0)^2 + (1/\Gamma)^2]\}$, whose FWHM (Full Width at Half Maximum) is used to determine the density [8]:

$$n_e = 8.02 \times 10^{12} \left(\frac{\Delta\lambda_{1/2}}{\alpha_{1/2}} \right)^{3/2} \text{ cm}^{-3}, \quad (5.13)$$

where $\Delta\lambda_{1/2}$ represents precisely the half-height width of the profile of the spectral line widening curve. Here the coefficient α used is tabulated in [135] and equal to 2.23×10^{-2} for the Balmer line alpha and 9.77×10^{-2} for the Balmer line beta, assuming a temperature of about 3.5 eV and an order of magnitude for the expected density of 10^{18} cm^{-3} . These characteristic plasma values are those expected for the system conditions of volume, pressure and current [127].

In Fig. 5.30 there is a longitudinal density analysis scan in the guiding window in steps of 20 ns. Fig. 5.31 shows instead a statistical analysis for the specified guiding delay of 300 ns. These analysed images show a sufficiently uniform average value over the entire length of the capillary of approximately $5 \times 10^{18} \text{ cm}^{-3}$ with about 8% of statistical error. This measurement was made by observing the Balmer alpha emission line, because it is more intense than the beta line and therefore has

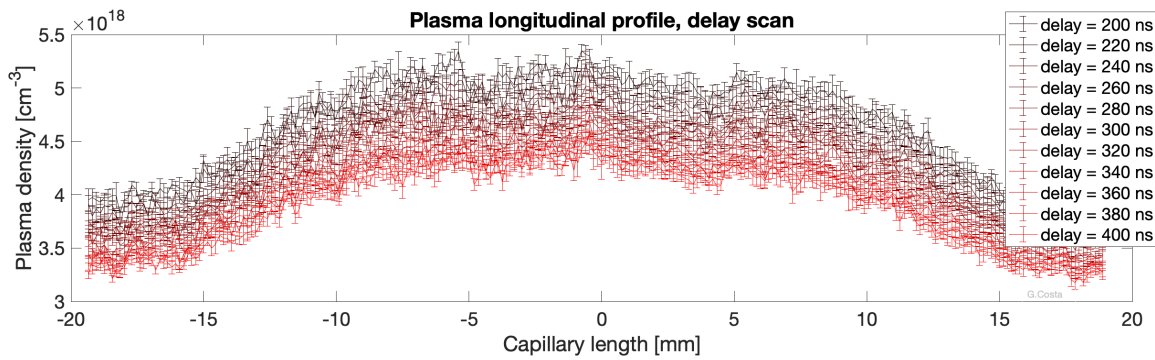


Figure 5.30. Analysis of longitudinal plasma profiles: time scan inside the guiding window from 200 ns to 400 ns in steps of 20 ns.

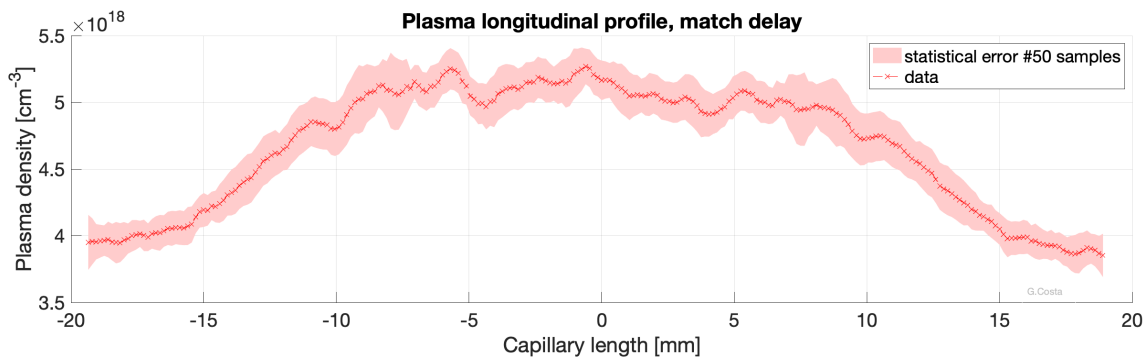


Figure 5.31. Statistical analysis of the longitudinal plasma profile in the chosen delay (300 ns), average and statistical error of 50 acquisitions.

a higher signal-to-noise ratio. However, it is affected by the thermal contribution, by means of the Doppler effect, significantly more than the Balmer beta line, which is weaker but gives a true value of the spectral widening due mainly to the Stark effect [7], thus of the plasma density (see Section 5.2). The two measurements are proportional to each other and differ by a factor of 2, so in this case it can be said that the average density measured on the longitudinal profile of the discharge is $\sim 2.5 \times 10^{18} \text{ cm}^{-3}$. In any case, as long as it is possible to fit these profiles with Lorentzian curves this means that obtaining the density from this type of measures that exploit the Stark effect is reliable. When, on the other hand, the widening of the emission lines becomes dominated by the thermal contribution, the line profiles are reproduced by Gaussian curves and it is not easy to split the two contributions to obtain the one of interest. Typically this occurs for densities higher than about $5 \times 10^{19} \text{ cm}^{-3}$ [135].

Likewise, Fig. 5.32 shows a transverse density profile of the same capillary with the same conditions. Even from the original image shown it can be seen that there is less widening in the central area of the capillary diameter than at the edges. The data analysis is made in a similar way to what previously described: in Fig. 5.33 (a) there is a delay scan in the guiding window, while a statistical result of the same delay previously considered is in Fig. 5.33 (b). The experimental data curve in Fig. 5.33 (b) is superimposed on the expected theoretical profile. The

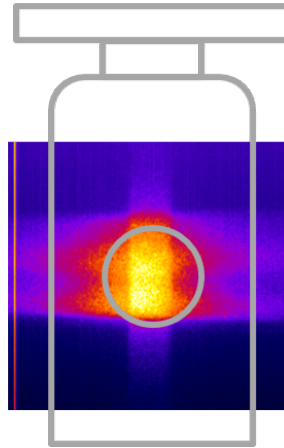


Figure 5.32. Example of transverse profile data of plasma radiation, on the capillary output plane. A sketch of the capillary profile has been superimposed. The hollow profile effect used for guiding is evident, along the vertical direction, i.e. the one representing the imaging of the source.

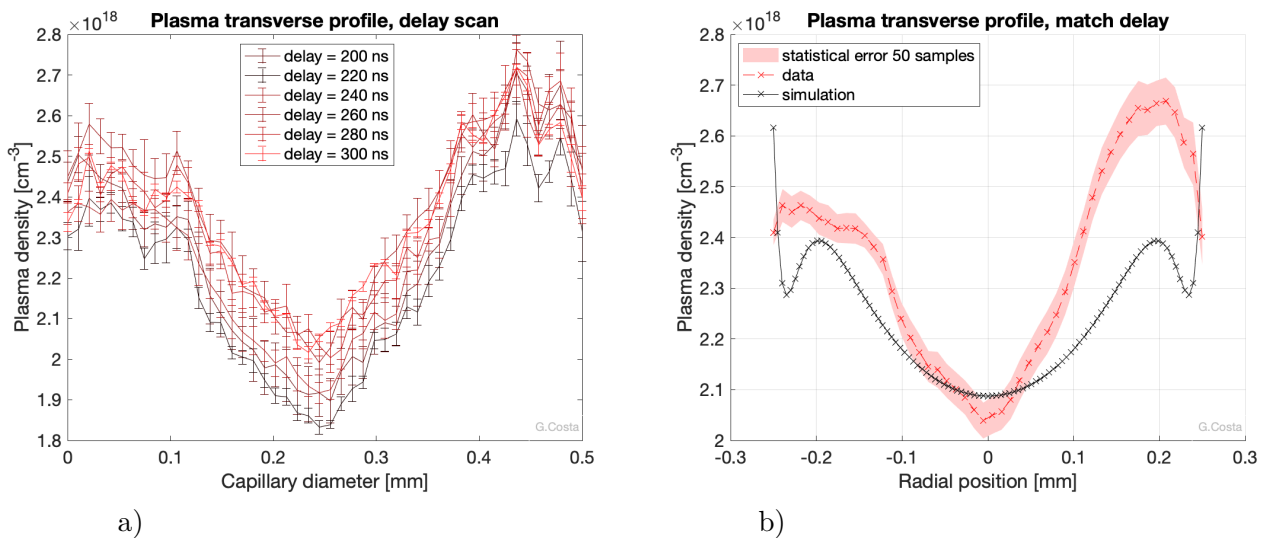


Figure 5.33. Analysis of transverse plasma profiles: time scan inside the guiding window from 200 ns to 300 ns in steps of 20 ns (a). Statistical analysis of the chosen delay (300 ns), average and statistical error on 50 acquisitions, with the simulated curve (b).

latter has been obtained from a 1D simulation, based on the model [9], described in Section 5.1.2. It has as input an average neutral gas density of $3 \times 10^{18} \text{ cm}^{-3}$, a maximum discharge current of 450 A and a voltage of 20 kV, in addition to gas composition and capillary parameters. This simulation uses the approximation of cylindrical geometry, so only half the diameter of the channel is computed. In order to allow a better visual comparison between experimental and theoretical transverse trend curves, the simulated curve has been mirrored, and the data have already been re-calibrated according to the fact that they are still images deriving from the widening of the spectral line α . Considering the approximations present in a 1D

model, and the fact that it returns a symmetrical profile by design, it is possible to conclude that the Δ_{ne} value obtained from the Eq. 5.3, which is $\sim 5.8 \times 10^{17} \text{ cm}^{-3}$, is in good agreement with the experimental data, as much as with the theoretical model used [9]: the value extracted from the data is $\sim 0.6 \times 10^{18} \text{ cm}^{-3}$. From the same 1D simulation it is also possible to obtain the average density inside the channel, which is $2.3 \times 10^{18} \text{ cm}^{-3}$, i.e. in perfect overlap, within the measurement error, with the experimental data obtained both for the longitudinal and transverse profile.

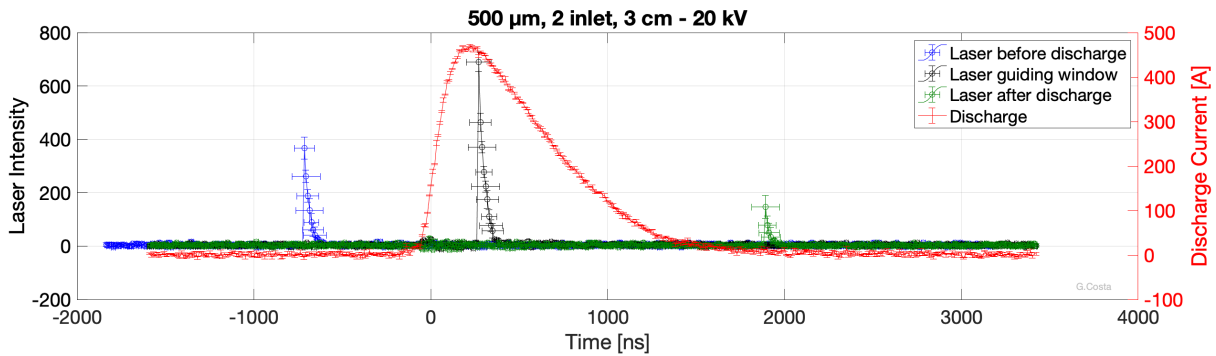


Figure 5.34. Statistical analysis of the laser signal output from the capillary for three different delays from the beginning of the discharge. Discharge curve with statistical average of the whole laser run, superimposed on the laser pulses. The average intensity obtained in the guiding window is approximately 88% of its initial value, since the beam transmission before the discharge (blue) is the 50% of the focus intensity.

Once these plasma conditions were found to be sufficiently satisfactory compared to the calculated theories, the guiding process was optimised and the results are shown in Fig. 5.34, in the form of waveforms: the laser pulses in the three different sample delays of the process are superimposed on an example discharge curve. The statistical error on the intensity derives from the fact that all waveforms are averaged over 50 samples for the same delay. That is to say, pulses with delays with respect to the discharge close to each other within 10 ns are averaged, considering the jitter previously mentioned. This generates the error reported on the time axis, and similarly it has been done for the discharge curve shown.

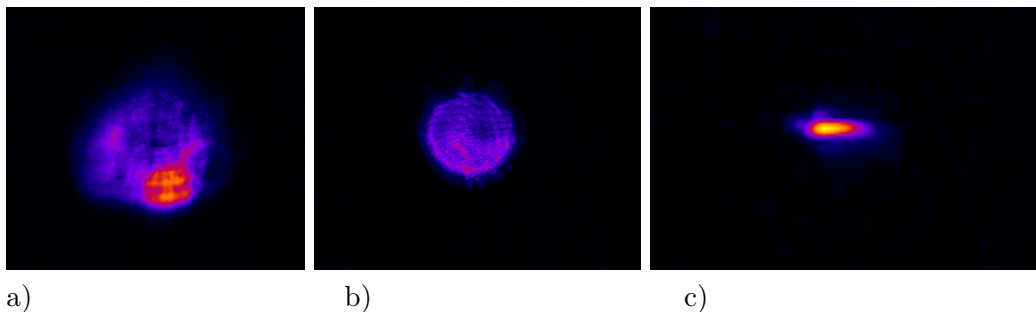


Figure 5.35. Images of the capillary output plane, subtracted from the background: a) pulse propagation without the capillary on the line, b) pulse propagation inside the capillary without plasma, c) pulse output from the guiding window.

Fig. 5.35 shows the three output pulse imaging results: (a) beam propagation inside the chamber with the capillary outside the laser line; (b) delay considered before discharge in the previous Fig. 5.34; (c) delay in the guiding window. In this case as well, the size of the beam before the arrival of the discharge is compatible with the size of the capillary, unlike the size and stability that the pulse assumes when guided. Fig. 5.36 shows instead some shots of the same delay (300 ns) during the same acquisition, while Fig. 5.37 shows the analysis concerning a couple of the previous examples. The average value of the pulse's FW at $1/e^2$ obtained for this time delay is $150 \mu m$ with an error of 2%.

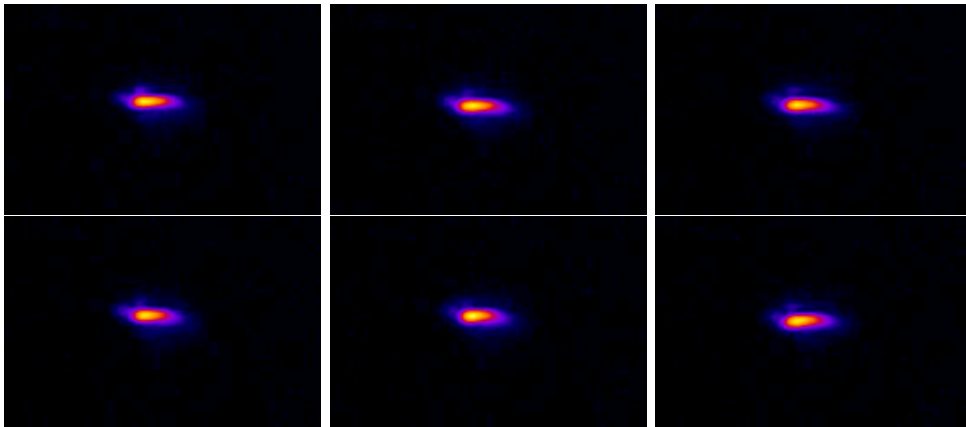


Figure 5.36. Example of statistical acquisition of guided beam out of the capillary, delay of 300 ns with respect to the beginning of the discharge.

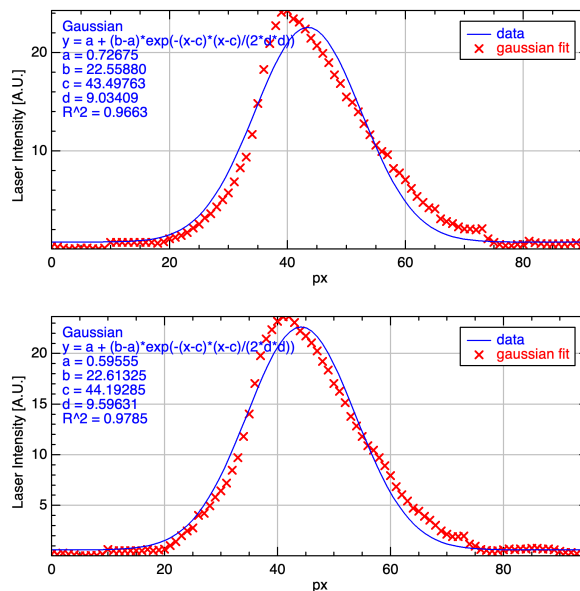


Figure 5.37. Examples of data analysis of horizontal profiles of guided spots. Although the laser spot is slightly larger than the focus spot, the transverse profile is really similar.

In addition to Tab. 5.5 which summarises the laser pulse driving results obtained

Table 5.5. Summary of the conditions and results obtained for the guiding experiments, with the necessary plasma density characteristics included. The experimental values are compared with the theoretical values obtained.

Channel	length 3 cm	diameter 0.5 mm	secondary inlets 2
H_2	p main inlet 380 mbar	channel density $3 \times 10^{18}\text{ cm}^{-3}$	gate evax 1 ms
HV Circuit	input voltage 20 kV	max current 450 A	trigger after gate 0 ms
Oscillator	r. rate 80 MHz	guiding window $(200 - 500)\text{ ns}$	increment $> 30\%$
Probe	energy 8 mJ best delay 300 ns	FW $1/e^2$ @ focus $120\text{ }\mu\text{m}$ guided spot $150\text{ }\mu\text{m}$	long. length 50 fs intensity $\sim 90\%$
Long. Density	exp. average $2.5 \times 10^{18}\text{ cm}^{-3}$	stat. error 8%	th. value $2.3 \times 10^{18}\text{ cm}^{-3}$
Transv. Density	exp. Δ_{ne} $0.6 \times 10^{18}\text{ cm}^{-3}$	stat. error 5%	th. Δ_{ne} $0.58 \times 10^{18}\text{ cm}^{-3}$

so far, from the results of this second guiding pulse data acquisition campaign, it is possible to conclude that [72, 73]:

- All the obtained effects attributable to the guiding are within the same time window found in the first campaign with the high repetition rate beam, both in terms of beam and plasma data.
- The fact that comparable results were obtained in the two campaigns by disassembling and reassembling the setup guarantees the repeatability of the experiment, as well as the fact that several capillaries of identical geometry were used, not observing relevant differences resulting from the use of different pieces. Substantial discrepancies were noted using targets that were not new enough, but with significant channel and inlet wear. This phenomenon has been quantitatively studied and more details on the subject will be given in Section 7.1.2.
- The improvements made in the setup to avoid inaccuracies and facilitate the understanding, and therefore the setting, of the initial parameters, have led to a better quality of the guiding process.
- Although the output guided beam is still slightly larger than the input beam, its transverse profile has improved considerably, and is similar to that of the focus pulse, in line with the data derived from the waveforms of signals.

- The pointing stability of the laser focus plays a crucial role in the guiding process by determining the alignment efficiency. In fact, significant differences in beam transmission in the plasma are observed for alignment deviations at the capillary entrance of more than $10\ \mu\text{m}$ and a few mrad [77].
- The installation of plasma diagnostics proved to be very useful and made it possible to identify and confirm the transverse hollow profile needed to guide the pulse used.

5.3.4 Guiding tests for different capillary geometry

The choice of the diameter of the capillary used was dictated by the possibility of adapting the laser beams to the ideal matching size for this diameter, as well as by the fact that these are dimensions that allow for good precision in the construction and cleaning of the workpiece. The opposite would be the case if the diameter of the channel were smaller: for example, the production of capillaries with a diameter of $300\ \mu\text{m}$ has been tested. Although the accuracy of 3D printing could be acceptable, the inlet channels were difficult to clean. This is due to the fact that the printer uses rubbery filling material to print the *vacuum*, which is difficult to free both chemically and mechanically from the curved inlets. Discharge tests carried out in capillaries with injection channels not completely and symmetrically free resulted in discharges inside the plastic material instead of in the channel.

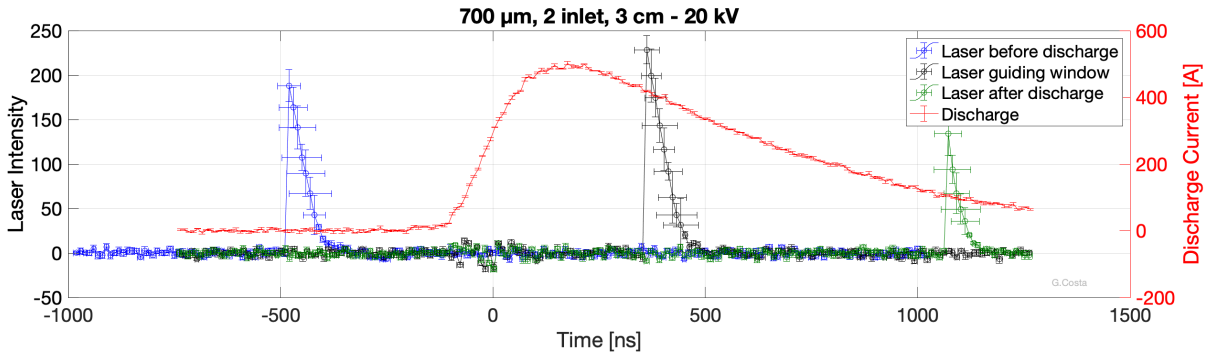


Figure 5.38. Statistical analysis of laser signals coming out of the capillary with a diameter of $700\ \mu\text{m}$, superimposed on the signal of a discharge curve also averaged. The delay shown in the central part of the discharge is the one that maximises the intensity of the laser pulse. The average intensity obtained in the guiding window is approximately 60% of its initial value, since the beam transmission before the discharge (blue) is the 50% of the focus intensity.

Instead, tests were carried out with capillaries with a diameter of $700\ \mu\text{m}$, i.e. slightly larger than the ideal one. As it can be seen in Fig. 5.38, and as expected, there is not a clear guiding effect because channel and laser spot do not match each other enough, considering the density reached in this capillary (see Fig. 5.39). The latter is lower than the $500\ \mu\text{m}$ channel case, because the parameters of gas pressure and maximum discharge current have not been changed (it was not possible to increase the circuit voltage, which is already used at its maximum level): this means that the starting density of the gas itself is lower. In addition, under these conditions

the transverse plasma profile obtained does not appear to have a significant difference in the axis-wall density value (see Fig. 5.40). On the contrary, according to the Eq. 5.4 and 5.3, the average density required for a channel with this diameter to guide the laser pulse in question is instead of $\sim 2.5 \times 10^{18} \text{ cm}^{-3}$, with a $\Delta_{ne} \simeq 5.8 \times 10^{17} \text{ cm}^{-3}$, so an even *deeper* hollow profile than the previous case.

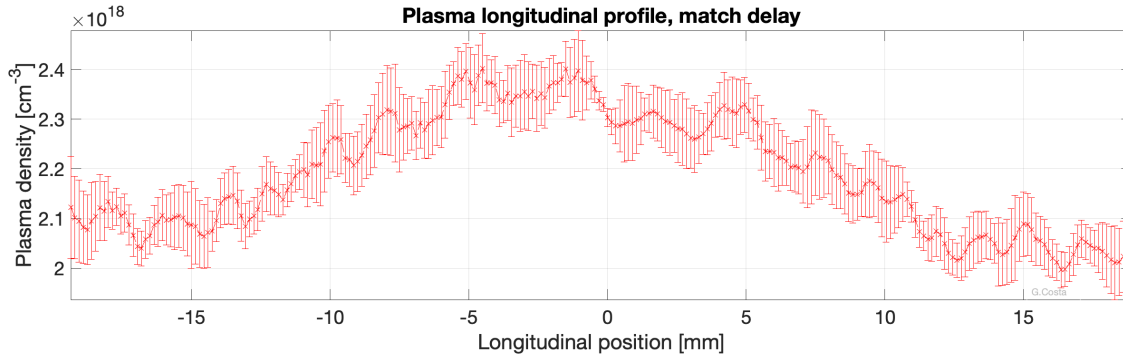


Figure 5.39. Longitudinal density profile analysis for the capillary with diameter $700 \mu\text{m}$. Since the other initial conditions have remained unchanged, the plasma density obtained is lower than that obtained for the capillary with a diameter of $500 \mu\text{m}$.

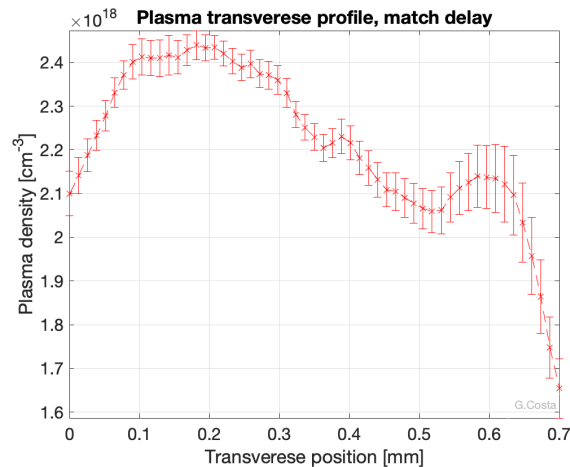


Figure 5.40. Transverse density profile analysis for the capillary with diameter $700 \mu\text{m}$. The trend obtained is not attributable to a hollow profile, and therefore it is not suitable for guiding the laser pulse.

Similarly to the tests carried out with a diameter, and therefore with an average density, not optimal, tests were made with capillaries of correct diameter ($500 \mu\text{m}$) compared to the experimental parameters, but with a worse longitudinal uniformity of the density value. This trend was reproduced by acting on the gas injection method, placing a single central inlet (see Fig. 5.41) instead of the double inlet distribution previously seen. This modification results in a higher density level in the central area of the channel (see Section 6.4), and generates an effect on the laser beam visible in Fig. 5.42. It is noted that although there is an increase in the intensity of the laser pulse in the guiding window, this is attenuated compared to the

ideal case, and similarly happens for the output laser spot. An effect that all tests rightly have in common is the behaviour of the beam outside the guiding window.

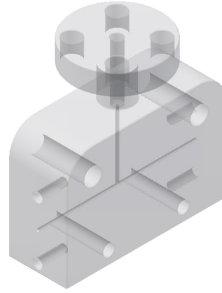


Figure 5.41. CAD image of the capillary with a length of 3 cm, a diameter of 500 μm and a single central inlet, also of diameter of 500 μm .

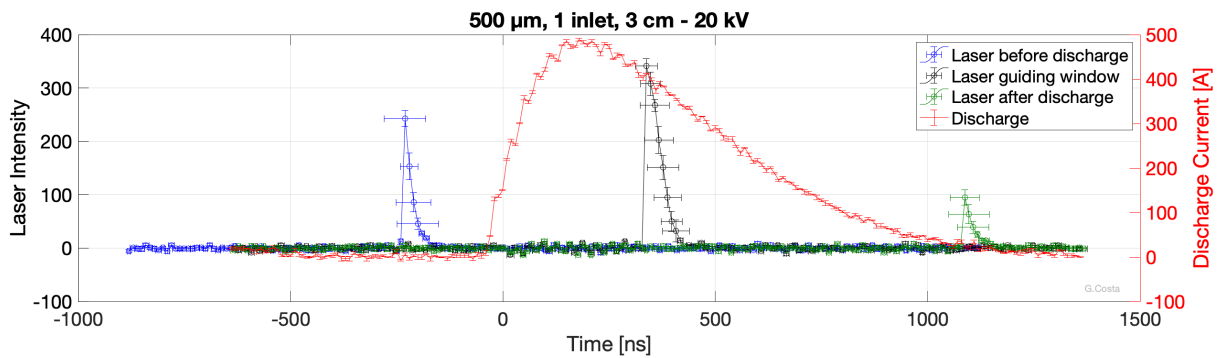


Figure 5.42. Statistical analysis of laser signals coming out of the capillary with a diameter of 500 μm and 1 inlet, superimposed on the signal of a discharge curve also averaged. The delay shown in the central part of the discharge is the one that maximises the intensity of the laser pulse. The average intensity obtained in the guiding window is approximately 70% of its initial value, since the beam transmission before the discharge (blue) is the 50% of the focus intensity.

The results obtained by modifying the target, i.e. altering the ideal conditions of the process, strengthen the results obtained of the ideal matching configuration between laser pulse and longitudinal and transverse plasma characteristics generated in the capillary.

Chapter 6

Plasma density measurements for alternative geometries

The fact that on-line measurements of plasma density are essential for understanding and optimising the guiding process was experimentally demonstrated in Chapter 5. In general, in plasma-based accelerators this measurement is necessary to understand the physical conditions of the interaction point, and thus to spatially and temporally match the beam (laser pulse or electron beam) to the plasma density.

In this Chapter, spectroscopic measurements of plasma density (including a study of plasma plumes) are presented, varying the geometrical characteristics of the capillary and the initial conditions.

In particular, a complete characterisation of the capillary used for the guiding process (length 3 *cm*, diameter 0.5 *mm*, two inlets) has been performed and will be presented in this Chapter.

6.1 Plasma density in a 500 μm -diameter capillary

In order to strengthen the assumptions made in Section 5.3.3 about the shape differences of Balmer's alpha and beta emission lines, due to temperature, an estimate of the ratio between the two has been made: using the spectroscopic system described (Fig 5.25), measurements were made to compare the width of Balmer's alpha emission line compared to the beta. An example of comparison is visible in Fig. 6.1. The capillary has a length of 3 *cm* and a diameter of 0.5 *mm*. The conditions used for the acquisition of the two lines are the same: same initial hydrogen pressure (~ 380 *mbar*), input voltage to the discharge circuit (20 *kV* - max current resulting 450 *A*), acquisition delay from the beginning of the discharge curve (300 *ns*).

It can be concluded that, in the central part of the channel, the result obtained is compatible with a difference of about a factor 2 in favour of Balmer's alpha line, as expected [7, 8]. It is also observed that the data taken with the beta line return a longitudinal profile of plasma much more unstable. The low intensity of the beta line causes a low signal to noise ratio, due to the low intensity of the line. It makes this measurement less reliable from the point of view of distribution, while it remains reliable in the mean value [8]. For this reason it has been chosen to carry out most of the density measurements within the capillaries by detecting Balmer's alpha line,

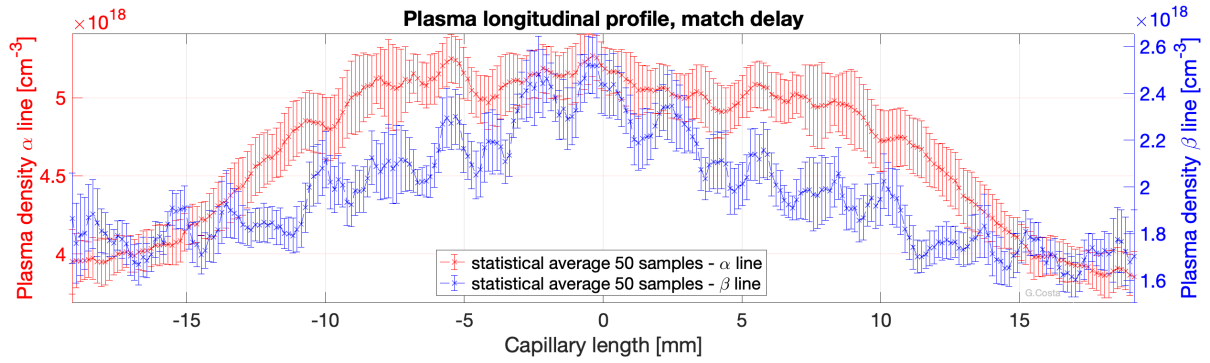


Figure 6.1. Comparison of the longitudinal plasma density profile measured using the Balmer alpha line (red) and beta line (blue). Between the two curves' intensities there is a factor 2, compatible within the error with the expected theoretical data [7,8].

and then taking into account the multiplicative correction factor. Therefore, for each new capillary installed the first thing was to verify this trend by making some measurements with the beta line.

Fig. 6.2 shows the scan of the mean values of longitudinal density with relative statistical error, superimposed on the discharge curve also averaged for each acquired time.

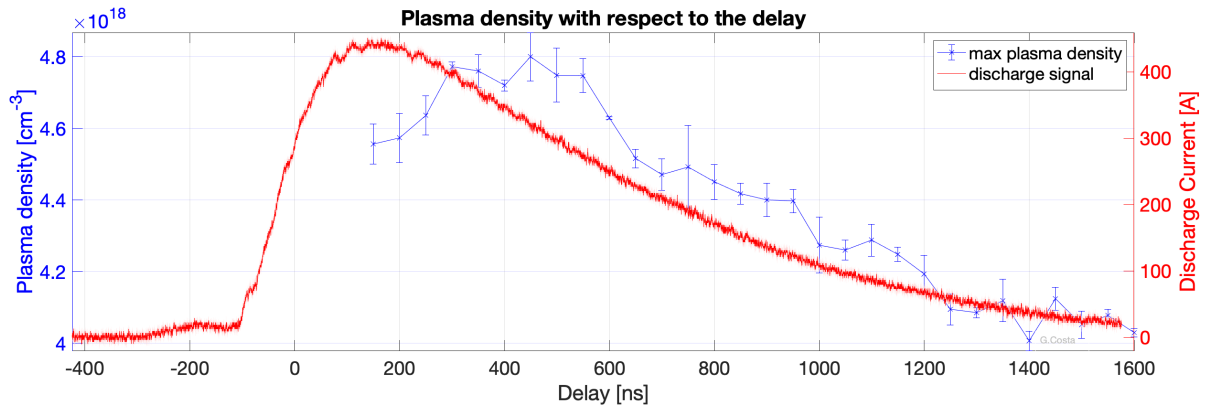


Figure 6.2. Scan of the mean values of longitudinal density with relative statistical error (blue), superimposed on the discharge curve also averaged for each acquired time (red). Statistical analysis of 50 samples.

Another interesting information is the knowledge of the plasma density evolution along the whole discharge curve [146]. Concerning this, using the same capillary, a long scan was performed by varying the delay between the start of the discharge and the image acquisition: from 0 to 1300 ns in steps of 50 ns. In these measurements a slightly lower than usual initial hydrogen pressure (few tens of mbar lower) at the main inlet was applied. This results in a slightly lower maximum plasma density than that usually obtained for the same capillary and the usual pressure of 380 mbar.

Fig. 6.2 also shows that for delays along the tail of the discharge curve, the measured plasma density decreases, and this is mainly due to electron recombination. On the other hand, around the beginning of the discharge (about 200 ns), it is not

possible to provide an average value for the plasma density. This is due to the shape of the current itself, since it grows rapidly in that area, and this results in significant variations on the 20 ns scale, which is the ICCD acquisition gate time. For this reason, it is not possible with this method to detect the low density values that exist in the first phase of plasma formation.

6.2 Plasma density saturation

Another thing that has been verified is the difference in plasma density obtained by varying the input voltage to the discharge circuit. Using the same capillary (3 cm length - 0.5 mm diameter - 2 inlet) and the same initial pressure conditions (380 mbar on the main inlet), the voltage applied to the electrodes was varied. In Fig. 6.3 is shown an image of the current curves obtained for the three different voltages considered, summarised in Tab. 6.1, while in Fig. 6.4 there is the comparison between the obtained plasma densities.

Table 6.1. Comparison between experimental and theoretical channel ionisation degree.

Voltage	Max Current	Th ionis.	Exp ionis.	Th density	Exp density
20 kV	450 A	81%	82% \pm 7%	2.3×10^{18}	$2.5 \times 10^{18} \pm 8\%$
15 kV	330 A	66%	67% \pm 6%	2.0×10^{18}	$1.9 \times 10^{18} \pm 8\%$
10 kV	250 A	59%	44% \pm 4%	1.8×10^{18}	$1.3 \times 10^{18} \pm 10\%$

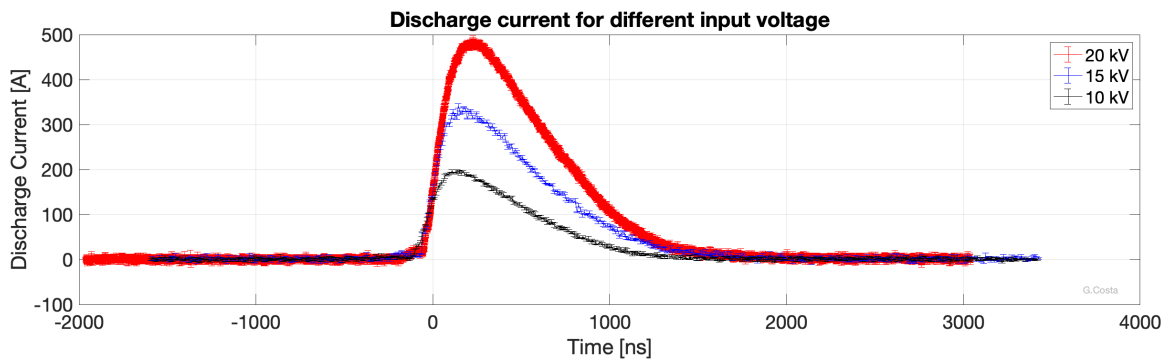


Figure 6.3. Different output current curves of the discharge circuit, for the same capillary, for three different input voltages: 20 kV (red), 15 kV (blu) and 10 kV (black).

In the table is reported the theoretical ionisation degree and the theoretical plasma density coming from 1D simulations, already introduced in Section 5.3.3 and based on the model [9]. These simulations have been carried out using as input the voltage applied to the capillary and the maximum current generated. The theoretical values thus obtained have been compared with the experimental values derived in the following way.

The experimental degree of ionisation has been derived starting from the pressure of the hydrogen entering the capillary through the main inlet ($p_0 = 380$ mbar), measured with a pressure gauge attached to the pressure reducer. Through this

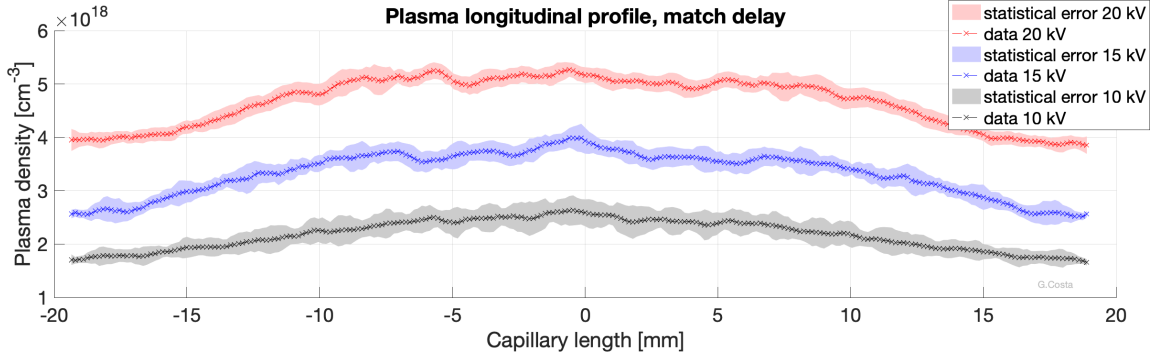


Figure 6.4. Comparison of plasma densities obtained with different voltages applied to the capillary extremities: 20 kV (red), 15 kV (blue) and 10 kV (black). The errors on the measured plasma density vary from 8% (20 kV), up to about 10% (10 kV) due to the different signal to noise ratio. Statistical analysis of 50 samples.

information, the pressure inside the channel at the end of the solenoid valve opening time was estimated: it was carried out by means of fluid-dynamics simulations in *OpenFOAM* (for details, see Appendix B), with the input of the characteristics of the gas used, the set pressure and the exact geometry of the entire capillary, extracted from a CAD design (volume of the geometry $\sim 6 \text{ mm}^3$).

As the calculation time is strongly determined by the pressure gradients considered, a preliminary study of the pressure values reached in the channel by varying the initial pressure applied to the main inlet was carried out. Fig. 6.5 shows the results of four different simulations of the same capillary (3 cm - 0.5 mm), for four different initial pressure values: (10 – 38 – 100 – 360) mbar, at the final time (1 ms). For this range of values and this channel geometry, a sub-sonic velocity regime is obtained. Assuming that the gas density varies linearly with the pressure, it can be concluded that, in the range considered, the pressure scales linearly with the initial pressure. For this reason, simulations in *OpenFOAM* to deduce the neutral gas trend when changing geometrical parameters have usually been performed for initial pressures on the main inlet of 100 mbar.

From this study, for the specific case of $p_0 = 380 \text{ mbar}$, it can therefore be deduced that the electronic density of the neutral gas inside the channel, at the starting point of the discharge, is about $3 \times 10^{18} \text{ cm}^{-3}$, considering the value of the maximum peaks. This value is the one that was subsequently used at the input for the 1D simulation of average plasma evolution following the discharge.

Knowing in this way the theoretical pressure inside the channel, it is therefore possible to estimate the density of the neutral gas in cm^{-3} through the gas equation of state

$$n_0 = \frac{p_0}{10k_B T}, \quad (6.1)$$

where k_B is the Boltzmann constant in J/K , and $T = 300 \text{ K}$ is the assumed temperature. The Eq. 6.1 returns the value of the molecular density of the gas. Therefore in this case, to compare n_0 with the electron density of plasma n_e , generated by discharge in H_2 , the first one must be multiplied by a factor 2. It is possible at this point to obtain an estimate of the *experimental* degree of ionisation measured,

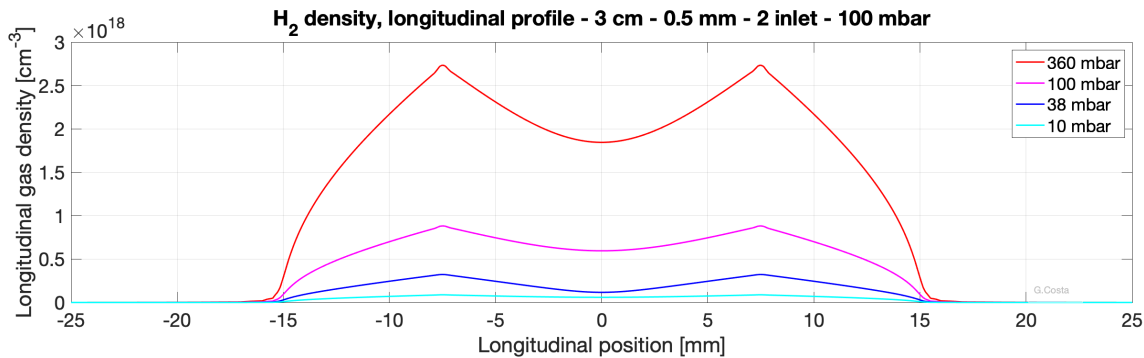


Figure 6.5. Results at the final time-step (1 *ms*) of four simulations of the longitudinal hydrogen profile, at the centre of the capillary channel, with initial pressures on the main inlet respectively of 360 *mbar* (red), 100 *mbar* (magenta), 38 *mbar* (blue), 10 *mbar* (light blue). The two maxima in the curves are at the two inlets where the gas pressure is highest.

simply by dividing the plasma density obtained with the different voltages by the electron density of the neutral gas. For the usual capillary used the simulated electronic density of the neutral gas thus obtained is equal to $2.8 \times 10^{18} \text{ cm}^{-3}$. This value therefore defines the maximum achievable plasma density with this geometry and these gas conditions in the case of complete ionisation.

The densities obtained for the 20 *kV* and 15 *kV* cases are consistent within the errors (about 8%) with the theoretical ones. Differently it happens for the 10 *kV* case where, although the statistical error is greater, it is not enough to compensate the difference. This is probably because a measurement with such a low discharge current generates a much less intense signal, and therefore more difficult to diagnose precisely with the same instrumentation. Another factor to keep in mind, together with the assumptions made regarding the model used and the resulting calculation, is the inaccuracy with which the initial pressure on the main capillary inlet is known. To this it is added the error that is made in estimating the internal density inside the channel through the fluid-dynamic model. This is especially due to the fact that it is not possible to simulate a precise opening and closing ramp of the solenoid valve, since, from specifications, it has an opening time of a few milliseconds (2 – 3 *ms*), time therefore compatible with the total opening gate for the experiment in the case of a capillary with a length of 3 *cm* and diameter 0.5 *mm*. Inaccuracies on the measured plasma density produce therefore by calculation a considerable error on the estimated experimental ionisation level. This error partly compensates for the differences shown.

In order to overcome these discrepancies, a data acquisition has been designed to indirectly measure the electronic density of neutral gas. It comes from the idea that if the amount of hydrogen inside the capillary that is injected is always the same and at the same pressure, when the complete ionisation occurs, there is a saturation in the plasma profile measured as the input voltage of the discharge circuit increases, i.e. as the maximum current increases. For this purpose, measurements of longitudinal plasma density have been carried out, with the same conditions of the measurements already presented in Fig. 6.4, pushing the input voltage to the

circuit up to 22 *kV*, which is the construction limit of the system. In Fig. 6.6 and 6.7 are reported respectively the current curves obtained from this scan and the relative longitudinal plasma density profiles. It is clear that the saturation seems to be already reached for 20 *kV*, that is the normal working value of the high voltage circuit: in Fig. 6.8 two plots of the average density trend obtained by varying the input voltage and, consequently, the current reached are shown.

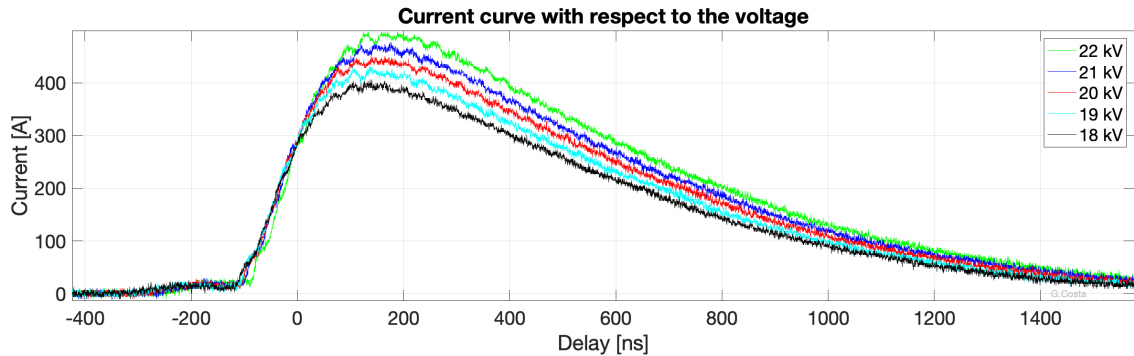


Figure 6.6. Scan of output current curves of the discharge circuit, for the same capillary, for different input voltages since 18 *kV* to 22 *kV*, with a step of 1 *kV*.

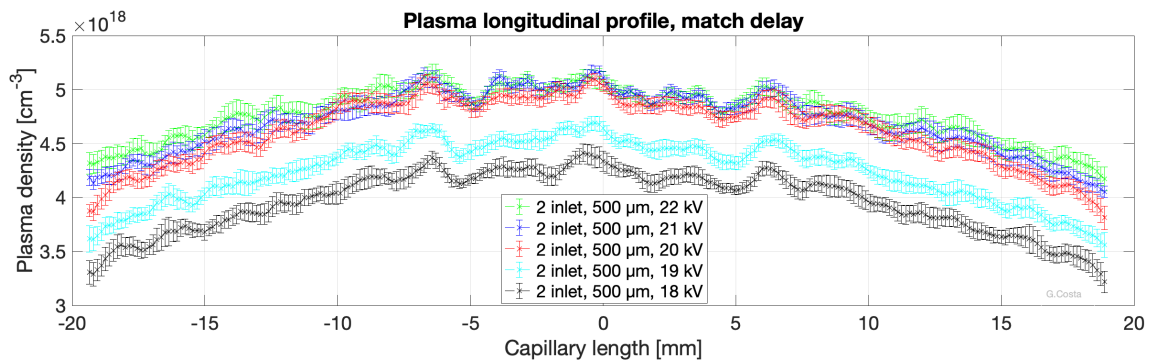


Figure 6.7. Scan of the longitudinal plasma density profiles with varying input voltage to the discharge circuit: from 18 *kV* to 22 *kV*, with step of 1 *kV*. Statistical analysis of 50 samples.

From this analysis, an estimate of the initial average neutral gas density can be concluded, using the plasma density measured at saturation and taking into account the factor 2 between the two: $n_0 = 2.5 \times 10^{18} \text{ cm}^{-3} \pm 8\%$, result consistent within approximations with the expected theoretical one. It can therefore be considered that the ionisation level previously calculated as the ratio between the plasma density (experimental or theoretical) obtained and the neutral gas density, seems to be underestimated: the theoretical degree of ionisation expected for the case at 20 *kV* is about 80%. Nevertheless it can only represent an estimation of the average value of the ionisation level, along the longitudinal and radial profile of the channel.

It is possible to show that this is the reason for this inconsistency by using the model [9]. By means of the latter, starting from the same initial conditions already discussed, it is possible to obtain the radial profile of ionisation, averaged over the

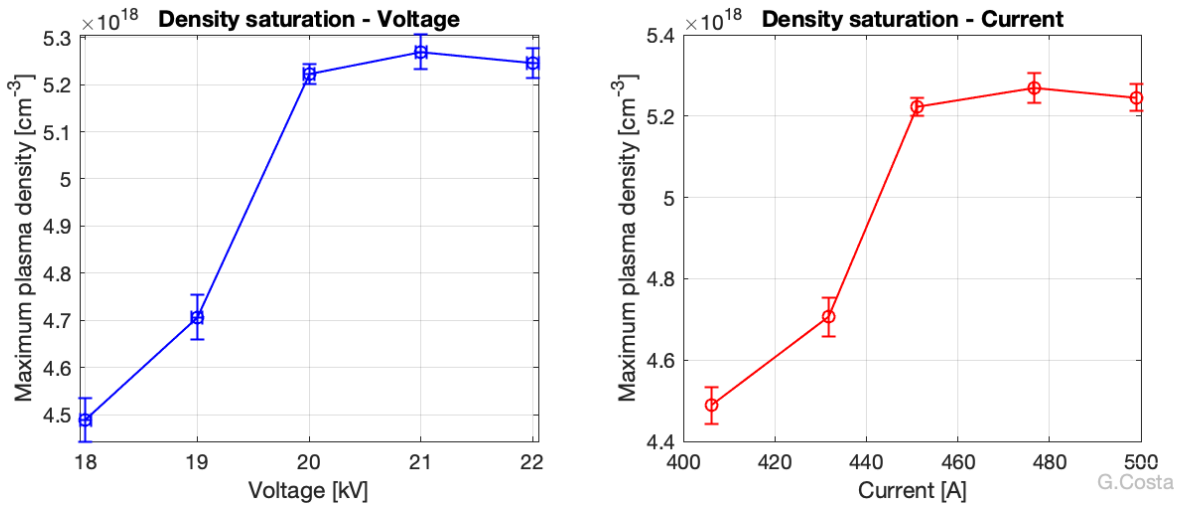


Figure 6.8. Saturation curve of the mean value of the plasma density with respect to the discharge voltage (left) and the maximum value of the current pulse (right) respectively.

length of the channel. As shown in Fig.6.9, the average value of the theoretical degree of ionisation is influenced and lowered by the behaviour near the walls. Therefore, it is possible to consider this profile in good agreement with the average ionisation value simply calculated above. Moreover, in the central part (transverse profile) of the capillary, the ionisation level is instead constant and, in an internal diameter of 300 μm , it exceeds 95%. Therefore, it is also possible to conclude that this data is compatible with the saturation of the density (Fig. 6.7) reached at around 450 A of peak discharge current.

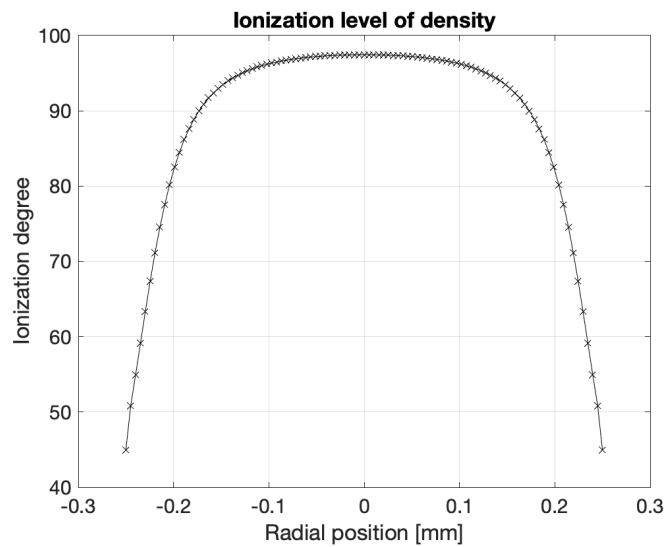


Figure 6.9. Degree of ionisation along the radial position of the channel, obtained through a 1D simulation using the model [9], input voltage 20 kV - input max current 450 A. The simulation presents cylindrical symmetry, therefore the quantities are calculated only for half of the channel diameter. The curves are then mirrored for visual convenience.

6.3 Different capillary diameters

Since different capillary diameters were used for all the various guiding tests, neutral gas trend simulations and plasma density characterisation measurements were carried out for all these diameters considered.

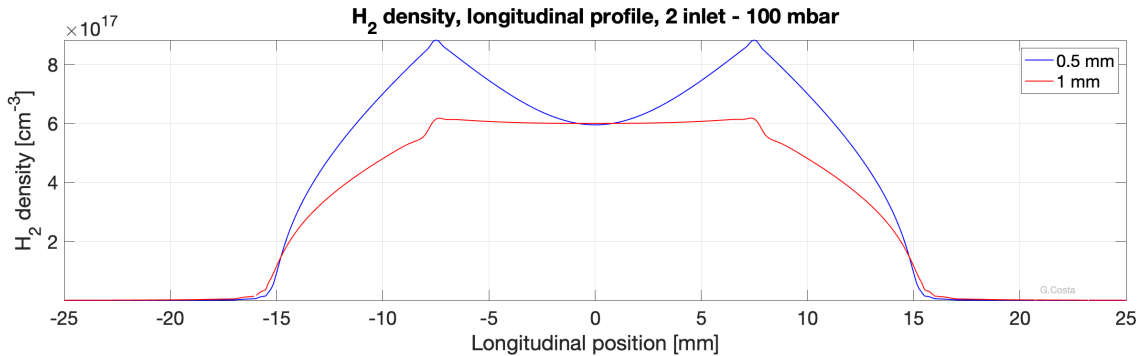


Figure 6.10. Comparison of the longitudinal gas density profile for capillaries with diameters of $500 \mu\text{m}$ (blue) and 1 mm (red). Curves obtained through OpenFOAM simulations, resulting at the end of the solenoid valve closure gate. The gas injection pressure applied is the same and equal to 100 mbar .

For example, Fig. 6.10 shows the results of two simulations in OpenFOAM for the capillary with two inlet geometry but different diameters: $500 \mu\text{m}$ and 1 mm . The input pressure applied to the main inlet is the same and equal to 100 mbar , in order to compare the two curves. They represent the longitudinal distribution of hydrogen density inside the channel. It can therefore be seen in the figure that the gas density reaches a higher peak value at the same pressure and lower volume, as expected. It is also possible to notice that a smaller diameter is more influenced by the presence and the position of the secondary inlets, due to the fact that, with the same initial pressure, but with a smaller inlet and capillary cross-section, a uniform pressure condition is not reached inside the channel, at the fluid-dynamic equilibrium. This difference in the longitudinal profile of gas density inside the channel (0.5 mm diameter), being relatively low (about 30%), is experimentally observed not to affect the longitudinal profile of plasma, i.e. the discharge current manages to homogenise the distribution.

Figs. 6.11 and 6.12 show indeed the comparison of longitudinal plasma density measurements between the usual capillary with a diameter of 0.5 mm and that with a diameter of 1 mm and with 0.7 mm respectively. In Fig. 6.11, the minimum before the centre of the capillary in the 1 mm diameter profile is probably due to a geometric imperfection within the channel.

As already discussed, the value of the neutral density n_0 can only be considered as an upper limit for the value of n_e found, as the latter also depends on the degree of ionisation of the gas achieved in the different diameters. In this regard, Fig. 6.13 shows the ionisation level for the three diameters considered. It was obtained by using the already mentioned 1D simulation employing the model [9], and it confirms that although the applied current is the same, the current density increases as the diameter decreases, which results in a higher level of ionisation for capillaries with

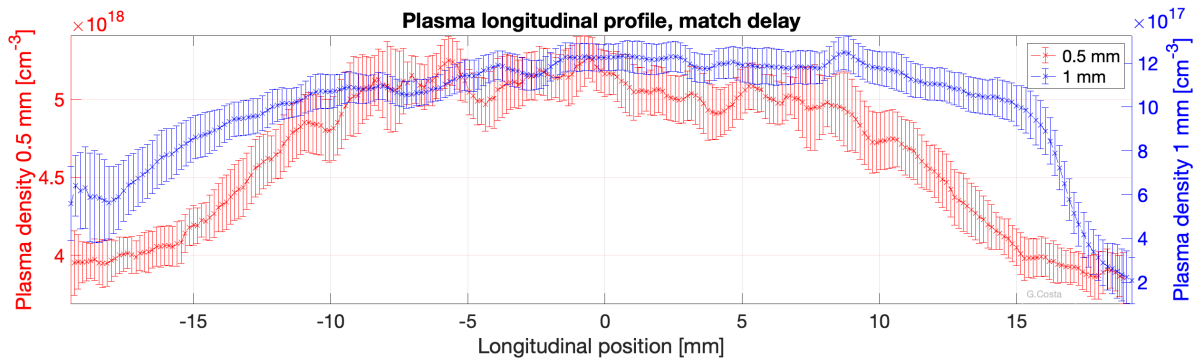


Figure 6.11. Comparison of the longitudinal plasma density profile for capillaries with diameters of $500 \mu\text{m}$ (red) and 1 mm (blue) respectively. The gas injection geometry and the discharge conditions are the same. Statistical analysis of 50 samples.

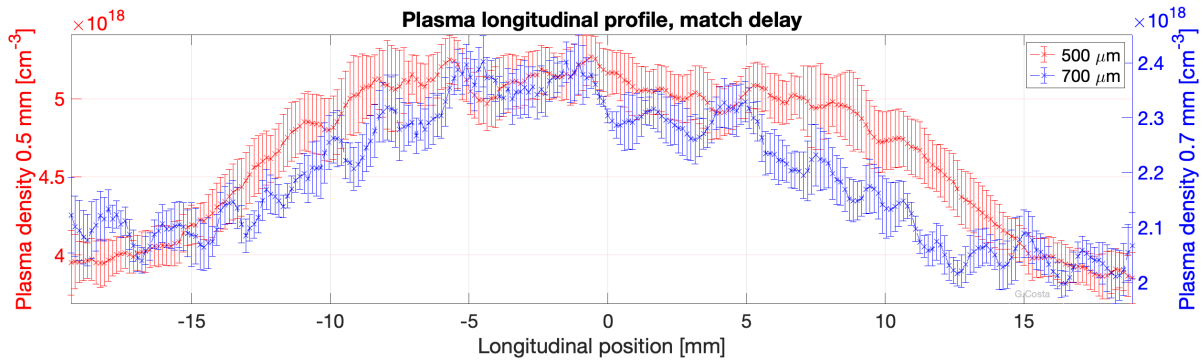


Figure 6.12. Comparison of the longitudinal plasma density profile for capillaries with diameters of $500 \mu\text{m}$ (red) and $700 \mu\text{m}$ (blue) respectively. The gas injection geometry and the discharge conditions are the same. Statistical analysis of 50 samples.

Table 6.2. Comparison of the electronic plasma densities, and the relative gas molar densities, both experimental and theoretical, together with the temperature value resulting from simulations, obtained for different diameters. The experimental errors on the density measurements, and thus on the molar densities, are about 8% in all three cases.

Diameter	Exp. $n_e [cm^{-3}]$	T [eV]	Ionis. degree	$n_{th} [mol]$	$n_{exp} [mol]$
$500 \mu\text{m}$	5×10^{18}	6 eV	81%	9.5×10^{-9}	1.2×10^{-8}
$700 \mu\text{m}$	2.3×10^{18}	5 eV	75%	1.9×10^{-8}	1.1×10^{-8}
1 mm	1.1×10^{18}	4.5 eV	67%	3.8×10^{-9}	1.0×10^{-8}

smaller diameters. The degree of ionisation is calculated from the temperature reached inside the channel: Fig. 6.14 shows the radial trend that it has for the three different diameters considered. It can be seen from Fig. 6.14 and Fig. 6.13 that a higher temperature, and therefore a higher level of ionisation, occurs in the centre of the channel, i.e. in the area ideally crossed by the current pulse. Tab. 6.2 summarises the results obtained in this way, which show a clear inverse quadratic proportionality of plasma density to volume, also taking into account the contribution of ionisation.

The reported values of temperature and degree of ionisation are averaged over the transverse plain of the channel.

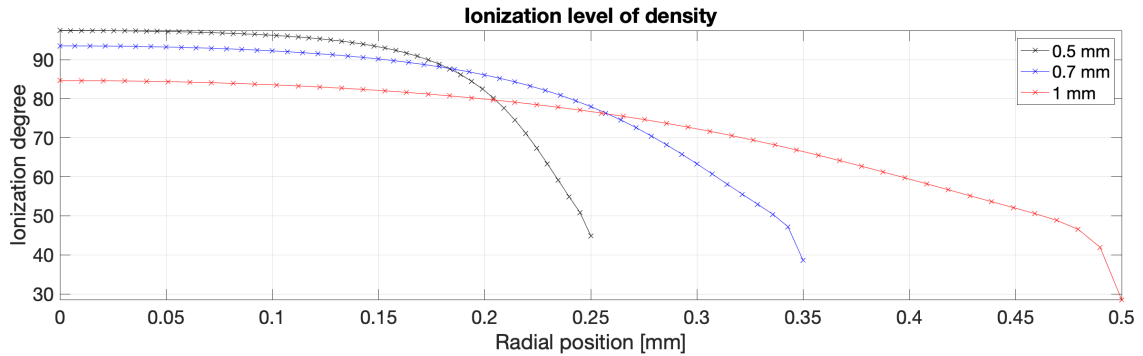


Figure 6.13. Degree of ionisation along the radial position of the channel, obtained through a 1D simulation using the model [9], input voltage 20 kV - input max current 450 A, three different diameters: 0.5 mm, 0.7 mm and 1 mm. The simulation presents cylindrical symmetry, therefore the quantities are calculated only for half of the channel diameter.

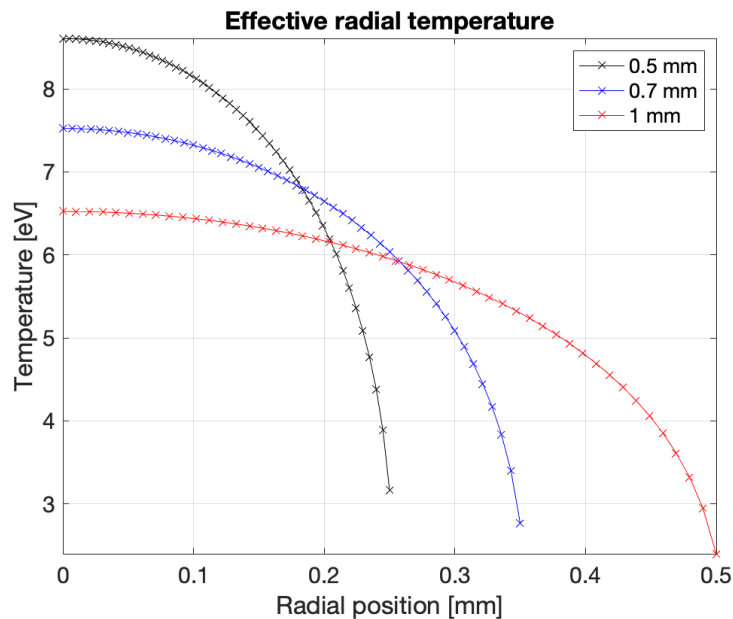


Figure 6.14. Temperature along the radial position of the channel, obtained through a 1D simulation using the model [9], input voltage 20 kV - input max current 450 A, three different diameters: 0.5 mm, 0.7 mm and 1 mm. The simulation presents cylindrical symmetry, therefore the quantities are calculated only for half of the channel diameter.

As the initial parameters are identical for all three capillaries measured, it is possible to estimate the difference in the expected plasma density in relation to the variations of diameter, hence of volume. Since it can be assumed $pV = n_{th}RT$, where R is the gas constant, the value of n_{th} , that is the amount of substance, can be calculated for each diameter. Similarly, the value of the measured n_{exp} can be

derived from the average plasma density n_e obtained through

$$n_{exp} = \frac{n_e V}{N_a}, \quad (6.2)$$

where N_a is the Avogadro constant. Considering the factor 2 resulting from the difference between the gas molecular density and the electronic plasma density, as well as the factor 2 resulting from the plasma measurements carried out by acquiring the Balmer alpha line, Tab. 6.2 shows also the results obtained in this way. It is noted that the upper limit for the measured values is in agreement with expectations in the two cases of diameter $700 \mu m$ and $1 mm$, while in the case of diameter $500 \mu m$, the amount of substance n_{exp} , derived from the simulated plasma density, is slightly higher than the estimated theoretical. As seen in the previous section, this case is at the limit of the density saturation condition, i.e. there is essentially a complete ionisation in the central zone of the channel. This justifies the discrepancy found, considering the approximations made to obtain the estimate of the theoretical amount of substance n_{th} .

6.4 Different capillary gas injection methods

In order to choose the most useful gas injection system in the channel to obtain a longitudinally uniform plasma profile, longitudinal plasma density measurements were carried out for different diameters and different numbers of secondary inlets. These were coupled with fluid-dynamic simulations of the neutral gas in OpenFOAM.

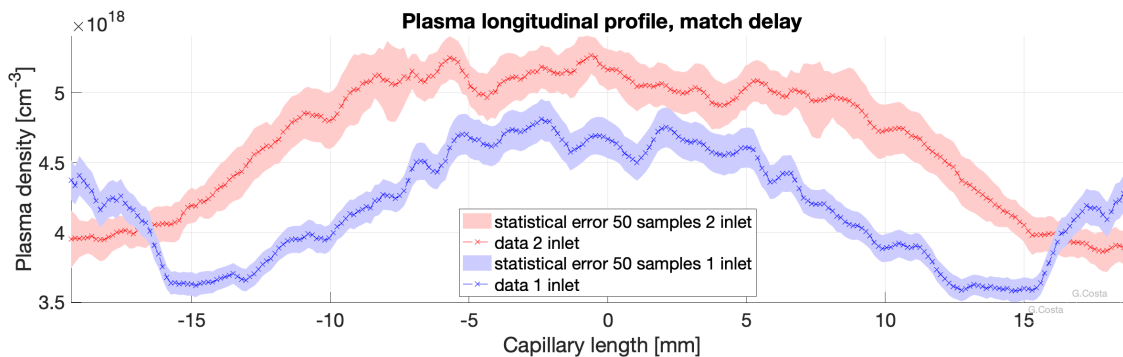


Figure 6.15. Comparison of the measured longitudinal plasma density profile for capillaries both with diameter of $500 \mu m$ and with two secondary inlet (red), 1 central inlet (blue). The gas injection and the discharge conditions are the same. Statistical analysis of 50 samples.

Fig. 6.15 shows the comparison of the longitudinal plasma profile for two capillaries with diameter $500 \mu m$ but different hydrogen distribution: in red the classical capillary with two inlets distributed at $1/3$ and $2/3$ of the total length (see Fig. 5.7), in blue a capillary with a single central inlet, already introduced in Fig. 5.41. It can be seen that the capillary with double inlet distribution has a more homogeneous distribution along the entire channel, while the capillary with single inlet distribution has a clearly higher density zone in the central part, in correspondence with the inlet. The slight difference in the density measured along the

longitudinal dimension of the capillary instead has an experimental motivation, for example an imperfect setting of the incoming pressure, or a non-optimised focusing of the plasma light on the spectrometer slit. However, this inaccuracy in no way affects the characteristics of the longitudinal trend. Fig. 6.16 shows the same comparison, but obtained using two 1 mm diameter capillaries, with one (red) and two inlets (blue). In this case, it can be said that there is no substantial difference between the plasma density profile with single and double inlet capillaries.

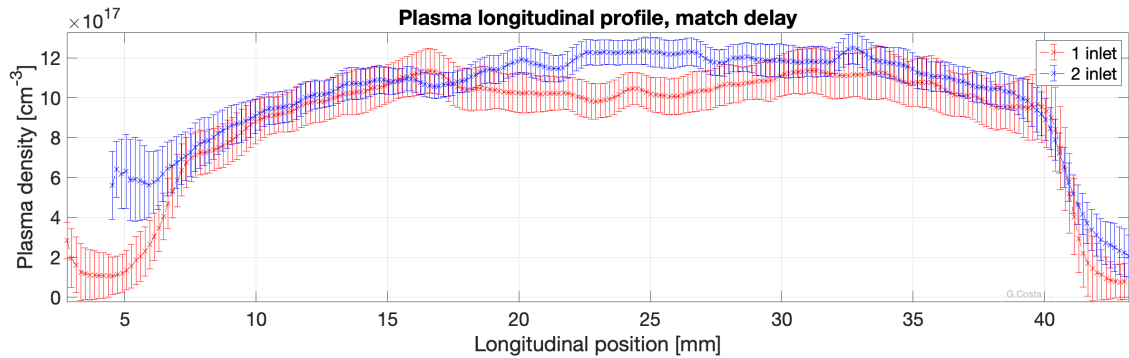


Figure 6.16. Comparison of the measured longitudinal plasma density profile for capillaries both with diameter of 1 mm and with two secondary inlets (blue), 1 central inlet (red). The gas injection and the discharge conditions are the same. Statistical analysis of 50 samples.

As previously discussed (see Section 5.3.3), investigating the distribution of neutral gas within the channel prior to discharge can be useful in establishing the distribution of secondary inlets, as well as channel dimensions. To this purpose, simulations in OpenFOAM are done to reproduce the final fluid-dynamic conditions, and thus study the velocity fields obtained as a function of geometry, which determine the final neutral gas pressure conditions inside the main channel: for example, it was observed that the influence that the distribution of the secondary inlets have on the neutral gas profile is greater as the diameter is smaller. This difference in neutral gas behaviour can explain the difference experimentally observed in the comparisons (single and double inlet) of the plasma profiles in the two cases with diameters of 0.5 mm (Fig. 6.15) and 1 mm (Fig. 6.16).

In support of this experimental evidence that the distribution of inlets has greater influence for smaller channel diameters, Fig. 6.17 shows a comparison of velocities for two simulations of capillaries with diameters 0.5 mm and 1 mm and two inlets, with the same initial pressure conditions. It can be seen that the velocity magnitude is greater in the areas below the two inlets in the 1 mm diameter case (longitudinal red, transverse magenta), than in the 0.5 mm diameter case (longitudinal blue, transverse light blue). The lower longitudinal velocity value in the middle of the capillary, in the case of the bigger diameter, leads to less head-losses and therefore to a more even distribution of the density.

In both cases of diameter considered, it can be verified that the transverse velocity has increases only at the secondary inlets, i.e. where the gas arrives: these are therefore negative peaks (see Fig. 6.17). In the rest of the capillary channel the motion is mostly longitudinal, because there is no turbulence. The longitudinal

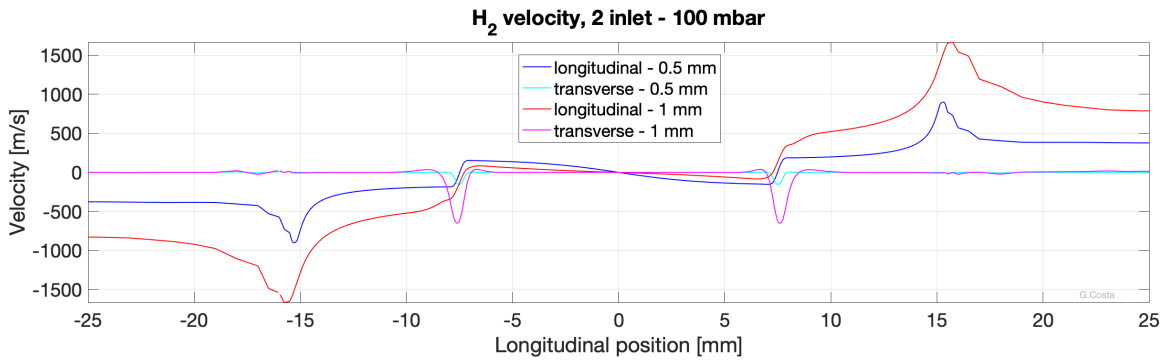


Figure 6.17. Comparison of the longitudinal and transverse gas velocity profile for capillaries both with 2 inlets, and different diameter of $500 \mu\text{m}$ (blue) and 1 mm (red). Curves from the same OpenFOAM simulations whose gas density profile was previously shown. The transverse component considered is that parallel to the central axis of the inlets.

velocities are symmetrical with respect to the centre of the channel and they change direction, therefore sign, between one side and the other of the inlets. It can also be noted that in the case of a diameter of 1 mm , the longitudinal velocity at the exit of the capillary becomes supersonic, since the speed of sound in hydrogen is 1286 m/s .

6.5 Plasma density ramps for different capillary geometries

The formation of plasma takes place at very high temperatures and pressures inside the capillary channel ($3 - 4 \text{ eV}$), compared to the initial vacuum chamber conditions ($T = 300 \text{ K} - p \approx 10^{-7} \text{ mbar}$). These different thermodynamic states between the inside and outside of the channel produce an expansion of the plasma, which results in the formation of a shock wave during gas ionisation. As a result, two plasma plumes will be produced at the ends of the capillary moving towards the vacuum. In these areas, the value of the plasma density tends to change strongly, due to the fact that the pressure that the plasma finds outside is not always the same [127]. Moreover, since the plasma in these areas is no longer confined, and is therefore free to expand in the chamber space, it has a value that is about two orders of magnitude lower than the value inside the channel. These two plumes of plasma represent a critical point for preserving the quality of a beam that exploits the energy of the plasma channel, whether it be a laser or an electron beam. For example, in the case of a laser pulse that is focused at the entrance to the capillary, it feels a relatively high density of plasma, few millimetres before the plane of focus, due to the ramp exiting the capillary entrance, and cannot be guided correctly. This is because, due to the interaction with the plasma ramp itself, the laser pulse dissipates part of its energy before focusing, transferring it to the plasma. The laser focal spot gets thus distorted and the focus plane altered. This issue is more critical more intense is the pulse. In the case of the experimental parameters seen in Chapter 5, this effect is negligible. In the case of an electron beam, on the other hand, the matching between the channel's plasma density and the electron bunches is also

crucial at the entrance and exit of the capillary, in order to preserve the quality of the beam. This becomes important, for example, in the case of passive plasma lens, a plasma capillary device that generates self-focusing of the electron beam due to the shielding process produced when the background plasma re-organises to preserve the overall neutrality. Here the presence of plasma jets arising from the end points of the capillary generates an elongation of the plasma channel in the vacuum chamber, and these jets extend the passive lens effects outside the capillary [147]. For reasons such as these, the control and optimisation of the plasma ramps over time is of fundamental importance. The characteristics of these ramps can be modified by changing the shape of the capillary itself, or more properly, the geometry of the channel [148].

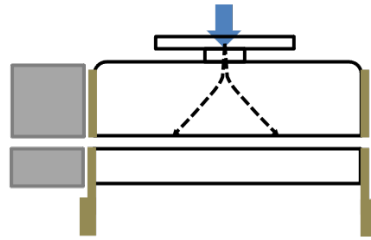


Figure 6.18. Schematic of a capillary with a straight spacer at the entrance, before the electrode. The channel of the spacer is the same size as the channel of the capillary. The blue arrow represents the gas injection direction.

For this purpose, extensions (spacers) of the capillary channel beyond the electrodes have been designed, produced and tested. An example is shown in Fig. 6.18, where there is a schematic of a traditional capillary of length 3 cm, with its gas injection flange at the top and the two electrodes at its sides. At the extremities of the capillary, after the electrodes, two 1 cm long spacers are mounted to control plasma ramps. They consist of an extension of the internal channel with the same diameter (1 mm). The length chosen for the spacers is the result of an experimental evidence showing that plasma plumes generally decay in this space for the specific capillary used and the usual initial conditions of these experimental tests [127, 148].

For capillaries of this size and length, plasma plumes outside the capillary without spacers typically extend a few millimetres and have intensities about two orders of magnitude lower than the maximum density value reached inside the same capillary [127]. For this reason, the transition between the vacuum of the interaction chamber and the plasma density inside the capillary is quite sharp. In cases where it is more useful to have a density ramp instead of such a transition, having a channel that keeps the plume of plasma density confined outside of the capillary is a possible solution.

In addition, to control the slope of the ramp, deflectors can be installed along the spacer channel to allow some of the plasma to flow in directions other than the beam propagation direction, while keeping some of the plasma confined to the main channel. Such spacer geometries have been studied and in Fig. 6.19 the CAD design of a capillary with a spacer of this type at the entrance is presented: it has a central channel with a diameter like that of the capillary channel (1 mm), and two symmetrical deflectors around the main channel.

In the Plasma_Lab laboratory of SPARC_LAB, several tests were carried out to detect the difference in density produced externally in the proximity of the capillary, along the beam line, i.e. along the main channel of the capillary. A comparison of plasma plumes density for different configurations of capillary plus spacers is shown in Fig. 6.20 In all cases the capillary used had a length of 3 cm and a diameter of 1 mm, while the spacer has a length of 1 cm.

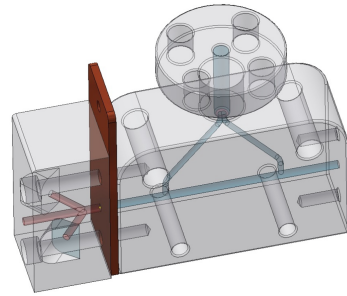


Figure 6.19. Image of the CAD file of the capillary with one of the two electrodes and a spacer with two symmetrical deflectors. The capillary has length 3 cm and channel diameter 1 mm, while the spacer has length 1 cm and size of all channels 1 mm. The thickness of the electrode is 1 mm.

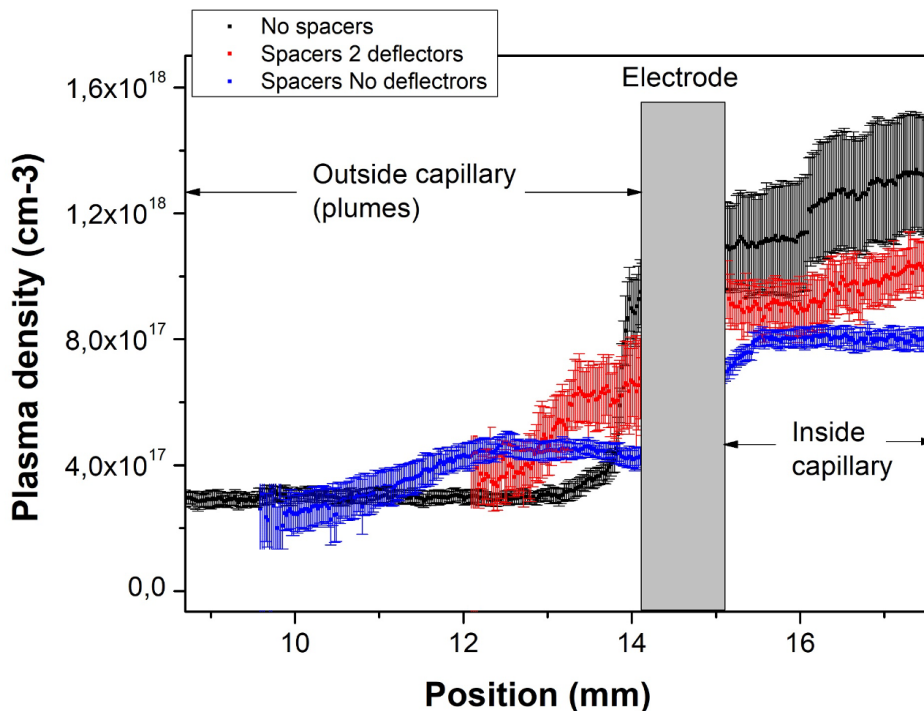


Figure 6.20. Spectroscopic measurements of plasma densities for different configurations of capillary plus spacers: capillary without spacers (black), capillary with straight spacers (blue), capillary with spacers with two symmetrical deflectors (red). Plasma density was detected only in the area of interest (end of capillary and plasma plumes), and along the main channel. The peak current used is 550 A. *Measurements made in Plasma_Lab.*

The tests carried out in this case focused on the capillary entrance area, detecting the plasma density, using the spectroscopic method already described above (5.3.3), for three different cases for which the capillary is the same (3 cm - 1 mm): in black are the data from the plasma plume of the capillary without spacers, in blue that of the capillary plus a straight spacer (see Fig. 6.18), in red that of the capillary plus a spacer with two deflectors (see Fig. 6.19). The trend concerning the density of the entire length of this specific capillary is that already shown in Fig. 6.11, while these measurements were carried out with a maximum plasma current of 500 A and a pressure of a few tens of mbar applied to the solenoid valve. What emerges from these results is in line with what was expected, i.e. with the purpose for which these extensions were designed: in the case of the absence of spacers, in fact, it can be seen that the plasma density drops rapidly, losing about 70% of the density it had inside the capillary near the electrode in about 1 mm outside the channel. It can be clearly seen that the presence of spacers changes the density of the plasma plumes along the beam line. It is therefore possible to conclude that with straight spacers (see Fig. 6.20, blue curve) about 3 times the distance from the electrode is required, compared to the case without spacers, to obtain the same decrease of the plasma density. In the case of spacers with deflectors (see Fig. 6.20, red curve), on the other hand, part of the plasma is ejected through the deflectors and this leads to a lower amount of plasma along the beam line, outside the capillary: the plasma density of the plumes seems to decrease linearly with distance, and it is no longer measurable after 2 mm from the electrode. It can also be considered that this dependence can then be controlled by the geometry of the deflectors: their starting distance from the electrode, their angle, and their size, to regulate how much plasma is expelled and at what point of the plumes.

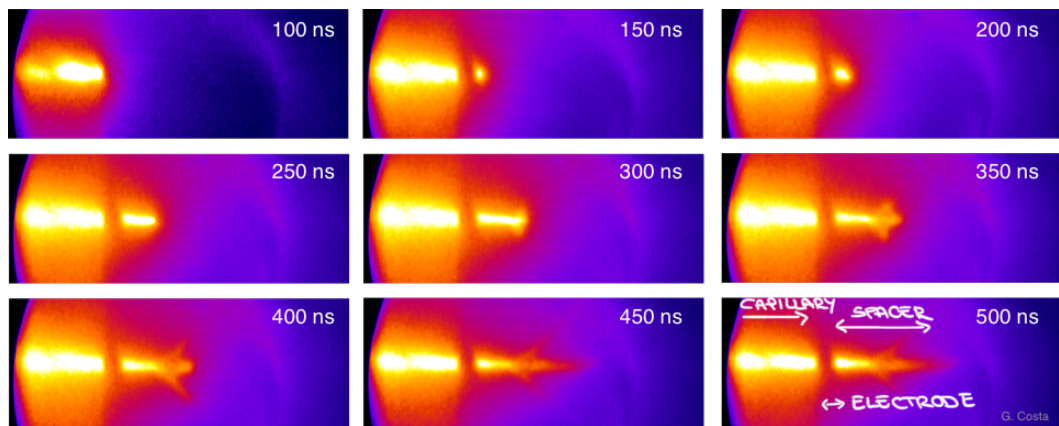


Figure 6.21. Images taken with the intensified CCD representing a temporal plasma intensity scan of the end of the capillary and a spacer with two symmetrical deflectors. The delays are from 100 ns to 500 ns from the start of the discharge, in steps of 50 ns. The dark area where there is no recombination light emission along the channel line is the electrode area, which is useful for dividing the capillary channel from the spacer channel. *Measurements made in Plasma_Lab.*

With the setup used, it is not possible to make plasma density measurements inside just the deflectors of the spacers, due to the small size of the objects and the

weak plasma intensity inside them. For this reason, in order to better visualise the contribution of the deflectors on the plasma ramps, acquisitions were made with the intensified CCD only, focusing on the final part of the capillary and the spacer with the two deflectors. A time-dependent scan is shown in Fig. 6.21: the presence of the electrode dividing the channel of the capillary (left) from that of the spacer (right) is very evident. The images shown are those relating to delays from 100 *ns* to 500 *ns* from the start of the discharge, in steps of 50 *ns*. These images describe qualitatively how the deflectors modify the plasma plumes.

It is therefore possible to conclude that the spacers produce measurable changes in the plasma plumes compared to the case of a standard capillary without spacers: these latter are therefore a tool for modulating the plasma ramps, e.g. according to the properties of the electron bunch to be accelerated.

To support these measurements of different plasma plume densities in relation to different types of spacers, simulations were carried out in OpenFOAM to study the different neutral densities and velocity trends between the main capillary channel and spacers and the deflector channel. The capillary was simulated with both the entrance and exit spacers, for the case of spacers with the deflectors. The density and the velocity along the main channel, i.e. along the beam line, are shown in Fig. 6.22, while the density and the relative velocity of the gas along the axis of one deflector are shown in Fig. 6.23. It can be seen from these curves that the plasma density within the deflector is much greater than that of the spacer channel (that is 1 *cm* from the end of the capillary) for about half of its longitudinal extent (0.5 *cm*). The same thing can be noticed by observing the velocity trend, which has a rapid decrease in the main channel of the spacers, while it undergoes a rapid increase in the first section of the deflector, reaching relevant absolute values of several hundreds of *m/s*.

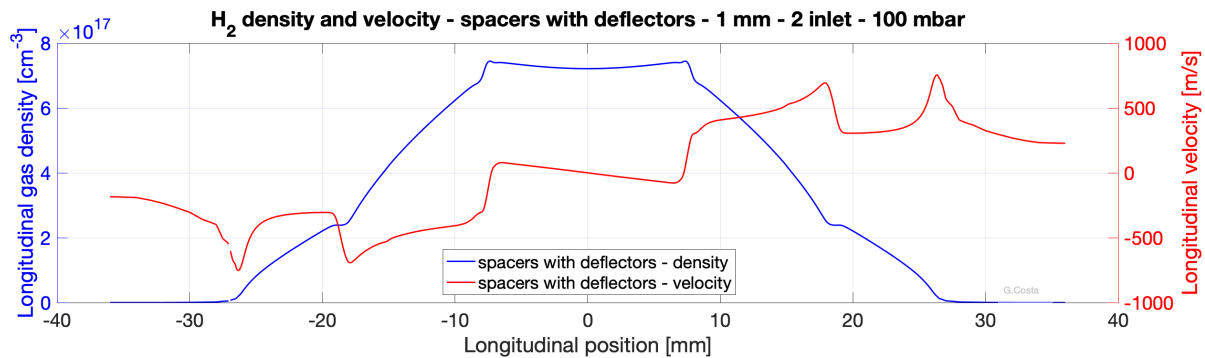


Figure 6.22. Neutral gas density and velocity along the main channel for the case of spacers with the deflectors. OpenFOAM simulations performed with the same capillary and the same initial conditions (100 *mbar*).

Regarding the longitudinal velocity inside the main channel of the spacers, (Fig. 6.22), it can be observed that, after an increase at the exit of the capillary channel, it has a rapid decrease in correspondence with the beginning of the deflector. This decrease is followed by a constant zone, which would not occur without the spacers (see Fig. 6.17). Then, at the exit of the spacers, as expected, there is a new increase of the velocity, which in this case, however, does not reach supersonic speeds, due to

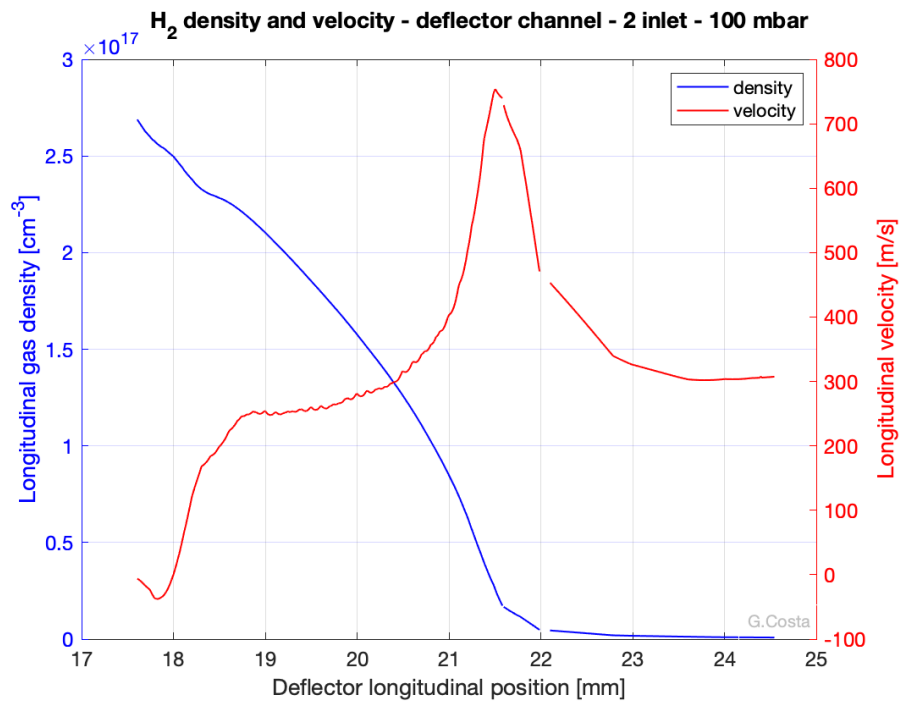


Figure 6.23. Neutral gas density and relative velocity along the axis of a deflector. The presence of gas is evident in the first half of the deflector length, beyond which the gas velocity drops significantly. OpenFOAM simulation performed with the geometry presented in Fig. 6.19.

the contribution of the deflectors.

Chapter 7

Future perspectives

This Chapter contains theoretical ideas of ongoing projects and their first experimental evidences, together with expected parameters and setups for future experiments, from the results presented so far.

7.1 Ongoing projects and their perspectives

As mentioned previously, the plasma module of a plasma-based accelerator requires accurate online diagnostics and good reliability in terms of the repeatability of the plasma generated, condition determined also by the average lifetime of the target, i.e. in this case the capillary.

Therefore, a preliminary study of interferometric diagnostic methods for the study of plasma density in capillaries is reported, together with a study of target aging. Finally, a characterisation of plasma density inside curved channels will be presented, in the context of an international project aiming at staging curved capillaries to guide different laser pulses.

7.1.1 Interferometric methods for capillary density measurements

As already discussed, one of the key parameters in a plasma-based accelerator is the plasma electron density. It is mandatory to know this characteristic along the interaction length for the purpose of optimising the acceleration process: e.g. to control the quality of the accelerated electron beam, or, as already seen, to drive the laser pulse guiding process (see Chapter 5). By means of spectroscopic techniques, plasma density can be revealed by the analysis of the broadening of self emitted lines caused by the Stark effect (see Section 5.2). These are on-line and non perturbing methods suitable for small (few mm thick or less) and low dense plasma (lower than 10^{19} cm^{-3}). On the other hand, there are targets and acceleration schemes where a density of 10^{19} cm^{-3} or more is required, e.g. for self-injection experiments. One of the most used non-perturbing method to detect the plasma density in these cases is the interferometric technique, which allows for single shot longitudinal analysis (see Chapter 4).

Interferometric methods are now also used for density measurements inside capillaries [6, 7, 149]. They have several practical advantages over spectroscopic

methods. For example, they require an easier and cheaper setup, consisting of a few optics and a CCD, which makes it more flexible and adaptable to an existing experimental setup. To these aspects it needs to be added the case in which it is necessary to have higher densities of 10^{19} cm^{-3} within a channel, for example for matching conditions with a laser beam with an extremely small focal spot (a few tens of μm). However, the curved shape of the inner walls of the capillaries is not suitable for plasma density measurement based on interferometry: for gas-filled capillaries, the dielectric structure outside the channel must also be taken into account, which can introduce optical distortions of various kinds. The implementation of Abel inversion to derive density profiles should therefore consider the phase shift due to the different surfaces crossed by the laser beam used for the interferometer, since a difference in thickness also generates a phase shift in the interference fringes. Because this condition is difficult to reconstruct, given the small size of the objects involved (hundreds of μm), capillaries with square internal cross-sections of the capillary channels have been adopted in some experiments [118, 131]. However, this choice contradicts the approximations on which the model [122] is based, which is widely used as the basis for reconstructions and simulations of plasma generated by a discharge process in a confined gas. In fact, the model assumes a cylindrical target geometry, so using channels with a square cross-section could make the plasma profile obtained different from that predicted. This discrepancy could also become even more relevant for experiments involving the guiding of a high-power laser pulse, for which the matching conditions with the transverse plasma profile are very tight (see Section 5.1).

In order to be able to use interferometric methods even with capillaries with a circular cross-section, a compensation study of the phase shift due to different material thickness as a function of the channel radius experienced by the laser was carried out using *Zemax* [150]. This is a ray-tracing software capable of simulating the propagation of light through different materials and geometries, and it also allows the definition of customised objects that can be used in its own simulation environment [151, 152]. The setup designed and simulated therefore involves optical elements coupled to the capillary used, along the line of one of the two branches of the laser used for the interferometer.

A scheme of the elements necessary to compensate the geometry of the channel walls is presented in Fig. 7.1:

- A first lens coupled with the first curved wall of the capillary (external and internal in this case) generates a telescope able to reproduce a collimated laser spot on the central plane inside the channel of the capillary;
- Similarly, the second wall (again, internal and external) of the capillary, coupled with a second lens, acts in a specular way;
- The third and final lens (which will be the one common to the two branches of the interferometer) completes the imaging of the longitudinal axis of the capillary. The system is designed to do 8x magnification.

Fig. 7.2 shows a detail of the described setup, consisting of the two capillary halves joined, between the first two lenses.

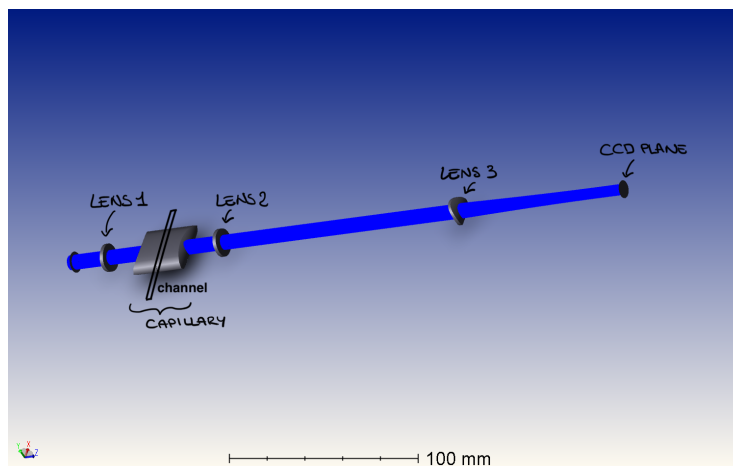


Figure 7.1. Setup made in Zemax, with the use of custom optics, to compensate for the phase shift that the internal walls of the capillary introduce, due to their curvature. It consists of three lenses in addition to the curved inner and outer surfaces of the channel.

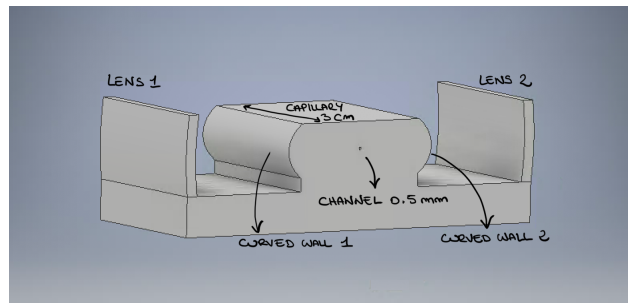


Figure 7.2. CAD file of the central part of the interferometric setup: the capillary between the first two lenses; the two halves of the capillary joined together form a channel with a diameter of 0.5 mm and a length of 3 cm.

The material chosen for making all these parts is the one already used for capillaries printed with a 3D printer (*VeroClear*, *Stratasys*): this makes it possible to quickly and inexpensively make the parts in-house, integrating the capillary channel itself within the geometry, obtaining the entire setup in a transparent plastic material. For this reason, the curvatures and distances of the elements have been optimised in Zemax according to the refractive index of this material [153,154].

Due to the material layer deposition method of the 3D printer, the printed objects do not have a sufficiently polished surface and the first tests with the laser beam showed an excessive absorption/diffusion of the pulse. For this reason, a mechanical polishing of the parts after printing was necessary. Two examples of unpolished parts compared with their polished counterparts are shown in Figs 7.3 a) and b), the first half of the capillary and the third lens, respectively.

This polishing clearly generates a variation in the thickness of the parts and, for thin parts, also a slight variation in curvature, caused by overheating. However, these variations, measured using a profile projector *Nikon V-12* with 10x magnification, were estimated to be around 2 tenths of a millimetre, and therefore considered to be

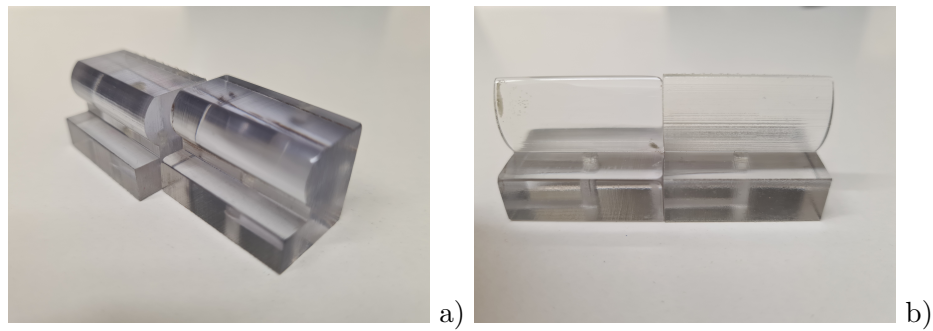


Figure 7.3. Photos of some example *VeroClear* printed components of the setup before and after polishing: a) first half of capillary, b) third lens.

negligible in the first tests on the system. Fig. 7.4 shows the differences in shape and thickness between a polished (left) and unpolished (right) part.

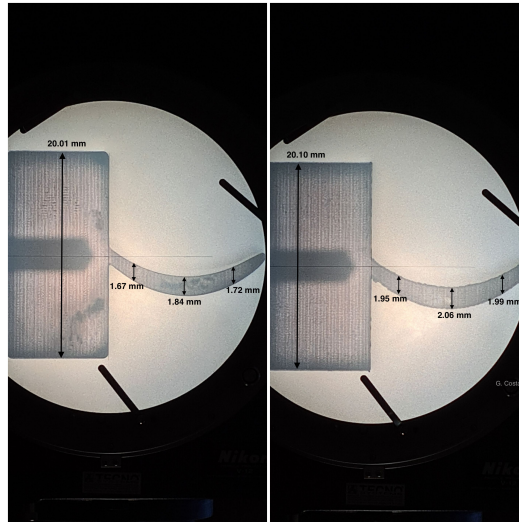


Figure 7.4. Photo of the comparison detected with the profile projector for the third lens before and after polishing. The difference in thickness is about 2 tenths of a millimetre.

From the experimental point of view, the first thing that was done was just a test of the refractive index of the material: a sample of material of known thickness was printed and tested by means of the existing Mach-Zehnder interferometer setup (already described in Section 4.3.1; see also Appendix A). In Fig. 7.5 an example of images of the inference of the recombined beams on the CCD camera is shown. The sample used in this case has a triangular shape, which is why the interference fringes in the images have a different shape depending on whether they are on one side or the other of the diagonal created by the sample. The latter is located on the right-hand side of the images, while on the left-hand side there are no obstacles other than air on that arm of the Mach-Zehnder. In Fig. 7.5 a) the delay between the reference arm of the interferometer and the one passing through the point of interest (air plus sample) is set, by means of the appropriate delay line, in order to focus the interference fringes in air between the two branches of the Mach-Zehnder.

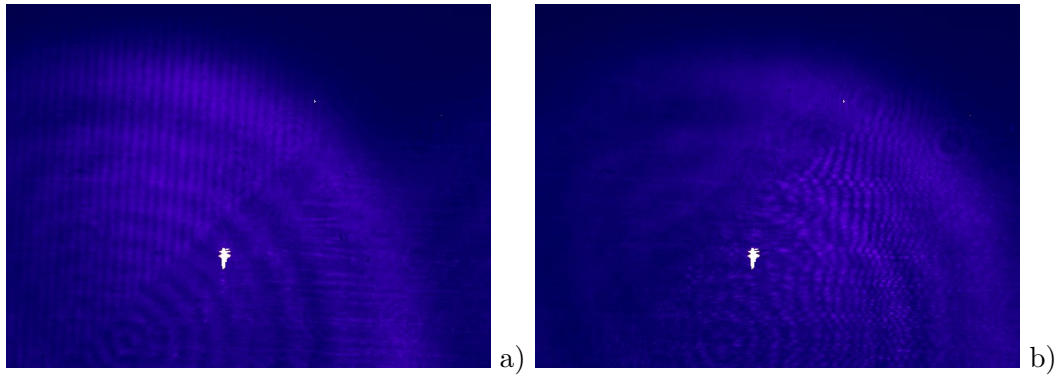


Figure 7.5. Interference fringes generated in air a) and in the *VeroClear* sample b), focused by varying the delay line between the two interferometer arms.

Conversely, in Fig. 7.5 b) the delay line was moved to focus on the interference fringes due to the presence of the sample. The difference in optical Δl path between these two configurations (i.e. the delay line shift) is proportionally related to the difference in refractive index of air and sample Δn :

$$\Delta l = d\Delta n = d(n_{\text{sample}} - n_{\text{air}}), \quad (7.1)$$

where d is the thickness of the sample through which the laser beam passes, approximately 2 mm . As the delay line is motorised, it can be concluded that, since $\Delta l = 1 \text{ mm}$ and $n_{\text{air}} \simeq 1$, $n_{\text{sample}} \approx 1.5$. The result obtained is in accordance with what was found in the literature: *VeroClear* refractive index about equal to 1.5 for $\lambda = 800 \text{ nm}$ [153, 154].

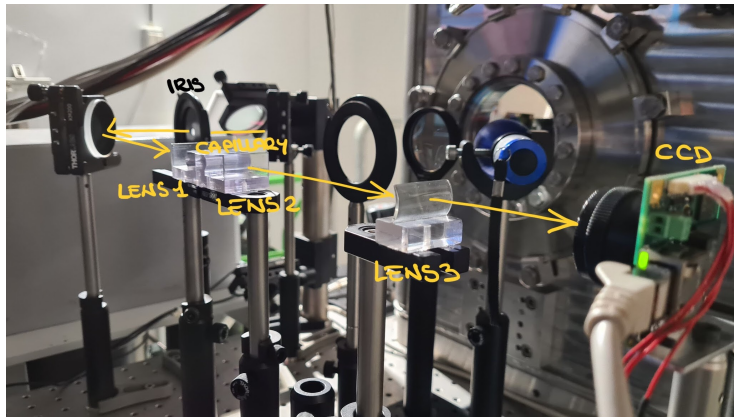


Figure 7.6. Installed experimental setup to compensate for the phase shift that the internal walls of the capillary introduce, due to their curvature. The yellow path represents the laser line; the two halves of the capillary are assembled together and the CCD is positioned in the final configuration, i.e. on the image plane.

The setup used to compensate for the interference fringe shift due to the curvature of the inner walls of the capillary is shown in Fig. 7.6. The existing Flame probe beam line was used for the test, from which a portion was split for this purpose. The initial collimated beam size simulated and experimentally reproduced by means of

an iris is 7.5 mm (diameter): Fig. 7.7 shows an image of the initial beam conditions on Zemax (a)) and the real beam detected by a CCD in the final plane (b)); the available beam is slightly larger than the CCD chip.

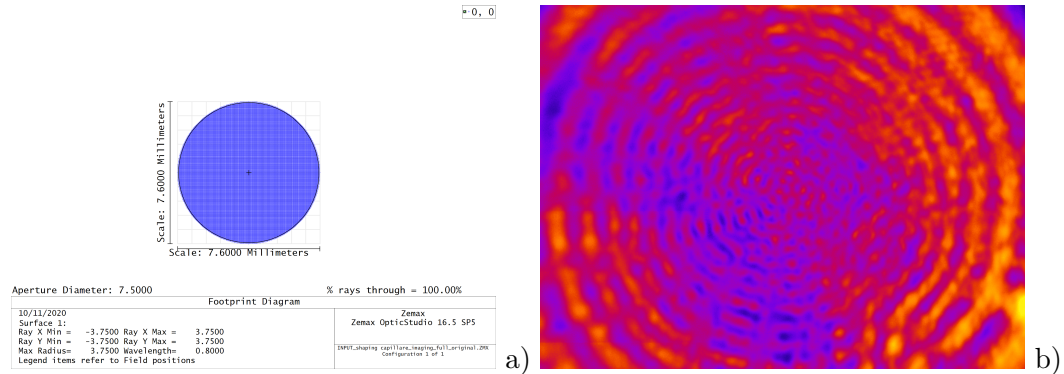


Figure 7.7. Beam initial conditions: a) simulated, b) experimental. The beam size is larger than the CCD chip size. The beam has a diameter of 7.5 mm .

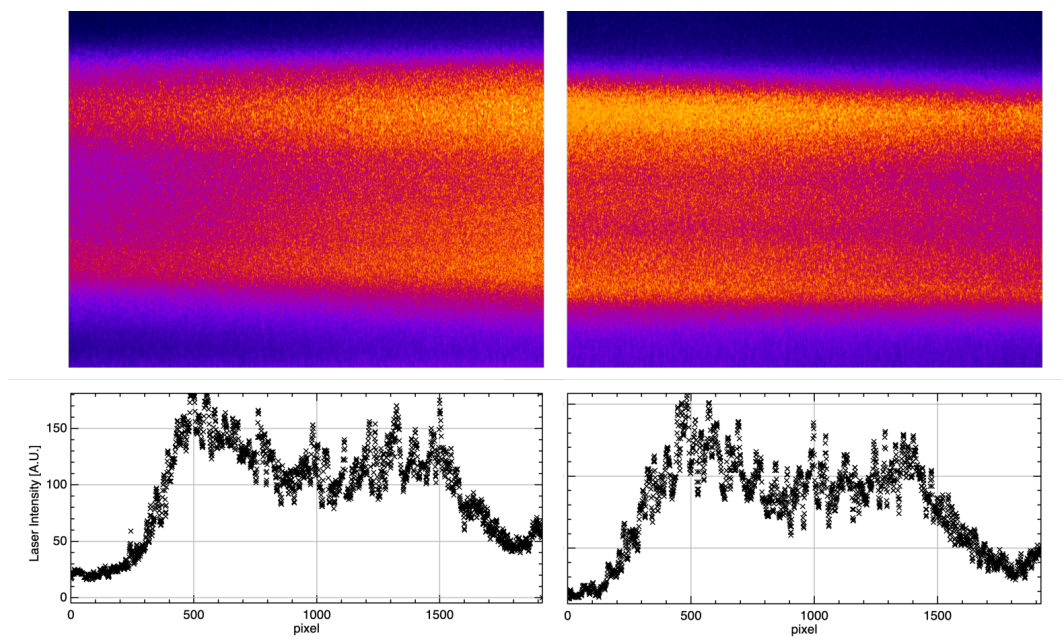


Figure 7.8. Images of the output beam at a distance of 4.5 cm from the second lens (up), and relative vertical profiles (down).

The focus produced in the centre of the capillary channel was tested qualitatively using thermal paper: an intense strip of approximately 8 mm in length was observed, while the total length of the channel was the standard 3 cm . The portions of the beam that do not overlap the size of the capillary channel are diffused into the plastic. For this reason, the system could be implemented with optical components capable of creating a beam already of cylindrical dimensions from the initial one, so that no energy is lost. At a distance of 4.5 cm from the second lens, the beam behaviour was detected using a CCD. As the obtained beam strip is horizontally

larger than the chip, two images are presented in Fig. 7.8, to verify its size and symmetry. The beam here should have both vertically and horizontally the same size as the starting beam, as obtained on the corresponding plane of the simulation in Fig. 7.9 a). However, experimentally a vertically flattened beam is obtained also after the capillary system plus the first two lenses. Other simulations were then carried out with the same geometry, but with small variations in the curvature of the lenses and/or distances between the optics, in order to reproduce, for example, the variations undergone by the lenses following their polishing. Fig. 7.9 b) shows, for example, the result on the same plane by varying only the curvature of the first lens by about 5%. The vertical beam size obtained experimentally is approximately 3.3 mm for both the horizontal halves of the beam, while the horizontal beam size found is approximately 8 mm . The example simulation with the corrected curvature tends to reproduce the shape of the experimental beam, although its vertical extent is about 4.4 mm .

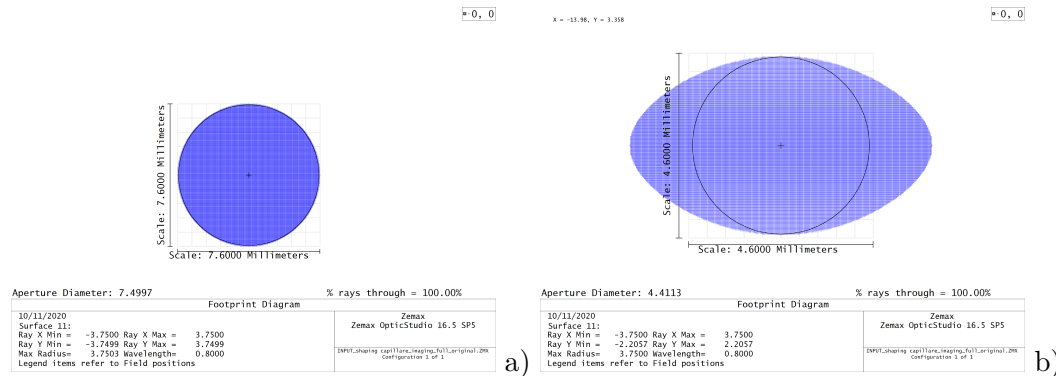


Figure 7.9. Simulated beam obtained at a distance of 4.5 cm from the second lens with the original setup a); beam in the same plane after the second lens, but varying the curvature of the first lens by about 5% b).

However, this discrepancy does not seem to have a major effect on the final result of the system: the imaging obtained on the CCD plane at a distance of about 100 mm from the third lens is shown in Figs. 7.10 a) (experimental) and 7.10 b) (Zemax); the dimensions of the measured beam are comparable both horizontally, 8 mm , and vertically, 1.54 mm , with the simulated beam, $7.5\text{ mm} \times 1.56\text{ mm}$.

It can finally be concluded that the differences in size obtained in the horizontal plane are probably due to reflections within the capillary channel, which are then carried to the final plane. The differences in vertical dimensions after the second lens, on the other hand, are probably due to the geometrical differences between the ideal and the realised setup: these could be substantially reduced by constructing the lenses in a non-plastic material, which does not require invasive post-production processing. On the other hand, as regards the internal distribution of the beam after the second lens (see Fig. 7.8), it can be seen that this seems to reproduce the internal geometry of the capillary channel, having a central emptying zone. However, as this is an unexpected phenomenon, new simulations and tests will have to be carried out to investigate this aspect.

The attenuation in intensity that the laser beam undergoes in this case, due to

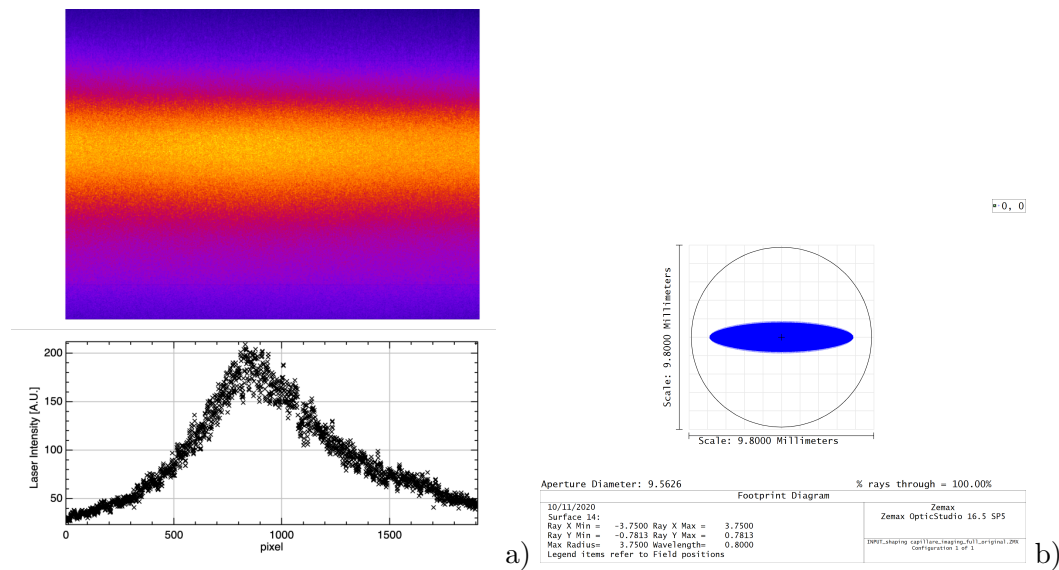


Figure 7.10. Final image plane: a) experimental beam with horizontal dimensions larger than the chip and vertical of about 1.5 mm (up), vertical profile (down), b) simulated beam in Zemax of dimensions 7.5 mm \times 1.56 mm.

passing through a considerable total thickness of plastic, must also be calculated and compensated for on the reference arm of the spectrometer, so that the two recombined beams have a comparable intensity. With this method it is theoretically also possible to measure the density of the neutral gas. The first tests of this type will be carried out over the next few months, using nitrogen, which has a higher refractive index than hydrogen, and therefore a significantly greater phase shift [155].

7.1.2 Capillary aging and new geometry designs

The discharge normally used to generate the hydrogen plasma in a plastic capillary [144], with a sub-millimetre channel diameter, eventually impacts on the geometry of the capillary channel itself. A typical discharge used at SPARC_LAB is generated by applying a voltage of up to 20 kV to the capillary electrodes, and can reach typical current peaks of about 500 A (see Fig. 6.6). Due to the material of which the capillaries are made of, ablation processes of the channel walls can be observed as a result of the discharge process itself. The production method chosen for the capillaries, which makes use of the 3D printing process, is useful for obtaining the desired capillary shape with a high spatial resolution: this makes it possible to meet the particular requirements of the experiment, as well as the possibility of studying differences in plasma trends resulting from the geometry of the channel. Furthermore, since capillaries can be printed with transparent plastic, they are particularly suitable for plasma diagnostics, spectroscopic or interferometric analysis (as already addressed in the course of this Chapter), commonly used for plasma density measurements.

Although, due to the energy exchange on the walls, the plasma in the centre of the capillary is heated more than at the edges of the channel, i.e. the discharge current passes mainly through the central part of the channel reducing the ablation

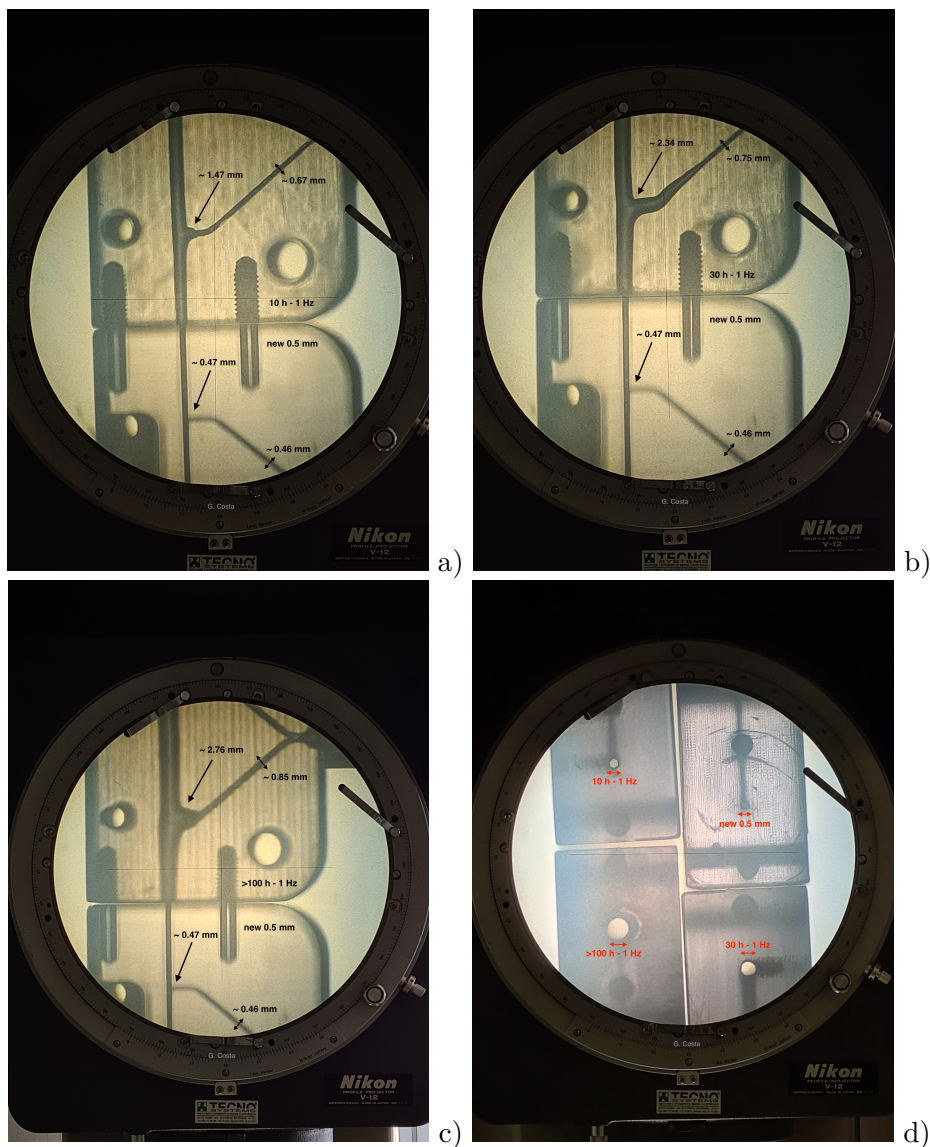


Figure 7.11. Comparison of used (up) versus new (down) capillary channel sizes for a) 10 hours use, b) 30 hours use, c) more than 100 hours use respectively. d) Comparison of the face exposed to the electrode from which the discharge starts for the same four pieces: new, used 10, 30 and more than 100 hours, from right to left and from top to bottom. Images obtained using a *Nikon V-12* profile projector.

of the walls, this must be taken into account when estimating the average life that these objects can have. The high temperature of the plasma, which therefore heats the capillary surface and alters the shape of the channel, also alters the optical properties of the capillary. In fact, there is a progressive decrease in the average value of the plasma density inside the channel linked to the wear of the object: the diameter of the channel increases and, under the same initial conditions of gas and discharge, the plasma density decreases (see Section 6.3). These effects of capillary ablation on plasma density, observed by looking at the average change in density

after thousands of shots [156], are confirmed by direct observation of the change in channel geometry.

The Figs. 7.11 a), b) and c) show three comparisons of measurements of capillary channels before and after use: these are capillaries of 3 cm length and 0.5 mm diameter. In these images we have at the bottom the measurement of a new capillary, and at the top the measurement of an identical capillary after use: in order of appearance these are approximately 10, 30 and more than 100 hours of operation at a frequency of 1 Hz so, respectively, approximately 36000, 108000 and more than 360000 shots. These measurements were carried out with the previously mentioned *Nikon V-12* profile projector, which is capable of returning 10x magnification of the internal capillary channels. It is easy to see how increasing the time of use increases the consumption of the part, and therefore the diameter of the channel. Ablation affects the channel quite uniformly, even though it is greater in the areas below the inlets: this is probably due to the intrinsic geometry of the inlets, which also favours a greater density of neutral gas in these areas (see Fig. 6.11).

Fig. 7.11 d) shows a comparison of the face exposed to the electrode from which the discharge starts, among all the capillaries considered: new, used 10, 30 and over 100 hours. It can be concluded that already after 10 hours of use at 1 Hz with a voltage of 20 kV applied to the electrodes, the channel has more than doubled its diameter, while, for a time of use of more than 100 hours, this value has almost quadrupled. Fig. 7.12 shows the differences in diameter measured in the different cases, as a function of the longitudinal position of the channel. In addition, it is possible to observe the already known tendency of channels with a larger diameter (1 mm or more) to be less affected by the phenomenon of wall ablation [156], a characteristic which obviously makes them reliable for a longer working time. It should be noted that measurements made using this method, exploiting the operation of a projector, are subject to a systematic error that tends to overestimate the size of the channel, due to the stratification of the material. The error committed in the case under consideration was estimated to be a few hundredths of a mm, and therefore negligible compared to the diameter variation observed. It has also been verified that the discharge alone is responsible for the observed ablation process, as the same measurements carried out with and without the presence of a laser pulse such as that used for the guiding tests (see Chapter 5), led to comparable results. In the case of guiding of a high power pulse (hundreds of TW), however, this aspect should be reconsidered.

This process of ablation of the inner walls of the capillary does not seem to be crucial for the quality of the plasma generated: for example, the spectroscopic measurements do not detect the emission lines of the plastic material, and the agreement of the plasma density results with the theoretical model indicates that there is no substantial change in the molecular composition of the plasma. However, since with the variation of the diameter of the channel also vary, as seen, the mean value and the trend of the plasma density, the ablation of the walls requires frequent capillary replacements, in order to guarantee the required target conditions for the experiment. Since the total average time for replacing a capillary is about half a day, a way of limiting the ablative process is essential for experiments with capillaries of less than one millimetre in diameter.

One possible solution is to use a stronger material for the main channel of the

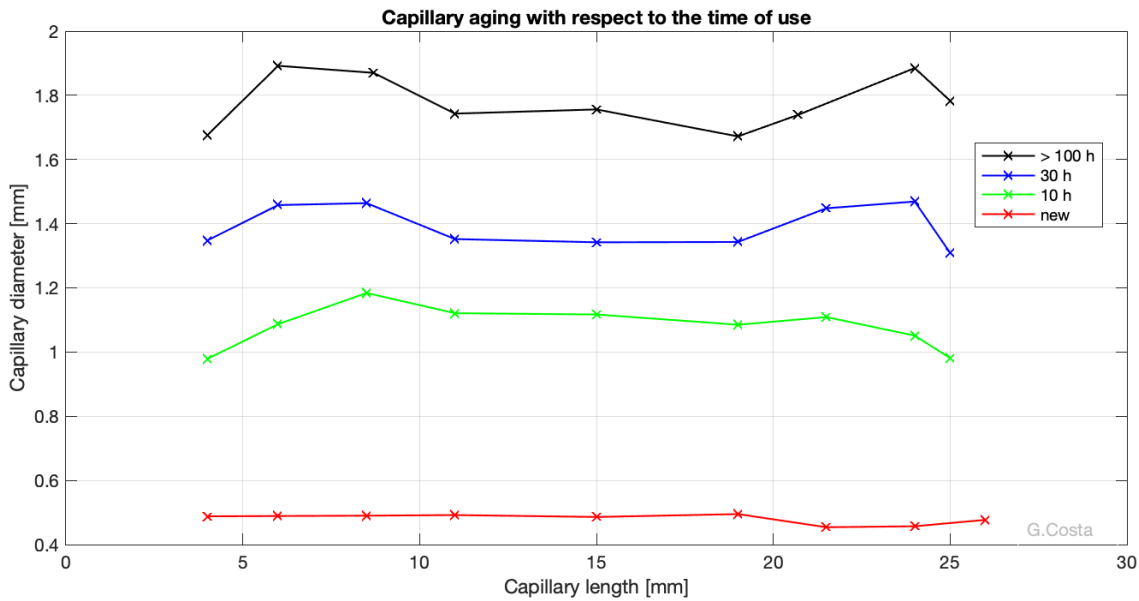


Figure 7.12. Trend in channel diameter as a function of longitudinal position, for different levels of capillary wear.

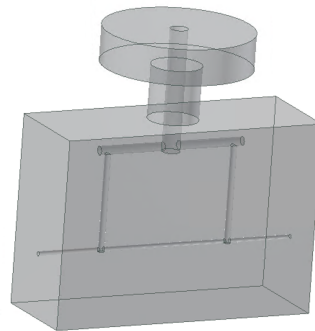


Figure 7.13. Example of a prototype of a new capillary model composed of two parts, able to facilitate the cleaning of the internal channels after printing, and in which it will be possible to install a sapphire tube along the line of the main channel of the capillary, to slow down the consumption of the internal walls due to ablation caused by the discharge.

capillary, so for example inserting sapphire tubes inside an already 3D printed capillary geometry. A prototype of this kind is already in progress (see Fig. 7.13): the capillary consists of two separately 3D printed pieces, which are then assembled together. The shape of the inlets has been modified so that they can be cleaned easily after printing: there is a channel that acts as a collector, the ends of which are closed during assembly, two straight inlets and a central channel that will then be shaped to accommodate a sapphire tube of the chosen diameter.

7.1.3 Curved capillary channel

The study and the experimentation of plasma generation within curved capillaries has become widespread in recent years, for various purposes within plasma-based accelerators [157, 158]. The ongoing intercontinental project CAMEL (Compact Accelerator Multistaged with Electrons and Lasers), in which the SPARC_LAB and Hebrew University of Jerusalem laboratories are participating, mainly deals with the process of driving in curved channels as a method to achieve the external injection configuration of plasma acceleration (see Section 2.1). The scheme proposed in this project aims to design and experimentally test a curved multistage plasma channel into which a high-brightness electron beam from the conventional accelerator can be injected in order to further accelerate these electron bunches using high-intensity laser system to generate the accelerating field. The project therefore provides for acceleration staging, which will be achieved by using additional stages following the initial acceleration stage. This means that electrons will be injected into consecutive acceleration stages which will be pumped by different lasers of modest energy (several hundreds of mJ). The coupling of the laser energies in the different stages will exploit the process of guiding within curved channels, conveyed into a single straight main channel along the line of the electron beam to be accelerated (see Fig. 7.14). This mechanism has the advantage of simplifying the feeding of the accelerating structure, as well as of reducing the distance between adjacent acceleration stages.

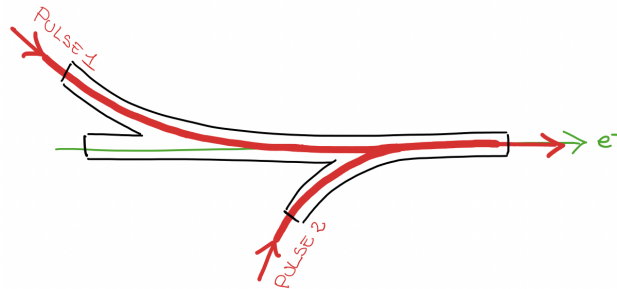


Figure 7.14. Schematic representation of the compact staging idea of the CAMEL project: several laser pulses (two shown) are conveyed and guided within curved plasma channels into a main straight channel, which can be used for electron beam acceleration.

The process of guiding a laser pulse within curved channels is therefore a fundamental building block of this experiment: obtaining the proper plasma density profile capable of reducing the energy losses of the laser beam, while maintaining its initial spatial profile is in this case of fundamental importance for the wakefield acceleration.

In the context of this project, various prototypes of curved capillaries were designed and realised. The final design chosen is shown in Fig. 7.15. The capillary has a length of 6 cm , and a channel with a diameter of 500 μm , which is split into two channels, both with a diameter of 500 μm , starting from the centre of the structure: one channel continues straight, the other is curved towards the opposite side of the previous one, with an angle of curvature approximately equal to 55 mm . This radius of curvature was chosen in order to maximise the separation between the two channels, within approximately the dimensions of a classic capillary used in

laboratory, so that the same holders and diagnostic tools could be used.

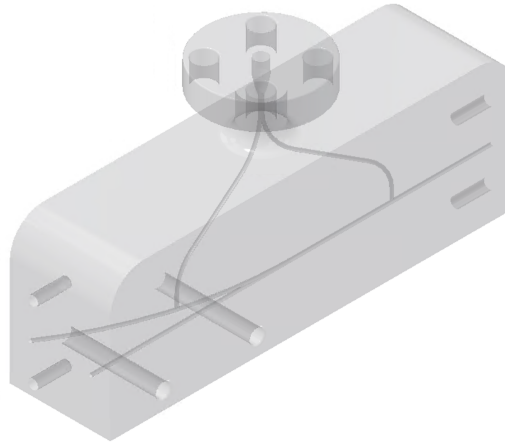


Figure 7.15. Image of the CAD file of the 6 cm long capillary, with a straight channel section that splits into two channels at the center of the capillary: one continues straight, the other has a radius of curvature of about 55 mm. The gas injection has two secondary inlets with smoothed curvatures to facilitate gas production and flow. The diameter of all channels is 500 μm .

Since the guiding process has to take place inside the curved-straight channel (left-right in Fig. 7.15), a special injection system was designed: it is once again via two secondary inlets of the same diameter as the channel, located at 1/3 and 2/3 of the length of the capillary: as can be seen in Fig. 7.15, the former feeds into the curved channel, while the latter feeds into the common channel. This chosen injection geometry is designed to allow the gas to be distributed as far as possible within the curved-common channel, just as the two electrodes used are designed to cover only the holes in this channel. This ensures that the discharge generated by the circuit used develops preferentially within the curved-straight channel, so within the one into which the pulse must be guided. The straight one, on the other hand, being the one predisposed for the electron line, does not need to be filled with plasma in its entirety: the electrons can enter the straight section of the channel without plasma, and then reach the accelerating field generated by the laser pulse in the plasma, in the second half of the capillary.

To demonstrate the operation of this gas injection system, an OpenFOAM simulation was carried out, whose results are shown in Fig. 7.16. The pressure conditions at the main inlet are those usually used, as well as the general initial conditions. The two secondary inlets have smoother bending radii, to facilitate the gas flow, as well as the production and cleaning of the conduits: this generates a maximum neutral gas density quite high and comparable to that obtained in a standard 3 cm long and 500 μm diameter capillary (see Fig. 6.5), although the configuration in point has a central channel twice as long. The blue curve in Fig. 7.16 represents the neutral gas density in the whole straight channel, from left (common section) to right. The red curve represents the density within the curved channel half. It can be seen that the two peaks below the inlets reach the same maximum value, while the uncommon half of the straight channel is practically empty. The area

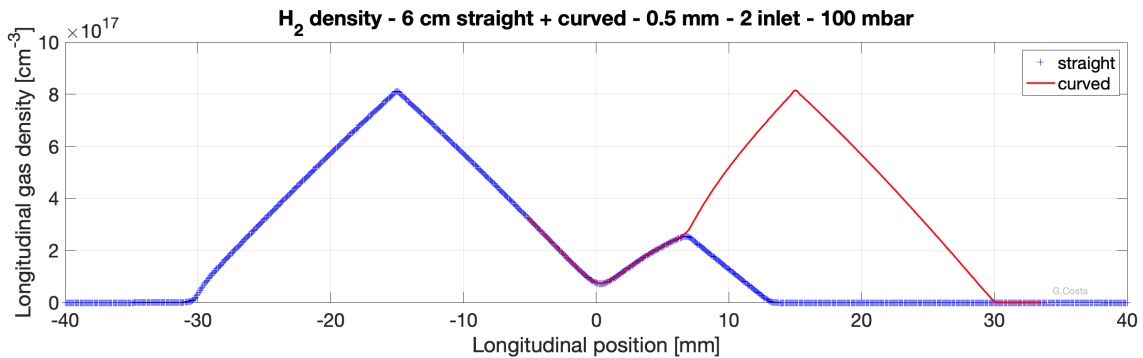


Figure 7.16. Longitudinal profiles of neutral gas density within the capillary in Fig. 7.15. In blue is the profile of the entire straight channel (on the left is the common side), in red is the profile inside the curved channel. Results coming from a OpenFOAM simulation with a pressure applied on the main inlet of 100 *mbar*.

around the centre of the capillary of the red curve shows a slight deformation due to the fact that the plotted curved profile is the intersection between the circumference that describes the curvature of the channel and the central plane of the capillary, inside the channel.

With this type of geometry, and with a proper holder on the Hexapod, discharge tests were performed in the curved channel, using the discharge circuit already described in Section 5.3.3. The discharge curve from the equivalent circuit (discharge circuit and capillary) is shown in Fig. 7.17: despite the different capillary geometry used and the different length of the channel, it can be observed that the discharge curve is well defined and stable. The triggers for the gas injection and discharge process were doubled, in order to obtain a clean discharge within the channel: a solenoid valve opening gate of 2 *ms* was therefore used. These increases were found experimentally, but they were already predicted by the neutral gas simulation carried out, which showed the need of a double time interval (compared to a channel with the same diameter but 3 *cm* length), to reach a condition of fluid-dynamic equilibrium.

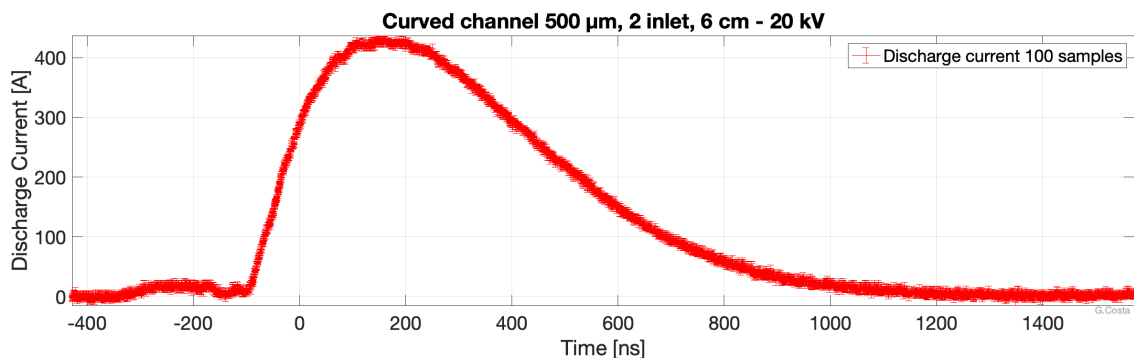


Figure 7.17. Average profile with statistical error of the discharge curve from the equivalent circuit of discharge plus capillary. Data are averaged over 100 acquisitions.

The discharge carried out can be seen in a photo in Fig. 7.18, where the plasma in the curved-straight channel is clearly visible, not in the remaining straight section

on the left. In the photo there is also the reflection of the channel containing the plasma on the support plane of the capillary holder, as well as an evident plasma plume coming out of the common straight channel, which is however also present at the exit of the curved channel.

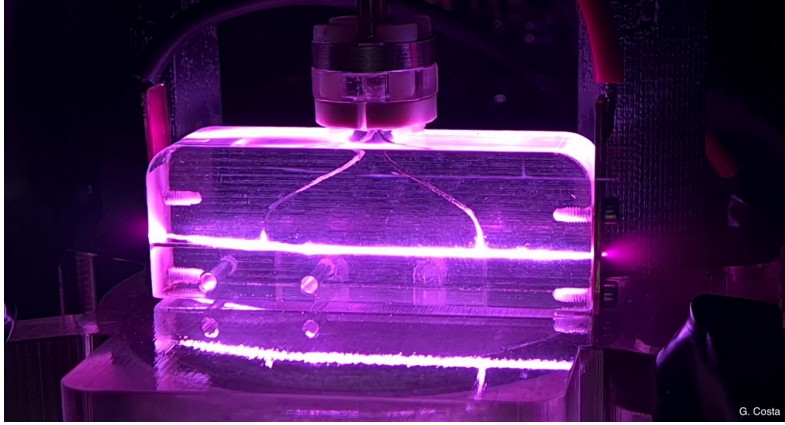


Figure 7.18. Photo of the discharge generated inside the curved channel with $500\ \mu\text{m}$ diameter in the $6\ \text{cm}$ long capillary. No plasma is present in the uncommon straight channel. At the bottom there is the reflection of the channel containing the plasma on the support plane of the capillary holder. Plasma plumes are present in entrance and exit from the curved-straight channel. The typical colour of the light emitted by pure hydrogen plasma (purple) is caused by the stronger lines emitted in the visible range, which are in the red (Balmer alpha line) and in the blue (Balmer beta) spectrum.

Longitudinal plasma density measurements were also carried out for this capillary, using the spectroscopic method (see Section 5.2), by means of the setup already described in the previous Section 5.3.3. An average longitudinal profile of plasma density within the curved channel is shown in Fig. 7.19. It can be observed that, although the above-mentioned neutral gas distribution had two density peaks below the inlets and a depression in the central area of the channel, the generated plasma is uniform in the area of interest of the channel, where there is an average plasma density of about $2.5 \times 10^{18}\ \text{cm}^{-3}$. Since the Balmer α emission line was used for these measurements, it is observed that the average plasma value reached is about a factor of two lower than that reached in a capillary with $500\ \mu\text{m}$ diameter and $3\ \text{cm}$ length (Fig. 6.11). Although these two cases considered have the same pressure conditions and reach the same values of maximum neutral gas density within the channel, in the case of the $6\ \text{cm}$ curved capillary channel, the distribution of neutral gas is less uniform along the length, therefore, since the discharge obviously acts also as a homogeniser, the average plasma density is lower.

As previously expressed, the initial pressure value applied on the main inlet in these OpenFOAM simulations is the reference one of $100\ \text{mbar}$, therefore a few hundred mbar lower than the one usually used experimentally. For this reason and in this case, the neutral gas density results obtained are used to predict the gas trend, the relative difference in pressure reached between different cases, as well as the relative difference in time used to fill the channels. Therefore the absolute values of neutral gas density achieved are instead not comparable with the experimental

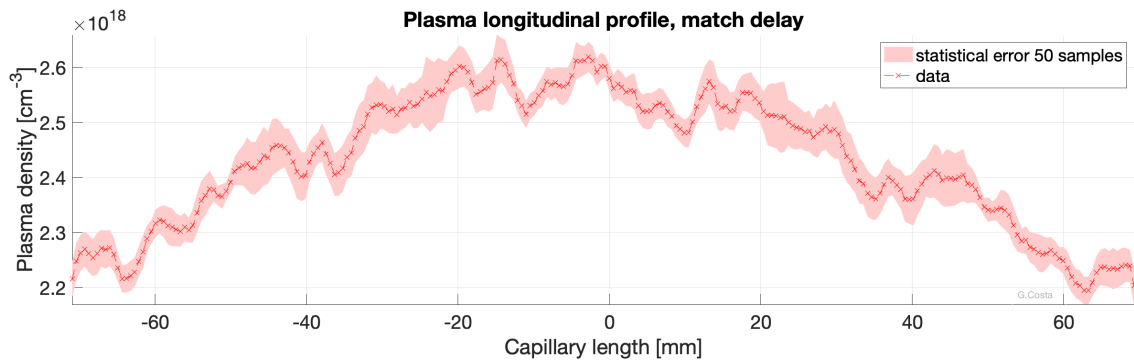


Figure 7.19. Statistical analysis of the longitudinal plasma profile of the 6 cm long curved capillary channel. Data averaged over 50 acquisitions, selected delay with respect to discharge start equal to 300 ns.

ones, net of the ionisation level.

This study of the guiding process within a curved channel also has another purpose, in addition to that outlined in the CAMEL project: i.e. the removal of a laser beam after its interaction with the plasma. This would allow for efficient and controlled pulse removal, for example keeping the electron beam line completely free of laser radiation, which would interfere with the particle diagnostics.

7.2 Future developments

The results of pulse guiding through plasma-filled capillary discharge and presented in Chapter 5 were obtained using a low power beam (see Table 5.3). However, laser-pulse plasma acceleration schemes require a high-power laser pulse (see Section 2.1). For this reason, starting from the goals achieved so far, an experimental setup is being designed for similar guiding tests using Flame’s high-power pulse (see Tab. 3.2). These high-power guiding tests are intended to prepare for the EXIN external injection experiment planned at SPARC_LAB (see Section 3.2.1).

In order to perform high-power guiding tests in the experimental bunker area of the FLAME laboratory, a new interaction chamber capable of hosting this new experiment has been designed and installed (see Fig. 7.20).

The line developed regarding beam transport and focusing before and after interaction point with the plasma is shown in Fig. 7.21: the high-power pulse from the compressor is transported into the new interaction chamber and focused by means of an off-axis parabola with focal length $f = 1\text{ m}$. In the interaction point the hexapod will be positioned together with the capillary, which will have its input plane on the plane of the pulse focus, as in the setup presented in Section 5.3.3. After the point of interaction, i.e. at the exit of the capillary, similarly to the low-power pulse guiding, an imaging system reproduces the laser spot at the exit of the capillary (right-hand line in Fig. 7.21). Also in this case a time-of-arrival detector of the laser with respect to the discharge will be placed on this line, necessary to synchronise the two. A safe energy threshold was verified via Zemax on the first window $W1$, preceding the dump.

The right-hand line after the interaction in Fig. 7.21), will instead be set up to

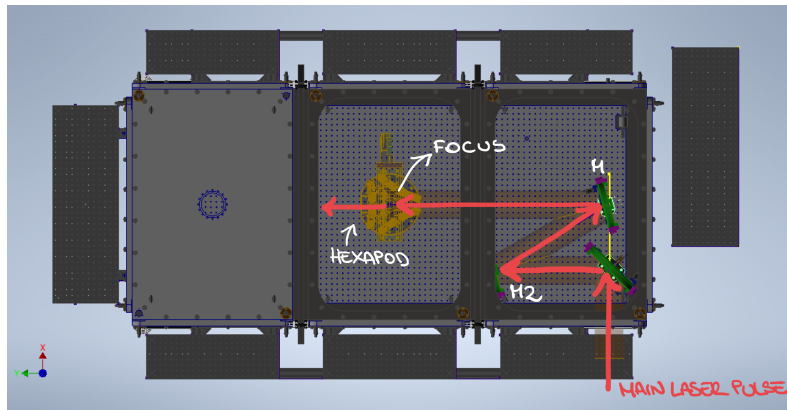


Figure 7.20. CAD drawing of the new interaction chamber for guiding high-power laser pulses, already installed in the Flame bunker. It has dimensions of approximately $2.3\text{ m} \times 1\text{ m}$.

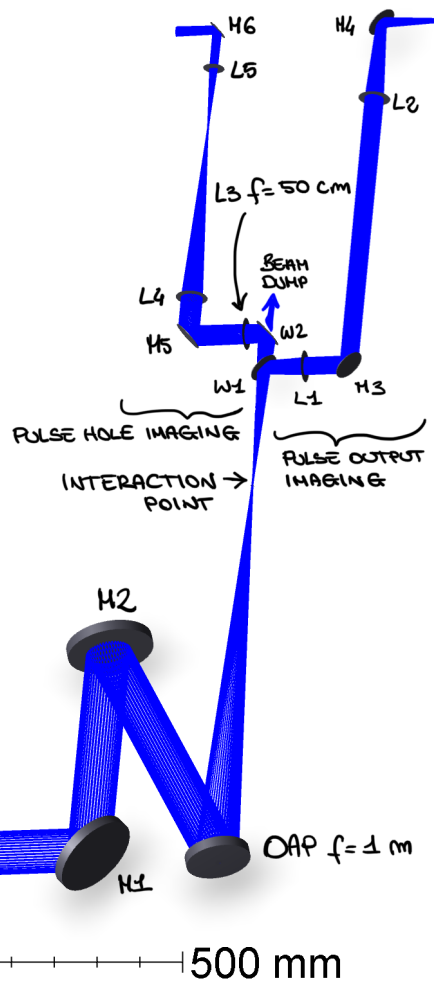


Figure 7.21. Zemax simulation of the transport and focusing of the main laser pulse, before and after the point of interaction with the plasma. After focusing there are two beam imaging systems: capillary exit plane (right), $L3$ plane to reproduce the pierced beam (left).

make an imaging of the beam that is pierced before focusing: the beam is captured with the first lens $L3$ of focal length equal to half of the one of the parabola, then through the lenses $L4$ and $L5$ an imaging of the plane of the lens $L3$ is made. The aim is to verify if the information of the pierced beam is transported after focusing also upstream of its controlled passage through the plasma, i.e. driving the pulse. This technique could be used to remove the central part of the laser pulse after interaction with the plasma. This could then be an alternative method to remove the laser beam in experiments in combination with collinear electron beams with the laser line: this would preserve the quality of the bunch and not alter the diagnostics of the electron beam.

The high-power pulse guiding experiment, using the described setup, has therefore the twofold purpose of testing not only the guiding process itself, but also the possible laser beam removal methods. Being able to control these techniques with the FLAME main laser is essential in preparation for the external injection project planned at SPARC_LAB in the near future, EXIN (see Section 3.2.1). More in detail, the latter concerns the possibility of reproducing a linear plasma wave regime, with a normalised laser intensity $a_0 \simeq 1$, in order to achieve strong fields, while preserving the stability of the process. In this scheme, the wakefield will be created by the ultra-short high-power FLAME laser pulse, propagating in a hydrogen gas-filled capillary discharge, such as those already described in Chapters 5 and 6. This wakefield will be used to accelerate the electron bunches produced by the SPARC photo-injector. The goal of this experiment is to demonstrate that a high-brightness electron beam can be accelerated by a plasma wave without any significant degradation of its quality.

Fig. 7.22 shows the schematic of the experimental line for the EXIN project: specifically, as far as the laser beam is concerned, the transport line from the FLAME bunker to the injection chamber is highlighted, containing a parabola with focal length $f = 3\text{ m}$, and the interaction chamber containing the hexapod positioned in the centre. The electron beam crosses the mirror for the laser entering the interaction chamber through a small hole (about 1 cm) in the mirror itself.

The parameters required for the laser pulse and the plasma density are summarised in Tab. 7.1.

Table 7.1. FLAME laser parameters for the EXIN project.

Normalised Intensity a_0	~ 1
FW $1/e^2$ @ focus	$50 - 70\ \mu\text{m}$
Temporal length	$35 - 40\ \text{fs}$
Plasma density	$1 - 2 \times 10^{17}\ \text{cm}^{-3}$

To match such a small laser pulse in the focus to the plasma guide, plasma densities of at least an order of magnitude higher are required, in order to use a channel with a diameter of a few hundreds of μm (see Eq. 5.4). For this reason, the possibility of an ns -duration laser heater will be evaluated, to increase the depth of the hollow channel needed to drive the pulse (as described in Section 5.1.4).

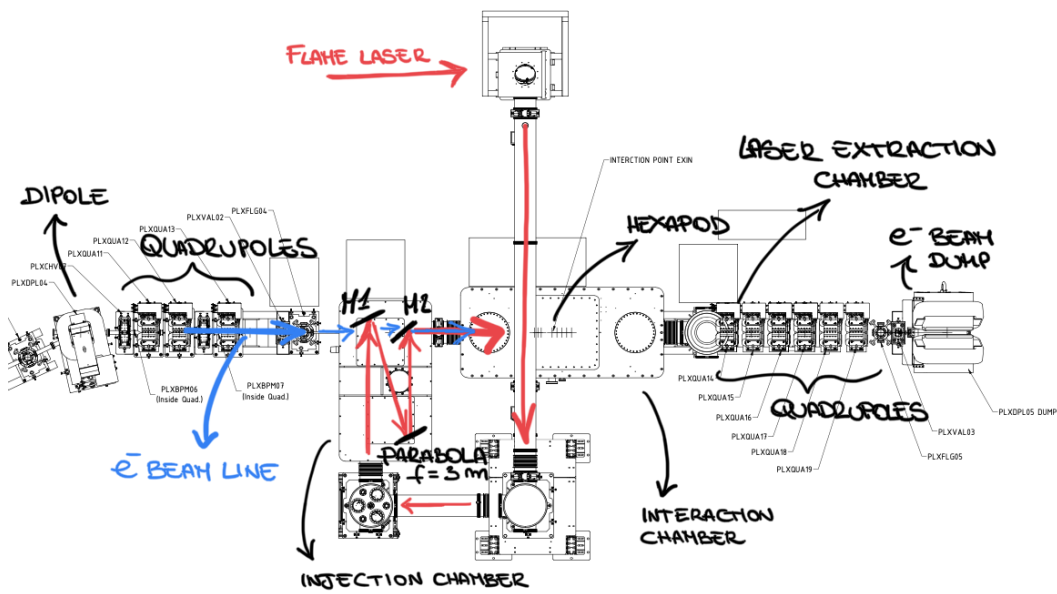


Figure 7.22. CAD design of a portion of the EXIN line: in addition to the laser transport chambers, the beam injection chamber, the plasma interaction chamber and the laser beam extraction chamber are highlighted.

Conclusions

PLASMA ACCELERATION aims to reduce the size of modern accelerators, in order to allow their wider use in all the sectors in which they are already used today, from medicine to industry, as well as in the research field [10]. The work of this project is devoted to the study and optimisation of plasma-targets for laser-plasma acceleration (see Chapter 2), identifying techniques to optimise them in both cases of the two schemes provided for this type of acceleration, self and external-injection. It has been carried out in the INFN SPARC_LAB laboratories (see Section 3.1).

For the plasma characterisation, different plasma density measurement techniques have been used, exploiting both interferometric and spectroscopic methods (see Chapters 4 - 5 - 7). The former are usually used to detect sources with very high densities (greater than 10^{19} cm^{-3}) but limited size (few millimetres), such as in the case of plasma channels generated in self-injection experiments, since they can be conveniently superimposed on a laser probe spot. The latter are typically used for sources extending up to several centimetres, generally of pre-formed plasma with densities of up to 10^{19} cm^{-3} , for experiments involving the external injection of electron beams.

For the case of self-injection, the mechanism of plasma generation by means of a high-power laser pulse from a gas jet has been considered. A mathematical model for studying the behaviour of supersonic gas jets has then been presented, together with related fluid-dynamic simulations and experimental plasma density data (see Chapter 4). Specifically, it has been verified that, by smoothing the shape of the nozzle, it is possible to obtain higher densities of the outgoing gas, and hence of the plasma generated by the pulse. Using approximately 300 *mJ* of the compressed FLAME laser pulse for helium plasma generation, interferometric measurements of plasma density for two different types of nozzle geometries have been carried out and reported. They show that appropriately modelling the nozzle shape results in an increase in peak plasma density of about a factor of 2.5, and a more uniform plasma profile.

All the rest of the work focused on the study and the implementation of the guiding process for laser pulses within pre-formed plasma channels, a process necessary to increase the acceleration length in the external-injection scheme (see Section 5.1). In detail, a special experimental station was set up to test the plasma generation in capillaries filled with hydrogen, and the guiding of low-power pulses inside them. It has therefore been demonstrated that a density plasma transverse hollow profile, uniform longitudinally, is capable of guiding a laser pulse, of approximately 10 *mJ* and ultra-short, over a distance of 3 *cm*. Using a channel diameter of 500 μm , by means of a discharge with a peak current of 450 *A*, a plasma density

$n_e = 2.5 \times 10^{18} \text{ cm}^{-3} \pm 8\%$ was generated, with a Δ_{n_e} of $0.6 \times 10^{18} \text{ cm}^{-3} \pm 5\%$. These conditions made it possible to drive the pulse with a spot of $120 \mu\text{m}$ FW $1/e^2$ (see Chapter 5).

In this context studies, fluid-dynamic simulations, spectroscopic plasma density measurements and pulse guiding tests have been carried out for different plasma channel geometries (see Chapter 6): both in terms of diameter size and hydrogen injection, together with a study on the modelling of plasma ramps outside the channel (see Section 6.5).

Based on the ideal conditions found for guiding the laser beam, a roadmap has been introduced which includes new applications from the point of view of plasma diagnostics, as well as new methods of injecting and removing laser pulses into pre-formed plasma channels (see Chapter 7). Specifically, a project concerning the possibility of carrying out interferometric measurements of plasma density through channels with a circular cross-section, without introducing phase shift in the measurement, has been presented (see Section 7.1.1): simulations combined with first measurements have been reported.

In the specific context of the international CAMEL project, instead, a model of capillary with partially curved channel has been designed and realised, inside which the plasma has been generated (see Section 7.1.3). The purpose of this technique is to allow, through curved channels, the injection of multiple laser pulses within a main straight channel. In a laser-plasma acceleration scheme with external-injection, this method would allow for very compact staging of the acceleration process.

Finally, the project for the guiding tests of a high power pulse, using the main laser of FLAME, was presented. For this purpose the guiding results obtained so far will be used, and these future tests are preparatory to an external-injection experiment that will exploit, in addition to the FLAME high power pulse, the electron beam produced by the SPARC Linac (see Section 7.2).

Appendix A

The Mach-Zender interferometer

Interferometric diagnostics are widely used to study gas and plasma densities in plasma-based acceleration experiments [118, 137, 159].

In most interferometers, the two interfering beams are generated from the same source, because experimentally the waves emitted by two independent light sources cannot be coherent, since the phase relationship between them changes vary rapidly over time. Splitting of the source beam can be done in two different ways: by wavefront or amplitude splitting. In the first case (e.g. the Fresnel interferometer) the wavefront of a spatially coherent light source, coming for example from a slit, is divided by passing through two closely spaced slits, so the two parts of the wavefront travel through different paths and then they are reunited to produce fringe patterns. This method is useful for narrow sources. In the second case, on the other hand, the amplitude (i.e. the intensity) of the beam is divided in two parts by partial reflection at a surface. Again the two parts travel through different paths and reunite on the detector/screen. This method is suitable for extended sources and it is the most used in laser plasma experiments. In general, the difference between the different types of interferometers used with these techniques is the fact that the two paths generated travel along the same line or not. Usually, a lens system is added to the interferometer patterns to provide image magnification.

In the *Mach-Zehnder* interferometer the probe beams are split in amplitude and follow different pathways before interfering. This simplifies the interpretation of the observed fringes by passing light through the test area only once [160, 161]. It is one the most used for plasma density measurements for its simplicity and its robustness [13, 71]. A typical setup for the Mach-Zehnder interferometer for plasma density measurement is given in Fig. A.1.

The beam is split into equal branches, one of which passes through the sample (in this case the gas or plasma), while the other (called the *reference beam*) does not. The two are then recombined using a second beam splitter, and the interference fringes between the two thus obtained are transported to a CCD. The fringe spacing and the plane of localisation of the fringes obtained with an external source can be controlled by varying the angle between the beams adjusting the last beam splitter before the imaging optic, while the difference between the two arms can be adjusted

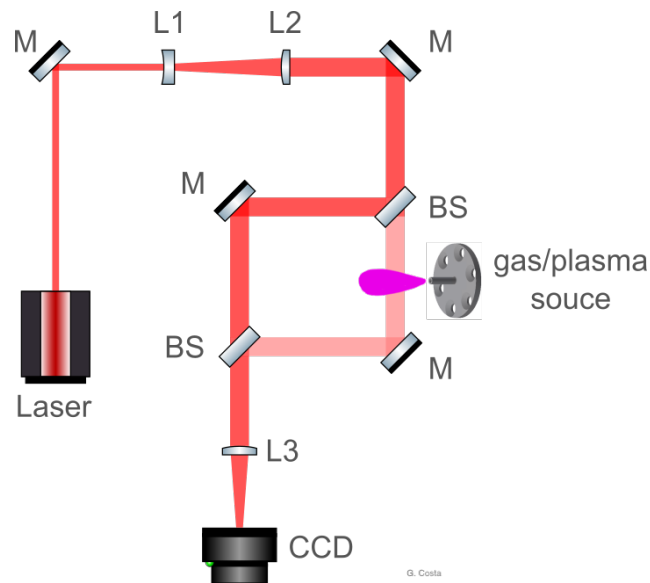


Figure A.1. Mach-Zender interferometer setup scheme for plasma density measurement.

by finely shifting one of them. From the interferogram thus created, it is possible to determine the refractive index of the medium through which the beams pass: if the same material (e.g. air) is present along the path of the two different branches, the fringes will be uniform along the entire overlap of the two beams. If, on the other hand, on one of the two branches there is, for example, also another sample, of smaller extension than that of the beam, the portion of the beam affected by the phenomenon will be subject to a phase shift. The shape of the fringes located at that point will be different, and it will therefore be possible to reconstruct a phase difference between the two conditions, which will depend on the difference in refractive index between the air and the sample, in this case.

Appendix B

OpenFOAM simulations for gas-filled capillaries

Simulations capable of reproducing the trend of the neutral gas before the discharge can help to understand how to obtain a gas profile that is as suitable as possible for the formation of a uniform plasma along the channel. It is important to understand which capillary geometry is most convenient (length, diameter, number of inlets, type of outlet), what type of gas or gas mixture, and what initial system conditions (pressure, temperature) to set up. The process of producing the capillary, CAD project, 3D printing and possible assembly of components, depends on the simulated results.

Starting from the existing CAD projects (example in Fig. (5.41)) with which the capillaries used in the laboratory are 3D-printed, simulations have been built in *OpenFOAM* (*Open-source Field Operation And Manipulation*, openfoam.com), a C++ toolbox for the development of customised numerical solvers, and pre/post-processing utilities for the solution of continuum mechanics problems, most prominently including Computational Fluid Dynamics (CFD). By means of the use of *sonicFOAM*, a transient solver for trans-sonic/supersonic turbulent flow of a compressible gas, it is possible to solve the Euler partial differential equations (Cauchy equations of conservation of mass and balance of momentum and energy), using both Dirichlet and Neumann boundary conditions, depending on the variables considered. The aim of the simulation is to obtain the distribution of the gas density inside and immediately outside the capillary, from the moment in which the gas is injected to the moment in which the discharge begins. In the simulated geometry of the capillary there is an inlet that replicates the solenoid valve open for the whole time of the simulation (typically 3 *ms*), on which a gas pressure (typically helium) is applied in the range between 50 *mbar* and 3000 *mbar*. There are two outlet zones that simulate the vacuum out in the proximity of the capillary. The thermal conductivity condition can be set on the capillary surface, imposing a fixed ambient temperature as a boundary condition in that region (fixed temperature isotherm), while null flow is set on this surface, which means a zero pressure derivative condition. For the CFL (Courant Friedrichs Lewy) convergence condition a Courant parameter, typically in the range 0.01 – 0.1, is set, while the time step of the simulation is variable in the range 10^{-15} - 10^{-7} , for each iteration.

Using the simulated gas pressure, temperature and velocity variables, it is possible to calculate the gas density for each point at each moment of the simulation. An example of the result of these simulations in OpenFOAM is in Fig. (B.1): It represents the 3D geometry of a capillary with a length of 3 cm and a diameter of 0.5 mm; in detail the neutral density (helium) n_0 and the gas pressure p at the final time. From this mesh it is then possible to trace the elementary and derived variables of interest, such as pressure, speed in the three directions and temperature for each calculated time instant. It can be deduced, for example, that the condition shown in Fig. B.1 is the thermodynamic equilibrium, i.e. the system evolves temporally leaving the values of the variables unchanged. This is useful to understand, depending on the geometry and the initial pressure applied on the main inlet, how to time the opening of the solenoid valve and the discharge trigger.

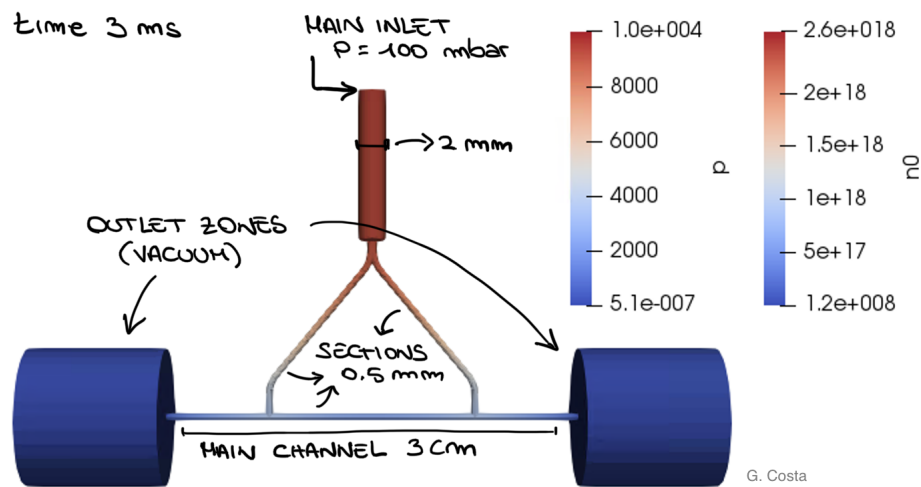


Figure B.1. OpenFoam simulation: gas density n_0 after 3 ms, for a capillary of length 3 cm and diameter 0.5 mm. The pressure on the main inlet is 100 mbar.

Another thing that can be deduced from fluid-dynamic simulations of this type, is the trend of the pressure as a function of the velocity fields, inside and immediately outside the capillary, for complex geometries, involving channel branching or curved channels (see Figs. B.2 and B.3), with specific gas injection systems. It can be deduced, for example, an estimate of the pressure outside the capillary near the outlets, which depends proportionally not only on the initial pressure value but also on the diameter of the channel in relation to its length. This ratio determines the increase in outlet velocity, which for some configurations can reach supersonic values. This last aspect in particular contributes to the characteristics of the plasma plumes generated as a result of the discharge. The design of spacers such as those shown in Fig. B.2 is aimed precisely at controlling gas and plasma leaving the main channel, an important aspect both for the matching with the beam (laser or electron beam) and for the management of the vacuum pumping system (more details in Section 6.5). The example of the results obtained instead in Fig. B.3 shows that the gas injected in the common and curved sections fills the channel from straight to curved, generating a negligible velocity and pressure field for gas in the other branch. This

guarantees a privileged path for the discharge that will be generated in the channel (more details in Section 7.1.3).

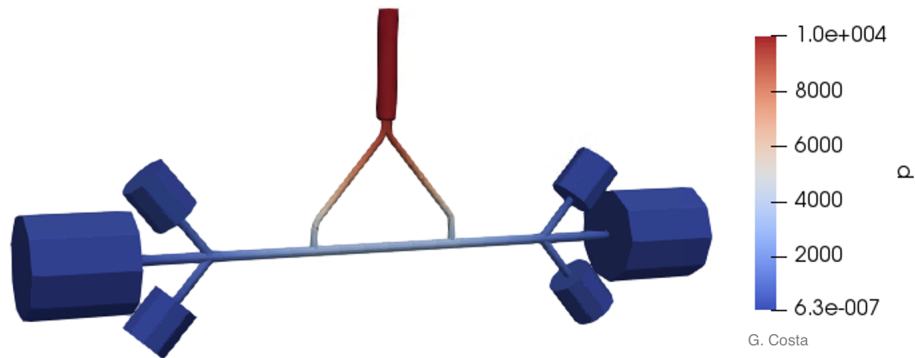


Figure B.2. OpenFoam simulation: gas pressure p after 3 ms, for a capillary of length 6 cm and diameter 0.5 mm, with a central bifurcation into two channels, one of which is curved. The pressure on the main inlet is 100 mbar.

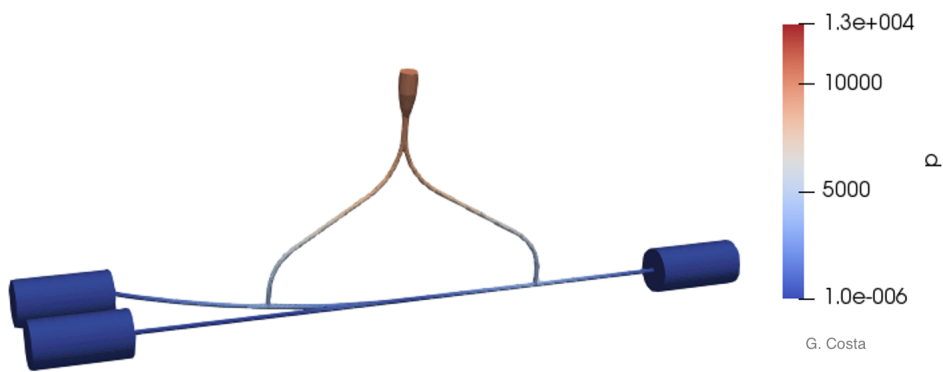


Figure B.3. OpenFoam simulation: gas pressure p after 3 ms, for a capillary of length 3 cm and diameter 1 mm, with two 1 cm long spacers at each end. The pressure on the main inlet is 100 mbar.

Bibliography

- [1] Paul Gibbon. Introduction to plasma physics. *arXiv preprint arXiv:2007.04783*, 2020.
- [2] T Tajima and JM Dawson. Laser electron accelerator. *Physical Review Letters*, 43(4):267, 1979.
- [3] Brigitte Cros. Laser-driven plasma wakefield: Propagation effects. *arXiv preprint arXiv:1705.10566*, 2017.
- [4] E Esarey, CB Schroeder, and WP Leemans. Physics of laser-driven plasma-based electron accelerators. *Reviews of Modern Physics*, 81(3):1229, 2009.
- [5] Donna Strickland and Gerard Mourou. Compression of amplified chirped optical pulses. *Optics communications*, 56(3):219–221, 1985.
- [6] DJ Spence and Simon Mark Hooker. Investigation of a hydrogen plasma waveguide. *Physical Review E*, 63(1):015401, 2000.
- [7] DG Jang, MS Kim, IH Nam, HS Uhm, and H Suk. Density evolution measurement of hydrogen plasma in capillary discharge by spectroscopy and interferometry methods. *Applied Physics Letters*, 99(14):141502, 2011.
- [8] Seong Y Oh, Han S Uhm, Hoonsoo Kang, In W Lee, and Hyyong Suk. Temporal evolution of electron density and temperature in capillary discharge plasmas. *Journal of Applied Physics*, 107(10):103309, 2010.
- [9] NA Bobrova, AA Esaulov, J-I Sakai, PV Sasorov, DJ Spence, Arthur Butler, Simon Mark Hooker, and SV Bulanov. Simulations of a hydrogen-filled capillary discharge waveguide. *Physical Review E*, 65(1):016407, 2001.
- [10] AP Chernyaev and SM Varzar. Particle accelerators in modern world. *Physics of Atomic Nuclei*, 77(10):1203–1215, 2014.
- [11] Eric Esarey, Phillip Sprangle, Jonathan Krall, and Antonio Ting. Overview of plasma-based accelerator concepts. *IEEE Transactions on plasma science*, 24(2):252–288, 1996.
- [12] Francis F Chen. Physical mechanism of current-free double layers. *Physics of plasmas*, 13(3):034502, 2006.

- [13] G Costa, MP Anania, F Bisesto, E Chiadroni, A Cianchi, A Curcio, M Ferrario, F Filippi, A Marocchino, F Mira, et al. Characterization of self-injected electron beams from lwfa experiments at sparc_lab. *Nuclear Instruments and Methods in Physics Research Section A: Accelerators, Spectrometers, Detectors and Associated Equipment*, 909:118–122, 2018.
- [14] Victor Malka, Jérôme Faure, Yann A Gauduel, Erik Lefebvre, Antoine Rousse, and Kim Ta Phuoc. Principles and applications of compact laser–plasma accelerators. *Nature physics*, 4(6):447–453, 2008.
- [15] AJ Gonsalves, K Nakamura, J Daniels, C Benedetti, C Pieronek, TCH De Raadt, S Steinke, JH Bin, SS Bulanov, J Van Tilborg, et al. Petawatt laser guiding and electron beam acceleration to 8 gev in a laser-heated capillary discharge waveguide. *Physical review letters*, 122(8):084801, 2019.
- [16] John M Dawson. Nonlinear electron oscillations in a cold plasma. *Physical Review*, 113(2):383, 1959.
- [17] Aleksander Ilyich Akhiezer and RV Polovin. Theory of wave motion of an electron plasma. *Soviet Phys. JETP*, 3, 1956.
- [18] T Katsouleas and JM Dawson. Unlimited electron acceleration in laser-driven plasma waves. *Physical Review Letters*, 51(5):392, 1983.
- [19] C Joshi, WB Mori, T Katsouleas, JM Dawson, JM Kindel, and DW Forslund. Ultrahigh gradient particle acceleration by intense laser-driven plasma density waves. *Nature*, 311(5986):525–529, 1984.
- [20] Pisin Chen, JM Dawson, Robert W Huff, and Thomas Katsouleas. Acceleration of electrons by the interaction of a bunched electron beam with a plasma. *Physical review letters*, 54(7):693, 1985.
- [21] Francis F Chen et al. *Introduction to plasma physics and controlled fusion*, volume 1. Springer, 1984.
- [22] Alexancer Pukhov and Jürgen Meyer-ter Vehn. Laser wake field acceleration: the highly non-linear broken-wave regime. *Applied Physics B*, 74(4):355–361, 2002.
- [23] Wei Lu, M Tzoufras, C Joshi, FS Tsung, WB Mori, J Vieira, RA Fonseca, and LO Silva. Generating multi-gev electron bunches using single stage laser wakefield acceleration in a 3d nonlinear regime. *Physical Review Special Topics-Accelerators and Beams*, 10(6):061301, 2007.
- [24] Francis F Chen. *Introduction to plasma physics*. Springer Science & Business Media, 2012.
- [25] Robert Bingham and R Trines. Introduction to plasma accelerators: the basics. *arXiv preprint arXiv:1705.10535*, 2017.
- [26] William L Kruer. The physics of laser plasma interaction, 1988.

- [27] Paul Gibbon. *Short pulse laser interactions with matter: an introduction*. World Scientific, 2005.
- [28] WL Kruer. The physics of laser plasma interactions (boulder, co, 2003).
- [29] JB Rosenzweig, B Breizman, T Katsouleas, and JJ Su. Acceleration and focusing of electrons in two-dimensional nonlinear plasma wake fields. *Physical Review A*, 44(10):R6189, 1991.
- [30] J Vieira, RA Fonseca, and LO Silva. Multidimensional plasma wake excitation in the non-linear blowout regime. *arXiv preprint arXiv:1607.03514*, 2016.
- [31] CGR Geddes, Cs Toth, J Van Tilborg, E Esarey, CB Schroeder, D Bruhwiler, C Nieter, J Cary, and WP Leemans. Production of high-quality electron bunches by dephasing and beam loading in channeled and unchanneled laser plasma accelerators. *Physics of Plasmas*, 12(5):056709, 2005.
- [32] Andrea Mostacci, M Bellaveglia, E Chiadroni, A Cianchi, M Ferrario, D Filippetto, G Gatti, and C Ronsivalle. Chromatic effects in quadrupole scan emittance measurements. *Physical Review Special Topics-Accelerators and Beams*, 15(8):082802, 2012.
- [33] Bradley Allan Shadwick, Carl B Schroeder, and Eric Esarey. Nonlinear laser energy depletion in laser-plasma accelerators. *Physics of Plasmas*, 16(5):056704, 2009.
- [34] CD Decker, WB Mori, K-C Tzeng, and T Katsouleas. The evolution of ultra-intense, short-pulse lasers in underdense plasmas. *Physics of Plasmas*, 3(5):2047–2056, 1996.
- [35] Mataloni Paolo and Dott Ghigo Andrea. Coherent light sources and optical techniques for thomson scattering and laser-plasma experiments. 2015.
- [36] Guo-Zheng Sun, Edward Ott, YC Lee, and Parvez Guzdar. Self-focusing of short intense pulses in plasmas. *The Physics of fluids*, 30(2):526–532, 1987.
- [37] P Sprangle, G Joyce, E Esarey, and A Ting. Laser wakefield acceleration and relativistic optical guiding. In *AIP Conference Proceedings*, volume 175, pages 231–239. American Institute of Physics, 1988.
- [38] Eric Esarey, Phillip Sprangle, Jonathan Krall, Antonio Ting, and Glenn Joyce. Optically guided laser wake-field acceleration. *Physics of Fluids B: Plasma Physics*, 5(7):2690–2697, 1993.
- [39] Tom Katsouleas. Physical mechanisms in the plasma wake-field accelerator. *Physical Review A*, 33(3):2056, 1986.
- [40] Phillip Sprangle, B Hafizi, JR Penano, RF Hubbard, A Ting, CI Moore, DF Gordon, A Zigler, D Kaganovich, and TM Antonsen Jr. Wakefield generation and gev acceleration in tapered plasma channels. *Physical Review E*, 63(5):056405, 2001.

- [41] M Ferrario, D Alesini, M Anania, A Bacci, M Bellaveglia, O Bogdanov, R Boni, M Castellano, E Chiadroni, A Cianchi, et al. Sparc_lab present and future. *Nuclear Instruments and Methods in Physics Research Section B: Beam Interactions with Materials and Atoms*, 309:183–188, 2013.
- [42] RW Assmann, MK Weikum, T Akhter, D Alesini, AS Alexandrova, MP Anania, NE Andreev, I Andriyash, M Artioli, A Aschikhin, et al. Eupraxia conceptual design report. *The European Physical Journal Special Topics*, 229(24):3675–4284, 2020.
- [43] M Ferrario, D Alesini, MP Anania, M Artioli, A Bacci, S Bartocci, R Bedogni, M Bellaveglia, A Biagioni, F Bisesto, et al. Eupraxia@ sparc_lab design study towards a compact fel facility at Inf. *Nuclear Instruments and Methods in Physics Research Section A: Accelerators, Spectrometers, Detectors and Associated Equipment*, 909:134–138, 2018.
- [44] Paul Andreas Walker, PD Alesini, AS Alexandrova, Maria Pia Anania, NE Andreev, I Andriyash, A Aschikhin, RW Assmann, T Audet, A Bacci, et al. Horizon 2020 eupraxia design study. In *Journal of Physics: Conference Series*, volume 874, page 012029. IOP Publishing, 2017.
- [45] D Alesini, S Bertolucci, ME Biagini, C Biscari, R Boni, M Boscolo, M Castellano, A Clozza, G Di Pirro, A Drago, et al. The sparc project: a high-brightness electron beam source at Inf to drive a sase-fel experiment. In *Free Electron Lasers 2002*, pages 345–349. Elsevier, 2003.
- [46] FG Bisesto, MP Anania, M Bellaveglia, E Chiadroni, A Cianchi, G Costa, A Curcio, D Di Giovenale, G Di Pirro, M Ferrario, et al. The flame laser at sparc_lab. *Nuclear Instruments and Methods in Physics Research Section A: Accelerators, Spectrometers, Detectors and Associated Equipment*, 909:452–455, 2018.
- [47] G Grittani, MP Anania, G Gatti, DANILO Giulietti, M Kando, M Krus, L Labate, T Levato, P Londrillo, F Rossi, et al. High energy electrons from interaction with a structured gas-jet at flame. *Nuclear Instruments and Methods in Physics Research Section A: Accelerators, Spectrometers, Detectors and Associated Equipment*, 740:257–265, 2014.
- [48] T Levato, M Calvetti, F Anelli, D Batani, R Benocci, L Cacciotti, CA Cecchetti, O Cerafogli, P Chimenti, A Clozza, et al. First electrons from the new 220 tw frascati laser for acceleration and multidisciplinary experiments (flame) at frascati national laboratories (Inf). *Nuclear Instruments and Methods in Physics Research Section A: Accelerators, Spectrometers, Detectors and Associated Equipment*, 720:95–99, 2013.
- [49] LA Gizzi, F Anelli, C Benedetti, CA Cecchetti, A Clozza, G Di Pirro, N Drenska, R Faccini, Danilo Giulietti, D Filippetto, et al. Laser-plasma acceleration with self-injection: A test experiment for the sub-pw flame laser system at Inf-frascati. *Il nuovo cimento C*, 32(3\4):433–436, 2009.

- [50] E Chiadroni, A Bacci, M Bellaveglia, M Boscolo, M Castellano, L Cultrera, G Di Pirro, M Ferrario, L Ficcadenti, D Filippetto, et al. The sparac linear accelerator based terahertz source. *Applied Physics Letters*, 102(9):094101, 2013.
- [51] A Cianchi, D Alesini, A Bacci, M Bellaveglia, R Boni, M Boscolo, M Castellano, L Catani, E Chiadroni, S Cialdi, et al. High brightness electron beam emittance evolution measurements in an rf photoinjector. *Physical Review Special Topics-Accelerators and Beams*, 11(3):032801, 2008.
- [52] M Ferrario, D Alesini, A Bacci, M Bellaveglia, R Boni, M Boscolo, M Castellano, E Chiadroni, A Cianchi, L Cultrera, et al. Experimental demonstration of emittance compensation with velocity bunching. *Physical review letters*, 104(5):054801, 2010.
- [53] M Ferrario, D Alesini, A Bacci, M Bellaveglia, R Boni, M Boscolo, M Castellano, L Catani, E Chiadroni, S Cialdi, et al. Direct measurement of the double emittance minimum in the beam dynamics of the sparac high-brightness photoinjector. *Physical review letters*, 99(23):234801, 2007.
- [54] J. Rosenzweig et Al. L. Palumbo. Technical design report for the sparac advanced photo-injector. 2004.
- [55] J Scifo, D Alesini, MP Anania, M Bellaveglia, S Bellucci, A Biagioni, F Bisesto, F Cardelli, E Chiadroni, A Cianchi, et al. Nano-machining, surface analysis and emittance measurements of a copper photocathode at sparac_lab. *Nuclear Instruments and Methods in Physics Research Section A: Accelerators, Spectrometers, Detectors and Associated Equipment*, 909:233–238, 2018.
- [56] D Filippetto, M Bellaveglia, M Castellano, E Chiadroni, L Cultrera, G Di Pirro, M Ferrario, L Ficcadenti, A Gallo, G Gatti, et al. Phase space analysis of velocity bunched beams. *Physical Review Special Topics-Accelerators and Beams*, 14(9):092804, 2011.
- [57] R Pompili, D Alesini, MP Anania, M Behtouei, M Bellaveglia, A Biagioni, FG Bisesto, M Cesarini, E Chiadroni, A Cianchi, et al. Energy spread minimization in a beam-driven plasma wakefield accelerator. *Nature Physics*, pages 1–5, 2020.
- [58] M Ferrario, D Alesini, A Bacci, M Bellaveglia, R Boni, M Boscolo, P Calvani, M Castellano, E Chiadroni, A Cianchi, et al. Laser comb with velocity bunching: Preliminary results at sparac. *Nuclear Instruments and Methods in Physics Research Section A: Accelerators, Spectrometers, Detectors and Associated Equipment*, 637(1):S43–S46, 2011.
- [59] V Shpakov, MP Anania, M Bellaveglia, A Biagioni, F Bisesto, F Cardelli, M Cesarini, E Chiadroni, A Cianchi, G Costa, et al. Longitudinal phase-space manipulation with beam-driven plasma wakefields. *Physical review letters*, 122(11):114801, 2019.

- [60] Riccardo Pompili, MP Anania, M Bellaveglia, A Biagioni, S Bini, F Bisesto, E Chiadroni, A Cianchi, G Costa, D Di Giovenale, et al. Recent results at sparc_lab. *Nuclear Instruments and Methods in Physics Research Section A: Accelerators, Spectrometers, Detectors and Associated Equipment*, 909:139–144, 2018.
- [61] A Cianchi, MP Anania, F Bisesto, E Chiadroni, A Curcio, M Ferrario, A Giribono, A Marocchino, R Pompili, J Scifo, et al. Frontiers of beam diagnostics in plasma accelerators: Measuring the ultra-fast and ultra-cold. *Physics of Plasmas*, 25(5):056704, 2018.
- [62] Riccardo Pompili, MP Anania, M Bellaveglia, A Biagioni, S Bini, F Bisesto, E Brentegani, F Cardelli, G Castorina, E Chiadroni, et al. Focusing of high-brightness electron beams with active-plasma lenses. *Physical review letters*, 121(17):174801, 2018.
- [63] E Chiadroni, MP Anania, M Bellaveglia, A Biagioni, F Bisesto, E Brentegani, F Cardelli, A Cianchi, G Costa, D Di Giovenale, et al. Overview of plasma lens experiments and recent results at sparc_lab. *Nuclear Instruments and Methods in Physics Research Section A: Accelerators, Spectrometers, Detectors and Associated Equipment*, 909:16–20, 2018.
- [64] Enrica Chiadroni, David Alesini, Maria Pia Anania, Marco Bellaveglia, Angelo Biagioni, Fabrizio Bisesto, Emanuele Brentegani, Fabio Cardelli, Alessandro Cianchi, Gemma Costa, et al. Status of plasma-based experiments at the sparc_lab test facility. In *9th Int. Particle Accelerator Conf.(IPAC'18), Vancouver, BC, Canada, April 29-May 4, 2018*, pages 603–606. JACOW Publishing, Geneva, Switzerland, 2018.
- [65] FG Bisesto, MP Anania, E Chiadroni, A Cianchi, G Costa, A Curcio, M Ferrario, M Galletti, R Pompili, E Schleifer, et al. Innovative single-shot diagnostics for electrons accelerated through laser-plasma interaction at flame. In *Laser Acceleration of Electrons, Protons, and Ions IV*, volume 10240, page 102400K. International Society for Optics and Photonics, 2017.
- [66] FG Bisesto, M Galletti, MP Anania, G Costa, M Ferrario, R Pompili, A Poyé, F Consoli, M Salvadori, M Cipriani, et al. Ultrafast electron and proton bunches correlation in laser–solid matter experiments. *Optics Letters*, 45(19):5575–5578, 2020.
- [67] Fabrizio Bisesto, Mario Galletti, Maria Pia Anania, Gemma Costa, Massimo Ferrario, Riccardo Pompili, Arie Zigler, Fabrizio Consoli, Mattia Cipriani, Martina Salvadori, et al. Simultaneous observation of ultrafast electron and proton beams in tnsa. *High Power Laser Science and Engineering*, 8, 2020.
- [68] M Salvadori, F Consoli, C Verona, M Cipriani, MP Anania, PL Andreoli, P Antici, F Bisesto, G Costa, G Cristofari, et al. Accurate spectra for high energy ions by advanced time-of-flight diamond-detector schemes in experiments with high energy and intensity lasers. *arXiv preprint arXiv:2003.01442*, 2020.

- [69] M Salvadori, F Consoli, C Verona, M Cipriani, PL Andreoli, G Cristofari, R De Angelis, G Di Giorgio, D Giulietti, MP Anania, et al. Assessment of sensitivity improvement for time-of-flight schemes in experiments with high intensity lasers. *Journal of Instrumentation*, 15(10):C10002, 2020.
- [70] A Curcio, M Anania, F Bisesto, E Chiadroni, A Cianchi, M Ferrario, F Filippi, D Giulietti, A Marocchino, M Petrarca, et al. Trace-space reconstruction of low-emittance electron beams through betatron radiation in laser-plasma accelerators. *Physical Review Accelerators and Beams*, 20(1):012801, 2017.
- [71] A Curcio, M Anania, F Bisesto, E Chiadroni, A Cianchi, M Ferrario, F Filippi, D Giulietti, A Marocchino, F Mira, et al. First measurements of betatron radiation at flame laser facility. *Nuclear Instruments and Methods in Physics Research Section B: Beam Interactions with Materials and Atoms*, 2017.
- [72] A Curcio, F Bisesto, G Costa, A Biagioni, MP Anania, R Pompili, M Ferrario, and M Petrarca. Modeling and diagnostics for plasma discharge capillaries. *Physical Review E*, 100(5):053202, 2019.
- [73] G Costa, MP Anania, A Biagioni, FG Bisesto, E Brentegani, M Ferrario, R Pompili, S Romeo, AR Rossi, A Zigler, et al. Plasma density profile measurements for ultra-short high power laser beam guiding experiments at sparc_lab. In *Journal of Physics: Conference Series*, volume 1596, page 012044. IOP Publishing, 2020.
- [74] Gemma Costa. Characterization of electron beams from plasma wakefield acceleration, 2017.
- [75] Leonida Antonio Gizzi, Carlo Benedetti, Carlo Alberto Cecchetti, Giampiero Di Pirro, Andrea Gamucci, Giancarlo Gatti, Antonio Giulietti, Danilo Giulietti, Petra Koester, Luca Labate, et al. Laser-plasma acceleration with flame and ilil ultraintense lasers. *Applied Sciences*, 3(3):559–580, 2013.
- [76] Andrea R Rossi, Alberto Bacci, Marco Belleveglia, Enrica Chiadroni, Alessandro Cianchi, Giampiero Di Pirro, Massimo Ferrario, Alessandro Gallo, Giancarlo Gatti, Cesare Maroli, et al. The external-injection experiment at the sparc_lab facility. *Nuclear Instruments and Methods in Physics Research Section A: Accelerators, Spectrometers, Detectors and Associated Equipment*, 740:60–66, 2014.
- [77] FG Bisesto, MP Anania, AL Bacci, M Bellaveglia, E Chiadroni, A Cianchi, A Curcio, D Di Giovenale, G Di Pirro, M Ferrario, et al. Laser–capillary interaction for the exin project. *Nuclear Instruments and Methods in Physics Research Section A: Accelerators, Spectrometers, Detectors and Associated Equipment*, 829:309–313, 2016.
- [78] R Wagner, S-Y Chen, Anatoly Maksimchuk, and D Umstadter. Electron acceleration by a laser wakefield in a relativistically self-guided channel. *Physical Review Letters*, 78(16):3125, 1997.

- [79] A Ting, CI Moore, K Krushelnick, C Manka, E Esarey, P Sprangle, R Hubbard, HR Burris, R Fischer, and M Baine. Plasma wakefield generation and electron acceleration in a self-modulated laser wakefield accelerator experiment. *Physics of Plasmas*, 4(5):1889–1899, 1997.
- [80] A Modena, Z Najmudin, AE Dangor, CE Clayton, KA Marsh, C Joshi, Victor Malka, CB Darrow, C Danson, D Neely, et al. Electron acceleration from the breaking of relativistic plasma waves. *nature*, 377(6550):606–608, 1995.
- [81] Victor Malka, S Fritzler, E Lefebvre, M-M Aleonard, F Burgy, J-P Chambaret, J-F Chemin, K Krushelnick, G Malka, SPD Mangles, et al. Electron acceleration by a wake field forced by an intense ultrashort laser pulse. *Science*, 298(5598):1596–1600, 2002.
- [82] TAW Wolterink. High-gradient gas-jet targets for laser wakefield acceleration. *University of Twente, Master of Science Thesis, Faculty of Science and Technology, Laser Physics and Nonlinear Optics*, 2011.
- [83] Warren B Mori, Wei Lu, Michail Tzoufras, Frank Tsung, Chan Joshi, Jorge Vieira, Ricardo Fonseca, and Luis Silva. Generating multi-gev electron bunches using laser wakefield acceleration in the blowout regime. In *APS Division of Plasma Physics Meeting Abstracts*, volume 48, pages ZO2–003, 2006.
- [84] Stuart PD Mangles, CD Murphy, Zufikar Najmudin, Alexander George Roy Thomas, JL Collier, Aboobaker E Dangor, EJ Divall, PS Foster, JG Gallacher, CJ Hooker, et al. Monoenergetic beams of relativistic electrons from intense laser–plasma interactions. *Nature*, 431(7008):535–538, 2004.
- [85] S Semushin and Victor Malka. High density gas jet nozzle design for laser target production. *Review of Scientific Instruments*, 72(7):2961–2965, 2001.
- [86] Victor Malka, C Coulaud, JP Geindre, V Lopez, Z Najmudin, D Neely, and François Amiranoff. Characterization of neutral density profile in a wide range of pressure of cylindrical pulsed gas jets. *Review of Scientific Instruments*, 71(6):2329–2333, 2000.
- [87] N Lemos, N Lopes, JM Dias, and F Viola. Design and characterization of supersonic nozzles for wide focus laser-plasma interactions. *Review of Scientific Instruments*, 80(10):103301, 2009.
- [88] Alfred John Ward-Smith. Internal fluid flow—the fluid dynamics of flow in pipes and ducts. *Nasa Sti/recon Technical Report A*, 81:38505, 1980.
- [89] Karen Deere. Summary of fluidic thrust vectoring research at nasa langley research center. In *21st AIAA applied aerodynamics conference*, page 3800, 2003.
- [90] Brian R Hollis. *Real Gas Flow Properties for NASA Langley Research Center Aerothermodynamic Facilities Complex Wind Tunnels*, volume 4755. Citeseer, 1996.

- [91] NASA. Isentropic flow equations, Apr 05 2018.
- [92] AA Ovsyannikov and Mikhail Fedorovich Zhukov. *Plasma diagnostics*. Cambridge Int Science Publishing, 2000.
- [93] H-J Kunze. Plasma diagnostics. In *Plasma Physics*, pages 349–373. Springer, 2005.
- [94] Mitsuo Takeda, Hideki Ina, and Seiji Kobayashi. Fourier-transform method of fringe-pattern analysis for computer-based topography and interferometry. *JosA*, 72(1):156–160, 1982.
- [95] AM Grigoryan and Alexander Poularikas. Multidimensional discrete unitary transforms. in the third edition transforms and applications handbook in the electrical engineering handbook series, 2010.
- [96] P Tomassini and A Giulietti. A generalization of abel inversion to non-axisymmetric density distribution. *Optics Communications*, 199(1-4):143–148, 2001.
- [97] Paolo Tomassini, Antonio Giulietti, Leonida A Gizzi, Marco Galimberti, Danilo Giulietti, Marco Borghesi, and Oswald Willi. Analyzing laser plasma interferograms with a continuous wavelet transform ridge extraction technique: the method. *Applied optics*, 40(35):6561–6568, 2001.
- [98] WP Leemans, CW Siders, E Esarey, NE Andreev, G Shvets, and WB Mori. Plasma guiding and wakefield generation for second-generation experiments. *IEEE Transactions on Plasma Science*, 24(2):331–342, 1996.
- [99] BHP Broks, W Van Dijk, and JJAM Van der Mullen. Parameter study of a pulsed capillary discharge waveguide. *Journal of Physics D: Applied Physics*, 39(11):2377, 2006.
- [100] Javier Alda. Laser and gaussian beam propagation and transformation. *Encyclopedia of optical engineering*, 2013:999–1013, 2003.
- [101] J Daniels. Measuring and modifying plasma density profiles to confine high power lasers. 2017.
- [102] P Monot, T Auguste, Paul Gibbon, F Jakober, G Mainfray, Av Dulieu, MALKALouis-Jacquet, G Malka, and JL Miquel. Experimental demonstration of relativistic self-channeling of a multiterawatt laser pulse in an underdense plasma. *Physical review letters*, 74(15):2953, 1995.
- [103] AB Borisov, AV Borovski, VV Korobkin, AM Prokhorov, OB Shiryayev, XM Shi, TS Luk, A McPherson, JC Solem, K Boyer, et al. Observation of relativistic and charge-displacement self-channeling of intense subpicosecond ultraviolet (248 nm) radiation in plasmas. *Physical review letters*, 68(15):2309, 1992.

- [104] S Jackel, R Burris, J Grun, A Ting, C Manka, K Evans, and J Kosakowski. Channeling of terawatt laser pulses by use of hollow waveguides. *Optics letters*, 20(10):1086–1088, 1995.
- [105] F Dorchies, JR Marques, B Cros, G Matthieussent, C Courtois, T Vélikorousov, P Audebert, JP Geindre, S Rebibo, G Hamoniaux, et al. Monomode guiding of 10 16 w/cm² laser pulses over 100 rayleigh lengths in hollow capillary dielectric tubes. *Physical review letters*, 82(23):4655, 1999.
- [106] CG Durfee III and HM Milchberg. Light pipe for high intensity laser pulses. *Physical review letters*, 71(15):2409, 1993.
- [107] P Volfbeyn, E Esarey, and WP Leemans. Guiding of laser pulses in plasma channels created by the ignitor-heater technique. *Physics of Plasmas*, 6(5):2269–2277, 1999.
- [108] Y Ehrlich, C Cohen, A Zigler, J Krall, P Sprangle, and E Esarey. Guiding of high intensity laser pulses in straight and curved plasma channel experiments. *Physical review letters*, 77(20):4186, 1996.
- [109] B Cros, C Courtois, G Malka, G Matthieussent, JR Marques, F Dorchies, François Amiranoff, S Rebibo, G Hamoniaux, N Blanchot, et al. Extending plasma accelerators: guiding with capillary tubes. *IEEE transactions on plasma science*, 28(4):1071–1077, 2000.
- [110] A Zigler, Y Ehrlich, C Cohen, J Krall, and P Sprangle. Optical guiding of high-intensity laser pulses in a long plasma channel formed by a slow capillary discharge. *JOSA B*, 13(1):68–71, 1996.
- [111] Y Ehrlich, C Cohen, D Kaganovich, A Zigler, RF Hubbard, P Sprangle, and E Esarey. Guiding and damping of high-intensity laser pulses in long plasma channels. *JOSA B*, 15(9):2416–2423, 1998.
- [112] SM Hooker, DJ Spence, and Roland A Smith. Guiding of high-intensity picosecond laser pulses in a discharge-ablated capillary waveguide. *JOSA B*, 17(1):90–98, 2000.
- [113] Tomonao Hosokai, Masaki Kando, Hideki Dewa, Hideyuki Kotaki, Syuji Kondo, Noboru Hasegawa, Kazuhisa Nakajima, and Kazuhiko Horioka. Optical guidance of terrawatt laser pulses by the implosion phase of a fast z-pinch discharge in a gas-filled capillary. *Optics Letters*, 25(1):10–12, 2000.
- [114] Arthur Butler, DJ Spence, and Simon Mark Hooker. Guiding of high-intensity laser pulses with a hydrogen-filled capillary discharge waveguide. *Physical Review Letters*, 89(18):185003, 2002.
- [115] BM Luther, Y Wang, MC Marconi, JLA Chilla, MA Larotonda, and JJ Rocca. Guiding of intense laser beams in highly ionized plasma columns generated by a fast capillary discharge. *Physical review letters*, 92(23):235002, 2004.

- [116] Wim P Leemans, Bob Nagler, Anthony J Gonsalves, Cs Tóth, Kei Nakamura, Cameron GR Geddes, ESCB Esarey, CB Schroeder, and SM Hooker. GeV electron beams from a centimetre-scale accelerator. *Nature physics*, 2(10):696–699, 2006.
- [117] K Nakamura, B Nagler, Cs Tóth, CGR Geddes, CB Schroeder, E Esarey, WP Leemans, AJ Gonsalves, and SM Hooker. GeV electron beams from a centimeter-scale channel guided laser wakefield accelerator. *Physics of Plasmas*, 14(5):056708, 2007.
- [118] AJ Gonsalves, TP Rowlands-Rees, BHP Broks, JJAM Van der Mullen, and SM Hooker. Transverse interferometry of a hydrogen-filled capillary discharge waveguide. *Physical review letters*, 98(2):025002, 2007.
- [119] AJ Gonsalves, J Daniels, W Waldron, SS Bulanov, PV Satorov, NA Bobrova, C Pieronek, S Antipov, F Liu, J Butler, et al. Increasing the repetition rate of capillary discharge waveguides. In *AIP Conference Proceedings*, volume 1777, page 040005. AIP Publishing LLC, 2016.
- [120] AJ Gonsalves, F Liu, NA Bobrova, PV Satorov, C Pieronek, J Daniels, S Antipov, JE Butler, SS Bulanov, WL Waldron, et al. Demonstration of a high repetition rate capillary discharge waveguide. *Journal of Applied Physics*, 119(3):033302, 2016.
- [121] DJ Spence, Arthur Butler, and Simon Mark Hooker. First demonstration of guiding of high-intensity laser pulses in a hydrogen-filled capillary discharge waveguide. *Journal of Physics B: Atomic, Molecular and Optical Physics*, 34(21):4103, 2001.
- [122] NA Bobrova, SV Bulanov, D Farina, R Pozzoli, TL Razinkova, JI Sakai, PV Satorov, and IV Sokolov. Mhd simulations of plasma dynamics in pinch discharges in capillary plasmas. *Laser and particle beams*, 18(4):623–638, 2000.
- [123] Phillip Sprangle, Eric Esarey, Jonathan Krall, and G Joyce. Propagation and guiding of intense laser pulses in plasmas. *Physical review letters*, 69(15):2200, 1992.
- [124] E Esarey and WP Leemans. Nonparaxial propagation of ultrashort laser pulses in plasma channels. *Physical Review E*, 59(1):1082, 1999.
- [125] Carlo Benedetti, CB Schroeder, Eric Esarey, and WP Leemans. Quasi-matched propagation of ultra-short, intense laser pulses in plasma channels. *Physics of Plasmas*, 19(5):053101, 2012.
- [126] F Robben and Lawrence Talbot. Measurement of shock wave thickness by the electron beam fluorescence method. *The Physics of Fluids*, 9(4):633–643, 1966.
- [127] A Biagioni, D Alesini, MP Anania, M Bellaveglia, S Bini, F Bisesto, E Brentegani, E Chiadroni, A Cianchi, O Coiro, et al. Temperature analysis in the shock waves regime for gas-filled plasma capillaries in plasma-based accelerators. *Journal of Instrumentation*, 14(03):C03002, 2019.

- [128] Phillip Sprangle and Eric Esarey. Interaction of ultrahigh laser fields with beams and plasmas. *Physics of Fluids B: Plasma Physics*, 4(7):2241–2248, 1992.
- [129] Eric Esarey, Phillip Sprangle, Jonathan Krall, and Antonio Ting. Self-focusing and guiding of short laser pulses in ionizing gases and plasmas. *IEEE journal of quantum electronics*, 33(11):1879–1914, 1997.
- [130] K Nakajima, D Fisher, T Kawakubo, H Nakanishi, A Ogata, Y Kato, Y Kitagawa, R Kodama, K Mima, H Shiraga, et al. Observation of ultrahigh gradient electron acceleration by a self-modulated intense short laser pulse. *Physical Review Letters*, 74(22):4428, 1995.
- [131] AJ Gonsalves, Kei Nakamura, Chen Lin, Jens Osterhoff, Satomi Shiraishi, CB Schroeder, CGR Geddes, Cs Tóth, Eric Esarey, and WP Leemans. Plasma channel diagnostic based on laser centroid oscillations. *Physics of Plasmas*, 17(5):056706, 2010.
- [132] NA Bobrova, PV Sasorov, C Benedetti, SS Bulanov, CGR Geddes, CB Schroeder, E Esarey, and WP Leemans. Laser-heater assisted plasma channel formation in capillary discharge waveguides. *Physics of Plasmas*, 20(2):020703, 2013.
- [133] A Ya Polishchuk and J Meyer-Ter-Vehn. Electron-ion relaxation in a plasma interacting with an intense laser field. *Physical Review E*, 49(1):663, 1994.
- [134] N David, DJ Spence, and Simon Mark Hooker. Molecular-dynamic calculation of the inverse-bremsstrahlung heating of non-weakly-coupled plasmas. *Physical Review E*, 70(5):056411, 2004.
- [135] Hans Griem. *Spectral line broadening by plasmas*. Elsevier, 2012.
- [136] Hans R Griem. *Principles of plasma spectroscopy*, volume 2. Cambridge University Press, 2005.
- [137] Fernando Brandi and Leonida Antonio Gizzi. Optical diagnostics for density measurement in high-quality laser-plasma electron accelerators. *High Power Laser Science and Engineering*, 7, 2019.
- [138] IH Hutchinson. *Principles of plasma diagnostics* (cambridge: Cambridge university). 2005.
- [139] J Torres, Jeroen Jonkers, MJ Van de Sande, JJAM Van der Mullen, Antonio Gamero, and Antonio Sola. An easy way to determine simultaneously the electron density and temperature in high-pressure plasmas by using stark broadening. *Journal of Physics D: Applied Physics*, 36(13):L55, 2003.
- [140] DG Jang, MS Kim, IH Nam, H Jang, and H Suk. Interferometric density measurement of the gas-filled capillary plasma and its comparison with the $h\beta$ line measurement. *Journal of Instrumentation*, 7(02):C02045, 2012.

- [141] N Konjević, M Ivković, and N Sakan. Hydrogen balmer lines for low electron number density plasma diagnostics. *Spectrochimica Acta Part B: Atomic Spectroscopy*, 76:16–26, 2012.
- [142] Francesco Filippi, Maria Pia Anania, Angelo Biagioni, Enrica Chiadroni, Alessandro Cianchi, Massimo Ferrario, Anna Giribono, Andrea Mostacci, Luigi Palumbo, and Arie Zigler. Plasma density profile characterization for resonant plasma wakefield acceleration experiment at sparc_lab. In *7th Int. Particle Accelerator Conf.(IPAC'16), Busan, Korea, May 8-13, 2016*, pages 2554–2556. JACOW, Geneva, Switzerland, 2016.
- [143] Michael A Lieberman and Alan J Lichtenberg. *Principles of plasma discharges and materials processing*. John Wiley & Sons, 2005.
- [144] MP Anania, E Chiadroni, A Cianchi, D Di Giovenale, M Ferrario, F Flora, GP Gallerano, A Ghigo, A Marocchino, F Massimo, et al. Design of a plasma discharge circuit for particle wakefield acceleration. *Nuclear Instruments and Methods in Physics Research Section A: Accelerators, Spectrometers, Detectors and Associated Equipment*, 740:193–196, 2014.
- [145] A Biagioni, D Alesini, MP Anania, S Arjmand, S Bini, E Chiadroni, A Cianchi, O Coiro, D Di Giovenale, G Di Pirro, et al. High-voltage pulser to produce plasmas inside gas-filled discharge capillaries. Technical report, SPARC-PL-19/001, 2019.
- [146] JM Garland, G Tauscher, S Bohlen, GJ Boyle, R D’Arcy, L Goldberg, K Pöder, L Schaper, B Schmidt, and J Osterhoff. Evolution of longitudinal plasma-density profiles in discharge capillaries for plasma wakefield accelerators. *arXiv preprint arXiv:2010.02567*, 2020.
- [147] A Marocchino, MP Anania, M Bellaveglia, A Biagioni, S Bini, F Bisesto, E Brentegani, E Chiadroni, A Cianchi, M Croia, et al. Experimental characterization of the effects induced by passive plasma lens on high brightness electron bunches. *Applied Physics Letters*, 111(18):184101, 2017.
- [148] S Arjmand, D Alesini, MP Anania, A Biagioni, E Chiadroni, A Cianchi, D Di Giovenale, G Di Pirro, M Ferrario, V Lollo, et al. Characterization of plasma sources for plasma-based accelerators. *Journal of Instrumentation*, 15(09):C09055, 2020.
- [149] Jiaqi Liu, Wentao Li, Jiansheng Liu, Zhiyong Qin, Wentao Wang, Rong Qi, Zhijun Zhang, Changhai Yu, Ming Fang, Ke Feng, et al. Measurement of the matched spot size in a capillary discharge waveguide with a collimated laser. *AIP Advances*, 8(10):105204, 2018.
- [150] Radiant Zemax. Zemax 13 optical design program user’s manual. *Zemax LLC*, 2014.
- [151] F Bisesto, M Galletti, and A Curcio. Zemax ray tracing model for plasma waveguides. *Laser Physics Letters*, 17(3):036001, 2020.

- [152] A Boné, N Lemos, G Figueira, and JM Dias. Quantitative shadowgraphy for laser–plasma interactions. *Journal of Physics D: Applied Physics*, 49(15):155204, 2016.
- [153] Daniel Wolfe and KW Goossen. Evaluation of 3d printed optofluidic smart glass prototypes. *Optics express*, 26(2):A85–A98, 2018.
- [154] Karl Willis, Eric Brockmeyer, Scott Hudson, and Ivan Poupayev. Printed optics: 3d printing of embedded optical elements for interactive devices. In *Proceedings of the 25th annual ACM symposium on User interface software and technology*, pages 589–598, 2012.
- [155] J Kim, VLJ Phung, K Roh, M Kim, K Kang, and H Suk. Development of a density-tapered capillary gas cell for laser wakefield acceleration. *Review of Scientific Instruments*, 92(2):023511, 2021.
- [156] F Filippi, MP Anania, A Biagioni, E Chiadroni, A Cianchi, Y Ferber, M Ferrario, and A Zigler. 3d-printed capillary for hydrogen filled discharge for plasma based experiments in rf-based electron linac accelerator. *Review of Scientific Instruments*, 89(8):083502, 2018.
- [157] J Luo, M Chen, WY Wu, SM Weng, ZM Sheng, CB Schroeder, DA Jaroszynski, E Esarey, WP Leemans, WB Mori, et al. Multistage coupling of laser-wakefield accelerators with curved plasma channels. *Physical review letters*, 120(15):154801, 2018.
- [158] A Zigler, M Botton, Y Ferber, G Johansson, O Pollak, E Dekel, F Filippi, MP Anania, F Bisesto, R Pompili, et al. Consolidating multiple femtosecond lasers in coupled curved plasma capillaries. *Applied Physics Letters*, 113(18):183505, 2018.
- [159] MC Downer, R Zgadza, A Debus, U Schramm, and MC Kaluza. Diagnostics for plasma-based electron accelerators. *Reviews of Modern Physics*, 90(3):035002, 2018.
- [160] Michael Bass. *Handbook of Optics: Volume IV-Optical Properties of Materials, Nonlinear Optics, Quantum Optics*. McGraw-Hill Education, 2010.
- [161] SS Harilal and MS Tillack. Laser plasma density measurements using interferometry. *Fusion Division, Center for Energy Research, University of California, San Diego, La Jolla, CA, 92093:0417*, 2004.

Acknowledgments

First of all, I would like to thank the two referees of this work, M. Galimberti and L. Gizzi, for kindly agreeing to review my PhD studies.

My gratitude goes to my project leader and PhD supervisor, M. Ferrario, for approving my wish to undertake my research in the SPARC_LAB group. My choice to study physics in life is thanks to the months of stage I did in high school exactly in this group. Ever more I realise how crucial it was for my motivation to be in this place so familiar to my mind.

The deepest thanks are definitely reserved for my supervisor A. Cianchi, for all the revisions, for his patience, but most importantly for having always believed in me, more than I did.

I absolutely have to thank my little strong FLAME-Laser-Plasma group, to whom I owe everything, in whom I grew up, and who allowed me to love the world of research. In particular, special thanks to Maria Pia who has always followed my path, to Fabrizio who has taught me almost everything I know, to Mario who has been omnipresent since he arrived, to Angelo for all the experience he has shared with me, to Fabio for his endless availability at any time.

A particular thanks to Riccardo for always providing me with his competence.

A big thank you goes to all the other people in the SPARC_LAB group, as well as in the Accelerator Division, who have worked with me over these years, because I strongly believe that the ideas of individuals gain strength and become great thanks to the cooperation and collaboration of a team.

It is with great satisfaction that I would like to thank all the technicians who took part in my research project in any way, because their contribution was fundamental in achieving the results.

Many thanks to Matteo, who shared the journey with me, always on my side.

Finally, my best thanks go to Marco, for his efficiency as a proofreader, but above all because explaining things to people who want to listen is my best way of understanding them.